OPTIMAL DIRECT YAW MOMENT CONTROL OF A 4WD ELECTRIC VEHICLE

A thesis

presented to

the Faculty of California Polytechnic State University,

San Luis Obispo

In Partial Fulfillment of the Requirements for the Degree

Master of Science in Mechanical Engineering

by

Winston Wight

October 2019

© 2019

Winston Wight

ALL RIGHTS RESERVED

COMMITTEE MEMBERSHIP

TITLE:	Optimal Direct Yaw Moment Control of a 4WD Electric Vehicle
AUTHOR:	Winston James Wight
DATE SUBMITTED:	October 30, 2019
COMMITTEE CHAIR:	Dr. Charles B. Birdsong, Ph.D. Professor of Mechanical Engineering
COMMITTEE MEMBER:	John Fabijanic Lecturer in Mechanical Engineering
COMMITTEE MEMBER:	Dr. William R. Murray, Ph.D. Professor of Mechanical Engineering

Dedicated to my parents, David and Susan.

Their love, support, and encouragement to made it possible to persevere.

AKNOWLEDGEMENTS

I would like to express my sincerest gratitude to my advisor, Dr. Birdsong, for his patient guidance over the course of this thesis and for the opportunity to participate in an exciting area of research. His insight and mentorship continuously pushed me explore every tributary along my path.

I would also like to extend my great appreciation to John Fabijanic and Dr. Murray for sharing their wisdom and advice over the course of my studies.

My special thanks are given to Dr. Widmann for encouraging me to pursue engineering and for making sure I was able to do so. Although not easy, it was a pursuit well worth undertaking.

ABSTRACT

OPTIMAL DIRECT YAW MOMENT CONTROL OF A 4WD ELECTRIC VEHICLE

This thesis is concerned with electronic stability of an all-wheel drive electric vehicle with independent motors mounted in each wheel. The additional controllability and speed permitted using independent motors can be exploited to improve the handling and stability of electric vehicles. In this thesis, these improvements arise from employing a direct yaw moment control (DYC) system that seeks to adapt the understeer gradient of the vehicle and achieve neutral steer by employing a supervisory controller and simultaneously tracking an ideal yaw rate and ideal sideslip angle. DYC enhances vehicle stability by generating a corrective yaw moment realized by a torque vectoring controller which generates an optimal torque distribution among the four wheels. The torque allocation at each instant is computed by finding a solution to an optimization problem using gradient descent, a well-known algorithm that seeks the minimum cost employing the gradient of the cost function. A cost function seeking to minimize excessive wheel slip is proposed as the basis of the optimization problem, while the constraints come from the physical limitations of the motors and friction limits between the tires and road. The DYC system requires information about the tire forces in real-time, so this study presents a framework for estimating the tire force in all three coordinate directions. The sideslip angle is also a crucial quantity that must be measured or estimated but is outside the scope of this study. A comparative analysis of three different formulations of sliding mode control used for computation of the corrective yaw moment and an evaluation of how successfully they achieve neutral steer is presented. IPG Automotive's CarMaker software, a high-fidelity vehicle simulator, was used as the plant model. A custom electric powertrain model was developed to enable any CarMaker vehicle to be reconfigured for independent control of the motors. This custom powertrain, called *TVC_OpenXWD* uses the torque/speed map of a Protean Pd18 implemented with lookup tables for each of the four motors. The TVC_OpenXWD powertrain model and controller were designed in MATLAB and Simulink and exported as C code to run them as plug-ins in CarMaker. Simulations of some common maneuvers, including the J-turn, sinusoidal steer, skid pad, and mu-split, indicate that employing DYC can achieve neutral steer. Additionally, it simultaneously tracks the ideal yaw rate and sideslip angle, while maximizing the traction on each tire. The control system performance is evaluated based on its ability to achieve neutral

steer by means of tracking the reference yaw rate, stabilizing the vehicle by means of reducing the sideslip angle, and to reduce chattering. A comparative analysis of sliding mode control employing a conventional switching function (CSMC), modified switching function (MSMC), and PID control (HSMC) demonstrates that the MSMC outperforms the other two methods in addition to the open loop system.

LIST OF FIGURES

Figure 2.1 Ackermann steering geometry [11]. 7
Figure 2.2 Ackermann control system proposed by Cordeiro. [12] 9
Figure 2.3 Simplified schematic of the DYC control structure [15]. 10
Figure 3.1 Vehicle equivalent mechanical model and body-fixed coordinate system [36]. 14
Figure 3.2 Free body diagram of a wheel [11]. 22
Figure 3.3 Friction circle concept for combined slip modelling [42]. 29
Figure 3.4 Maximum torque vs. speed performance curves for the (a) 70W Maxon 45 Flat Brushless motor and (b) 80 kW Protean Pd18 motor [43, 44]. 31
Figure 3.5 A graphical representation of the motor map showing the torque curves for throttle levels evenly spaced between 0% and 100% throttle. Interstitial curves are interpolated. 32
Figure 4.1 Understeer characteristics during a ramp steer test at 150 km/h: comparison of the passive vehicle and TV-controlled vehicle [39]. 37
Figure 6.1 Unified structure of the force estimator and sideslip angle observer. 66
Figure 6.2 Vertical tire force estimation diagram 68
Figure 6.3 Components of lateral acceleration during normal cornering [30]. 70
Figure 7.1 Torque response of the TVC during straight driving when front and rear wheels have equal stiffness. Vehicle starts at rest, accelerates to 100 km/h, and holds speed. 93
Figure 7.2 Torque response of the TVC to a step steer and moment where u = 45 km/h, δf, step = 120 deg/s and M_z = 2000 Nm. 93
Figure 7.3 Front wheel steer angle for the ramp steer maneuver at u = 45 km/h. 96
Figure 7.4 Yaw rate response during the ramp steer maneuver when u = 45 km/h and δ_{ss} = 120˚. 97
Figure 7.5 Controller steady-state error and CSMC/HSMC switching frequency. 98
Figure 7.6 Sideslip angle response during the ramp steer maneuver when u = 45 km/h and δ_{ss} = 120˚. 98
Figure 7.7 Torque response of the DYC system using the modified sliding mode controller during the ramp steer maneuver when u = 45 km/h and δ_{ss} = 120˚. 99
Figure 7.8 Second-order response at the entrance and termination of the second phase of the J-turn. 100
Figure 7.9 Comparison of the longitudinal force estimate and nonlinear model on the left front tire during a ramp steer maneuver when u = 45 km/h and δ_{ss} = 120˚. 101
Figure 7.10 Comparison of the longitudinal force estimate and nonlinear model on the right front tire during a ramp steer maneuver when u = 45 km/h and δ_{ss} = 120˚. 102
Figure 7.11 Comparison of the longitudinal force estimate and nonlinear model on the left rear tire during a ramp steer maneuver when u = 45 km/h and δ_{ss} = 120˚. 102
Figure 7.12 Comparison of the longitudinal force estimate and nonlinear model on the right rear tire during a ramp steer maneuver when u = 45 km/h and δ_{ss} = 120˚. 103

Figure 7.13 Comparison of the lateral force estimate and nonlinear model on the left front tire during a ramp steer maneuver when u = 45 km/h and δ_{ss} = 120°. 104
Figure 7.14 Comparison of the lateral force estimate and nonlinear model on the right front tire during a ramp steer maneuver when u = 45 km/h and δ_{ss} = 120°. 105
Figure 7.15 Comparison of the lateral force estimate and nonlinear model on the left rear tire during a ramp steer maneuver when u = 45 km/h and δ_{ss} = 120°. 105
Figure 7.16 Comparison of the lateral force estimate and nonlinear model on the right rear tire during a ramp steer maneuver when u = 45 km/h and δ_{ss} = 120°. 106
Figure 7.17 Comparison of the vertical force estimate and nonlinear model on the left front tire during a ramp steer maneuver when u = 45 km/h and δ_{ss} = 120°. 107
Figure 7.18 Comparison of the vertical force estimate and nonlinear model on the right front tire during a ramp steer maneuver when u = 45 km/h and δ_{ss} = 120°. 108
Figure 7.19 Comparison of the vertical force estimate and nonlinear model on the left rear tire during a ramp steer maneuver when u = 45 km/h and δ_{ss} = 120°. 108
Figure 7.20 Comparison of the vertical force estimate and nonlinear model on the right rear tire during a ramp steer maneuver when u = 45 km/h and δ_{ss} = 120°. 109
Figure 7.21 Front wheel steer angle for the sinusoidal steer maneuver at u = 60 km/h. 110
Figure 7.22 Yaw rate response during the sinusoidal steer maneuver when u = 60 km/h. 112
Figure 7.23 Dynamic response of the vehicle when r_d = 0 deg/s and u = 60 km/h. at the end of the sine steer maneuver. 112
Figure 7.24 Sideslip angle response during the sinusoidal steer maneuver when u = 60 km/h. 113
Figure 7.25 Torque response of the DYC system using the modified sliding mode controller during the sinusoidal steer maneuver when u = 60 km/h. 113
Figure 7.26 Comparison of the longitudinal force estimate and nonlinear model on the left front tire during a sinusoidal steer maneuver when u = 45 km/h and δ_{ss} = 120°. 115
Figure 7.27 Comparison of the longitudinal force estimate and nonlinear model on the right front tire during a sinusoidal steer maneuver when u = 45 km/h and δ_{ss} = 120°. 115
Figure 7.28 Comparison of the longitudinal force estimate and nonlinear model on the left rear tire during a sinusoidal steer maneuver when u = 45 km/h and δ_{ss} = 120°. 116
Figure 7.29 Comparison of the longitudinal force estimate and nonlinear model on the right rear tire during a sinusoidal steer maneuver when u = 45 km/h and δ_{ss} = 120°. 116
Figure 7.30 Comparison of the lateral force estimate and nonlinear model on the left front tire during a sinusoidal steer maneuver when u = 45 km/h and δ_{ss} = 120°. 118
Figure 7.31 Comparison of the lateral force estimate and nonlinear model on the right front tire during a sinusoidal steer maneuver when u = 45 km/h and δ_{ss} = 120°. 119
Figure 7.32 Comparison of the lateral force estimate and nonlinear model on the left rear tire during a sinusoidal steer maneuver when u = 45 km/h and δ_{ss} = 120°. 119

Figure 7.33 Comparison of the lateral force estimate and nonlinear model on the right rear tire during a sinusoidal steer maneuver when u = 45 km/h and δ_{ss} = 120° 120
Figure 7.34 Comparison of the vertical force estimate and nonlinear model on the left front tire during a sinusoidal steer maneuver when u = 45 km/h and δ_{ss} = 120° 121
Figure 7.35 Comparison of the vertical force estimate and nonlinear model on the right front tire during a sinusoidal steer maneuver when u = 45 km/h and δ_{ss} = 120° 121
Figure 7.36 Comparison of the vertical force estimate and nonlinear model on the right front tire during a sinusoidal steer maneuver when u = 45 km/h and δ_{ss} = 120° 122
Figure 7.37 Comparison of the vertical force estimate and nonlinear model on the right rear tire during a sinusoidal steer maneuver when u = 45 km/h and δ_{ss} = 120° 122
Figure 7.38 Yaw rate response during the skid pad maneuver when a_x = 0.2 m/s^2 and ρ = 0.0238 m^{-1} 124
Figure 7.39 Sideslip angle response during the skid pad maneuver when a_x = 0.2 m/s^2 and ρ = 0.0238 m^{-1}. 124
Figure 7.40 Understeer gradient during the skid pad maneuver when a_x = 0.2 m/s^2 and ρ = 0.0238 m^{-1} 126
Figure 7.41 Torque response of the DYC system using the modified sliding mode controller during the skid pad maneuver when a_x = 0.2 m/s^2 and ρ = 0.0238 m^{-1}. 127
Figure 7.42 Comparison of the longitudinal force estimate and nonlinear model on the left front tire during a skid pad test where a_x = 0.2 m/s^2. 128
Figure 7.43 Comparison of the longitudinal force estimate and nonlinear model on the right front tire during a skid pad test where a_x = 0.2 m/s^2. 129
Figure 7.44 Comparison of the longitudinal force estimate and nonlinear model on the left rear tire during a skid pad test where a_x = 0.2 m/s^2. 129
Figure 7.45 Comparison of the longitudinal force estimate and nonlinear model on the right rear tire during a skid pad test where a_x = 0.2 m/s^2. 130
Figure 7.46 Comparison of the lateral force estimate and nonlinear model on the left front tire during a skid pad test where a_x = 0.2 m/s^2. 131
Figure 7.47 Comparison of the lateral force estimate and nonlinear model on the right front tire during a skid pad test where a_x = 0.2 m/s^2. 131
Figure 7.48 Comparison of the lateral force estimate and nonlinear model on the left rear tire during a skid pad test where a_x = 0.2 m/s^2. 132
Figure 7.49 Comparison of the lateral force estimate and nonlinear model on the right rear tire during a skid pad test where a_x = 0.2 m/s^2. 132
Figure 7.50 Comparison of the vertical force estimate and nonlinear model on the left front tire during a skid pad test where a_x = 0.2 m/s^2. 133
Figure 7.51 Comparison of the vertical force estimate and nonlinear model on the right front tire during a skid pad test where a_x = 0.2 m/s^2. 134
Figure 7.52 Comparison of the vertical force estimate and nonlinear model on the left rear tire during a skid pad test where a_x = 0.2 m/s^2. 134

Figure 7.53 Comparison of the vertical force estimate and nonlinear model on the right rear tire during a skid pad test where a_x = 0.2 m/s^2..... 135
Figure 7.54 Yaw rate response during the skid pad maneuver where t = 29 s and u = 100 km/h when the friction patch is hit..... 136
Figure 7.55 Sideslip angle response during the braking mu-split maneuver where t = 29 s and u = 100 km/h when the friction patch is hit..... 137
Figure 7.56 Torque response of the DYC system using the modified sliding mode controller during the braking mu-split maneuver where t = 29 s and u = 100 km/h when the friction patch is hit..... 137
Figure 7.57 Demonstration of the yaw response of the three control methods in CarMaker during the braking mu-split test. The greyish-blue patch represents the low mu slick and the results, from left to right are with (a) conventional sliding mode, (b) hybrid sliding mode and (c) modified sliding mode..... 138
Figure 7.58 Comparison of the longitudinal force estimate and nonlinear model on the left front tire for a braking mu-split test where u = 100 km/h when the left tires hit a slick with μ = 0.5 at t = 29 s. 139
Figure 7.59 Comparison of the longitudinal force estimate and nonlinear model on the right front tire for a braking mu-split test where u = 100 km/h when the left tires hit a slick with μ = 0.5 at t = 29 s. 140
Figure 7.60 Comparison of the longitudinal force estimate and nonlinear model on the left rear tire for a braking mu-split test where u = 100 km/h when the left tires hit a slick with μ = 0.5 at t = 29 s. 140
Figure 7.61 Comparison of the longitudinal force estimate and nonlinear model on the right rear tire for a braking mu-split test where u = 100 km/h when the left tires hit a slick with μ = 0.5 at t = 29 s. 141
Figure 7.62 Comparison of the lateral force estimate and nonlinear model on the left front tire for a braking mu-split test where u = 100 km/h when the left tires hit a slick with μ = 0.5 at t = 29 s. 142
Figure 7.63 Comparison of the lateral force estimate and nonlinear model on the right front tire for a braking mu-split test where u = 100 km/h when the left tires hit a slick with μ = 0.5 at t = 29 s. 142
Figure 7.64 Comparison of the lateral force estimate and nonlinear model on the left rear tire for a braking mu-split test where u = 100 km/h when the left tires hit a slick with μ = 0.5 at t = 29 s. 143
Figure 7.65 Comparison of the lateral force estimate and nonlinear model on the right rear tire for a braking mu-split test where u = 100 km/h when the left tires hit a slick with μ = 0.5 at t = 29 s. 143
Figure 7.66 Comparison of the vertical force estimate and nonlinear model on the left front tire for a braking mu-split test where u = 100 km/h when the left tires hit a slick with μ = 0.5 at t = 29 s. 144
Figure 7.67 Comparison of the vertical force estimate and nonlinear model on the right front tire for a braking mu-split test where u = 100 km/h when the left tires hit a slick with μ = 0.5 at t = 29 s. 145
Figure 7.68 Comparison of the vertical force estimate and nonlinear model on the left rear tire for a braking mu-split test where u = 100 km/h when the left tires hit a slick with μ = 0.5 at t = 29 s. 145
Figure 7.69 Comparison of the vertical force estimate and nonlinear model on the right rear tire for a braking mu-split test where u = 100 km/h when the left tires hit a slick with μ = 0.5 at t = 29 s. 146

LIST OF TABLES

Table 3-1 Motor map of the Protean Pd18 where torque is a function of the rotational speed (rpm) and throttle (%). Values between the discrete levels in this table are interpolated. Values highlighted green must be added manually, while the values in orange are computed automatically from them [41]. *31*

Table 3-2 Vehicle parameter sets used in simulation. 4MIDEV data generated from default dataset for a medium-class vehicle with RT 195 65R15 p2.50 tires. *32*

Table 5-1 Selected parameter values for Primal-Dual Gradient Algorithm. *63*

NOMENCLATURE

CSMC	*Conventional sliding mode control*
DYC	*Direct yaw control*
EKF	*Extended Kalman filter*
EOM	*Equation of motion*
ESC	*Electronic stability control*
FEV	*Fully electric vehicle*
FWD	*Front-wheel drive*
HEV	*Hybrid electric vehicle*
HSMC	*Hybrid sliding mode control (SMC+PID)*
ICV	*Internal combustion vehicle*
IMU	*Inertial measurement unit*
IWM	*In-wheel motor*
MSMC	*Modified sliding mode control*
RWD	*Rear-wheel drive*
SAE	*Society of Automotive Engineers*
SMC	*Sliding mode control*
SSIV	*Small-scale intelligent vehicle*
TVC	*Torque vectoring control*
TVD	*Torque vectoring differential*
UKF	*Unscented Kalman filter*
UTFE	*Unified tire force estimator*
4MIDEV	*Four in-wheel motor independent drive electric vehicle*

4WD	*Four-wheel drive*
4WS	*Four-wheel steer*

TABLE OF CONTENTS

1 Introduction *1*

2 Literature Review and Background *4*

2.1 Torque Vectoring Control Approaches **5**

2.1.1 Equal Torque Method 5

2.1.2 Ackermann Method 6

2.1.3 Direct Yaw Moment Control 9

3 Vehicle Model *13*

3.1 Vehicle Equivalent Mechanical Model **13**

3.2 Vehicle Equations of Motion **15**

3.3 Wheel Equations of Motion **21**

3.3.1 Tire Model: Pacejka's Magic Formula 22

3.3.2 Tire Model: Dugoff's Model 27

3.4 Electric Motors **30**

3.4.1 Peak Torque Curve 30

3.4.2 Electric Motor Map 31

3.5 Vehicle Parameterization **32**

4 Direct Yaw Moment Control (DYC) *35*

4.1 Supervisory Control **35**

4.2 Sliding Mode Control **40**

4.2.1 Sliding Mode Methods 41

4.3 Speed Controller **51**

5 Torque Vectoring Control *52*

5.1 Dynamic Constraints **53**

5.2 Objective Function **58**

5.2.1 Longitudinal Slip Power Loss 58

5.3 Primal-Dual Gradient Algorithm **61**

6 Unified Tire Force Estimator *65*

6.1 Longitudinal Tire Force Estimation 66

6.2 Vertical Tire Force Estimation 68

6.2.1 Roll Plane Model 69

6.2.2 Lateral Acceleration Correction 69

6.2.3 Lateral Load Transfer Models 70

6.2.4 Kalman Filter Design for Vertical Force Estimation 75

6.3 Lateral Tire Force Estimation 76

6.3.1 Nonlinear State-Space Model 77

6.3.2 Kalman Filter Design for Lateral Force and Sideslip Estimation 82

7 Simulation Results 89

7.1 Unified Tire Force Estimator Summary 91

7.2 Open Loop TVC Results 92

7.3 Closed Loop DYC Results 94

7.3.1 J-Turn 95

7.3.2 Sine Steer Test 109

7.3.3 Skid Pad Test 123

7.3.4 Braking Mu Split Test 135

8 Conclusion and Recommendations 147

8.1 Conclusions 147

8.2 Recommendations 148

8.2.1 Implementation on the Cal Poly SSIV 148

8.2.2 Refinement of the Unified Tire Force Estimator 149

8.2.3 Experiment with New Cost Functions 149

9 Appendix 150

9.1 Direct Yaw Moment Control 150

9.1.1 Supervisory Controller (K=0) 151

9.1.2 Conventional Sliding Mode Controller 152

9.1.3 Modified Sliding Mode Controller 153

9.1.4 Primal-Dual Gradient Descent 154

9.1.5 Torque-Vectoring Controller 156

9.1.6 Wheel System Longitudinal Velocity 157

9.1.7 Torque Constraints (Level 1) 158
9.1.8 Torque Constraints--Motor (Level 2) 159
9.1.9 Torque Constraints—Road Adhesion (Level 2) 160
9.1.10 Torque Constraints—Friction Circle (Level 2) 161
9.1.11 Dynamic Constraint Matrix 162
9.2 Unified Tire Force Estimator 163
9.2.1 Longitudinal Tire Force Estimator Block with I/O 164
9.2.2 Lateral Tire Force Estimation 165
9.2.3 Vertical Tire Force Estimation 170
10 Bibliography 175

1 INTRODUCTION

Electric vehicles symbolize a call to duty for the automotive industry to meet the challenges of tomorrow. New regulations capping emissions and pollution create pressure to make the switch from internal combustion engines to a new alternative, but few technologies have offered a combination of range, performance, and supporting infrastructure that rivals that of conventional vehicles. As the use of electric vehicles increases around the world, academic and private researchers are putting more and more effort into improving the technologies supporting them. Although battery life and durability have been major challenges, they are continuously improving and are supported by current research into energy recovery and performance enhancement. Electric vehicles are generally classified according to the configuration of their powertrain and related components (FEV, HEV, F/R/4WD, IWM, TVD, 4MIDEV) which includes the type of energy storage as well as the number and location of the motors.

Among the numerous classifications of electric vehicles, one of the most compelling is the four in-wheel motor independent drive electric vehicle (4MIDEV) as it has the greatest capacity for development and optimization. These vehicles are equipped with motors mounted within each wheel carrier. This results in a significant change in vehicle structure and base performance due to the redistribution of sprung and unsprung mass. The independence of the motors from one another means that, in the context of electronic stability control (ESC), there are more controllable signals than states. When there are more potential control inputs than states in a system, it means that there may be more than one possible combination of control commands to satisfy some desired behavior. Consequently, there is a large bandwidth to achieve several control objectives simultaneously without loss of quality in controller performance. Recent research conducted by the Seventh Framework Program has demonstrated that fully electric vehicles (FEVs) outfitted with independently controlled in-wheel motors can alter their steady state and transient handling response using active control schemes. In addition, the fast response time and high controllability of electric motors within each wheel can bring significant benefit to the control of lateral dynamics in all situations [1, 2].

At its base level, this thesis aims to exploit the previously mentioned advantages brought by the 4MIDEV. The most significant improvement with respect to conventional combustion vehicles is the ability to provide each wheel with a different torque signal. This improvement permits the design of an optimal TVC algorithm. Torque vectoring is a technology that allows enhanced performance by setting the understeer characteristics of a vehicle going through a turn purely by varying the torque distribution. Depending on the driving scenario, the understeer characteristic can be set to enhance performance or safety. This is also made possible in combustion vehicles by use of advanced

mechanical torque vectoring differentials and is usually adopted in all-wheel drive vehicles. However, even in these cases, the combustion vehicle suffers from slower response times and traction loss while shifting gears. With all this considered, having four independently controlled motors gives the potential for enormous improvements in the application of torque vectoring.

Toward the realization of functional torque vectoring control via DYC, it is necessary to define several stages of yaw moment control. The first stage of control uses a supervisory controller which, for a given steer angle and velocity, computes the reference yaw rate and sideslip angle corresponding to a desired understeer gradient using a simple bicycle model. The next stage of control is referred to as the high-level controller and generates a corrective yawing moment on the vehicle body from the difference between the two reference signals and their actual values at each time step. The last stage is a low-level controller, or TVC, which computes the optimal torque distribution that satisfies the corrective yawing moment as well as the base torque required to maintain a velocity setpoint. The primary objective of this thesis is to compare the ability of three DYC systems with different high-level controllers but the same low-level controller in achieving neutral steer, which is achieved by tracking the output of the supervisory controller while simultaneously maximizing available traction at any given moment. In the absence of feedback from the UTFE, the force terms in the sliding mode control command are replace with PID control to minimize steady-state error, which would otherwise occur. However, PID control reduces the transient performance of the controller.

The control systems were implemented in IPG CarMaker, a high-fidelity vehicle simulation package with several maneuvers, including the J-turn, double lane change, skid pad. Results of the simulations under each controller configuration were compared to evaluate the tracking performance and power usage of each configuration and highlight the relative strengths and weaknesses.

This thesis is organized into eight chapters. In Chapter 1, an introduction to the research background, research motivations and research objectives are given. To address these objectives, extensive research was reviewed to establish the state-of-the-art of vehicle dynamics, yaw control methods, parameter and state estimation, numerical optimization and validation techniques relevant to electronic stability control. Chapter 2 presents a comprehensive literature review to summarize the topics. In Chapter 3, the complete vehicle model and tire model are presented to predict the true longitudinal and lateral dynamics of the vehicle. In Chapter 4, based on the vehicle equations of motion, the mathematical relationships governing closed loop control of yaw rate and sideslip angle are derived. The control of yaw-dynamics fundamentally changes the understeer characteristic of a vehicle, which is discussed in detail. Sideslip angle cannot be measured directly without exotic sensors. These sensors are very expensive and are currently not integrated into commercial vehicles. Likewise, tire-road friction coefficient and force are crucial values, but are incredibly difficult to

measure. However, both variables can be estimated to a reasonable degree using estimation algorithms. The vehicle model is simplified to the well-known bicycle model and is used in Chapter 5 to develop the optimal torque vectoring system. A simplified model is used to minimize computational cost in the embedded system environment. Algorithms to estimate both sideslip angle and tire forces are derived in Chapter 6. In Chapter 7, the estimators are integrated with the DYC system and were simulated in CarMaker to verify that the system with conventional sliding mode control (CSMC) and with modified sliding mode control (MSMC) remains stable with force feedback and sees better performance than the system with hybrid sliding mode control (HSMC). In Chapter 8, conclusions on the entire study are given and recommendations for future work are presented.

2 LITERATURE REVIEW AND BACKGROUND

A large proportion of individuals around the world depend on passenger vehicles for transportation. In 2017 there were 270.4 million registered vehicles in the United States alone. With so many people behind the wheel, passenger vehicles were involved in 56% of all traffic crashes in the US in 2016. Of those traffic crashes, 30% were either resulted in death or injury [3]. In addition to the psychological impact of crashes, their annual cost in damages was 3% of the world gross domestic product, totaling almost one trillion USD in 2000 [4].

Some statistics suggest that over 90% of all traffic collisions occur due to a loss of control of the vehicle by the driver. Such a scenario arises when the driver is unaware of an impending skid or tire lockup [5, 4]. The role control loss plays in traffic collisions highlights the fact that the typical driver is not adept at detecting the stability limits from driver feedback alone. Historically, passenger vehicles have been self-contained, mechanical machines, forcing the driver to determine safe maneuvers based on the self-aligning propagated back to the steering wheel and acceleration [6]. Automated control has only become practical recently because of developments in digital electronics that allows features such as ESC systems and collision avoidance systems to be programmed directly into an embedded system [7, 4]. The concept of electronic stability control and active vehicle safety goes back quite a way, but the advent of low cost, high performance microcontrollers have enabled more advanced mathematical structures to be used in the implementation of such systems. Now, there is a plethora of published academic and commercial research dedicated to the control of passenger vehicle powertrains to enhance the handling and safety of modern vehicles.

While there are many promising solutions, research shows the control of independent in-wheel electric motors on each wheel is particularly promising because they respond far faster than a conventional drivetrain equipped with mechanical differentials. Moreover, electric motors can generally produce more torque and can leverage more advanced control methods in software. An electric powertrain of this type can begin reacting quickly by virtue of the low time constant associated with electric motors and optimize evasive maneuvers with control of each individual motor. These independent motors make it possible to generate a stabilizing yaw-moment by allocating a portion of the available power to each wheel to generate a differential traction or braking force between the left and right tires. This type of control is referred to as *torque vectoring.* Developments in active differentials enable torque vectoring control in combustion vehicles by modulating clutch engagement and braking to each individual wheel. This method results in a slower response and greater wear on the system because mechanical powertrains tend to have a greater effective rotational inertia at the extremities of the powertrain and depends on more moving parts than in the electric powertrain.

2.1 TORQUE VECTORING CONTROL APPROACHES

Torque vectoring is a special subset of algorithms within electronic stability control concerned with the stabilization of a vehicle's yaw dynamics during emergency maneuvers by continuously manipulating the driving and braking torque supplied to each of four individual electric motors attached to the wheel carriers. The allocated torque generates a corrective yawing moment about the vehicle to keep it traveling along some desired trajectory. Such a system has an advantage over traditional differential systems because of its fast response time and high degree of controllability. In extreme cornering events lateral weight transfer is significant, greatly reducing the ability of the inside wheels to generate lateral force. In an open differential, power will try to dissipate along the path of least resistance so more power will be sent to the inside wheel, causing it to spin while the outside wheel has a high adhesion margin. Limited slip differentials and torque vectoring differentials reduce this effect, but still lack the speed and controllability of electric motors. Methods for control using differential systems are outside the scope of this thesis and only torque vectoring with in-wheel motors was considered. This section presents a comprehensive review of several torque-vectoring control strategies. Of these strategies, the direct yaw moment control method was chosen because it breaks steps involved in torque vectoring into modular blocks, which are easily interpreted. DYC systems are generally classified in three categories: yaw rate based, vehicle sideslip angle based DYC, and simultaneous control of yaw rate and sideslip angle. The equal torque methods and Ackermann methods have also been reviewed to highlight what makes DYC effective.

Beyond enhancing active vehicle safety and handling performance, torque vectoring with all four wheels enables the system to meet several control objectives simultaneously and optimally. For instance, it has been shown that fuel-optimal torque vectoring control can extend the range of a FEV by up to 8.45% while simultaneously improving the cornering performance of the vehicle [8, 9]. For the previously mentioned reasons, this thesis revolves around developing a torque vectoring controller that can improve all dimensions of vehicle performance over an internal combustion vehicle (ICV) [10].

2.1.1 EQUAL TORQUE METHOD

The most basic condition for control of two independent motors is to send an equal torque command. Control methods based on this principle are called equal torque methods and their behavior is analogous to an open differential because they apply equal torque to the left and right wheels without constraining power distribution so that a velocity difference can occur as:

$$P_i = T_i \omega_i \tag{2.1}$$

$$T_R = T_L = T \tag{2.2}$$

where P_i is power, T_i is torque, and ω_i is angular velocity [10, 11]. Index i denote the lateral position of the tire (right/left). The equal torque methods provide an electric vehicle with a cornering performance like that of an ICV vehicle with an open differential. It is worth noting that equal torque methods cannot be classified as DYC because the torques do not generate a net moment.

2.1.2 ACKERMANN METHOD

Ackermann steering geometry enables the inner and outer wheels on an axle to spin without wheel slip at very low speeds and can be expressed mathematically as:

$$cot\delta_2 - cot\delta_1 = \frac{d_r}{L} \tag{2.3}$$

where d_r is the rear track width, L is the wheelbase, and δ_1, δ_2 are the steer angles of the front left and front right wheels, respectively. At low speeds, the lateral forces applied on the vehicle are very small so the motion can be described well by the kinematics that are purely a result of geometry. As a result, the tire slip angles are negligible and the turn radius r_i is defined as the distance from point O to inside front tire and the turn radius r_o is defined as the distance from point O to the outside tire, as shown in Figure 2.1.

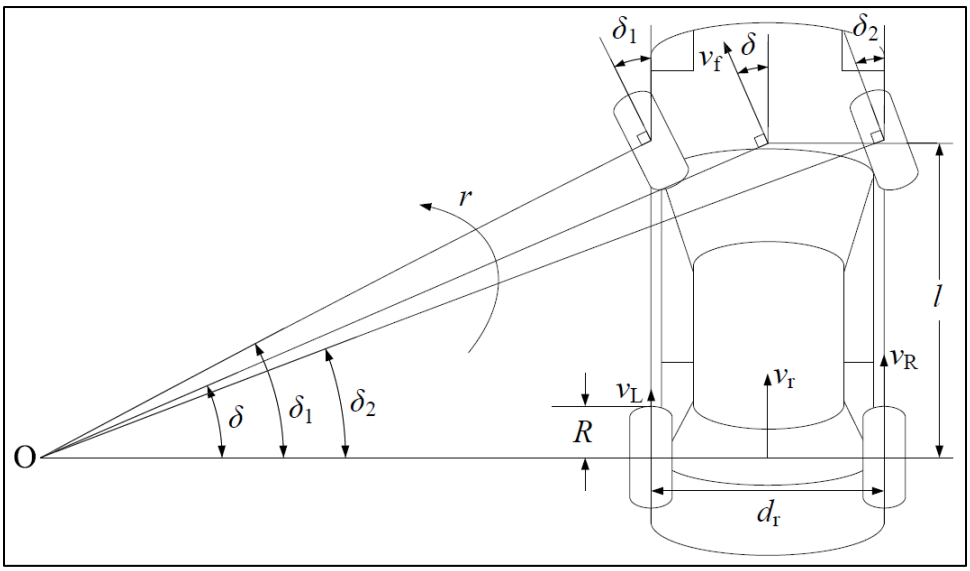

Figure 2.1 Ackermann steering geometry [11].

To summarize, the assumptions of the Ackermann method are as follows:

- Vehicle has Ackermann steering geometry,
- Very low speed (~<10 mph),
- No wheel slip.

With these assumptions, the angular velocities of the rear driving wheels can be expressed as:

$$\omega_L = \frac{v_L}{R} = \frac{v_r}{R}\left(1 - \frac{d_r tan\delta}{2L}\right), \tag{2.4}$$

$$\omega_R = \frac{v_R}{R} = \frac{v_r}{R}\left(1 + \frac{d_r tan\delta}{2L}\right). \tag{2.5}$$

where R represents the tire radius, δ is the average of the front wheel steer angles, v_r is the velocity at the center of the rear axle, and v_L and v_R are the velocities of the left and right wheel centers, respectively.

It has been shown that at low speed the above two equations approximate the actual wheel speeds well [11, 7]. A significant body of research has been established with the objective of forcing the

actual wheel speeds to track the Ackermann wheel speeds. These control systems are commonly referred to as the "electric differential." When the vehicle with an electric differential enters a turn, the control system acts on the independent motors such that the angular velocity of the inner wheel is reduced and that of the outer wheel is increased until they converge to the Ackermann wheel velocities. It should be noted that the Ackermann methods focus on control of the wheel angular velocities rather than the yaw moment. A yaw moment can be developed by these systems, but only indirectly. Therefore, they cannot be classified as direct yaw control and are only introduced here to show how control solutions evolved from simple methods.

Ackermann steering geometry was used to design a control system for a RWD FEV with two independent permanent magnet brushed DC motors as shown in Figure 2.2. This geometry was used to define reference angular velocities for the rear wheels while the actual angular velocities were estimated using a motor model and from data provided by voltage and current sensors. The error formed by the actual and reference angular velocities are input into a first-order SMC which causes the actual velocities to track the reference values. The sliding model controller defines a sliding surface in the phase-plane of the error signal which the error is forced towards until it returns to the origin. This sliding surface can be expressed by:

$$s = \dot{e}_{\omega} + k_e e_{\omega}. \tag{2.6}$$

where e_{ω} is the angular velocity error and k_e is a design parameter.

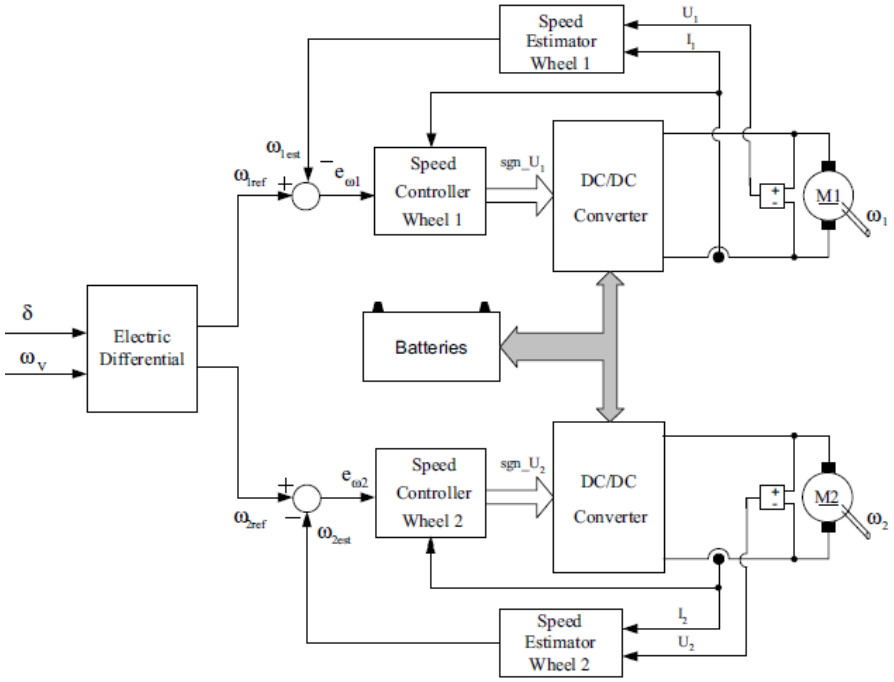

Figure 2.2 Ackermann control system proposed by Cordeiro. [12]

2.1.3 DIRECT YAW MOMENT CONTROL

The equal torque method and Ackermann method present obvious drawback, particularly that they do not actively control the drivetrain ends and assume a linear vehicle model, and do not provide acceptable performance for most of a vehicle's operating range. Researchers have dedicated a great deal of effort to the development of control algorithms utilizing the full breadth of vehicle dynamics in order to achieve better performance even at the vehicle's stability limits. A major advantage of DYC is that it takes into consideration the vehicle dynamics and directly adjusts the yaw moment generated as an effect of the difference in torque between the motors in order to regulate the vehicle states. DYC systems can stabilize lateral motion of a vehicle in emergencies and has been shown to be the most effective method of motion control compared with other existing control systems like four-wheel steer [12, 11].

While researchers have published work related to DYC systems with different approaches, the control architecture is generally the same. The upper controller must ensure stability of the chassis by commanding whatever yawing moment is necessary to meet the driver's request. It uses measurements from wheel speed sensors, a yaw rate sensor, an accelerometer and a steering angle

sensor. The lower controller ensures that the yawing moment commanded by the upper controller is developed by utilizing the wheel rotational dynamics and modulating the torque sent to each motor.

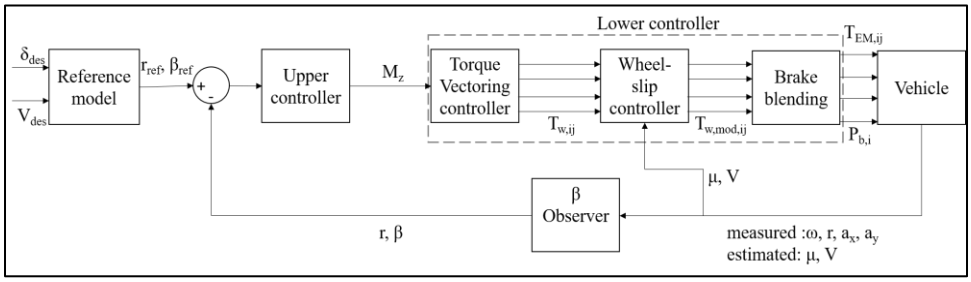

Figure 2.3 Simplified schematic of the DYC control structure [15].

Figure 2.3 shows the overall architecture for a DYC system. A reference model develops reference signals for the yaw states of the system from the requested steer angle and velocity. This steer angle and velocity come from the driver or path-planning controller and are detected with sensors on the steering column and accelerator pedal, depending on whether the system is in a standard vehicle or an autonomous vehicle. A higher control layer not shown here converts the requested torque into a requested velocity. This layer is outside the scope of the thesis presented here. The controller error vector is converted to a stabilizing yaw moment, M_z by the upper (high-level) controller. This moment is converted into individual wheel torques that would generate the ideal wheel forces by the torque-vectoring controller. The ideal forces assume infinite grip and cannot be realized because the motors can only put out so much torque and the tire-road friction coefficient limits the maximum instantaneous force that can be put down by the tires without sliding. A wheel slip controller estimates the road conditions and modifies the torque signals so that the values are achievable by the motors and tires. Based on the sign of the torque signal, the brake blending function performs the steps to send the signal to the appropriate system. A passenger vehicle can theoretically meet the request for a stabilizing yaw moment by the following:

- Differential traction only ($T_{w,mod,ij} > 0$ for all i, j),
- Differential braking only ($T_{w,mod,ij} < 0$ for all i, j),
- Combined traction and braking (no constraint on sign of $T_{w,mod,ij}$).

In third case, the motors and friction brakes respectively handle traction and braking. Brake blending must detect the sign of $T_{w,mod,ij}$ and determine whether to send the signal to the motor driver or the

brake controls. The torque-vectoring controller, wheel-slip controller and brake-blending function together perform the task of the DYC lower controller.

DYC of electric drivetrains can be broken up into three categories: yaw rate feedback, sideslip angle feedback and simultaneous yaw rate and sideslip feedback [11]. Studies have shown overwhelmingly that simultaneous feedback control of yaw rate and sideslip is the most effective means of stabilizing the yaw dynamics of a vehicle at low and high speeds [11, 12]. This nested type of control is more complex because the sideslip angle must be estimated. However, the inclusion of this state is desirable when stabilizing a vehicle at high accelerations because it makes the system more robust and less susceptible to uncertainty about the friction coefficient [13]. This thesis limits the scope of its investigation of DYC systems to simultaneous feedback control of yaw rate and sideslip angle in the interest of developing new control laws rather than control architectures [14, 15, 16, 13, 17, 18, 19, 12, 7, 4]. It is worth noting that there is a large body of published research for yaw rate feedback control [20, 2, 21, 22, 13, 23, 24, 25, 26, 15] and sideslip angle feedback control [11].

As introduced in Chapter 1, the yaw rate and vehicle sideslip are known to be the two fundamental states that govern the vehicle handling and stability. Controlling only one of these states may bring about problems in some driving scenarios. For instance, on low friction roads the vehicle sideslip can grow rapidly, resulting in loss of control of the vehicle and spinout [17-19]. In this circumstance, vehicle sideslip feedback would stabilize the vehicle. On the other hand, controlling the vehicle sideslip alone guarantees vehicle stability but may not produce desirable yaw rate response that is required to achieve some maneuver. In order to eliminate the downsides from controlling one state individually, numerous recent DYC works adopt feedback control of both states simultaneously, as shown in Figure 2.3 [14, 27, 11, 28]

Sliding mode control has received attention for DYC design because of its robustness against uncertainties and disturbances, making it ideal for controlling nonlinear systems like vehicles. Central to SMC is the design of the switching, which is often employed as a function of the yaw rate and vehicle sideslip errors [11, 4, 14, 23, 18, 12, 27]:

$$s = \dot{\psi} - \dot{\psi}_{ref} + \xi(\beta - \beta_{ref}). \tag{2.7}$$

where $\dot{\psi}_{ref}$ and β_{ref} are the reference yaw rate and vehicle sideslip respectively, ξ is a design parameter that is greater than zero and varies the relative weight. However, the switching function is not unique and can be chosen depending on the application to achieve different results [11, 27].

Notably, there is no guarantee that the conventional switching function shown in Equation (2.7) will drive the yaw rate error and sideslip angle error to zero because *s* will be zero either when:

$$\left|\psi - \psi_{ref}\right| = -\xi\left|\left(\beta - \beta_{ref}\right)\right|. \tag{2.8}$$

The form of Equation (2.8) means that $s = 0$ either when the error is zero or when the yaw rate error and the sideslip angle error term, including the weighting parameter are non-zero, have equal magnitude, and opposite signs. And. In this application, the sliding mode control command comes from the equation of motion for the yaw rate, which is derived in Chapter 3. This equation of motion includes terms with the lateral tire force, which typically depends on a high-fidelity tire model, a sensor, or estimation algorithm. All these methods have tradeoffs. The tire model requires a large amount of data to characterize the way force is generated but can model the tire force very accurately. However, even with all this data, the force it predicts is only valid for the conditions under which the tires were tested. Sensors can do a better job of quantifying the tire force, but these sensors are highly complex and expensive. On the other hand, tire force estimation results in a greater degree of error than the other methods but can achieve satisfactory results for a wide range of operation with a simple tire model and sensor fusion. Kalman filters can achieve reasonable performance in tire force estimation by comparing data from an IMU with forces predicted by a relatively simple model. However, the estimator performance is not guaranteed and the tuning process can be very tedious [29, 30, 31, 32, 33, 34, 6, 35].

3 VEHICLE MODEL

Despite the availability of a validated automobile simulator for this thesis, a full two-track vehicle model was derived with the purpose of designing the tire force estimators and enabling vehicle simulation in the MATLAB/Simulink environment in the absence of a proprietary license. CarMaker grants the user a lot of flexibility in defining the type of vehicle, but it relies on a vast number of parameters, some of which are difficult to interpret. The vehicle model is configured for a medium-class vehicle with standard dimensions and parameters assuming that: it is a 4MIDEV, so the vehicle is driven by independent motors in the hub of each wheel and the battery is located under the hood to maintain a center of gravity is closer to the front axle; the pitch dynamics are neglected: there is no weight transfer from the rear axle to the front axle or vice-versa.

The following sections present the equations of motion for the nonlinear longitudinal, lateral, yaw and roll dynamics of the vehicle as well as the Magic Formula tire model and electric motor characteristics generating the forces upon which these dynamics depend. A separate tire model, the Dugoff model, will be used for the Kalman filter estimation and, although this model is presented in the following sections, its actual use and description follows in Chapter 6.

3.1 VEHICLE EQUIVALENT MECHANICAL MODEL

In order to derive the vehicle equations of motion, a vehicle equivalent model was first established. A vehicle consists of two major parts: the sprung mass and unsprung mass, which can be regarded as two rigid bodies connected by flexible suspension elements. Figure 3.1 shows the vehicle equivalent model and vehicle fixed coordinate system. The top body represents the sprung mass constituting the chassis and vehicle body and the bottom one represents the unsprung mass constituting the wheels and axles. The *XYZ* coordinate system is the global reference frame, which does not move with the vehicle body. The *xyz* coordinate system is attached to the unsprung mass with the origin, *A* located directly beneath the center of mass. There is also a sprung mass coordinate system that will be called the *x'y'z'* coordinate system which is coincident with the *xyz* coordinate system when the vehicle is stationary. Both the global coordinate system and body-fixed coordinate systems are defined according to the Society of Automotive Engineers (SAE) J1733 sign convention standard [36].

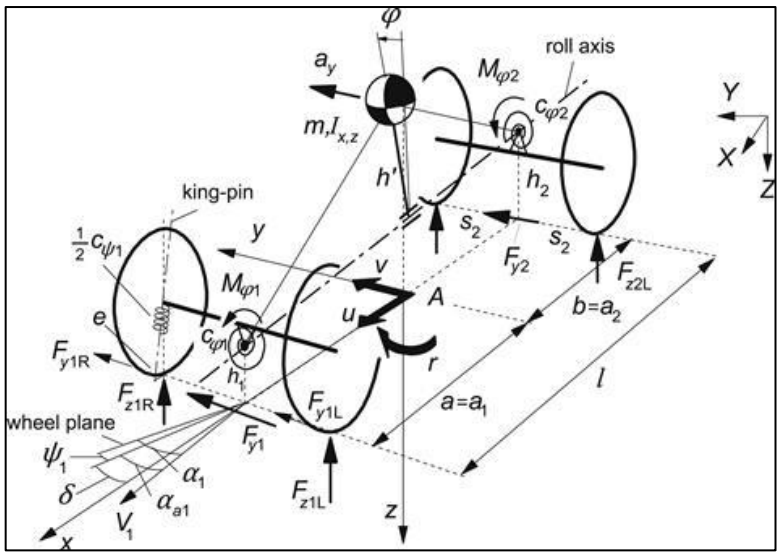

Figure 3.1 Vehicle equivalent mechanical model and body-fixed coordinate system [36].

The two bodies were assumed to yaw together about the *z*-axis such that the angle between the *x*-axis and *x'*-axis is always zero. Furthermore, the roll motion of the unsprung mass about the *x* axis was neglected. The vertical motion and pitch motion of the two masses were neglected as well because these motions are related primarily to vehicle ride while the focus of this thesis is on vehicle handling and stability [11].

The black and white sphere represents the composite center of mass of the sprung and unsprung mass. The variable *h'* (called h_S throughout this work) represents the distance between the center of mass and the roll axis; *a* and *b* are the distance from the front axle to the center of mass and the distance from the rear axle to the center of mass along the *x*-axis respectively and their sum is equivalent to the wheelbase *l*. The variables s_1 and s_2 represent half the front track width and rear track width respectively, *e* is the pneumatic trail, $C_{\psi i}$ is the cornering stiffness of the ith tire. The variables h_1 and h_2 represent the height of the roll center above the front axle and rear axle respectively and $c_{\varphi i}$ and $M_{\varphi i}$ are the roll stiffness and roll moment on the ith axle. For the remainder of this work, c_φ will be equivalent to k_φ to differentiate it from the tire cornering stiffness. F_{ijk} represents a tire force, where $i = \{x, y, z\}, j = \{1, 2\}$ *and* $k = \{L, R\}$. The variables *r* and *p* represent the yaw rate and the roll rate respectively and φ represents the roll angle of the sprung mass and are related to the rotational states of the vehicle. On the other hand, *u*, *v*, and a_y represent the longitudinal velocity, lateral velocity and lateral acceleration respectively. The body mass is denoted by *m* and the moments of inertia with respect to the center of mass and horizontal and vertical axes by I_x, I_z, I_{xz}. The variables δ and α represent the average front axle steering angle and the average front tire slip angle respectively. It is

assumed that ψ_1, V_1 and α_{a1}, which represent steering angle, velocity and slip angle induced by body roll, are small enough to be neglected. The situation depicted by the vehicle equivalent mechanical model is that of a vehicle negotiating a turn at constant velocity with friction or throttle being applied [35].

3.2 VEHICLE EQUATIONS OF MOTION

A set of vehicle equations of motion was necessary to compute the state of the vehicle in response to driver inputs such as steering, throttle and braking. The driver inputs are combined with state feedback to form the control signals, which are used to compute the optimal torque distribution among the wheels. The torque signal to each electric motor and the applied steering angle constitute the inputs to the vehicle model. The states of the model are the longitudinal velocity, lateral velocity, yaw rate, roll rate, and the angular velocity of each wheel. The outputs are the longitudinal velocity, yaw rate, roll rate, and wheel angular velocities. Most IMUs are unable to directly measure longitudinal velocity so it would have to be integrated from acceleration or estimated. However, it was assumed the velocity was available as an output for the sake of simulation. It was possible to split the vehicle model into two parts: translational dynamics which describes the longitudinal and lateral motion of the vehicle within the *xy* plane, and rotational dynamics, which describes the roll and yaw rotation of the sprung mass about the *x'*-axis and *y'*-axis respectively. The rotational dynamics of the wheels about their spin axis will be considered within rotational dynamics.

Lagrange's equations for virtual work were employed to derive the equations of motion using the system depicted in Figure 3.1. The angular velocity of the wheels will not be considered states of the sprung mass, so the system is assumed to have four states relating to the translation and rotation of the vehicle body. This system has four degrees of freedom, so four generalized coordinates q_i are selected to describe the motion. The vehicle system has kinetic energy T and potential energy U with external generalized forced Q_i associated with the generalized coordinates acting on it. The general form of Lagrange's equation is:

$$\frac{d}{dt}\frac{\partial T}{\partial \dot{q}_i} - \frac{\partial T}{\partial q_i} + \frac{\partial U}{\partial q_i} = Q_i \tag{3.1}$$

For small yaw angles, equations of motion defined in the global *XYZ* coordinate system may be adequate to derive the equations of motion. Since this study is concerned primarily with turning and handling, the body-fixed coordinate system will usually be in a configuration much different from

that of the global reference frame. Lagrange's equation can be modified to describe motion in the body-fixed reference frame by using a rotation transformation about the *Z*-axis. The relation between the global and body-fixed state variables is:

$$u = \dot{X}cos\psi + \dot{Y}sin\psi \tag{3.2}$$

$$v = \dot{X}sin\psi + \dot{Y}cos\psi \tag{3.3}$$

$$r = \dot{\psi} \tag{3.4}$$

This transformation results in a set of coupled Lagrange equations. A more detailed derivation of the modified equations can be found in [35]. The modified Lagrange equations for *u*, *v*, *r* and φ are:

$$\frac{d}{dt}\frac{\partial T}{\partial u} - r\frac{\partial T}{\partial v} = Q_u \tag{3.5}$$

$$\frac{d}{dt}\frac{\partial T}{\partial v} + r\frac{\partial T}{\partial u} = Q_v \tag{3.6}$$

$$\frac{d}{dt}\frac{\partial T}{\partial r} - v\frac{\partial T}{\partial u} + u\frac{\partial T}{\partial v} = Q_r \tag{3.7}$$

$$\frac{d}{dt}\frac{\partial T}{\partial p} - \frac{\partial T}{\partial \varphi} + \frac{\partial U}{\partial \varphi} = Q_\varphi \tag{3.8}$$

The generalized forces were derived from the virtual work:

$$\delta W = \sum_{j-1}^{4} Q_j \delta q_j \tag{3.9}$$

where q_j refers to the body-fixed coordinates *x, y, ψ* and *φ*. For the vehicle model, the virtual work is found using the virtual displacements for each coordinate:

$$\delta W = \sum F_x \delta x + \sum F_y \delta y + \sum M_z \delta \psi + \sum M_\varphi \delta \varphi \tag{3.10}$$

and the generalized forces can be found by resolving Newton's Second Law on Figure 3.1 to find the net force in the *x* and *y* direction as well as the net moment about the *z*-axis and *x*-axis to find the yawing moment and rolling moment respectively. These resolve into:

$$Q_u = \sum F_x \tag{3.11}$$

$$= (F_{x11} + F_{x12})cos\delta - \big(F_{y11} + F_{y12}\big)sin\delta + F_{x21} + F_{x22} - F_{drag} - F_f$$

$$Q_v = \sum F_y \tag{3.12}$$

$$= (F_{x11} + F_{x12})sin\delta + \big(F_{y11} + F_{y12}\big)cos\delta + F_{y21} + F_{y22}$$

$$Q_r = \sum M_z \tag{3.13}$$

$$= a(F_{x11} + F_{x12})sin\delta + a\big(F_{y11} + F_{y12}\big)cos\delta - b\big(F_{y21} + F_{y22}\big) \ldots$$
$$+ s_1\big[(-F_{x11} + F_{x12})cos\delta + \big(F_{y11} - F_{y12}\big)sin\delta\big] + s_2(-F_{x21} + F_{x22})$$

$$Q_\varphi = \sum M_x \tag{3.14}$$

$$= -\big(b_{\varphi 1} + b_{\varphi 2}\big)\dot{\varphi}$$

The tire forces are indexed as F_{ijk} where $i = \{x, y, z\}$, $j = \{F, R\}$, $k = \{L, R\}$. The second index, j represents the axle and the third index k represents the side. The roll moment results from the shock absorbers in the suspension with damping coefficients $b_{\varphi 1}$ and $b_{\varphi 2}$ for the front and rear axle respectively. F_{drag} represents the resistive force imposed on the vehicle due to aerodynamic drag and is equivalent to:

$$F_{drag} = \frac{1}{2}\rho C_d A_f V^2 \tag{3.15}$$

where ρ is the air density C_d is the dimensionless drag coefficient of the vehicle A_f is the frontal area of the vehicle and V is the velocity of the vehicle. Excluding maneuvers in which the vehicle is drifting, the vehicle is not expected to experience sideslip angles beyond 5° so it is reasonable to assume that the overwhelming contribution to the drag force is due to the longitudinal velocity of the vehicle. As a result, the equation used for F_{drag} in this thesis is:

$$F_{drag} = \frac{1}{2}\rho C_d A_f u^2 \tag{3.16}$$

The last longitudinal force term F_f is the resistive force due to the total rolling resistance caused by hysteresis effects between the tires and road. The force due to rolling resistance is equivalent to:

$$F_f = \sum_{i=1}^{2}\sum_{j=1}^{2} f_{ij} F_{zij} \tag{3.17}$$

Since lateral weight transfer effects are included in the vehicle model, the rolling resistance contribution due to the left and right wheels will change as the vehicle negotiates a turn. The above equation allows for the possibility that the road is not a homogenous surface. The variable f represents the friction coefficient due to hysteresis and is a function of the road roughness. If the left and right wheels of the vehicle go over a surface with different roughness, the rolling resistance contribution will vary on the left and right side of the vehicle. Throughout this work, it is assumed that the road is homogenous, so the expression becomes:

$$F_f = f \sum_{i=1}^{2} \sum_{j=1}^{2} F_{zij} \tag{3.18}$$

In order to evaluate Lagrange's equation and obtain the equations of motion for the vehicle body, it is necessary to obtain an expression for the kinetic energy and potential energy from the vehicle equivalent mechanical model in Figure 3.1. If the roll angle and the roll axis inclination angle between the front and rear axis θ_r are small, the kinetic energy becomes:

$$\begin{aligned} T = \frac{1}{2} m[(u - h_S \varphi r)^2 + (v + h_S \dot{\varphi})^2] + \frac{1}{2} I_x \dot{\varphi}^2 + \frac{1}{2} I_y (\varphi r)^2 \ldots \\ + \frac{1}{2} I_z (r^2 - \varphi^2 r^2 + 2\theta_r r \dot{\varphi}) - I_{xz} r \dot{\varphi} \end{aligned} \tag{3.19}$$

The roll axis inclination angle θ_r is neglected in this study, as it is generally quite small. The potential energy U comes from compression in the suspension springs and from the height of the center of gravity. Again, assuming small angles, the potential energy can be expressed as:

$$U = \frac{1}{2} \left(k_{\varphi 1} + k_{\varphi 2}\right) \varphi^2 - \frac{1}{2} m g h_S \varphi^2 \tag{3.20}$$

The equations of motion are finally established by taking the partial derivatives of the kinetic energy and potential energy expressions with respect to u, v, r, p and φ. An expression for the equations of motion for the longitudinal velocity, lateral velocity, yaw rate, and roll rate arises from substituting the partial derivatives as well as the expressions for the virtual forces back into Lagrange's equation. The assumption of small roll angles is maintained in these equations of motion, but they remain nonlinear functions of the steering angle because some maneuvers require large steering angles. These equations of motion can be expressed as:

$$m(u - rv - h_S\varphi\dot{r} - 2h_S r\dot{\varphi}) \ldots = (F_{x11} + F_{x12})cos\delta - \big(F_{y11} + F_{y12}\big)sin\delta + F_{x21} \ldots + F_{x22} + F_{drag} + F_f \quad (3.21)$$

$$m(v + ru + h_S\ddot{\varphi} - h_S r^2\varphi) \ldots = (F_{x11} + F_{x12})sin\delta + \big(F_{y11} + F_{y12}\big)sin\delta + F_{y21} + F_{y22} \quad (3.22)$$

$$I_z\dot{r} + I_{xz}\dot{p} - mh_S(\dot{u} - rv)\varphi \ldots = a(F_{x11} + F_{x12})sin\delta + a\big(F_{y11} + F_{y12}\big)cos\delta \ldots - b\big(F_{y21} + F_{y22}\big) \ldots + s_1\big[(-F_{x11} + F_{x12})cos\delta + \big(F_{y11} - F_{y12}\big)sin\delta\big] \ldots + s_2(-F_{x21} + F_{x22}) \quad (3.23)$$

$$(I_x + mh_S)\ddot{\varphi} + mh_S(\dot{v} + ru) - I_{xz}\dot{r} - \big(mh_S^2 + I_y - I_z\big)r^2\varphi \ldots + \big(b_{\varphi 1} + b_{\varphi 2}\big)\dot{\varphi} + \big(k_{\varphi 1} + k_{\varphi 2} - mgh_S\big)\varphi = 0 \quad (3.24)$$

The small roll and compliance steer angles ψ_i, which is the steer generated by the suspension during cornering, have been neglected to simplify the equations of motion. It is worth noting that there is a significant degree of nonlinearity in the state derivative terms on the left-hand side of the equations of motion. Order of magnitude analysis can be employed to linearize the state derivative terms. Assuming all deviations from rectilinear motion are small, all products of states including roll can be considered negligible and the equations of motion can be rewritten as follows:

$$m(u - rv) = (F_{x11} + F_{x12})cos\delta - \big(F_{y11} + F_{y12}\big)sin\delta + F_{x21} + F_{x22} \ldots + F_{drag} + F_f \quad (3.25)$$

$$m(v + ru + h_S\dot{p}) \ldots = (F_{x11} + F_{x12})sin\delta + \left(F_{y11} + F_{y12}\right)cos\delta + F_{y21} \ldots + F_{y22} \tag{3.26}$$

$$I_z\dot{r} - I_{xz}\dot{p} = a(F_{x11} + F_{x12})sin\delta + a\left(F_{y11} + F_{y12}\right)cos\delta \ldots - b\left(F_{y21} + F_{y22}\right) \ldots + s_1\left[(-F_{x11} + F_{x12})cos\delta + \left(F_{y11} - F_{y12}\right)sin\delta\right] \ldots + s_2(-F_{x21} + F_{x22}) \tag{3.27}$$

$$(I_x + mh_S)\dot{p} + mh_S(\dot{v} + ru) - I_{xz}\dot{r} \ldots = -\left(k_{\varphi 1} + k_{\varphi 2} - mgh_S\right)\varphi - \left(b_{\varphi 1} + b_{\varphi 2}\right)\dot{\varphi} \tag{3.28}$$

Neglecting the state products with roll in Equations (3.25), (3.26), (3.27) and (3.28) removes much of the nonlinearity with respect to the states and state derivatives. However, these equations remain highly nonlinear in the expressions for the longitudinal and lateral tire forces. A marked advantage of this assumption is that Equation (3.27) is linear with respect to *r* which makes the derivation of the DYC control law in Chapter 4 notably simpler.

The last component necessary to solve the above system of equations is to derive an expression for computing the longitudinal and lateral tire forces. The tire forces depend on the slip ratio and slip angle as well as the tire normal loads. In order to compute these quantities, the equations of motion of each wheel and a model for generating tire forces from the wheel dynamics must be developed.

3.3 WHEEL EQUATIONS OF MOTION

Longitudinal force arises from a difference between the vehicle velocity and effective velocity of the spinning wheels. It is adequate to assume that undriven wheels roll without slipping, but not for driven wheels. Since the core of this thesis is torque vectoring for a 4MIDEV, slip occurs on all four wheels. Moreover, the wheels are all independent of each other, so the slip on each wheel must be treated independently as well. An equation of motion to calculate the effective velocity of each wheel is derived in this section. The wheel free body diagram shown in Figure 3.2 illustrates the forces acting on the wheel that produce angular acceleration about its center.

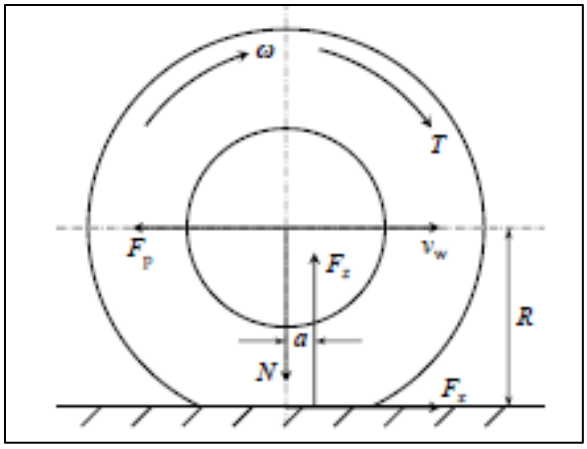

Figure 3.2 Free body diagram of a wheel [11].

Newton's Second Law can be applied to equate the change in angular momentum to the moments acting about the center of the wheel:

$$\dot{H}_G = \sum M_G \tag{3.29}$$

$$J\frac{d\omega_{ij}}{dt} = T_{ij,motor} - T_{ij,brake} - F_{xij}R - F_f R \tag{3.30}$$

where J denotes the mass moment of inertia of the wheel assembly, ω denotes the wheel angular velocity, T represents the applied motor torque, F_x represents the longitudinal tire force, R represents the effective wheel radius, F_f represents the rolling resistance, and a represents the tire trail. This expression assumes that all the wheels have the same mass moment of inertia and radius and neglects the torque contribution due to the trail. As indicated by the indexes i and j, this expression is used to compute the angular velocity of each wheel independently.

3.3.1 TIRE MODEL: PACEJKA'S MAGIC FORMULA

Pacejka's semi-empirical Magic Formula equation is employed to model the tire forces in this study. The Magic Formula has been shown to predict tire forces quite accurately [35]. Although the Magic

Formula is generally considered a steady-state model, it captures some of the tire dynamics caused by tire deformation that are often neglected in other models. The Magic Formula equation takes the following form:

$$y(x) = Dsin\{Carctan[Bx - E(Bx - arctanBx)]\} \tag{3.31}$$

and:

$$Y(X) = y(x) + S_v \tag{3.32}$$

$$x = X + S_H \tag{3.33}$$

where X is the slip ratio σ or the slip angle α, $Y(X)$ represents the tire force F_x or F_y, S_v and S_H are the vertical and horizontal shift due to camber, respectively. B, C, D, and E denote the stiffness factor, shape factor, peak value, and curvature factor, respectively. It is worth noting that the constant cornering stiffness representing the slope of the force-slip curve at the origin $(x = y = 0)$, C_α for a tire can be computed from the product BCD [29]. Depending on the set of tire parameters available, a set of Magic Formula parameters can be computed from cornering stiffness and vice-versa. This is useful in the implementation of the Dugoff Model presented in the following section. A more in-depth description of the Magic Formula can be found in [32]. The calculation of the longitudinal and lateral forces requires computing of the slip ratio σ, slip angle α, and vertical load F_z. The tire slip ratio is defined as [4, 29]:

$$\sigma = \frac{R\omega - V_{wx}}{\max\{abs(R\omega), abs(V_{wx})\}} \tag{3.34}$$

where V_{wx} denotes the longitudinal velocity of the wheel center in the wheel coordinate system, or the velocity in the wheel heading direction. The denominator switches using MATLAB's *max* and *abs*

functions to reflect the fact that the optimal torque computed by the TVC can be either a braking torque or an accelerating torque. The velocity of the wheel center is computed as follows [29]:

$$V_{wx11} = (u - rs_1)cos\delta + (v + ra)sin\delta, \tag{3.35}$$

$$V_{wx12} = (u + rs_1)cos\delta + (u + ra)sin\delta, \tag{3.36}$$

$$V_{wx21} = u - rs_2, \tag{3.37}$$

$$V_{wx22} = u + rs_2. \tag{3.38}$$

where, again s_i is half the track width of the front and rear axles and a is the distance between the front axle and the center of gravity of the vehicle. Calculation of the slip ratio is only one of the two forms of slip required to calculate the tire forces. The lateral force is dependent on the slip angle, which is defined as the angle between the wheel heading direction and the velocity vector of the wheel center [11]. Neglecting the small contribution due to roll steer, the slip angle for each tire is expressed as:

$$\alpha_{11} = \delta - \arctan\left[\frac{v + ar}{u - s_1 r}\right], \tag{3.39}$$

$$\alpha_{12} = \delta - \arctan\left[\frac{v + ar}{u + s_1 r}\right], \tag{3.40}$$

$$\alpha_{21} = -\arctan\left[\frac{v - br}{u - s_2 r}\right], \tag{3.41}$$

$$\alpha_{22} = -\arctan\left[\frac{v - br}{u + s_2 r}\right]. \tag{3.42}$$

The last component necessary to compute the tire longitudinal and lateral forces is the tire vertical load. The Magic Formula peak factor D can be computed as different functions of this normal load,

but in most cases it is sufficient to assume that the peak factor increases linearly with the normal load and can be written as:

$$D = \mu F_z \tag{3.43}$$

where μ is the maximum friction coefficient, or "grip" resulting from the tire road interface. The tire vertical load consists of four factors: the static load, unsprung weight transfer, geometric load transfer, and elastic load transfer [37]. The static load is defined as the weight distribution of the vehicle when at rest and can be simply calculated by summing the moments acting on the vehicle center of gravity, resulting in an expression for the front and rear axle:

$$F_{zf,static} = \frac{1}{2l} mgb, \tag{3.44}$$

$$F_{zr,static} = \frac{1}{2l} mga. \tag{3.45}$$

The next component of the normal force to consider is the geometric weight transfer. The geometric weight transfer is found by resolving the non-rolling overturning moment caused by the lateral acceleration acting through the center of gravity of the vehicle. However, the left-hand side of the vehicle lateral equation is not simply the lateral acceleration and so information about the state of the vehicle would be lost by taking the above approach. Instead, the right-hand side can be used to resolve the geometric weight transfer. The geometric weight transfer effect is a consequence to the moment about the *x*-axis generated by the forces on the right-hand side of the vehicle lateral equation of motion as seen in Figure 3.1 [38]:

$$\Delta F_{zf,geometric} = \left[(F_{x11} + F_{x12})sin\delta + \left(F_{y11} + F_{y12}\right)cos\delta\right]h_1, \tag{3.46}$$

$$\Delta F_{zr,geometric} = \left(F_{y21} + F_{y22}\right)h_2. \tag{3.47}$$

where h_1 and h_2 denote the front and rear roll center heights, respectively.

The final component of the lateral weight transfer equation is the elastic weight transfer. This component results from the rolling moment on the sprung mass developed in the suspension springs and dampers as a result of the roll dynamics. The elastic weight transfer is written as:

$$\Delta F_{zr,elastic} = k_{\varphi r}\varphi + b_{\varphi r}p \tag{3.48}$$

This thesis is concerned primarily with the control of a vehicle at constant velocity, but this is not always possible. In especially extreme maneuvers, the dual control tasks of tracking desired yaw dynamics and maintaining a steady velocity can be too much, and the velocity may increase or decrease. Although the model neglects vehicle pitch dynamics, the contribution of pitch on the tire normal load should not be ignored in these cases. Like for the geometric load transfer, the pitching weight transfer is caused by the moment from the acceleration in the same direction as the weight transfer. Like in that case, information would be lost if the acceleration were used, so the sum of the forces acting in the longitudinal direction is used instead. As such, the following terms are included in the load transfer model to account for longitudinal acceleration:

$$\Delta F_{zf,long} = -h_{CG}\sum F_x, \tag{3.49}$$

$$\Delta F_{zr,long} = h_{CG}\sum F_x. \tag{3.50}$$

Now, combining the above terms, the tire normal loads for each wheel considering both longitudinal and lateral load transfer, are written as follows [11]:

$$F_{z11} = \frac{1}{2l}\left(mgb + \Delta F_{zf,long}\right) - \frac{1}{2s_1}\left(\Delta F_{zf,elastic} + \Delta F_{zf,geometric}\right), \tag{3.51}$$

$$F_{z12} = \frac{1}{2l}\left(mgb + \Delta F_{zf,long}\right) + \frac{1}{2s_1}\left(\Delta F_{zf,elastic} + \Delta F_{zf,geometric}\right), \tag{3.52}$$

$$F_{z21} = \frac{1}{2l}\left(mga + \Delta F_{zr,long}\right) + \frac{1}{2s_2}\left(\Delta F_{zr,elastic} + \Delta F_{zr,geometric}\right), \quad (3.53)$$

$$F_{z22} = \frac{1}{2l}\left(mga + \Delta F_{zr,long}\right) - \frac{1}{2s_2}\left(\Delta F_{zr,elastic} + \Delta F_{zr,geometric}\right). \quad (3.54)$$

The expanded form is:

$$F_{z11} = \frac{1}{2l}\left(mgb - h_{CG}\sum F_x\right) - \frac{1}{2s_1}\left(k_{\varphi f}\varphi + b_{\varphi f}p + h_1\sum F_{yf}\right), \quad (3.55)$$

$$F_{z12} = \frac{1}{2l}\left(mgb - h_{CG}\sum F_x\right) + \frac{1}{2s_1}\left(k_{\varphi f}\varphi + b_{\varphi f}p + h_1\sum F_{yf}\right), \quad (3.56)$$

$$F_{z21} = \frac{1}{2l}\left(mga + h_{CG}\sum F_x\right) + \frac{1}{2s_2}\left(k_{\varphi r}\varphi + b_{\varphi r}p + h_2\sum F_{yr}\right), \quad (3.57)$$

$$F_{z22} = \frac{1}{2l}\left(mga + h_{CG}\sum F_x\right) - \frac{1}{2s_2}\left(k_{\varphi r}\varphi + b_{\varphi r}p + h_2\sum F_{yr}\right). \quad (3.58)$$

At this point the most fundamental components of the vehicle model have been described, including a vehicle equivalent model from which the four vehicle equations of plane motion and the four-wheel equations of motion were derived. The Magic Formula tire model was postulated and expressions for the slip ratio, slip angle, and tire normal loads were presented. However, the form of the Magic Formula tire model presented assumes pure slip the longitudinal *(x)* and lateral *(y)* direction. In many cases a vehicle experiences a combination of longitudinal slip and lateral slip and will reach its cornering limits far sooner than what would be predicted by this model. The TVC proposed in Chapter 5 includes a traction control component that limits the torque in combined slip conditions.

3.3.2 TIRE MODEL: DUGOFF'S MODEL

The core component in a model-based tire force estimator is Dugoff's tire model. Although Dugoff's model generally yields worse predictions of the actual tire forces, especially at greater vertical tire

loads, this model has several advantages over Pacejka's Magic Formula: it only depends on the longitudinal tire stiffness coefficient C_λ and lateral stiffness coefficient C_α and the Magic Formula depends on thirteen or more; Dugoff's model easily handles pure longitudinal, pure lateral, and combined slip scenarios, unlike the Magic Formula and it does not depend on complex trigonometric functions [39, 4, 29, 34]. These advantages make the Dugoff model ideal for online tire force estimation because a well-tuned estimator compensates for some of the modelling error.

Like the Magic Formula, Dugoff's model depends on the longitudinal slip ratio and the slip angle. The longitudinal force is given by:

$$F_x = -C_\lambda \frac{\sigma}{1+\sigma} f(\tau), \tag{3.59}$$

where τ is a combined slip correction factor and $f(\tau)$ is a nonlinear function described below. The lateral force follows a similar form to the longitudinal force calculation and is written as:

$$F_y = -C_\alpha \frac{tan\alpha}{1+\sigma} f(\tau), \tag{3.60}$$

and $f(\tau)$ takes the form:

$$f(\tau) = \begin{cases} (2-\tau)\tau, & if\ \tau < 1 \\ 1, & if\ \tau \geq 1' \end{cases} \tag{3.61}$$

where:

$$\tau = \frac{\mu F_z (1+\sigma)}{2\{(C_\sigma \sigma)^2 + (C_\alpha \alpha)^2\}^{1/2}}. \tag{3.62}$$

It is obvious from the formulas for Dugoff's tire model that there is a coupled relationship between the longitudinal and lateral tire forces. The tire adhesion capability used for generating longitudinal tire force limits how much lateral force can be generated in the contact patch, and vice versa. This coupled relationship is often referred to as the *friction circle* or *Kamm circle* concept. This concept is shown in Figure 3.3. The total possible tire force that can be generated in the contact patch F is equivalent to μF_z. Whatever maneuver is taken, the resultant of the longitudinal and lateral tire forces cannot exceed F or the vehicle may begin skidding. The friction circle is a simplification of the *friction ellipse*, which assumes that the force that can be generated in the direction of the wheel heading is greater than that which can be generated perpendicular to the wheel heading. This concept becomes even more complex when the limits are assumed to vary with the state of the vehicle. However, the friction ellipse and more complex forms are beyond the scope of this thesis.

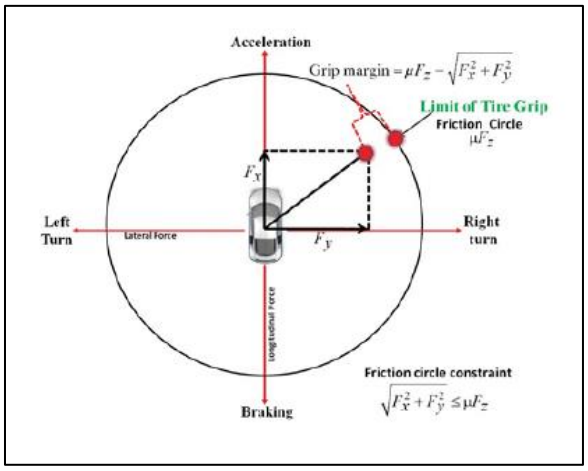

Figure 3.3 Friction circle concept for combined slip modelling [42].

Dugoff's tire model is fitting for use with real-time estimation like a nonlinear Kalman filter because the partial derivates are much easier to compute. The unscented Kalman filter (UKF) can model high degrees of nonlinearity, but requires computation from the nonlinear model, which can be computationally expensive. On the other hand, the extended Kalman filter (EKF) relies on a first-order Taylor series linearization of the nonlinear function at each time step. In both instances, the Magic Formula would take longer to compute and the Kalman filter would rely far more on the model's predicted output than the estimated output.

3.4 ELECTRIC MOTORS

The characteristic performance of the electric motors used in simulation is a crucial final step in developing the complete model for a 4MIDEV. Electric motors are characterized by unique torque-speed curves. The maximum torque a motor can produce at any instant is a function of the current motor speed and always decreases as speed increases because of the fundamental relationship between torque, speed and power:

$$P = T\omega \tag{3.63}$$

where P is the consumed power, T is the torque produced by the motor and ω is the motor speed.

3.4.1 PEAK TORQUE CURVE

Depending on the type of motor, the characteristic peak torque curve can look very different. In all cases, the peak torque is a nonlinear function of motor speed. The motor can produce its maximum rated torque for a range of speeds so long as the consumed power does not exceed the power supplied to the motor. Once the motor begins operating at maximum power, the torque decreases as speed increases. This reduction in torque can be linear or quadratic, depending on the motor construction.

Figure 3.4 shows the peak torque curves for the two classes of motors. One motor is a small motor which may be used for RC cars or other low power applications, while the other motor is a much bigger, more powerful motor designed specifically for automotive applications.

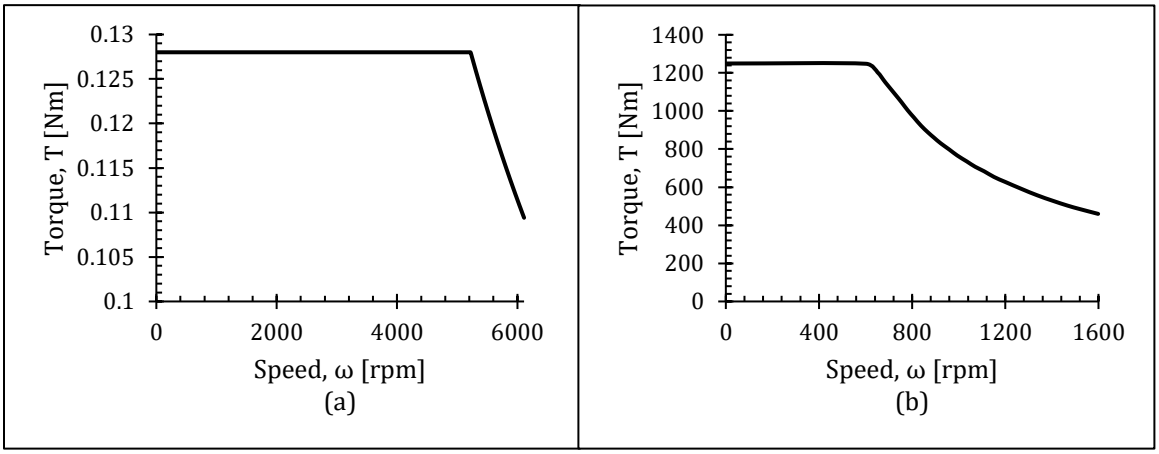

Figure 3.4 Maximum torque vs. speed performance curves for the (a) 70W Maxon 45 Flat Brushless motor and (b) 80 kW Protean Pd18 motor [43, 44].

One stark difference between the two motors is their shape. The Maxon motor here has a piecewise linear relationship between torque and speed, while the Protean, the motor used to in the CarMaker simulation has a piecewise nonlinear relationship where the maximum torque is constant up to about 650 rpm (roughly 70 km/h) after which the relationship becomes quadratic. The torque can remain constant up to this point because the motor has not reached its maximum power, but as soon as the maximum power of the motor is achieved, then the torque starts to drop. These curves indicate the maximum torque that can be achieved on each wheel for a given speed and are implemented in simulation as 1D look-up tables in Simulink and Carmaker. The Maxon curve requires very few interpolating points because it is linear, but the Protean curve requires a fine linear interpolation to sufficiently fit the maximum torque beyond 650 rpm.

3.4.2 ELECTRIC MOTOR MAP

The peak torque curve determines the maximum possible torque at any motor speed. However, this says nothing about how the torque is generated for operating points below the maximum. In order to model sub-peak torques, the torque must be mapped not just to the motor angular velocity but also the throttle input by the driver. Table 3-1 shows a motor map to compute torque values, which also includes the peak values and is illustrated in Figure 3.5.

Table 3-1 Motor map of the Protean Pd18 where torque is a function of the rotational speed (rpm) and throttle (%). Values between the discrete levels in this table are interpolated. Values highlighted green must be added manually, while the values in orange are computed automatically from them [40].

% rotational speed in rpm									
99999	0	200	400	600	800	1000	1200	1400	1600
% gas pedal | motor torque in Nm									
0	0	0	-5	-5	-5	-6	-7	-8	-9
0.2	250	250	250	250	193	150	125	106	92
0.4	500	500	500	500	386	300	250	212	183
0.6	750	750	750	750	579	450	375	318	275
0.8	1000	1000	1000	1000	772	600	500	424	366
1	1250	1250	1250	1250	965	750	625	530	458

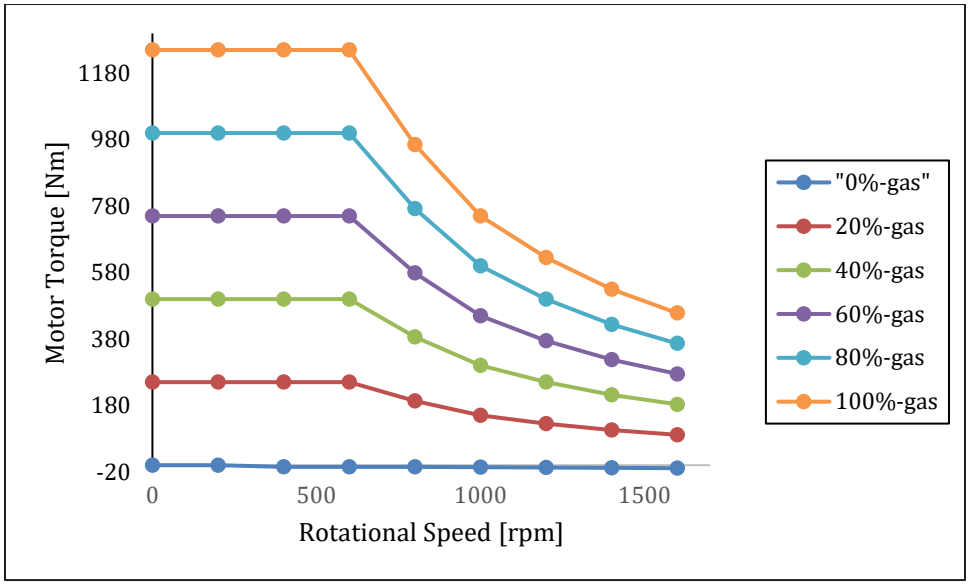

Figure 3.5 A graphical representation of the motor map showing the torque curves for throttle levels evenly spaced between 0% and 100% throttle. Interstitial curves are interpolated.

3.5 VEHICLE PARAMETERIZATION

CarMaker uses over one hundred parameters defining the vehicle. Table 3-2 shows a minimum set of parameters to characterize the geometry, suspension, tires, and environmental conditions of the vehicle for simulation and for design of the control system in Chapters 4, 5, and 6. Parameters relating to the suspension and tires had to be assumed because CarMaker does not make these available to the user. This parameter set represents a medium class sedan, but any parameterization can be used. Adapting the control system for a new vehicle involves defining new values for this list and tuning the controller parameters.

Table 3-2 Vehicle parameter sets used in simulation. 4MIDEV data generated from default dataset for a medium-class vehicle with RT 195 65R15 p2.50 tires.

		Medium class 4MIDEV		
Name	*Symbol*	*Value*	*Unit*	*Comments*
Mass	m	1,321	kg	
Sprung mass	m_s	727.0	kg	
Roll moment of inertia	I_x	508.7	kg-m2	
Pitch moment of inertia	I_y	1,891.2	kg-m2	
Yaw moment of inertia	I_z	2,083.5	kg-m2	

Roll-yaw product of inertia	I_{xz}	5.642	kg-m2	
Tire polar moment of inertia	J	1.085	kg-m2	
Wheelbase	l	2.708	m	
Front semi-wheelbase	a	1.056	m	
Rear semi-wheelbase	b	1.652	m	
Front track width	2_{s1}	1.500	m	
Rear track width	2_{s2}	1.498	m	
Height of CG	h_{cg}	0.536	m	
Drag coefficient	C_d	0.32	-	
Frontal Area	A_f	2.139	m^2	
Tire radius	R	0.308	m	
Steering ratio	i_{st}	20	-	
Height of front axle roll center	h_1	0	m	Assumed value—inaccessible in IPG CarMaker
Height of rear axle roll center	h_2	0.05	m	Assumed value—inaccessible in IPG CarMaker
Distance from roll axis to CG	h_S	0.02	m	Assumed value—inaccessible in IPG CarMaker
Front axle roll stiffness	$k_{\phi 1}$	21,938	N/m	Assumed value—inaccessible in IPG CarMaker
Rear axle roll stiffness	$k_{\phi 2}$	17,976	N/m	Assumed value—inaccessible in IPG CarMaker
Front roll damping coefficient	$b_{\phi 1}$	868.5	Ns/m	Assumed value—inaccessible in IPG CarMaker
Rear roll damping coefficient	$b_{\phi 2}$	727.0	Ns/m	Assumed value—

				inaccessible in IPG CarMaker
Front tire cornering stiffness	$C_{\alpha f}$	36,724	N/rad	Assumed value—inaccessible in IPG CarMaker
Rear tire cornering stiffness	$C_{\alpha r}$	36,724	N/rad	Assumed value—inaccessible in IPG CarMaker
Front tire longitudinal stiffness	$C_{\lambda f}$	381	N	Assumed value—inaccessible in IPG CarMaker
Rear tire longitudinal stiffness	$C_{\lambda r}$	381	N	Assumed value—inaccessible in IPG CarMaker
Grip coefficient	M	0.5/0.8	-	0.5 for Mu-Split, 0.8 otherwise.
Rolling resistance coefficient	f	0.015	-	
Air density	ρ	1.24	kg/m^3	

4 DIRECT YAW MOMENT CONTROL (DYC)

This study employs DYC architecture for the design of the control system. This architecture addresses the issue of directional stability of vehicles near their handling limits by imposing a corrective moment by applying differential traction among the tires. It has been demonstrated that the corrective yaw moment produced by DYC is the most effective method of motion control when compared with other systems such as four-wheel steering (4WS) [12]. Different versions of DYC have been developed to respond to different control requirements, including yaw rate control, sideslip control and the simultaneous control of yaw rate and sideslip. PID control is often employed for high-level control in the former two cases because there is only one control objective. In the case of simultaneous control, it is advantageous to use other controllers such as sliding-mode control (SMC) which synthesizes the yaw rate and sideslip error into a switching function that drives the error states toward a desired trajectory on the phase plane within some region of attraction. The focus of this section is to develop two methods of computing the corrective yawing moment using SMC: a force-estimate feedback-based controller and a combined SMC/PI controller, both of which aim to control the yaw rate and sideslip angle simultaneously. The supervisory controller, which generates the reference signals for the DYC system to track, is established before formulating the controllers.

4.1 SUPERVISORY CONTROL

A supervisory controller computes the reference, or ideal yaw rate r and sideslip angle β as well as the admissible control region from gas and steering angle demanded by a driver or path-planning controller. The reference signals come from the ideal handling characteristic that the control engineer selects. Automotive engineers use the understeer gradient to evaluate the stability of a vehicle. The understeer gradient relates δ, the steering angle of the vehicle, to the radius of the turn, wheelbase, weight distribution, and the lateral acceleration. The following equation defines the linear form of the understeer gradient:

$$\delta = 57.3 l \rho_t + \left(\frac{F_{zf}}{C_{\alpha f}} - \frac{F_{zr}}{C_{\alpha r}}\right) \sum F_y \tag{4.1}$$

and:

$$K = \frac{F_{zf}}{C_{\alpha f}} - \frac{F_{zr}}{C_{\alpha r}} \tag{4.2}$$

where ρ_t denotes the curvature of the turn. The understeer gradient determines the fundamental turning characteristic and stability limits of the vehicle. Three possible characteristics exist: neutral steer ($K = 0$), understeer ($K > 0$) and oversteer ($K < 0$). These understeer gradients can be expressed in terms of the relative magnitude in the tire slip angle:

$$K = \begin{cases} 0, & if\ \alpha_f = \alpha_r \\ positive, & if\ \alpha_f > \alpha_r \\ negative, & if\ \alpha_f < \alpha_r \end{cases} \tag{4.3}$$

A limit understeering vehicle will lose grip on the front axle first due to the larger slip angle on the front axle, while a limit oversteering vehicle will lose grip on the rear axle first. An understeering vehicle is considered stable at its limit because a reasonably skilled driver could maintain control of the vehicle. On the other hand, an oversteering vehicle is considered unstable because rear wheel skidding tends to make the vehicle fishtail and spin out. A neutral steering vehicle is ideal in most cases because it maximizes the lateral acceleration that a vehicle can achieve for a given velocity and longitudinal acceleration. This is clear from the equation relating steering angle to lateral acceleration above. When the understeer gradient is zero, the additive dynamic term drops out and the required steering angle is equivalent to the kinematic steering angle:

$$\delta = 57.3 l \rho_t \tag{4.4}$$

The understeer gradient varies nonlinearly for all three possibilities. Figure 4.1 compares the understeer gradient for an electric Formula 1 racing vehicle with equal torque distribution and with torque-vectoring control with a neutral steer selected as the desired understeer gradient. The two vehicles perform similarly far away from the stability limit but begin deviating when the lateral acceleration exceeds 15 m/s^2. As the slope increases, the steering input becomes less effective at controlling the heading of the vehicle. This loss of control begins at 15 m/s^2 for the passive vehicle with a maximum lateral acceleration of 23 m/s^2. On the other hand, the torque-vectoring vehicle

extends effectiveness of steering input on the vehicle heading all the way up its maximum lateral acceleration, 25 m/s^2.

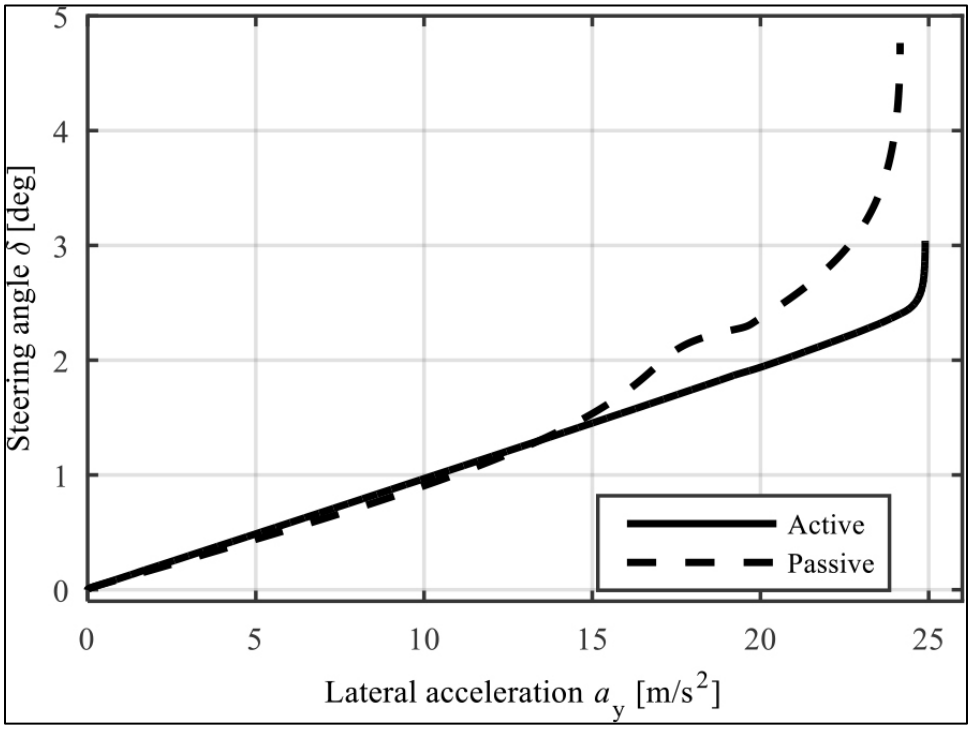

Figure 4.1 Understeer characteristics during a ramp steer test at 150 km/h: comparison of the passive vehicle and TV-controlled vehicle [38].

A linear vehicle model with two degrees of freedom called the bicycle model, with appropriate constraints on the dynamics, is proposed as a desired model to be followed by the controller. The advantage of using the bicycle model is that it is quick and easy to compute. The governing equations of the bicycle model come from a linearization of the nonlinear eight-degree-of-freedom model derived in 3 and neglecting roll dynamics. This linearized model is expressed in state-space form as [12]:

$$\begin{bmatrix}\dot{\beta}\\ \dot{r}\end{bmatrix} = \begin{bmatrix} -\dfrac{C_{\alpha f}+C_{\alpha r}}{mu} & \dfrac{-aC_{\alpha f}+bC_{\alpha r}}{mu^2} \\ \dfrac{-aC_{\alpha f}+bC_{\alpha r}}{I_z} & \dfrac{-a^2C_{\alpha f}-b^2C_{\alpha r}}{I_z u}\end{bmatrix}\begin{bmatrix}\beta\\ r\end{bmatrix} + \begin{bmatrix}\dfrac{C_{\alpha f}}{mu}\\ \dfrac{aC_{\alpha f}}{I_z}\end{bmatrix}\delta \tag{4.5}$$

The steady-state values of the yaw rate and sideslip angle are computed by setting $\dot{\beta}$ and $\dot{r}$ equal to zero and solving for β and r, leading to the expressions:

$$r_{ss} = \frac{u}{l + \left[\frac{m}{l}\left(\frac{b}{C_{\alpha f}} - \frac{a}{C_{\alpha r}}\right)\right]u^2}\delta \tag{4.6}$$

$$\beta_{ss} = \left(1 - \frac{mau^2}{blC_{\alpha r}}\right)\frac{b}{l + \left[\frac{m}{l}\left(\frac{b}{C_{\alpha f}} - \frac{a}{C_{\alpha r}}\right)\right]u^2}\delta \tag{4.7}$$

The expression for the steady-state yaw rate is substituted into the expression for the steady-state sideslip angle and is written as:

$$\beta_{ss} = r_{ss}\left(\frac{b}{u} - \frac{ma}{lC_{\alpha r}}u\right) \tag{4.8}$$

Referring to the equations of motion for the vehicle in 3, the lateral acceleration in the global reference frame is:

$$a_y = \dot{v} + ur \tag{4.9}$$

Setting $\dot{v}$ equal to zero, the vehicle steady-state lateral acceleration is:

$$a_{yss} = ur_{ss} \tag{4.10}$$

Rearranging the above expression yields a second equation for the steady-state yaw rate:

$$r_{ss} = \frac{a_{yss}}{u} \tag{4.11}$$

However, the steady-state lateral acceleration (expressed in g's) is limited by the grip coefficient of the road. Therefore, the maximum steady-state yaw rate must be limited to:

$$|r_{ss}| \leq \frac{\mu g}{u} \tag{4.12}$$

The torque-vectoring controller will be able to achieve a selected understeer gradient within the admissible control region. The equation for the steady-state yaw rate can be rewritten in terms of the desired understeer gradient as follows:

$$r_{ss} = \frac{u}{l + Ku^2}\delta \tag{4.13}$$

Since the largest performance benefit comes from a neutral steer vehicle, the desired understeer gradient throughout this thesis is set to zero, simplifying the expression for the steady-state yaw rate to:

$$r_{ss} = \frac{u}{l}\delta \tag{4.14}$$

Using the expression for the steady-state yaw rate and its admissible control region, the desired yaw rate can be expressed piecewise [12]:

$$r_d = \begin{cases} \frac{u}{l}\delta, & if \ \left|\frac{u}{l}\delta\right| < \frac{\mu g}{u} \\ \frac{\mu g}{u} sgn\left(\frac{u}{l}\delta\right) & otherwise \end{cases} \tag{4.15}$$

The sideslip angle is also significant in the control of vehicle yaw stability. A controller that tracks only yaw rate can still become unstable due to an uncontrolled increase in the sideslip angle. The sideslip angle is defined as the angle between the vehicle *x*-axis and the velocity vector at the center of gravity:

$$\beta = \frac{v}{u} \tag{4.16}$$

The sideslip angle cannot be measured without expensive sensors. These sensors generally are not used commercially as the cost may dissuade consumers. However, the sideslip angle can be estimated by combining sensor signals from an inertial measurement unit (IMU) and encoders on each wheel using sensor fusion techniques. The expression for the steady-state sideslip angle can be used to compute the desired sideslip angle β_d, but a simpler method is to assume the desired sideslip is always zero. This guarantees that the sliding-mode controller will continue to request a substantial torque distribution even when the yaw rate error goes to zero so long as there is a non-zero sideslip angle, which is always the case when turning. For this study:

$$\beta_d = 0 \tag{4.17}$$

The desired yaw rate and sideslip angle have been defined and an admissible control region has been established to limit the states of the reference model to feasible values. Depending on which of the two is available, the vehicle model derived in Chapter 3 and CarMaker may compute the yaw rate and sideslip angle in simulation, or the sideslip angle may be estimated for real-time applications. These states are fed back to produce the error states that are input into the high-level controller. This high-level controller is derived in the following subsection.

4.2 SLIDING MODE CONTROL

The objective of the high-level controller is to compute a desired total tractive force $F_{x,d}$ and corrective yaw moment $M_{z,d}$ to simultaneously track the desired vehicle cruising velocity and yaw dynamics. The desired tractive force comes from the driver (e.g. accelerator/brake pedal input). In the case of DYC control for a vehicle with either FWD or RWD, it is difficult to achieve both of the control objectives. The case where there are only two driving wheels makes the system determinant in

planar motion because the dimension of the control vector is the same as the state vector and there is a set of unique equilibrium points for the system [28, 41, 12]:

$$\dim\left(\begin{bmatrix}\delta\\T_1\\T_2\end{bmatrix}\right) = \dim\left(\begin{bmatrix}\beta\\r\\u\end{bmatrix}\right) \tag{4.18}$$

where T_1 and T_2 denote the torque vectoring distribution on a single axle. When negotiating a particularly sharp turn, differential driving torque on a single axle may be insufficient to generate the necessary yawing moment. In this case, a braking torque must be supplied to the inside wheel while a driving torque is applied to the outside wheel. The implication of this is that the velocity must decrease to generate the desired yaw moment. On the other hand, the 4MIDEV is an underdetermined system because the dimension of the control vector is greater than the dimension of the state vector, shown as:

$$\dim\left(\begin{bmatrix}\delta\\T_{11}\\T_{12}\\T_{21}\\T_{22}\end{bmatrix}\right) > \dim\left(\begin{bmatrix}\beta\\r\\u\end{bmatrix}\right) \tag{4.19}$$

which results in non-unique solutions to the equations of motion. The obvious implication of adding non-redundant actuators to drive the system is that it is more likely that there is a feasible combination of actuation signals to generate the desired velocity and yawing moment simultaneously. Moreover, this configuration can achieve some optimal behavior such as minimizing the total power demand from the electric motors.

The high-level controller is sub-divided into two parts, namely: a speed controller and a yaw moment controller. In this study, a PID controller handles the task of speed control while a sliding-mode controller handles the yaw moment control.

4.2.1 SLIDING MODE METHODS

The potential problems of only controlling the vehicle yaw rate or sideslip angle have already been discussed. In order to avoid the potential downside of only controlling one of these variables,

numerous multi-input DYC methods have been employed in research to adopt both states simultaneously as control variables. SMC is commonly used because of its good tracking and robustness to uncertainty in the observed values of the state. This is particularly useful for real-time implementation of DYC on a vehicle because of the stochastic nature of sensor signals. In this case, SMC has the added benefit of potentially compensating for accrued error in the sideslip observer and tire force estimator. This chapter proposes three variations of SMC. The CSMC depends directly on lateral force feedback from the tire force estimator and implements the switching function that is linear combination of the yaw rate and sideslip angle; the HSMC disconnects the tire force feedback and replaces it with a PI controller to compensate for the lack of tire force estimation; the MSMC employs force feedback and a modified switching function using a linear combination of the normalized absolute values of the yaw rate and sideslip angle to guarantee simultaneous convergence of the yaw rate and sideslip angle. This function also eliminates the possibility that the switching function equals zero when there is nonzero error [11]. The rationale for using force feedback is that it improves the transient response of the SMC and tracks the steady-state values of the yaw rate and sideslip well. The integral gain of the proportional-integral (PI) controller results in better tracking in the steady-state region but has a worse transient response than the force-based controller has. Instead of using a linearized and simplified vehicle control model, the sliding mode controller uses the complete nonlinear equations of motion proposed in Chapter 3 allowing the control design to be more effective over a wide operating range [11]. Chapter 7 presents a comparative simulation of the DYC system with three variations on SMC.

SMC is widely used in DYC systems and most commonly relies on a switching function, which is a linear combination of the error states. The definition of the conventional switching function follows:

$$s = r - r_d + \xi(\beta - \beta_d) \tag{4.20}$$

but in implementation a state observer estimates the sideslip angle and the switching function becomes:

$$\begin{aligned} s &= r - r_d + \xi\left(\hat{\beta} - \beta_d\right) \\ &= e_r + \xi \hat{e}_\beta \end{aligned} \tag{4.21}$$

where r_d and β_d are the desired yaw rate and desired sideslip angle discussed in Chapter 4 and ξ is a positive weight coefficient which reflects the allowable sideslip angle deviation [42]. The switching function in Equation (4.20) is ubiquitous in research but has a major limitation. An SMC works by driving the trajectories of the controlled states towards the sliding surface $s = 0$ and holding the trajectories on this surface. Ideally, this would occur when the error states converge to zero which is guaranteed when e_r and e_β have the same sign. Since the signs of the errors may change depending on the operating conditions, it is possible that $s = 0$ when $e_r = -\xi e_\beta$. In this case, the SMC will fail to track the desired values.

4.2.1.1 CONVENTIONAL DYC WITH FORCE FEEDBACK

One of the reasons SMC pairs well with DYC is that it directly depends on the nonlinear vehicle dynamics derived in Chapter 3. The advantage of using the nonlinear equation of motion for yaw in the computation of the control policy is that it avoids error that would otherwise arise due to linearization of the system or use of the simple bicycle model as is often the case with other control techniques. In many cases this error grows the more the states depart from the operating point about which the system was linearized—this is not the case with SMC, which produces stable dynamics for a wide operating range.

The nonlinear yaw dynamics are introduced into the control law by first taking the time derivative of the switching function:

$$\dot{s} = \dot{r} - \dot{r}_d + \xi\left(\dot{\hat{\beta}} - \dot{\beta}_d\right) \tag{4.22}$$

A fundamental principle of sliding mode control theory requires that, to drive the trajectories to the sliding surface $s = 0$, the following condition should be satisfied [11]:

$$\frac{1}{2}\frac{d}{dt}s^2 = s\dot{s} \tag{4.23}$$

$$s\dot{s} \leq -\eta|s|$$

where η is a positive constant. Away from the sliding surface $s > 0$ so (4.23) simplifies to:

$$\dot{s} \leq -\eta \tag{4.24}$$

Rearrangement of Equation (3.27) yields the following expression for $\dot{r}$:

$$\begin{aligned} \dot{r} = \frac{1}{I_z}(I_{xz}\dot{p} + a(F_{y11} + F_{y12})cos\delta - b(F_{y21} + F_{y22}) \\ + s_1(F_{y11} - F_{y12})sin\delta + \Delta M_z) \end{aligned} \tag{4.25}$$

where ΔM_z is the corrective yaw moment generated by the differential torque on all four wheels and is written as:

$$\Delta M_z = s_1(F_{x12} - F_{x11})cos\delta + s_2(F_{x22} - F_{x21}) + a(F_{x11} + F_{x12})sin\delta \tag{4.26}$$

The expression (4.25) is substituted into (4.22) to obtain the equation for $\dot{s}$ in terms of the yaw dynamics:

$$\begin{aligned} \dot{s} = \frac{1}{I_z}[I_{xz}\dot{p} + a(F_{y11} + F_{y12})cos\delta - b(F_{y21} + F_{y22}) + s_1(F_{y11} - F_{y12}) \\ + \Delta M_z] - \dot{r}_d + \xi\left(\dot{\hat{\beta}} - \dot{\beta}_d\right) \end{aligned} \tag{4.27}$$

In order to satisfy the condition (4.23), the following control policy is proposed [11, 42]:

$$\Delta M_z = \Delta M_{z,eq} - ksign(s) \tag{4.28}$$

where k is a designed controller gain and $\Delta M_{z,eq}$ is referred to as the *equivalent control* in sliding mode control theory [11]. The *equivalent control* is the control policy that would force $\dot{s}$ to zero and

depends on the chosen switching function *s*, which for the (4.20) can be expressed as follows by setting $\dot{s} = 0$ in (4.27) and rearranging the terms:

$$\Delta M_{z,eq} = I_z\left[\dot{r}_d - \xi\left(\dot{\hat{\beta}} - \dot{\beta}_d\right)\right] - a\left(F_{y11} + F_{y12}\right)cos\delta + b\left(F_{y21} + F_{y22}\right) - s_1\left(F_{y11} - F_{y12}\right)sin\delta \tag{4.29}$$

Combining (4.29) with (4.28) results in the control policy that used to control the vehicle yaw dynamics:

$$\Delta M_z = I_z\left[\dot{r}_d - \xi\left(\dot{\hat{\beta}} - \dot{\beta}_d\right)\right] - a\left(F_{y11} + F_{y12}\right)cos\delta + b\left(F_{y21} + F_{y22}\right) - s_1\left(F_{y11} - F_{y12}\right)sin\delta - ksign(s) \tag{4.30}$$

Substituting the full expression for the control policy back into (4.27) results in the following expression for the sliding mode dynamics:

$$\dot{s} = \frac{1}{I_z}[I_{xz}\dot{p} - \left(ksign(s)\right)] \tag{4.31}$$

Substituting (4.31) into (4.23) imposes the following condition on the gain *k:*

$$I_z[I_{xz}\dot{p} - ksign(s)] \leq -\eta \tag{4.32}$$

Rearranging the above inequality results in:

$$k \geq (I_z\eta + f)sign(s) \tag{4.33}$$

where $f = I_{xz}\dot{p}$. Since I_{xz} is constant and the roll acceleration $\dot{p}$ is constrained, it is assumed that the term f is bounded such that $|f| \leq I_{xz}\dot{p}$. A user-defined constant bound $F \geq I_{xz}\dot{p}_{max}$ is defined. The gain k is bound by:

$$k = I_z \eta sign(s) + F \tag{4.34}$$

As indicated in (4.30), that the SMC policy requires information about the yaw rate r, sideslip angle β, and tire forces. The yaw rate is measured from an on-board gyroscope, the sideslip angle and tire forces are estimated using the techniques employed in [20, 29, 43, 44] with cascaded Kalman filters.

As long as the chosen value for k satisfies condition (4.48) the error states are guaranteed to converge simultaneously to the sliding surface $s = 0$. It is noted that the measurement or estimation errors can be compensated for by increasing or decreasing the value of F. In effect, this adapts the value of the switching gain k. The governing equation for varying F is calculated as follows:

$$\begin{aligned} \Delta M_{eq} = I_z\left[\dot{r}_d - \xi\left(\dot{\hat{\beta}} - \dot{\beta}_d\right)\right] - a\left(\hat{F}_{y11} + \hat{F}_{y12}\right)cos\delta + b\left(\hat{F}_{y21} + \hat{F}_{y22}\right) \\ - s_1\left(\hat{F}_{y11} - \hat{F}_{y12}\right)sin\delta \end{aligned} \tag{4.35}$$

and the varying expression for f can be written as:

$$\begin{aligned} f = I_{xz}\dot{p} + a\left[\left(F_{y11} - \hat{F}_{y11}\right) + \left(F_{y12} - \hat{F}_{y12}\right)\right]cos\delta \\ - b\left[\left(F_{y21} - \hat{F}_{y21}\right) + \left(F_{y22} - \hat{F}_{y22}\right)\right] \\ + s_1\left[\left(F_{y21} - \hat{F}_{y11}\right) - \left(F_{y12} - \hat{F}_{y12}\right)\right] \end{aligned} \tag{4.36}$$

The chosen value of F is then adapted based on the force estimation errors by the designed maximum value of the lateral tire force estimation error. The design parameter F then needs to be chosen such that:

$$F \geq I_{xz}\dot{p}_{max} + 2(a + b + s_1)\Delta F_y \tag{4.37}$$

where ΔF_y denotes the maximum estimation error of the lateral tire forces. The above expression for F implies that by adapting the value chosen for F in such a way the measurement and estimation errors can be suppressed [11]. Since adaptation of F is equivalent to adaptation of k, it enlarges the demanded yaw-moment and exacerbates chattering.

The proposed control policy ΔM is discontinuous due to the *sign* terms which lead to chattering, effectively making the policy a "bang-bang" type control. This chattering can increase wear and even damage the actuators depending on the chattering frequency and is difficult to deal with when it comes to the conventional formulation of SMC. The conventional SMC (CSMC) policy is computed as follows:

$$\begin{aligned}\Delta M_{eq} = I_z\left[\dot{r}_d - \xi\left(\dot{\hat{\beta}} - \dot{\beta}_d\right)\right] - a\left(\hat{F}_{y11} + \hat{F}_{y12}\right)cos\delta + b\left(\hat{F}_{y21} + \hat{F}_{y22}\right) \\ - s_1\left(\hat{F}_{y11} - \hat{F}_{y12}\right)sin\delta - ksign(s)\end{aligned} \tag{4.38}$$

One way of dealing with this chattering is to implement a low-pass filter to attenuate the chattering signal. The trade-off for smoothing the control signal is that information is lost in the process. If the signal is attenuated too much, the performance of the controller will suffer. Designing a low-pass filter for the SMC requires tuning of the cut-off frequency to balance signal smoothing and information loss. A low-pass filter can be implemented as a simple first-order transfer function of the form:

$$\Delta M_{z_{LPF}} = \frac{1}{\tau_c s + 1}\Delta M_z \tag{4.39}$$

where τ_c denotes the time constant of the low-pass filter.

4.2.1.2 DYC WITH INTEGRAL GAIN

An adaptation to the above control policy follows in the absence of tire force estimation. Integral gain is used in control theory to eliminate steady-state error, which arises due to uncertainty in the vehicle

model and parameters. Thus, integral gain could replace the force terms to simplify the computation of the control policy. However, the transient response in this method generally performs worse than that of the force-based methods because it replaces the nonlinearity in the force terms with integral compensation, which is linear in the error states. Moreover, proportional-integral-derivative (PID) control is generally implemented as a single-input single-output (SISO) control and cannot be used with the switching function so it cannot compensate both e_r and e_β. Since the sideslip angle generally remains small up to the point when the tires start skidding the PID controller in this study is designed to compensate only the yaw rate error e_r and is written as:

$$\Delta M_{PI} = K_{Pr}(r - r_d) + K_{Ir}\frac{1}{s}(r - r_d) \tag{4.40}$$

where K_{Pr} and K_{Ir} are the proportional and integral gain for yaw-moment control, respectively and the derivative gain is zero. The subscript *r* differentiates this PID control from that of the speed controller proposed in Chapter 4.

Replacing the estimated tire force terms in (4.38) with (4.40) results in the proposed hybrid sliding mode-PI control policy [4, 11, 16].

$$\Delta M_z = I_z\left[\dot{r}_d - \xi\left(\dot{\hat{\beta}} - \dot{\beta}_d\right)\right] + K_P(r - r_d) + K_I\frac{1}{s}(r - r_d) - ksat\left(\frac{s}{\Phi}\right) \tag{4.41}$$

4.2.1.3 DYC WITH FORCE FEEDBACK AND MODIFIED SWITCHING FUNCTION

The final variation on SMC for the purpose of DYC follows the same logic as that in Section 4.2.1.1. However, this method relies on a more sophisticated switching function aimed at the simultaneous convergence of the yaw rate and sideslip angle onto the sliding-surface $s=0$. It is shown that this switching function proposed in [11] outperforms both variations of the conventional sliding-mode controllers. In this section, the same derivation for the conventional SMC with force feedback is carried out with this alternative switching function. This switching function is a linear combination of the normalized absolute values of the error states and is expressed as:

$$s = \frac{\rho}{|\Delta r|_{max}}|r - r_d| + \frac{1-\rho}{|\Delta\beta|_{max}}|\beta - \beta_d| \tag{4.42}$$

where $\rho \in [0,1]$ is a design parameter and $|\Delta r|_{max}$ and $|\Delta\beta|_{max}$ are the maximum absolute values of the yaw rate error and vehicle sideslip error chosen by the designer, respectively. Due to the absolute values of the error states in the above switching function, the switching function only becomes zero when the yaw rate error and sideslip error converge simultaneously. This eliminates the alternative possibility that the switching function goes to zero when the yaw rate error and sideslip error are non-zero with opposite signs. The error states are normalized with respect to designed maximum values and ρ is dimensionless and defines the relative importance of the error states. At its extremes, when $\rho=1$, the switching function is only a function of yaw rate error, and when $\rho=0$, the switching function is only a function of sideslip angle error.

The resulting derivative of the switching function (4.42) is written as:

$$\dot{s} = \frac{\rho}{|\Delta r|_{max}}|\dot{r} - \dot{r}_d| + \frac{1-\rho}{|\Delta\beta|_{max}}(\dot{\beta} - \dot{\beta}_d) \tag{4.43}$$

The following control policy is defined to satisfy the sliding condition (4.23) [11]:

$$\Delta M_z = \Delta M_{eq} - ksign(r - r_d) \tag{4.44}$$

The *sign* function in the expression for ΔM_z depends on the yaw error instead of the switching function in this case because the sign of the switching function (4.42) is always positive and tracking the yaw error is a higher priority than tracking the sideslip angle in this study.

The *equivalent control* in this derivation is more complex than in the conventional sliding-mode control policy proposed in Section 4.2.1.1 by virtue of a more complex switching function. The proposed equivalent control in this case is expressed as:

$$\Delta M_{eq} = I_z\left\{\dot{r}_d - \frac{|\Delta r|_{max}}{|\beta|_{max}}\frac{1-\rho}{\rho}\dot{\beta}sign[(r-r_d)\beta]\right\} - a\left(F_{y11}+F_{y12}\right)cos\delta + b\left(F_{y21}+F_{y22}\right) - s_1\left(F_{y11}-F_{y12}\right)sin\delta \tag{4.45}$$

Substituting ΔM_{eq} into (4.44) and then substituting the expanded equation for ΔM_z into (4.25), the following function for $\dot{s}$ can be derived:

$$\dot{s} = \rho/(I_z|\Delta r|_{max}[fsign(r-r_d) - k] \tag{4.46}$$

where $f = I_{xz}\dot{p}$ and *k* is a designed gain on the controller switching term defined in Section 4.2.1.1. The same process used previously to determine the bounding values for *k* is used in the derivation of this control policy as well and is now calculated as:

$$k \geq fsign(r-r_d) + \frac{\eta I_z|\Delta r|_{max}}{\rho} \tag{4.47}$$

$$k = \frac{\eta I_z|\Delta r|_{max}}{\rho} + F \tag{4.48}$$

where *F* is chosen using the adaptation law (4.37).

Like in the case of the conventional SMC, chattering is exacerbated by the adaptation of *F*. However, the modified variation replaces the *sign* function in control policy with the *sat* function and the policy takes on the following form:

$$\Delta M_z = I_z\left\{\dot{r}_d - \frac{|\Delta r|_{max}}{|\beta|_{max}}\frac{1-\rho}{\rho}\dot{\beta}sat\left[\frac{(r-r_d)\beta}{\Phi_1}\right]\right\} - a\left(F_{y11}+F_{y12}\right)cos\delta + b\left(F_{y21}+F_{y22}\right) - s_1\left(F_{y11}-F_{y12}\right)sin\delta - ksat\left(\frac{r-r_d}{\Phi_2}\right) \tag{4.49}$$

where Φ denotes a boundary layer thickness used to limit chattering to a region near the sliding surface so that control action along most of the trajectory remains smooth [11].. In this case, there are two *sign* terms in the control policy so boundary layer thicknesses Φ_1 and Φ_2 and are selected as independent design parameters.

This chapter focused on defining three variations of SMC to be compared. The two algorithms that use tire force feedback include an adaptation law on the switching gain *k* to compensate for some of the measurement and estimation error propagated by the IMU and cascaded Kalman filters. The hybrid sliding-mode and PI control simplifies the control policy by replacing the tire force feedback with integral gain. This section presented a derivation of the governing equations for three variations of DYC. The corrective yaw moment computed by the DYC is fed to the torque vectoring controller derived in Chapter 5.

4.3 SPEED CONTROLLER

The speed controller is a PID controller, which generates a throttle command based on the velocity error of the vehicle. The input to the speed controller is the difference between the desired velocity and current velocity. For large deviations in the velocity, the controller applies a large throttle to accelerate the vehicle with equal torque signals sent to all four wheels via the torque-vectoring controller. When the vehicle is just driving straight ahead this analogous to the equal-torque distribution on a conventional all-wheel drive (AWD) vehicle with equipped with passive differentials. The speed controller takes the following form:

$$\%\, throttle\ = K_P e_u + K_I \int e_u dt + K_D \frac{d}{dt} e_u \tag{4.50}$$

where K_P and K_I are the proportional and integral gain of the speed controller, respectively. The Laplace transformation is applied to Equation 4.50 allowing it to be expressed in the frequency domain:

$$\%\, throttle = K_P e_u + K_I \frac{1}{s} e_u + K_D s e_u \tag{4.51}$$

The velocity error is:

$$e_u = u_d - u \tag{4.52}$$

The throttle signal goes to the TVC directly and maps to the base torque T_{base} using the electric motor map in Table 3-1. T_{base} is a constraint on the TVC and it limits the allocation such that the sum of all four motor torques must be T_{base}. This constraint ensures that the TVC tracks the desired velocity and the corrective yaw moment simultaneously. This torque is easily mapped to the total driving force $F_{xtot,d}$ with the following expression:

$$F_{xtot,d} = \frac{1}{R} T_{base}. \tag{4.53}$$

5 TORQUE VECTORING CONTROL

There is a wide variety of techniques that can be used to achieve torque vectoring control (TVC). At any instant each of the four motors can independently produce torque ranging from its peak driving torque to a full braking torque and various combinations of torques can be produced for a given vehicle state. A system such as this is referred to as an *underdetermined system* where there is a higher degree of freedom in the control vector than in the state vector and is an ideal application for

optimal control. One of the greatest challenges with electric vehicles is battery life and range. Since the electric motors for a 4MIDEV are some of the biggest consumers of power on the vehicle, optimal torque vectoring control is often concerned with minimizing power consumption. On the other hand, electric vehicles are becoming increasingly viable in racing where performance is key. A common technique in this case is to distribute the torque according to the normalized vertical tire force so that the torque is distributed according to the peak force potential for each tire at any moment. The objective function used in this thesis is framed to minimize longitudinal slip power loss by minimizing the slippage on each tire while tracking the desired trajectory and the desired speed [16, 38, 17]. In other words, the TVC is an optimal traction controller.

5.1 DYNAMIC CONSTRAINTS

The torque distribution must be constrained by $M_{z,d}$ and $F_{x,d}$ as well as physical limitations of the force that can be generated by each wheel. The first two constraints arise from the wheel geometry and vehicle yaw dynamics. Recall that the desired yaw moment can be written in the form (4.26):

$$\Delta M_z = s_1(F_{x12} - F_{x11})cos\delta + s_2(F_{x22} - F_{x21}) + a(F_{x11} + F_{x12})sin\delta \tag{5.1}$$

Equation (5.1) can be written in as a vector product:

$$M_{z,d} = \boldsymbol{b_1 T} \tag{5.2}$$

where $\boldsymbol{b_1}$ is a 1x4 row vector where each element corresponds to sum of terms in (4.26) multiplied by the longitudinal force on each tire. Linearizing the relationship between the motor torque and longitudinal force on the wheels results in the following expression:

$$\boldsymbol{F_x} = \frac{\boldsymbol{T}}{R} \tag{5.3}$$

with $\boldsymbol{F_x}$ being the vector of longitudinal tire forces and $\boldsymbol{T}$ is the vector of motor torques. Combining (5.3) and (4.26), $\boldsymbol{b_1}$ can be written as:

$$\boldsymbol{b_1} = \left[\frac{asin\delta - s_1 cos\delta}{R} \quad \frac{asin\delta + s_1 cos\delta}{R} \quad -\frac{s_2}{R} \quad +\frac{s_2}{R}\right]. \tag{5.4}$$

The second constraint that must be satisfied is the total force $F_{x,d}$ demanded in order for the system to satisfy the driver input from the gas and brake pedals. The force on each tire must sum to this total force as follows:

$$F_{x,d} = F_{x11} + F_{x12} + F_{x21} + F_{x22} \tag{5.5}$$

Again, linearizing the forces as in expression (5.3) allows the equation for the total longitudinal force to be rewritten in terms of torque:

$$F_{x,d} = \boldsymbol{b_2 T} \tag{5.6}$$

where $\boldsymbol{b_2}$ denotes the vector:

$$\boldsymbol{b_2} = \left[\frac{1}{R} \quad \frac{1}{R} \quad \frac{1}{R} \quad \frac{1}{R}\right]. \tag{5.7}$$

With the two constraints expressed as vector they can be combined into a single equation:

$$\boldsymbol{BT - c = 0} \tag{5.8}$$

and:

$$\boldsymbol{B} = \begin{bmatrix} \boldsymbol{b_1} \\ \boldsymbol{b_2} \end{bmatrix}, \tag{5.9}$$

$$\boldsymbol{c} = \begin{bmatrix} M_{x,d} \\ F_{x,d} \end{bmatrix}. \tag{5.10}$$

The above constraints were related to the outputs of the speed controller and yaw-moment controller in DYC. Let us now turn our attention to the physical constraints on the motor torque. The limitations imposed on the motor torque for the purpose of torque-vectoring control comes from the rated performance of the motor discussed in Chapter 3; the road adhesion limit and the friction circle relationship. The road adhesion limit determines the maximum torque that can be applied assuming pure longitudinal slipping and the friction circle relationship accounts for combined slipping cases. These values change with the state of the vehicle, and hence they must be calculated at every time step, and the final limitation is the minimum of the three [16].

This thesis assumes that the four motors are the same so the motor performance of each is identical. The limiting torque is calculated at each time step by computing the rotational speed of the motors from the built-in encoders. The rotational speed is then fed into a one-dimensional look-up table, which computes the current peak torque of the motor for the speed at that instant. For the Pd18 motors, the look-up table for peak torque approximates the following equation:

$$|T_{max,em,i}| = \begin{cases} \dfrac{T_{peak,em}\eta}{i} & if\ 0 \le \omega_{em} < \omega_{em,0} \\ \dfrac{P_{peak}\eta}{\omega_{em}^2 i} & if\ \omega_{em,0} \le \omega_{em} \le \omega_{em,max} \end{cases} \tag{5.11}$$

where $T_{peak,em}$ denotes the constant peak torque of the motor in the operating range where the power demand is less than the peak motor power; η denotes the efficiency of the electric motors; i_{trans} denotes the transmission ratio between the motor and wheel; ω_{em} denotes the current rotational speed of the motor; $\omega_{em,0}$ is the rotational speed where the motor begins operating at peak power and the torque begins decreasing quadratically with increasing speed; P_{peak} denotes the peak power of the motor which is determined by the motor construction; $\omega_{em,max}$ denotes the maximum rotational speed that can be achieved by the motors and is determined by motor construction.

The Brushless 45 Maxon maximum torque are computed in a similar way as with the Pd18 motors with minor differences. The equation for the torque limitation for the Maxon motors as:

$$\left|T_{max,em,i}\right| = \begin{cases} \dfrac{T_{peak,em}\eta}{i_{trans}} & if\ 0 \le \omega_{em} < \omega_{em,0} \\ \dfrac{P_{peak}\eta}{\omega_{em} i_{trans}} & if\ \omega_{em,0} \le \omega_{em} \le \omega_{em,max} \end{cases} \tag{5.12}$$

Modeling the torque limitation for the electrical motors is identical (with the exception of the performance parameters) for operating points below peak power. Once the motor operates at its maximum rated power, the maximum torque for the Pd18 decreases to $1/\omega_{em}^2$ and the maximum torque for the brushless Maxon decreases proportional to $1/\omega_{em}$ [45, 46].

The second constraint on the motor torque comes from the road adhesion. According to the Magic Formula tire model described in Chapter 3, the peak force that can be achieved by a tire is given by $D = \mu F_z$. In general, the road adhesion coefficient is different in the wheel heading direction and in the direction perpendicular to the heading. This would lead to the pair of equations:

$$D_x = \mu_x F_z\,, \tag{5.13}$$

$$D_y = \mu_y F_z\,. \tag{5.14}$$

but in this thesis it is assumed that the directional coefficients are the same so the force in the longitudinal and lateral directions are governed by a single parameter μ. In order to maximize the torque effectiveness and minimize slip, the torque must be limited such that the longitudinal force it produces does not exceed the peak force. Once again employing the linearization (5.3), the road adhesion limitation is written as:

$$\left|T_{max,ad,ij}\right| = \mu_j F_{zij} R \tag{5.15}$$

where *i* symbolizes the front and rear axle and *j* symbolizes the left or right side. The road adhesion coefficients for the tires on the left and right sides can differ to allow the simulation of mixed-mu road conditions.

The final restriction arises from the friction circle in which the concept of the road adhesion limit is applied to the resultant of the forces in the tire x and y-directions. The following inequality defines this restriction:

$$\left(\frac{F_{xij}}{\mu_j F_{zij}}\right)^2 + \left(\frac{F_{yij}}{\mu_j F_{zij}}\right)^2 \leq 1 \tag{5.16}$$

Equation (5.16) is rearranged by carrying all terms to the right-hand side of the inequality except for F_{xij} and combining with (5.3). The following equality replaces the inequality when the tires operate at the edge of the friction circle:

$$\left|T_{max,fc,ij}\right| = R\mu_j F_{zij}\sqrt{1 - \frac{F_{yij}}{\mu_j F_{zij}}} \tag{5.17}$$

These torque limitations clearly depend on information about the tire forces. Chapter 4 discussed the necessity of a real-time estimator provides feedback to the DYC. Likewise, these torque limitations also depend on force estimate feedback. Hence, the latter two limitations become the following:

$$\left|\hat{T}_{\mathrm{max,ad,ij}}\right| = \mu_j \hat{F}_{zij} R \tag{5.18}$$

$$\left|\hat{T}_{\mathrm{max,fc,ij}}\right| = R\mu_j \hat{F}_{zij}\sqrt{1 - \frac{\hat{F}_{yij}}{\mu_j \hat{F}_{zij}}} \tag{5.19}$$

The three torque limitations combine to become a single condition that the maximum torque is the minimum of the previous three restrictions computed at each time step:

$$|T_i| \leq \min\left(T_{max,em,ij}, T_{max,ad,ij}, T_{max,fc,ij}\right) \tag{5.20}$$

and in vector form the condition is:

$$\boldsymbol{T_{min} \leq T \leq T_{max}} \tag{5.21}$$

5.2 OBJECTIVE FUNCTION

At the core of optimal control theory is the objective function, also referred to as the cost function. The goal of this optimization is to find a torque distribution that satisfies the objective function. An optimization algorithm searches for either the minimum or maximum of the objective function depending on the objective. In the case of unconstrained optimization, the optimization finds the minimum or maximum over the entire solution domain. However, the solutions to the objective function will be constrained based on the limitations developed in Section 5.1. In this thesis, the primal-dual gradient descent algorithm handles linear equality constraints, and inequality constraints as a dynamic system to solve the objective function [16, 47, 48, 49]. The reason for using constrained optimization is that it is better suited to address the physical limitations of a system in the real world. This section presents a derivation of the objective function and the primal-dual gradient descent algorithm that constitute the torque vectoring controller in the DYC system.

5.2.1 LONGITUDINAL SLIP POWER LOSS

The longitudinal slip power loss objective function poses the minimization problem as one aimed at reducing the power lost due to longitudinal slip. This function effectively works as an optimal traction control algorithm, whereas conventional traction control may saturate the torque in a way that does not minimize power loss or meet the control demand from the direct yaw controller. The equation to minimize the longitudinal slip power loss is [17]:

$$J_{sl} = \min_{\boldsymbol{T}} \sum_{i=1,j=1}^{2} \left|F_{x,ij} V_{s,x,ij}\right| \tag{5.22}$$

where V_{sij} denotes the longitudinal slip velocity of each tire and is expressed as:

$$V_{s,x,ij} = V_{w,x,ij}\sigma_{ij} \tag{5.23}$$

combining (5.23) with (3.34) and (3.35) to (3.38) and substituting back into (5.22) allows the objective function to be rewritten as:

$$J = \min_{\boldsymbol{T}} \sum_{i=1,j=1}^{2} \frac{T_{ij}}{R} V_{w,x,ij}\lambda_{ij} \tag{5.24}$$

Gradient descent depends on there being a smooth, continuous gradient of the objective function with respect to the minimization variable. Another condition placed upon the gradient is that the minimization variable must not vanish. This condition poses a problem with the above objective function, since it is only first-order with respect to the torque. The slip ratio depends on the tire force in the *Magic Formula* tire model in Chapter 3.3.1, but the nested trigonometric functions would make the gradient very complex. The gradient simplifies by using the following linear tire model instead:

$$F_{xij} = C_{\lambda,ij}\sigma_{ij} \tag{5.25}$$

rearranging the linear model, the slip ratio is written as a function of the longitudinal tire force and the constant longitudinal tire stiffness. This simplification tracks the true tire force sufficiently well in a small region near the origin of the tire force curve but overestimates the true force in the region near the maximum tire force. Hence, the gradient descent is more likely to converge to a local minimum rather than the global minimum as the slip ratio increases. However, this assumption should be sufficient as long as the tires operate at slip-ratios less than that of the maximum force which is usually in the range of ±10% slip. Applying the linear tire model, the objective function is rewritten as:

$$J_{sl} = \min_{\boldsymbol{T}} \sum_{i=1,j=1}^{2} \frac{T_{ij}^2}{C_{\lambda,ij} R^2} V_{w,x,ij} \tag{5.26}$$

Defining a matrix $\boldsymbol{D}$ as:

$$\boldsymbol{D} = \begin{bmatrix} \frac{V_{w,x,11}}{C_{\lambda,11} R^2} & 0 & 0 & 0 \\ 0 & \frac{V_{w,x,12}}{C_{\lambda,12} R^2} & 0 & 0 \\ 0 & 0 & \frac{V_{w,x,21}}{C_{\lambda,21} R^2} & 0 \\ 0 & 0 & 0 & \frac{V_{w,x,21}}{C_{\lambda,21} R^2} \end{bmatrix} \tag{5.27}$$

the objective function can be expressed in matrix form as:

$$J_{sl} = \min_{\boldsymbol{T}} \boldsymbol{T}^T \boldsymbol{D} \boldsymbol{T} \tag{5.28}$$

The full optimization problem is described by the following system:

$$\min_{\boldsymbol{T}} \quad J = \boldsymbol{T}^T \boldsymbol{D} \boldsymbol{T} \tag{5.29}$$

$$s.t. \quad \boldsymbol{B}\boldsymbol{T} - \boldsymbol{c} = 0 \tag{5.30}$$

$$\boldsymbol{T} - \boldsymbol{T_{min}} \geq 0 \tag{5.31}$$

$$\boldsymbol{T_{max}} - \boldsymbol{T} \geq 0 \tag{5.32}$$

5.3 PRIMAL-DUAL GRADIENT ALGORITHM

this section gives a more in-depth description of the primal-dual gradient descent algorithm and its application to the minimization problem. Gradient descent finds the optimal solution to the constrained minimization problem if one exists. The basic gradient descent algorithm is an unconstrained optimization, but the gradient method introduces the constraints as dynamic equations, which converge in finite time. A set of design parameters govern the transient behavior of these constraint equations. In some steps, the constraint equations may not be able to satisfy the constraints, but the final solution is guaranteed to be optimal [16].

The minimization problem can be rewritten in the generalized formulation:

$$\min_{\boldsymbol{T}} \quad J = f(x) \tag{5.33}$$

$$s.t. \quad \boldsymbol{h}(\boldsymbol{x}) = 0 \tag{5.34}$$

$$g(\boldsymbol{x}) \leq 0 \tag{5.35}$$

where $\boldsymbol{x} \in \mathbb{R}^n$, $f: \mathbb{R}^n \rightarrow \mathbb{R}$ is a strictly convex function, $\boldsymbol{h(x)} = \boldsymbol{Ax} - \boldsymbol{c}: \mathbb{R}^n \rightarrow \mathbb{R}^m$, $\boldsymbol{b} \in \mathbb{R}^m$ and $g(\boldsymbol{x}) = (g_i(\boldsymbol{x})), i = 1,\ldots, p: \mathbb{R}^n \rightarrow \mathbb{R}^p$ are convex $\mathbb{C}^2$-class functions [49]. The optimization variables change with the gradient of the cost function. The gradient descent and primal-dual dynamics is written as:

$$l(\boldsymbol{x}, \boldsymbol{\lambda}, \boldsymbol{\gamma}) = f(\boldsymbol{x}) + \boldsymbol{\lambda}^T \boldsymbol{h}(\boldsymbol{x}) + \boldsymbol{\gamma}^T \boldsymbol{g}(\boldsymbol{x}) \tag{5.36}$$

and its gradient is:

$$\frac{\partial l}{\partial \boldsymbol{x}} = \nabla f(\boldsymbol{x}) + \nabla \boldsymbol{h}(\boldsymbol{x})^T \boldsymbol{\lambda} + \nabla \boldsymbol{g}(\boldsymbol{x})^T \boldsymbol{\gamma} \tag{5.37}$$

Equation (5.37) is the *Lagrangian* of the optimization problem. $\nabla f(\boldsymbol{x})$ denotes the gradient of the objective function with respect to the optimization variable; $\nabla \boldsymbol{h}(\boldsymbol{x})$ and $\nabla \boldsymbol{g}(\boldsymbol{x})$ are gradient operators on $\boldsymbol{h(x)}$ and $\boldsymbol{g(x)}$, respectively and act such that:

$$\nabla \boldsymbol{h}(\boldsymbol{x}) = A \tag{5.38}$$

$$\nabla g_1 = -1 \tag{5.39}$$

$$\nabla g_2 = 1 \tag{5.40}$$

The modified gradient descent algorithm for this problem is formulated for discrete time steps and is given by:

$$\boldsymbol{x}^{k+1} = \boldsymbol{x}^k - \alpha_k(\nabla f(\boldsymbol{x}^k) + \boldsymbol{A}^T\boldsymbol{\lambda}^k + \nabla \boldsymbol{g}(\boldsymbol{x}^k)^T\boldsymbol{\gamma}^k \tag{5.41}$$

$$\boldsymbol{\lambda}^{k+1} = \boldsymbol{\lambda}^k + \beta_k \boldsymbol{h}(\boldsymbol{x}^k) \tag{5.42}$$

$$\boldsymbol{\gamma}^{k+1} = [\boldsymbol{\gamma}^k + \boldsymbol{\kappa}_k \boldsymbol{g}(\boldsymbol{x}^k)]_+ \tag{5.43}$$

where k denotes the current time step; α, β and κ denote fixed learning rate parameters for the Lagrangian, and primal-dual dynamic equations for the equality constraint and inequality constraint, respectively and $[\cdot]_+ = \max\{\cdot, 0\}$ applied componentwise. Note that the update equation for $\boldsymbol{x}^k$ seeks to minimize the Lagrangian with respect to its $\boldsymbol{x}$ argument while the update equations for $\boldsymbol{\lambda}^k$ and $\boldsymbol{\gamma}^k$ seek to maximize the Lagrangian with respect to their $\boldsymbol{x}$ arguments. The form of the update equation for $\boldsymbol{\gamma}^k$ is a *projected gradient algorithm.* The reason for the projection is that the vector of Lagrange multipliers is required to be nonnegative in order to satisfy the *Karush-Kuhn-Tucker* condition. Only the gradient is necessary, this algorithm is a *first order Lagrangian algorithm* [49]. The last step in the algorithm is a condition on the Lagrangian to evaluate the stable convergence of the $f(\boldsymbol{x})$ to the global minimum. For some $\boldsymbol{x}^*$ to be a global minimizer of $f(\boldsymbol{x})$, the following necessary condition must be satisfied:

$$\boldsymbol{P}\nabla f(\boldsymbol{x}^*) = 0 \tag{5.44}$$

where:

$$\boldsymbol{P} = \boldsymbol{I} - \boldsymbol{A}^T(\boldsymbol{A}\boldsymbol{A}^T)^{-1}\boldsymbol{A} \tag{5.45}$$

Although the above condition is necessary to prove there is a global minimum over the constraint set $\{\boldsymbol{x} : \boldsymbol{Ax} = \boldsymbol{b}\}$, it is not only sufficient if the *f* is a convex function, which in this case, it is. Applying the gradient descent algorithm to the objective function in Section 5.2 and the constraints in Section 5.1, the final expression for the optimal torque vectoring problem becomes:

$$\boldsymbol{T}^{k+1} = \boldsymbol{T}^k - \alpha_k\left(-2\boldsymbol{D}\boldsymbol{T} + \boldsymbol{B}\lambda^k + \gamma_1^k - \gamma_2^k\right) \tag{5.46}$$

$$\lambda^{k+1} = \lambda^k + \beta_k(\boldsymbol{B}\boldsymbol{T} - \boldsymbol{c}) \tag{5.47}$$

$$\gamma_1^{k+1} = [\gamma^k + \boldsymbol{\kappa}_k(\boldsymbol{T}_{\boldsymbol{min}} - \boldsymbol{T})]_+ \tag{5.48}$$

$$\gamma_2^{k+1} = [\gamma^k + \boldsymbol{\kappa}_k(\boldsymbol{T} - \boldsymbol{T}_{\boldsymbol{max}})]_+ \tag{5.49}$$

Equations (5.46) through (5.49) constitute a discrete dynamic system, which has stability margins and may oscillate. It is up to the designer to obtain a desired optimization performance by tuning the optimization, including the learning rate parameters, the maximum number of iterations, and the function tolerance. Table 5-1 shows the parameters chosen to achieve the desired dynamic response in this study. The chosen values for α, κ, and γ result in the second-order dynamic response with minimal overshoot and a short rise time shown in Figure 7.8.

Table 5-1 Selected parameter values for Primal-Dual Gradient Algorithm.

	Value	*Comments*
α	0.1	Learning rate for torque update
κ	0.01	Learning rate for equality constraint update
γ	0.01	Learning rate for inequality constraint update
Max # iterations	2e4	
Tolerance	1e-3	Resolution of the optimization. This is a user-defined minimum difference in computed torque from one iteration to the next. Reaching this tolerance means the optimization has succeeded in finding the optimal distribution.

6 UNIFIED TIRE FORCE ESTIMATOR

The incorporation of electronic stability control systems into modern vehicles has greatly increased the safety of driving. Stability control traditionally has relied on knowledge of the state of the vehicle obtained from sensors including inertial measurement units (IMUs), gyroscopes, wheel encoders and the global positioning system (GPS). While these signals are useful, they only provide information about the position and motion of the vehicle. Detection of the tire forces would enhance the robustness of active safety systems, but tire force sensors are prohibitively expensive and as such are generally limited to use in a research environment. The only alternative to direct detection of these forces is to estimate them. There is a copious amount of published research dedicated to designing estimation algorithms with varying degrees of success. Many of these methods can predict the true tire forces quite well, but only work well in a limited operating range. This limited operating range is since many algorithms depend on a simplified system model that must neglect certain dynamic effects so that the algorithms are compatible with real-time systems. These dynamic effects include tire wear and changes in the sprung mass.

Stochastic filters such as Kalman filters can address the estimation problem to a certain degree. The output of the Kalman filter is a fusion of the predicted states from the model and states detected by the sensors. The sensor input captures all the nonlinearities in the real plant and the filter output updates at each time step using the weighted difference between the predicted state and the actual state. This technique is not perfect and propagates estimation error like any other. Especially in the case when Kalman filters are cascaded together where the estimation of one filter is dependent on the output of another estimator, these errors can become significant. Acknowledging the drawbacks on tire force estimation, this thesis proposes a unified structure for the estimation of the longitudinal, lateral, and vertical tire forces using a series of Kalman filters. In practical implementation all three tire forces are computed at each instant and are then available to be fed back to other subsystems such as the direct yaw-moment controller and torque-vectoring controller proposed in Chapter 4 and Chapter 5, respectively. Figure 6.1 illustrates the overall structure of the estimation algorithm. It is worth noting that the lateral force estimation block is dependent on the estimated vertical tire forces, so some degree of error propagates forward. Rather than accepting the longitudinal and lateral acceleration signals directly from the accelerometer, the Lateral Force Estimation accepts it from the Vertical Force Estimation block. The reason for this is that the accelerometer detects the acceleration with respect to the current orientation of the vehicle, thus if there is any pitch or roll angle, part of the sensed acceleration comes from gravity, and error is introduced into the sensor signals, like in Figure 6.3. The Vertical Force Estimation block combines the detected accelerations with the states of a

suspension and the pitch and roll model shown in Figure 6.2 to correct the error introduced by gravity when the vehicle accelerates.

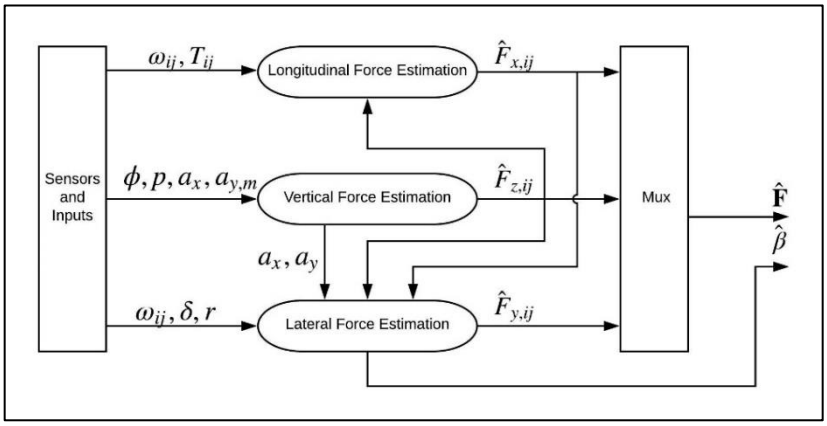

Figure 6.1 Unified structure of the force estimator and sideslip angle observer.

A unique feature of the lateral force estimation subsystem is that it employs the full nonlinear vehicle model with the Dugoff tire model introduced in Chapter 3. An advantage of this feature is that it allows for the prediction of states that cannot be directly sensed without exotic sensors or require the integration of accelerometer outputs. Integration of these states would produce large errors. The most crucial state of this type is the vehicle sideslip angle because it is a control variable for the DYC system. As a result, the unified estimation algorithm acts both as a tire force estimator and a sideslip observer [44, 29].

This section is broken into three sections dedicated to the tire force in each coordinate direction in ascending order of complexity: the first section presents the algorithm for longitudinal tire force estimation; the following section presents the vertical tire force algorithm, and the last section presents the lateral tire force algorithm.

6.1 LONGITUDINAL TIRE FORCE ESTIMATION

As discussed in Chapter 3, the longitudinal tire force develops as a nonlinear function of the slip ratio σ. In general, estimation of nonlinear functions is quite difficult. In this case, however, the tire force does not require a special filter and directly computes the force from a torque sensor and wheel encoder. Rearranging the wheel equation of motion (3.30), the following equation can be obtained [12]:

$$F_{xij}R = T_{ij} - J\dot{\omega}_{ij} \tag{6.1}$$

The above equation is rewritten in the Laplace domain [44, 50] as:

$$F_{x,ij}R = T_{ij} - Js\omega_{ij} \tag{6.2}$$

The wheel encoders detect the angular velocity of the wheels using quadrature and not the angular acceleration, so the angular acceleration comes from differentiating the encoder signal. This process introduces error because of measurement noise, but a low pass filter would be sufficient to attenuate the higher frequency fluctuation in the computed angular acceleration. On the other hand, the motor torque can be determined from the current *I* through the motor and voltage *V* across the motor terminals. In the absence of current and voltage sensing capabilities, the motor's torque map may perform a look-up of the torque as a function of wheel speed. The final equation for the longitudinal tire force estimate is:

$$\hat{F}_{x,ij} = \frac{1}{\tau s + 1}\frac{T_{ij}}{R} - \frac{1}{\tau s + 1}\frac{J}{R}s\omega_{ij} \tag{6.3}$$

where an appropriate τ is chosen to balance noise attenuation and signal fidelity. It is important to note that the longitudinal tire force estimate requires that the torque and force are proportional. When the tires operate near the perimeter of the friction circle and the tires reach the apex of the force curve, additional torque has a diminishing marginal impact on this force. Hence, this algorithm will only provide good estimates as long as the slip ratio remains small and is often bounded by $|\sigma| \leq 0.10$ in industry. If the rolling resistance term is not negligible then the expression for the tire force estimate becomes:

$$\hat{F}_{x,ij} = \frac{1}{\tau s + 1}\frac{T_{ij}}{R} - \frac{1}{\tau s + 1}\frac{J}{R}s\omega_{ij} - \frac{f\hat{F}_{z,ij}}{R} \tag{6.4}$$

where *f* is the rolling resistance coefficient and $\hat{F}_{z,ij}$ is the estimated vertical tire force. In normal cornering maneuvers for a full-scale vehicle, the order of magnitude of the vertical tire force 10^3 and the order of magnitude of the rolling resistance coefficient of asphalt is 10^{-3}, which resolves to a very small force due to rolling resistance. Unless the vehicle in question is off-road, it is generally acceptable to neglect the contribution of rolling resistance.

6.2 VERTICAL TIRE FORCE ESTIMATION

The vertical load distribution is essential for understanding the vehicle behavior in terms of steering, vehicle stability and cornering stiffness. This force determines the maximum cornering capability which dictates the acceptable operating range of safety systems as well as the boundary of the friction circle within which the tires must operate. It is practically impossible to estimate the lateral tire force without estimating the vertical tire force in some manner. The proposed algorithm consists of two blocks as shown in Figure 6.2.

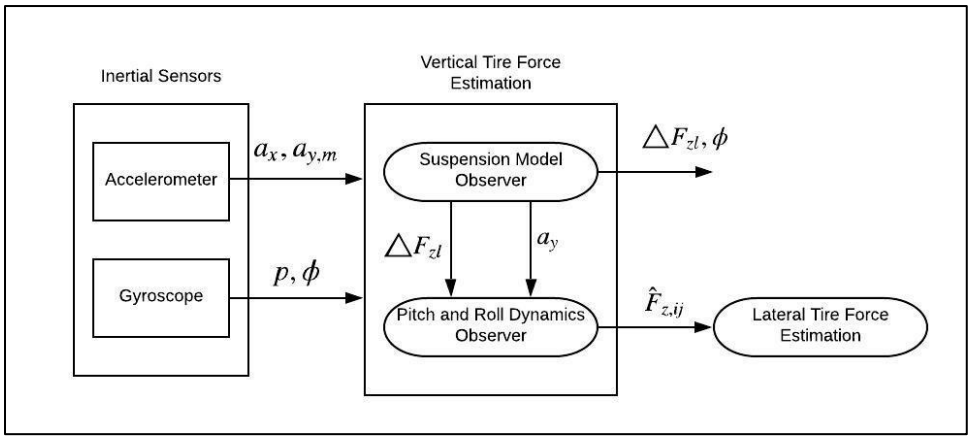

Figure 6.2 Vertical tire force estimation diagram

The inputs to the vertical tire force estimator come from the accelerometer and gyroscope units embedded in the inertial measurement unit (IMU). These inputs include the measured longitudinal and lateral acceleration a_x and a_y, respectively, the roll rate p and the roll angle φ. The intermediate variables in the algorithm include the left load transfer ΔF_{zl} and the lateral acceleration corrected for roll angle, a_y. The output of the algorithm is $\hat{F}_{z,ij}$, the vertical tire force on wheel ij.

The objective of the first part of the algorithm is to estimate the lateral load transfer. It uses a linear Kalman filter based on the vehicle's roll dynamics that arise due to the suspension, which is equivalent to estimating the elastic load transfer term discussed in Chapter 3.2. The second part estimates the geometric load transfer due to pitch and roll dynamics that arise from the longitudinal and lateral acceleration. In general, these effects are coupled, but if the coupling effect is neglected the geometric load transfer is simply a linear combination of terms including longitudinal acceleration and lateral acceleration. If one includes the coupled acceleration in the model, the estimated forces will track the true forces poorly during aggressive maneuvers unless a more complex, nonlinear filter is used. However, this study assumes the geometric load transfer is decoupled, allowing the use of a linear Kalman filter in the second part of the algorithm. In other words, two cascaded linear Kalman filters resolve the vertical force estimate. The algorithm depends on the assumptions that the positions of the roll centers do not change; that the suspension functions in its linear zone according to Hooke's Law; and the road is flat without irregularities [29].

6.2.1 ROLL PLANE MODEL

The single degree of freedom roll plane model that represents only the roll motion as follows describes the roll dynamics of the vehicle body:

$$I_x\dot{p} + \left(b_{\varphi 1} + b_{\varphi 2}\right)p + \left(k_{\varphi 1} + k_{\varphi 2}\right)\varphi = m_s h_s (a_y + g sin\varphi) \tag{6.5}$$

and the steady-state equation for the lateral load transfer applied to the left side of the vehicle is the sum of the geometric load transfer and the elastic load transfer:

$$\Delta F_{zl} = -\left(\frac{k_{\varphi 1}}{s_1} + \frac{k_{\varphi 2}}{s_2}\right)\varphi - \frac{m_s a_y}{l}\left(\frac{bh_1}{s_1} + \frac{ah_2}{s_2}\right) \tag{6.6}$$

6.2.2 LATERAL ACCELERATION CORRECTION

During movement, the accelerometer is unable to distinguish between the acceleration caused by vehicle motion and the gravitational acceleration. When the vehicle rolls, a portion of the sensed lateral acceleration comes from gravity. Since the gravity component is not of interest the acceleration needs correction. One way of correcting the acceleration is to compute it with the following equation:

$$a_{y,m} = a_y cos\varphi + gsin\varphi \tag{6.7}$$

Another way of correcting the acceleration is using sensor fusion. The vertical tire force estimator corrects the acceleration by comparing the measured acceleration to the acceleration predicted by the load transfer model that outputs planar acceleration. The measured acceleration contributes some nonlinearity to the predicted vertical force, while the model compensates for the gravity component of the measurement. Figure 6.3 illustrates how the lateral acceleration measured by an IMU mounted on the sprung mass results from the combination of the cornering acceleration and the gravitational acceleration.

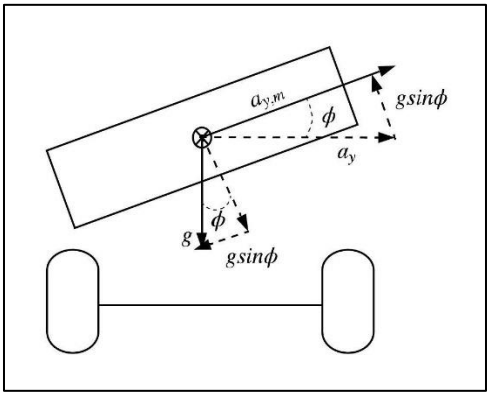

Figure 6.3 Components of lateral acceleration during normal cornering [29].

6.2.3 LATERAL LOAD TRANSFER MODELS

6.2.3.1 LINEAR ELASTIC LOAD TRANSFER MODEL

The Kalman filters used in this stage of the estimation structure are linear because the models on which they depend are linear. Hence, the models are a linear combination of the states and inputs, or in state-space form. These filters are stochastic, so stochastic state-space models are used. The following expression is the general form of a stochastic state-space model:

$$\boldsymbol{x}_k = \boldsymbol{A}\boldsymbol{x}_{k-1} + \boldsymbol{B}\boldsymbol{u}_k + \boldsymbol{w}_k\,, \tag{6.8}$$

$$\boldsymbol{y}_k = \boldsymbol{H}\boldsymbol{x}_k + \boldsymbol{v}_k \tag{6.9}$$

where $\boldsymbol{x_k}$ is the state vector at time step k; $\boldsymbol{A}^{n\,x\,n}$ is the state transition matrix; $\boldsymbol{B}^{n\,x\,p}$ is the input-to-state matrix; $\boldsymbol{u}_k$ is the control signal, $\boldsymbol{w}^{n\,x\,1}$ is the process noise vector; $\boldsymbol{y}^{m\,x\,1}$ is the measurement vector; $\boldsymbol{H}^{m\,x\,n}$ is the state-to-measurement matrix, and $\boldsymbol{v}^{n\,x\,1}$ is the measurement noise vector.

In the case of this linear stochastic system, the process and measurement noise are assumed Gaussian, white, uncorrelated, and have zero-mean. Hence, only the diagonal covariance matrix is necessary to describe the noise. First, the linear vehicle model for both parts of the vertical force estimator are proposed, and then the covariance matrices for the process and measurement noise are proposed.

Differentiating equation (6.6) with respect to time and combining and discretizing (6.5) through (6.7) results in the state-space model. The state vector $\boldsymbol{x}_k$ consists of the following states:

$$\boldsymbol{x}_k = \left[\Delta F_{zl,k}, a_{y,k}, \dot{a}_{y,k}, \varphi, p\right]^T \tag{6.10}$$

and is initialized as a null vector [29].

The system has no input vector, so the matrix $\boldsymbol{B}$ is null. The measurement vector $\boldsymbol{y}_k$ is determined by the relevant sensor signals available on the vehicle and is written as:

$$\boldsymbol{y}_k = \left[a_{y,m,k}, \varphi, p, \Delta F_{zl}\right]^T \tag{6.11}$$

The lateral acceleration $a_{y,m}$ is measured from the accelerometer, the roll angle φ and roll rate p are both measured by the gyroscope and the left load transfer is ΔF_{zl} is calculated from (6.6). With the state and measurement vectors chosen, the corresponding matrices $\boldsymbol{A}$ and $\boldsymbol{H}$ for the suspension model observer are given by:

$$\boldsymbol{A} = \begin{bmatrix} 1 & 0 & -t\frac{m_s}{l}\left(\frac{bh_1}{s_1}+\frac{ah_2}{s_2}\right) & 0 & -t\left(\frac{k_{\varphi 1}}{s_1}+\frac{k_{\varphi 2}}{s_2}\right) \\ 0 & 1 & t & 0 & 0 \\ 0 & 0 & 1 & 0 & 0 \\ 0 & 0 & 0 & 1 & t \\ 0 & tm_s\frac{h_s}{I_x} & 0 & t\frac{m_s g h_s-(k_{\varphi 1}+k_{\varphi 2})}{I_x} & 1-t\frac{b_{\varphi 1}+b_{\varphi 2}}{I_x} \end{bmatrix}, \tag{6.12}$$

$$\boldsymbol{H} = \begin{bmatrix} 0 & 1 & 0 & g & 0 \\ 0 & 0 & 0 & 1 & 0 \\ 0 & 0 & 0 & 0 & 1 \\ 1 & 0 & 0 & 0 & 0 \end{bmatrix}. \tag{6.13}$$

The constant *t* denotes the sampling time.

6.2.3.2 NONLINEAR GEOMETRIC LOAD TRANSFER MODEL

During normal driving, the vehicle accelerates longitudinally and laterally because of the longitudinal and lateral forces. These accelerations redistribute the vertical forces between wheels on the same axle as well as across the axles. The subject of the previous section was the estimation of the load transfer from one side of the vehicle to the other, laterally. In this section, a second filter incorporates this estimate to evaluate the vertical load on each tire.

The previous section assumed load transfer purely due to the suspension dynamics. This section concerns only the load transfer due to acceleration of the vehicle body, neglecting the suspension dynamics. Assuming coupling of the longitudinal and lateral acceleration necessitates the use of a more complex, nonlinear function for lateral load shift. The lateral load shift for the coupled model follows:

$$F_{z,11} = \frac{m}{2}\left(\frac{b}{l}g - \frac{h_{cg}}{l}a_x\right) - m\left(\frac{b}{l}g - \frac{h_{cg}}{l}a_x\right)\frac{h_{cg}}{2s_1 g}a_y \tag{6.14}$$

$$F_{z,12} = \frac{m}{2}\left(\frac{b}{l}g - \frac{h_{cg}}{l}a_x\right) + m\left(\frac{b}{l}g - \frac{h_{cg}}{l}a_x\right)\frac{h_{cg}}{2s_1 g}a_y \tag{6.15}$$

$$F_{z,21} = \frac{m}{2}\left(\frac{a}{l}g + \frac{h_{cg}}{l}a_x\right) - m\left(\frac{a}{l}g + \frac{h_{cg}}{l}a_x\right)\frac{h_{cg}}{2s_2 g}a_y \tag{6.16}$$

$$F_{z,22} = \frac{m}{2}\left(\frac{a}{l}g + \frac{h_{cg}}{l}a_x\right) + m\left(\frac{a}{l}g + \frac{h_{cg}}{l}a_x\right)\frac{h_{cg}}{2s_2 g}a_y \tag{6.17}$$

While the above system of equations alone would provide a decent estimate of the vertical tire force on each wheel, it neglects complex factors such as changes in the height of the center of gravity and roll center. A second, extended Kalman filter (EKF) constitutes the Pitch and Roll Dynamics Observer module in Figure 6.2, which compensates for the modeling error. The EKF is a nonlinear form of Kalman Filter and is preferable for this role because of the nonlinear-coupled terms in the system of equations.

This Kalman filter uses the same general form (6.8) and (6.9) as that in the previous section. The vehicle state vector $\boldsymbol{x}_k \epsilon \mathbb{R}^8$ is given as:

$$\boldsymbol{x}_k = \left[F_{z,11,k}, F_{z,12,k}, F_{z,21,k}, F_{z,22,k}, a_{x,k}, \dot{a}_{x,k}, a_{y,k}, \dot{a}_{y,k}\right]^T \tag{6.18}$$

The state vector is initialized as:

$$\boldsymbol{x}_0 = \left[\frac{F_{zf,static}}{2}, \frac{F_{zf,static}}{2}, \frac{F_{zr,static}}{2}, \frac{F_{zr,static}}{2}, 0, 0, 0, 0\right]^T \tag{6.19}$$

where the first four elements correspond to the vertical tire force on each wheel when the vehicle is at rest which is expressed in Chapter 3.3. The measurement vector $\boldsymbol{y}_k \epsilon \mathbb{R}^5$ is given by:

$$\boldsymbol{y}_k = \left[\Delta F_{zl,k}, \left(F_{z,11,k} + F_{z,12,k}\right), a_{x,k}, a_{y,k}, \sum F_{z,ij,k}\right]\text{^}T \tag{6.20}$$

where ΔF_{zl} and a_y come are outputs of the Suspension Model Observer module, $F_{z,11} + F_{z,12}$ is calculated directly from equations (6.14) and (6.15), a_x is measured using an accelerometer and $\sum F_{z,ij,k}$ is the constant total weight of the vehicle. The nonlinear state evolution function follows:

$$\boldsymbol{f} = [f_1, f_2, f_3, f_4, f_5, f_6, f_7, f_8]^T \tag{6.21}$$

where:

$$f_1 = x_{1,k-1} + t\left[-\frac{h_{cg}}{2l}mx_{6,k-1} - m\frac{bh_{cg}}{lw_1}x_{8,k-1} + m\frac{h_{cg}^2}{bw_1 g}x_{5,k-1}x_{8,k-1} + m\frac{h_{cg}^2}{lw_1 g}x_{6,k-1}x_{7,k-1}\right],$$

$$f_2 = x_{1,k-1} + t\left[-\frac{h_{cg}}{2l}mx_{6,k-1} + m\frac{bh_{cg}}{lw_1}x_{8,k-1} - m\frac{h_{cg}^2}{bw_1 g}x_{5,k-1}x_{8,k-1} - m\frac{h_{cg}^2}{lw_1 g}x_{6,k-1}x_{7,k-1}\right],$$

$$f_3 = x_{3,k-1} + t\left[\frac{h_{cg}}{2l}mx_{6,k-1} - m\frac{bh_{cg}}{lw_1}x_{8,k-1} - m\frac{h_{cg}^2}{bw_1 g}x_{5,k-1}x_{8,k-1} - m\frac{h_{cg}^2}{lw_1 g}x_{6,k-1}x_{7,k-1}\right],$$

$$f_4 = x_{4,k-1} + t\left[\frac{h_{cg}}{2l}mx_{6,k-1} + m\frac{bh_{cg}}{lw_1}x_{8,k-1} + m\frac{h_{cg}^2}{bw_1 g}x_{5,k-1}x_{8,k-1} + m\frac{h_{cg}^2}{lw_1 g}x_{6,k-1}x_{7,k-1}\right],$$

$$f_5 = x_{5,k-1} + tx_{6,k-1},$$

$$f_6 = x_{6,k-1},$$

$$f_7 = x_{7,k-1} + tx_{8,k-1},$$

$$f_8 = x_{8,k-1}.$$

In considering the relationship between the states and outputs in this case, each output of the model measurement function is a linear combination of the states. Consequently, the model measurement function is linear and is easily formulate as:

$$\boldsymbol{h} = [h_1, h_2, h_3, h_4, h_5]^T \tag{6.22}$$

$$h_1 = x_{1,k} - x_{2,k} + x_{3,k} - x_{4,k},$$

$$h_2 = x_{1,k} + x_{2,k},$$

$$h_3 = x_{5,k},$$

$$h_4 = x_{7,k},$$

$$h_5 = x_{1,k} + x_{2,k} + x_{3,k} + x_{4,k}.$$

The Pitch and Roll Dynamics Observer uses an EKF. The prediction step of the filter involves the computation of the Jacobian of the state evolution function and measurement function and linearizing the system at each time step for the given state. The steps to computing the new state estimate is practically identical to that of the linear Kalman filter after computing the Jacobians. Appendix 9.2.3.3 describes the systematic implementation of the EKF.

6.2.4 KALMAN FILTER DESIGN FOR VERTICAL FORCE ESTIMATION

The last component necessary to complete the estimator is to lay out the update algorithm to generate estimates in real-time. The Kalman filter computation has three steps: initialization, prediction and correction. In the initialization step an initial value of the state-vector and covariance matrix are set and only occurs once, usually when the system initializes. In the prediction step, the elements of the state-vector $\boldsymbol{x}$ and covariance matrix $\boldsymbol{P}$ are predicted for the next time step k using the system model derived in the previous two sections. In the correction step, fusion of the model prediction and sensor input results in an estimate of the state vector and covariance matrix for time step k. The initialization values for the state-vector are given in the previous sections and an initial covariance matrix should be chosen to be positive definite.

The prediction step of the Kalman filter is carried out as follows:

$$\hat{\boldsymbol{x}}_{k|k-1} = \boldsymbol{A}\hat{\boldsymbol{x}}_{k-1|k-1} + \boldsymbol{B}\boldsymbol{u}_k \,, \tag{6.23}$$

$$\boldsymbol{P}_{k|k-1} = \boldsymbol{A}\boldsymbol{P}_{k-1|k-1}\boldsymbol{A}^T + \boldsymbol{Q} \,. \tag{6.24}$$

where **Q** denotes the designed process covariance matrix. The following series of computations constitute the correction step:

$$\boldsymbol{K}_k = \boldsymbol{P}_{k|k-1}\boldsymbol{H}^T\left[\boldsymbol{H}\boldsymbol{P}_{k|k-1}\boldsymbol{H}^T + \boldsymbol{R}\right]^{-1} , \tag{6.25}$$

where $\boldsymbol{K}$ denotes the Kalman gain matrix. The estimate of the state is:

$$\boldsymbol{x}_{k|k} = \boldsymbol{x}_{k|k-1} + \boldsymbol{K}_k\left[\boldsymbol{y}_k - \boldsymbol{H}\boldsymbol{x}_{k|k-1}\right]. \tag{6.26}$$

The estimated covariance is then computed as:

$$\boldsymbol{P}_{k|k} = [\boldsymbol{I} - \boldsymbol{K}_k\boldsymbol{H}]\boldsymbol{P}_{k|k-1} \tag{6.27}$$

The update algorithm composed of equations (6.23) through (6.27) is the linear Kalman filter. In addition to this filter, the vertical tire force estimation employs an EKF, which Figure 6.2 presents. The linear systems representing the elastic and geometric load transfer models are observable if the observability matrix $\boldsymbol{O}$ has rank *n*. Multiplication of the state evolution matrix and measurement matrix results in the observability matrix seen below:

$$\boldsymbol{O} = \left[\boldsymbol{H}, \boldsymbol{HA}, \boldsymbol{HA^2}, \cdots, \boldsymbol{HA}^{n-1}\right]^T. \tag{6.28}$$

6.3 LATERAL TIRE FORCE ESTIMATION

As depicted in Chapter 4 and 5, the estimation of both the vertical and lateral tire forces enables the use of more complex control laws to stabilize the vehicle. Estimation of the lateral force is considerably more complex than in the case of both the longitudinal and vertical tire forces. The lateral force is highly nonlinear and is not directly observable, making the estimation process challenging. Assuming the vehicle only ever operates in the linear region of the lateral force curve, the estimate of the per-axle lateral force follows:

$$F_{y1} = \frac{ma_y b - I_z\dot{r}}{l\cos\delta} \tag{6.29}$$

$$F_{y2} = \frac{ma_y a + I_z\dot{r}}{l} \tag{6.30}$$

The force lateral force on each tire of the axle is proportional to the estimated vertical force. The advantage of this method is that it represents the lateral forces for normal driving situations well without *a priori* knowledge of the road friction and only relies on available measurements. On the other hand, it is only valid for a very limited range of lateral accelerations and any noise or error in the measured signals corrupt the results.

This section seeks to develop a stochastic lateral force estimator with a wide operating range and robustness against sensor noise. As shown in Figure 6.1 the lateral force depends on the output of the longitudinal and vertical force estimators. We have already derived the vertical force estimator and now have access to all the input signals upon which the lateral algorithm depends. This section employs another Kalman filter and it depends on the nonlinear vehicle model with the Dugoff tire model to address the nonlinearity in the tire force and observability problem. In this case, the vehicle model neglects suspension and roll dynamics as well as road grade and irregularities.

6.3.1 NONLINEAR STATE-SPACE MODEL

Assuming the road surface has already been classified and assigned an appropriate road adhesion coefficient, a stochastic, discrete-time, model-based Kalman filter is sufficient to predict the sideslip angle and lateral tire forces with input from kinematic sensors. Since the model is nonlinear, a nonlinear state-space formulation is necessary. The equation for the general form of a nonlinear state-space model is:

$$\boldsymbol{x}_k = f_{k-1}(\boldsymbol{x}_{k-1}, \boldsymbol{u}_k) + \boldsymbol{w}_k \tag{6.31}$$

$$\boldsymbol{y}_k = h(\boldsymbol{x}_k) + \boldsymbol{v}_k \tag{6.32}$$

where $\boldsymbol{x_k}$ is the state vector at time step k, f_{k-1} is the state evolution function, $\boldsymbol{w}^{n\,x\,1}$ is the process noise vector, $\boldsymbol{y}^{m\,x\,1}$ is the measurement vector, h is the observation function and $\boldsymbol{v}^{n\,x1}$ is the measurement noise vector. The state vector is as follows:

$$\begin{aligned} \boldsymbol{x}_k &= \left[x_{1,k}, x_{2,k}, x_{3,k}, x_{4,k}, x_{5,k}, x_{6,k}, x_{7,k}\right]^T, \\ &= \left[r_k, u_k, v_k, F_{y,11,k}, F_{y,12,k}, F_{y,21,k}, F_{y,22,k}\right]^T. \end{aligned} \tag{6.33}$$

where r_k, u_k and v_k denote the yaw rate, longitudinal velocity and lateral velocity, and $F_{y,ij,k}$ is the lateral tire force on tire ij at time step k, respectively. The state vector is initialized as a null vector so that:

$$\boldsymbol{x}_0 = [0, 0, 0, 0, 0, 0, 0]^T . \tag{6.34}$$

The equation for the vehicle sideslip angle is expressed in discrete time as:

$$\beta_k = arctan\frac{v_k}{u_k} \tag{6.35}$$

and is evaluated directly from the estimated states of the Kalman filter. The yaw and lateral dynamics are clearly dependent on the longitudinal tire forces. In [29] the front longitudinal tire forces are also states of the lateral tire force estimator, but this method limits the region of the nonlinear state-space within which the states are observable because the longitudinal for state has only one non-zero term and appears only in a single term in the model measurement function. Inclusion of the longitudinal force in as a state would tend to decrease the degree of observability in Equation (6.78). This thesis proposes a modified form of the nonlinear state-space model in which the longitudinal forces are inputs, not states, since the Unified Tire Force Estimator estimates them separately. The input vector is written as:

$$\boldsymbol{u}_k = \left[u_{1,k}, u_{2,k}, u_{3,k}, u_{4,k}, u_{5,k}, u_{6,k}, u_{7,k}, u_{8,k}, u_{9,k}\right]^T, \tag{6.36}$$

$$= \left[\delta_k, F_{z,11,k}, F_{z,12,k}, F_{z,21,k}, F_{z,22,k}, F_{x,11,k}, F_{x,12,k}, F_{x,21,k}, F_{x,22,k}\right]^T.$$

where δ_k, $F_{z,ij,k}$ and $F_{x,ij,k}$ denote the steering angle, vertical force on tire ij and longitudinal force on tire ij, respectively. The measurement vector $\boldsymbol{y}_k$ consists of the yaw rate, longitudinal velocity and longitudinal and lateral accelerations:

$$\boldsymbol{y}_k = \left[y_{1,k}, y_{2,k}, y_{3,k}, y_{4,k}\right]^T, \tag{6.37}$$

$$= \left[r_k, u_k, a_{x,k}, a_{y,k}\right]^T.$$

Typical IMUs do not measure the longitudinal velocity so it would need to be determined through integration or filtering of the acceleration. If the vehicle were in a two-wheel-drive configuration the longitudinal velocity could be approximated as the mean of the rolling wheel velocities calculated from the wheel-encoder data. However, a four-wheel-drive vehicle such as in this study experiences slip on all four wheels, so the all four wheels propagate error if used for velocity estimation. Longitudinal velocity estimation is outside the scope of this study.

The nonlinear state evolution function *f* which relates the state at time step *k* to the previous state at time step *k-1* and the input $\boldsymbol{u}_k$ is [29]:

$$f = [f_1, f_2, f_3, f_4, f_5, f_6, f_7]^T \tag{6.38}$$

where:

$$f_1 = x_{1,k-1} + \frac{t}{I_z}[a\left(x_{4,k-1}cosu_{1,k} + x_{5,k-1}\cos \mathrm{u}_{1,\mathrm{k}} + \left(u_{6,k} + u_{7,k}\right)sinu_{1,k} - b\left(x_{6,k-1} + x_{7,k-1}\right)\ldots\right.$$
$$\left. + s_1\left[\left(x_{4,k-1} - x_{5,k-1}\right)sinu_{1,k}\right) + \left(-u_{6,k} + u_{7,k}\right)cosu_{1,k}\right] + s_2\left(-u_{8,k} + u_{9,k}\right)\Big],$$

$$f_2 = x_{2,k-1} + tx_{1,k-1}x_{3,k-1} + \frac{t}{m}\left[-\left(u_{6,k} + u_{7,k}\right)cosu_{1,k} - \left(x_{4,k-1} + x_{5,k-1}\right)sinu_{1,k}\right],$$

$$f_3 = x_{3,k-1} - tx_{1,k-1}x_{2,k-1}\ldots$$
$$+ \frac{t}{m}\left[-\left(u_{6,k} + u_{7,k}\right)sinu_{1,k} + \left(x_{4,k-1} + x_{5,k-1}\right)cosu_{1,k} + x_{6,k-1} + x_{7,k-1}\right],$$

$$f_4 = x_{4,k-1} + \frac{tx_{2,k-1}}{\sigma_{rl,f}}\left[-x_{4,k-1} + \bar{F}_{y,11}\left(\alpha_{11,k-1}, u_{2,k}\right)\right],$$

$$f_5 = x_{5,k-1} + \frac{tx_{2,k-1}}{\sigma_{rl,f}}\left[-x_{5,k-1} + \bar{F}_{y,12}\left(\alpha_{12,k-1}, u_{3,k}\right)\right],$$

$$f_6 = x_{6,k-1} + \frac{tx_{2,k-1}}{\sigma_{rl,r}}\left[-x_{6,k-1} + \bar{F}_{y,21}\left(\alpha_{21,k-1}, u_{4,k}\right)\right],$$

$$f_7 = x_{7,k-1} + \frac{tx_{2,k-1}}{\sigma_{rl,r}}\left[-x_{7,k-1} + \bar{F}_{y,22}\left(\alpha_{22,k-1}, u_{5,k}\right)\right],$$

where t is the sampling rate, $\bar{F}_{y,ij}$ corresponds to the force predicted by the Dugoff tire model and $\alpha_{ij,k-1}$ is the tire slip angle and is computed with equations (3.39) through (3.42). The equations for the tire slip angle in terms of the states are computed by:

$$\alpha_{11,k-1} = u_{1,k} - \operatorname{atan}\left(\frac{x_{3,k-1} + ax_{1,k-1}}{x_{2,k-1} - s_1 x_{1,k-1}}\right), \tag{6.39}$$

$$\alpha_{12,k-1} = u_{1,k} - \operatorname{atan}\left(\frac{x_{3,k-1} + ax_{1,k-1}}{x_{2,k-1} + s_1 x_{1,k-1}}\right), \tag{6.40}$$

$$\alpha_{21,k-1} = -\operatorname{atan}\left(\frac{x_{3,k-1} - bx_{1,k-1}}{x_{2,k-1} - s_2 x_{1,k-1}}\right), \tag{6.41}$$

$$\alpha_{22,k-1} = -\operatorname{atan}\left(\frac{x_{3,k-1} + bx_{1,k-1}}{x_{2,k-1} + s_2 x_{1,k-1}}\right). \tag{6.42}$$

The observation equation, h is:

$$h = [h_1, h_2, h_3, h_4]^T \tag{6.43}$$

where:

$$h_1 = x_{1,k},$$

$$h_2 = x_{2,k},$$

$$h_3 = \frac{1}{m}[-(x_{4,k} + x_{5,k})sinu_{1,k} + (u_{6,k} + u_{7,k})cosu_{1,k}],$$

$$h_4 = \frac{1}{m}\left[(x_{4,k} + x_{5,k})cosu_{1,k} + (u_{6,k} + u_{7,k})sinu_{1,k} + x_{6,k} + x_{7,k}\right].$$

6.3.1.1 DUGOFF TIRE MODEL WITH FIRST ORDER DYNAMICS

The tire model used in this study was first described in Chapter 3.3.2. This tire model computes both the longitudinal force $F_{x,ij}$ and lateral force $F_{y,ij}$ for pure slip or combined loading using a model of the friction circle. However, it is unnecessary to consider combined slip in the context of the lateral tire force estimation because the torque allocation output by the torque vectoring controller upon which the longitudinal tire force estimation depends accounts for combined slip already. Hence, for any given lateral force, the longitudinal force will drop to remain in the friction circle. Consequently, the Dugoff model can be simplified to compute lateral force only. The simplified model is expressed as [34, 29]:

$$F_{y,ij} = -C_{\alpha,ij} tan\alpha_{ij} f(\tau_{ij}) \tag{6.44}$$

where $f(\tau)$ is still given by equation (3.61) but the equation for τ becomes:

$$\tau = \frac{\mu F_{z,ij}}{2C_{\alpha,ij}|tan\alpha_{ij}|} \tag{6.45}$$

The slip angle for each wheel is computed with equations (3.39) through (3.42).

Equations f_4 through f_7 utilize a dynamic form of the Dugoff tire model. If it is assumed that the tire force is a first-order response to an imposed slip angle, the dynamic expression for the lateral tire force can be written as:

$$\tau_c \dot{F}_y + F_y = \bar{F}_y, \tag{6.46}$$

where τ_c is a relaxation time constant, F_y is the dynamic lateral force and $\bar{F}_y$ is the quasi-static tire force calculated by the Dugoff tire model. The relaxation time constant can be approximated by:

$$\tau_c = \frac{C_\alpha}{Ku}, \tag{6.47}$$

where *K* is the effective tire lateral stiffness. This relaxation time constant is the time it would take to build the tire force to 63.2% of the steady-state force. Multiplying the relaxation time constant be the vehicle's velocity, *u*, results in a relaxation length:

$$\sigma_{rl} = \frac{C_\alpha}{K}, \tag{6.48}$$

where σ is the approximate distance the tire must travel before 63.2% of the steady-state tire force is achieved for the given longitudinal velocity. The relaxation length is a physical quantity that varies substantially with changes in vertical tire force and longitudinal velocity and cannot be known precisely without tires equipped with load cells and extensive testing. However, in this study it is considered sufficient to assume the relaxation distance is a fixed parameter. While there is no precise information about the relaxation distance available for this study, a general rule of thumb is that it is of the order of magnitude of the wheel radius at nominal vertical load [35].

Equation (6.46) can be rewritten in terms of the relaxation length as:

$$\dot{F}_y = \frac{u}{\sigma_{rl}}\left(-F_y + \bar{F}_y\right). \tag{6.49}$$

Equation (6.49) is used in f_4 through f_7 because, in reality, the tire force is not generated instantly. If this were the case, the lateral tire force estimation could feasibly return a high frequency oscillating force estimate. More importantly, this enables the lateral force to be written as an ordinary differential equation and discretized for use in the state evolution function.

6.3.2 KALMAN FILTER DESIGN FOR LATERAL FORCE AND SIDESLIP ESTIMATION

The stochastic discrete-time nonlinear state-space model for the nonlinear Kalman filter was developed. Like in the case of vertical tire force estimation, a Kalman filter is used to estimation the

lateral dynamics. Due to the high degree of nonlinearity, a linear Kalman filter is not sufficient. Two other alternatives exist: The extended Kalman filter (EKF) and the unscented Kalman filter (UKF). These filters are both used to estimate nonlinear functions with a key difference: the EKF depends on a first-order Taylor series linearization of the model at each operating point and the UKF employs the full nonlinear function. Hence, the UKF generally does a better job of estimating highly nonlinear functions but is slower than the EKF when the linearization is simple. The UKF was chosen for this application for two reasons. The first reason is that the lateral tire force is a highly nonlinear function of tire slip angle and the second reason is that the linearization of the Dugoff tire model is not trivial.

The update algorithm for the UKF is fundamentally different from that of the linear Kalman filter and EKF. The latter two filters follow the same set of steps: initialization, prediction and correction with the added step of linearizing the system model at each step. On the other hand, the UKF employs something called the *Unscented Transformation*, which is a method for calculating the statistics of a random variable [29, 51].

The UT uses a set of weighted points, or *sigma points*, which represent samples of probability distributions. These points are chosen such that they completely capture the true mean and covariance of the Gaussian variable accurately up to the third-order Taylor series expansion for any nonlinearity. The sigma points are calculated in the steps that follow.

6.3.2.1 THE UNSCENTED TRANSFORMATION

The UT generates a set of $2n+1$ sigma points $\boldsymbol{\chi}$ which approximate some n dimensional vector of random variables x_i with sample mean $\bar{\boldsymbol{x}}$ and covariance $\boldsymbol{P}_{xx}$. This transformation can be interpreted as a Monte Carlo simulation of the input-output set fed through the nonlinear function, f using a minimum sample set, and the final estimate can be interpreted as a regression on this input-output data. The sigma points are computed as follows:

$$\boldsymbol{\chi}_0 = \bar{\boldsymbol{x}} \;\; for\; i = 0, \tag{6.50}$$

$$\boldsymbol{\chi}_i = \bar{\boldsymbol{x}} + \left(\sqrt{(n+\kappa)\boldsymbol{P}_{xx}}\right)_i \quad for\; i = 1, \cdots, 2n, \tag{6.51}$$

$$\boldsymbol{\chi}_{i+n} = \bar{\boldsymbol{x}} - \left(\sqrt{(n+\kappa)\boldsymbol{P}_{xx}}\right)_{i-n} \quad for\; i = n+1, \cdots, 2n, \tag{6.52}$$

with the corresponding weight parameters:

$$w_0^{(m)} = \frac{\kappa}{n+\kappa} \quad for\ i = 0, \tag{6.53}$$

$$w_0^{(c)} = \frac{\kappa}{n+\kappa} + (1 - \alpha^2 + \beta^2) \quad for\ i = 0, \tag{6.54}$$

$$w_i^{(m)} = \frac{1}{2(n+\kappa)} \quad for\ i = 1, \cdots, 2n, \tag{6.55}$$

$$w_i^{(c)} = \frac{1}{2(n+\kappa)} \quad for\ i = 1, \cdots, 2n, \tag{6.56}$$

where the term $\left(\sqrt{(n+\kappa)\boldsymbol{P}_{xx}}\right)_i$ is the ith column of the matrix square root of $(n+\kappa)\boldsymbol{P}_{xx}$ and w_i are the weights associated with the ith sigma point. The parameter κ is given by:

$$\kappa = \alpha^2(n+\kappa) - n, \tag{6.57}$$

where α influences the spread of the points around $\bar{\boldsymbol{x}}$ and is usually some small positive number, κ is a secondary scaling parameter and β is related to the probability density function and selected based on prior knowledge of the distribution. For this study it is assumed that α is bounded by:

$$1e10^{-4} \leq \alpha \leq 1, \tag{6.58}$$

whereas κ = max(*0*, *3-n*) = *0* and β = *2*, which is considered optimal for a Gaussian distribution [51, 29].

Once the sigma points and corresponding weights are computed, the sigma points are fed through the nonlinear function to map the input-output response of the sigma points to the nonlinear model as follows:

$$\boldsymbol{z}_i = f(\boldsymbol{\chi}_i). \tag{6.59}$$

The mean and covariance of $\boldsymbol{z}$ is computed from the weight average and weighted outer product of the transformed sigma points $\boldsymbol{z_i}$, respectively*:*

$$\bar{\boldsymbol{z}} = \sum_{i=0}^{2n} w_i^{(m)} \boldsymbol{z}_{i,} \tag{6.60}$$

$$\boldsymbol{P}_{zz} = \sum_{i=0}^{2n} w_i^{(c)} (\boldsymbol{z}_i - \bar{\boldsymbol{z}})(\boldsymbol{z}_i - \bar{\boldsymbol{z}})^T \tag{6.61}$$

6.3.2.2 UKF ALGORITHM

The UKF algorithm consists of three steps that are related to but different from those of the linear and extended Kalman filters. These steps, sequentially, are the state prediction, taking into account process noise; the observation prediction, taking into account observation noise and finally the cross-correlation prediction [29, 51, 44].

The process model is written in the familiar form:

$$\boldsymbol{x}_{k+1} = f(\boldsymbol{x}_k, \boldsymbol{u}_k). \tag{6.62}$$

A set of *2n+1* transformed sigma points are computed by feeding the original sigma points from Equations (6.50), (6.51) and (6.52) through the nonlinear process model:

$$\boldsymbol{\chi}_{i,k+1|k} = f\left(\boldsymbol{\chi}_{i,k-1}, \boldsymbol{u}_{k-1}\right). \tag{6.63}$$

The predicted mean of the state vector is the weighted average of the transformed augmented sigma points:

$$\bar{\boldsymbol{x}}_{k|k-1} = \sum_{i=0}^{2n} w_i^{(m)} \boldsymbol{\chi}_i, \tag{6.64}$$

and the predicted covariance is computed as follows:

$$\boldsymbol{P}_{k|k-1} = \boldsymbol{Q}_k + \sum_{i=0}^{2n} w_i^{(c)} \left(\boldsymbol{\chi}_i - \bar{\boldsymbol{x}}_{k|k-1}\right)\left(\boldsymbol{\chi}_i - \bar{\boldsymbol{x}}_{k|k-1}\right)^T, \tag{6.65}$$

where $\boldsymbol{R}$ is the covariance matrix of the process noise $\boldsymbol{w}$.

Next, the augmented set of sigma points feed through the observation model to obtain another set of transformed sigma points:

$$\boldsymbol{\gamma}_{i,k} = h\left(\boldsymbol{\chi}_{i,k-1}, \boldsymbol{u}_{k-1}\right). \tag{6.66}$$

In this same manner as before, the mean observation vector is computed as:

$$\bar{\boldsymbol{y}}_{k|k-1} = \sum_{i=0}^{2n} w_i^{(m)} \boldsymbol{\gamma}_{i,k}. \tag{6.67}$$

and the innovation, or observation covariance is:

$$\boldsymbol{P}_{YY,k} = \boldsymbol{R}_k + \sum_{i=0}^{2n} w_i^{(c)} \left(\boldsymbol{\gamma}_{i,k} - \bar{\boldsymbol{y}}_{k|k-1}\right)\left(\boldsymbol{\gamma}_{i,k} - \bar{\boldsymbol{y}}_{k|k-1}\right)^T, \tag{6.68}$$

where is $\boldsymbol{R}$ is covariance matrix of the observation noise, $\boldsymbol{v}$. Next, the cross-correlation matrix is determined by:

$$\boldsymbol{P}_{XZ,k} = \sum_{i=0}^{2n} w_i^{(c)} \left(\boldsymbol{\chi}_{i,k} - \bar{\boldsymbol{x}}_{k|k-1}\right)\left(\boldsymbol{\gamma}_{i,k} - \bar{\boldsymbol{y}}_k\right)^T. \tag{6.69}$$

Then the Kalman gain can be computed according to:

$$\boldsymbol{K}_k = \boldsymbol{P}_{XZ,k}\boldsymbol{P}_{YY,k}^{-1}, \tag{6.70}$$

and finally is used to update the estimated state and covariance:

$$\bar{\boldsymbol{x}}_k = \bar{\boldsymbol{x}}_{k|k-1} + \boldsymbol{K}_k\left(\boldsymbol{y}_k - \bar{\boldsymbol{y}}_{k|k-1}\right), \tag{6.71}$$

$$\boldsymbol{P}_k = \boldsymbol{P}_{k|k-1} - \boldsymbol{K}_k\boldsymbol{P}_{YY,k}\boldsymbol{K}_k^T \tag{6.72}$$

The observability of the nonlinear system is complex and the degree of observability may vary over time. In this study, the Lie derivative is used. The Lie derivative for h_i of order $(r+1)$ is defined as:

$$L_f^{r+1}h_i(\boldsymbol{x}) = \frac{\partial L_f^r h_i(\boldsymbol{x})}{\partial \boldsymbol{x}} f(\boldsymbol{x}, u) \tag{6.73}$$

where

$$L_f^1 h_i(\boldsymbol{x}) = \frac{\partial h_i(\boldsymbol{x})}{\partial \boldsymbol{x}} f(\boldsymbol{x}, u), \tag{6.74}$$

where $i \in \{1, \ldots, p\}$.

The nonlinear observability function o_i for the observation function h_i is defined as:

$$o_i = \begin{bmatrix} dh_i(\boldsymbol{x}) \\ dL_f^1 h_i(\boldsymbol{x}) \\ \vdots \\ dL_f^{n-1} h_i(\boldsymbol{x}) \end{bmatrix}, \tag{6.75}$$

where *d* is the partial derivative operator:

$$dh_i = \left[\frac{\partial h_i}{dx_1}, \cdots, \frac{\partial h_i}{dx_n}\right]. \tag{6.76}$$

The system observability matrix is calculated as:

$$\boldsymbol{O} = \begin{bmatrix} o_1 \\ \cdots \\ o_p \end{bmatrix}. \tag{6.77}$$

The system is observable if and only if the observability matrix has rank *n*. A nonlinear system may gradually become unobservable in some areas of the phase space. To quantify the degree of observability, an observability index can be used and is defined as:

$$\Lambda(\boldsymbol{x}_k) = \frac{\lambda_{min}[\boldsymbol{O}^T\boldsymbol{O}, \boldsymbol{x}_k]}{\lambda_{max}[\boldsymbol{O}^T\boldsymbol{O}, \boldsymbol{x}_k]}, \tag{6.78}$$

where $\lambda_{max}[\boldsymbol{O}^T\boldsymbol{O}, \boldsymbol{x}_k]$ denotes the maximum eigenvalue of the dot product of the observability matrix estimated at each point $\boldsymbol{x}_k$ at each time step. The minimum eigenvalue is computed in the same fashion. Thus, $0 \leq \Lambda(\boldsymbol{x}_k) \leq 1$ where the lower bound is reached when the system is unobservable at state $\boldsymbol{x}_k$ [29].

7 SIMULATION RESULTS

This section presents a comparative study of the results of the three configurations of the Direct Yaw Moment Controller (DYC). All three systems share the same parameters and algorithms for the Torque Vectoring Controller (TVC) and Unified Tire Force Estimator (UTFE). Chapter 5 and Chapter 6 discuss these parameters and algorithms, respectively, in much more detail. The primary differences between the DYC methods lies in the formulation of the switching function and in the handling of tire force feedback which are discussed in more detail in Chapter 4. For clarity, these three methods are referred to as "conventional sliding mode control (CSMC)", "hybrid sliding mode control (HSMC)" and "modified sliding mode control (MSMC) which are discussed in 4.2.1.1, 4.2.1.2, and 4.2.1.3, respectively. In addition to these methods, a fourth system referred to as "open loop" is simulated. The open loop system is unable to produce torque differentials and represents how a conventional vehicle might perform. These control systems control the vehicle motion via its powertrain; hence, it relies on a model of the vehicle to produce feedback signals. CarMaker, a high-fidelity vehicle simulation tool, is employed to simulate four vehicle maneuvers and evaluate the differences in performance when equipped with each controller. In addition to being able to simulate maneuvers, CarMaker provides a virtual sensor toolbox which enables the simulation of real IMU, encoder and steering angle sensor signals. CarMaker validates its models using real measurement data from test vehicles equipped with a suite of sensors and can simulate responses to common maneuvers within 5% of the same vehicle's actual response to the same stimulus.

Before the closed loop control performance of the vehicle can be evaluated, the open loop performance of the TVC must be shown to be stable. Two tests are simulated to show that the TVC remains stable when subjected to zero stimulation of the yaw mode and when subjected to a step input. The first of the two tests is to disconnect the high-level controller and accelerate from rest up to some velocity, u_{final} then remain at speed. When there is no stimulation of the vehicle's yaw mode and the only signal fed to the TVC is the base torque, T_{base} that evolves from the electric motor map discussed in Chapter 3. In this case, there should be no difference in the torque produced by the motors on the left and right sides of the powertrain. In the second of the two tests, the vehicle is accelerated from rest up to a steady-state velocity and is then subjected to a step steer and yaw moment input at the same time. This test demonstrates that the TVC is stable when the yaw mode is highly excited and steady.

Even if the open loop system is stable, it does not guarantee it will remain stable when the loop is closed. In order to ascertain the stability of the closed loop systems and investigate their performance, four closed loop tests are performed. The first of these tests is a J-turn whereby the driver increases the steering angle linearly while holding the velocity steady for a period, after which they hold the

steering angle steady at some final value. This maneuver excites the yaw mode while minimizing the time variance. This maneuver is followed by a sinusoidal steering sweep. The effect of a sinusoidal steering maneuver is like that of a lane-change. In this case, the driver maintains steady velocity while providing a sinusoidal steering input. This test excites the yaw mode with a greater time rate of change than the J-turn. The third of the four maneuvers is a skid pad. A skid pad is effectively the inverse of a J-turn. During the skid pad a driver slowly accelerates from rest while turning through a circular road of constant curvature. The test ends when the vehicle is no longer able to negotiate the turn, either because it fishtails or goes off the road. Fishtailing is characteristic of terminal oversteer while "going of the road" is characteristic of terminal understeer. A more detailed discussion of oversteer and understeer is found in Chapter 4. In this test the lateral acceleration increases steadily and minimizes nonlinearity in the load transfer which would arise from the suspension dynamics and coupling of the longitudinal and lateral acceleration expressed in (6.14), (6.15), (6.16) and (6.17). Such an effect can enable the steering angle to be expressed as a single-variable function of lateral acceleration and allows the characteristic understeer gradient of the vehicle to emerge. The linearized function (4.1) indicates that the slope of this function is the understeer gradient, which depends on the difference of the ratio of the front axle vertical load to front tire cornering stiffness and front axle rear axle vertical load to rear tire cornering stiffness. DYC attempts to control the yaw dynamics in such a way that this difference is zero, so that the understeer gradient, and thereby the slope relating lateral acceleration to steer angle, becomes zero. In other words, the skid pad test enables the performance of the controller to be framed as how successfully the controller drives the slope of this function to zero. The final test is referred to as a "braking mu-split" test. Here, the vehicle accelerates to freeway speed, after which the two left tires hit a strip of road with a much lower coefficient of friction, which could represent snow or ice. The driver slams on the brakes, but the left tires are unable able to translate a fraction of the braking torque into braking force, so the vehicle tends to spin out clockwise. In this scenario, the high-level controller detects that the vehicle is beginning to spin even though the driver has not input a steering angle and generate a corrective yaw moment to offset the clockwise spin while, at the same time, satisfy the torque constraints imposed by the TVC based on the friction circle and load on each individual tire. The performance of the controllers is framed as how effectively they reduce or even prevent spinout.

All implementation of the work presented in the preceding chapters was done within the MATLAB and Simulink environments. Once complete, the Simulink model was built as C code using a CarMaker's TLC compiler and exported to the CarMaker API as the custom plug-in PowerTrain model TVC_OpenXWD. All simulations were run, and results obtained using a high-fidelity custom medium-class vehicle model designed in the spirit of a BMW 5 Series sedan.

7.1 UNIFIED TIRE FORCE ESTIMATOR SUMMARY

The Unified Tire Force estimator is a crucial component in maximizing the effectiveness of the force-based sliding mode controller. The output of the sliding mode controller depends on the computation of the moment about the vehicle body z-axis, which is a function of the switching function, controller gain and lateral tire forces according to (4.38) and (4.49). A set of three individual estimation modules constitutes the estimator, but it is "unified" in the sense that the lateral estimation step, the final and, by far, most involved step depends on the estimates from the longitudinal estimation step and vertical estimation step. The UTFE outputs a 3D vector of tire forces for each individual tire and outputs twelve force estimates.

This chapter investigates the UTFE in open loop only so that the controllers and estimators can be evaluated independent of each other. There is no real benefit to evaluate the closed loop behavior of the estimator because its objective, tracking the real tire forces as closely as possible, is entirely unrelated to and independent of the objectives of the Direct Yaw Moment Controller. Furthermore, it is more desirable to investigate the DYC with the UTFE out of the loop because it is difficult to discern the influence of the UTFE on the performance of the controllers. The results of the UTFE are presented for each closed loop maneuver in this section and is evaluated by how closely it tracks the nonlinear RT 195 65R15 p2.50 tires from CarMaker's Tire Data Set Generator. This generator uses the Magic Formula and tire characteristics defined by the European Standard Tire and Rim Technical Organization (ETRTO) to develop nonlinear tire curves from measurement data. It is important to note that when referring to the UTFE, "open loop" means that the states feedback to it and the forces are estimated, but they do not feed back to the SMC. Rather, the RT model forces feedback. As stated before, this is to decouple the controller and estimator for the purpose of analysis.

The force estimation sections for each of the simulated maneuvers demonstrate estimator performance for the x, y, and z forces that are consistently different. The vertical (z-direction) force estimate tracks the RT model very well for a variety of operating conditions. The longitudinal force estimate tracks the RT model well for less aggressive maneuvers but even then, it deviates if there is significant load transfer, rolling resistance, or application of brakes. On the other hand, the lateral force estimate is somewhat unpredictable because it is highly nonlinear and is relatively difficult to observe. Sometimes it performs well, but in some cases, it is even unable to track the shape of the RT tire force response. One would not be wrong to say that the lateral force estimates and, to a degree, the longitudinal force estimates are mediocre. These forces are incredibly difficult to predict even using measurement data and the Magic Formula tire model. A large amount of data is required to develop an accurate model. On the other hand, the UTFE produces decent estimates with a great deal of robustness considering that there is substantial uncertainty in the tire and suspension parameters.

7.2 OPEN LOOP TVC RESULTS

The TVC constitutes the foundation of this study by the fact that it is principally responsible for allocating the torque to each end of the powertrain of the vehicle. More so than the yaw moment controller, the TVC is at risk of instability due to its dynamic nature, especially if an inappropriate set of learning parameters is chosen for the primal-dual gradient descent algorithm. The stability of the controller was investigated through open loop simulations with the TVC disconnected from the yaw-moment controller and sending it only throttle and the angular velocity of the wheels, the two signals necessary to compute the base torque from the electric motor map of the Pd18 motors. The learning rates chosen for the algorithm are those listed in Table 5-1. The objective function is the longitudinal slip power loss function described in Chapter 5. Slip power loss occurs when the slip ratio becomes excessive, so minimizing slip power loss is essentially a form of traction control.

Figure 7.1 shows the result of the torque allocation for a scenario in which the vehicle is initially to 100 km/h from rest and then maintains that speed until the simulation ends. The torque allocates a high torque during the period that the vehicle is acceleration. Once the top speed is achieved, the torque drops sharply to a level required only to maintain the speed. Notably, the torque on all four wheels is identical. This is due to the cost function that was adopted: torque is biased towards the wheels with a greater longitudinal stiffness, C_λ. In this study, it was assumed that all four wheels have the same stiffness, so the minimum power loss would occur if the wheels were all driven with the same torque.

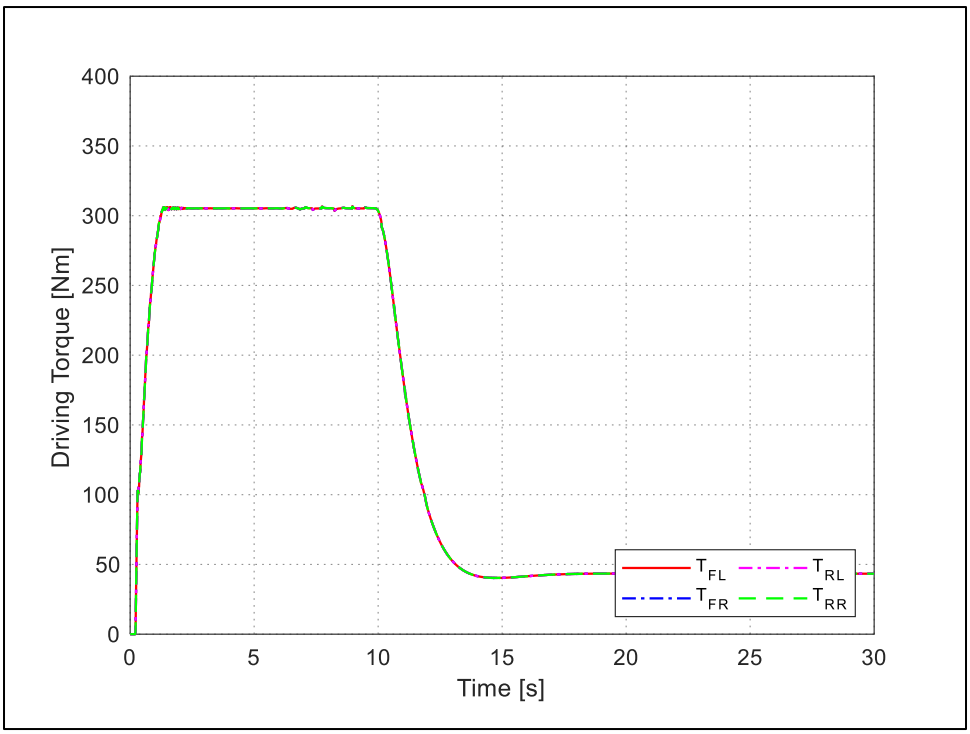

Figure 7.1 Torque response of the TVC during straight driving when front and rear wheels have equal stiffness. Vehicle starts at rest, accelerates to 100 km/h, and holds speed.

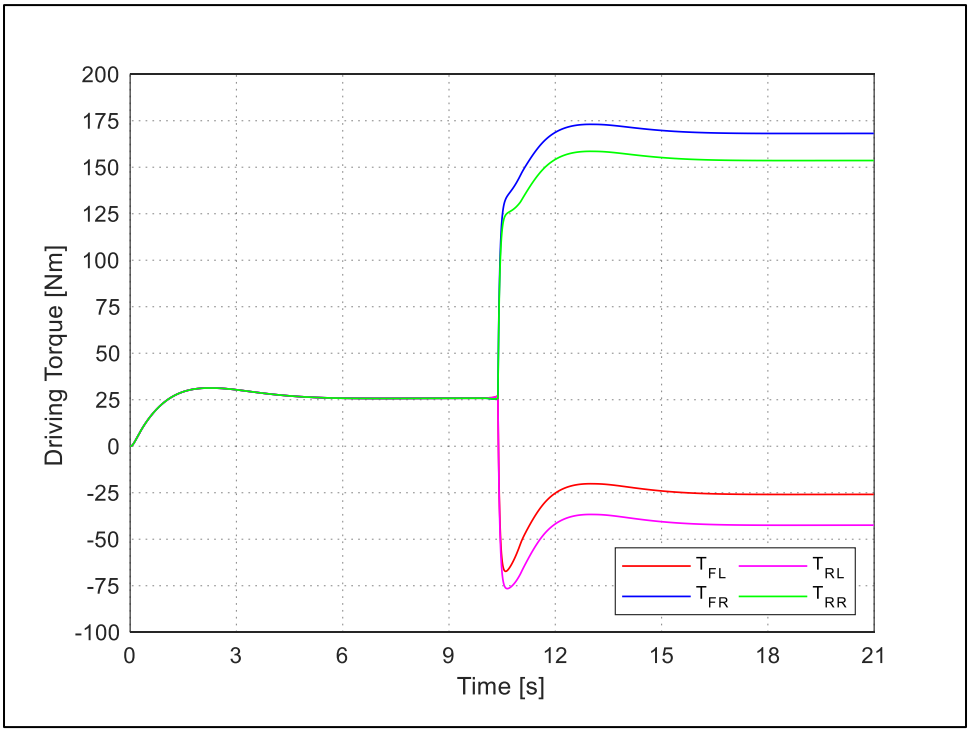

Figure 7.2 Torque response of the TVC to a step steer and moment where u = 45 km/h, $\dot{\delta}_{f,step}$ = 120 deg/s and M_z = 2000 Nm.

If, for instance, the longitudinal stiffness of the tires on the front axle were greater than on the rear axle, the front axle could bear a greater torque than the rear axle for the same slip, so the allocation would bias towards the front axle and shift T_{FL} and T_{FR} up.

Figure 7.2 shows the torque response of the torque allocation when subjected to a simultaneous step input of steer and yaw moment at t = 10 s. The vehicle is steered to the left, so the desired yaw moment is counterclockwise. A step input is not achievable and so the step is modeled as a ramp steer that is one second long. The torque sent to the outside wheels is positive, driving, and the torque sent to the inside wheels is negative, braking. Interestingly, the torque sent to the front outside wheel is greater than the rear outside wheel, but the opposite is true for the inside wheels—the magnitude of the braking torque from the motor on the rear inside wheel is greater than it is for the front inside wheel. The front axle bears a greater portion of the vehicle weight, so one would think both front wheels would produce more torque than the rear wheels. However, the front wheels also steer. Typically, when torque is applied, the moment arm is the distance between the wheel and the centerline of the car, or half the track width. Since the front wheels turn, they also have a longer moment arm than the rear wheels and so can generate a greater moment for the same torque. This demonstrates the very important job the torque-vectoring controller has of juggling the tire load, friction limits and steering angle when coming up with a torque allocation solution.

7.3 CLOSED LOOP DYC RESULTS

This section presents results from simulations in CarMaker of the complete closed loop system. After demonstrating the effectiveness and stability of the torque-vectoring controller in open loop, the next step was to connect it to the supervisory controller, yaw moment controller and Unified Tire Force Estimator (UTFE). This system works by feeding the throttle and steering angle imposed by the driver and the current vehicle velocity to a supervisory controller which computes setpoints for the yaw rate and sideslip angles which would result in the understeer gradient, K, being driven to zero. These setpoints go to the yaw moment controller. Other signals fed to the yaw moment controller are the yaw rate detected by the IMU and the sideslip angle and lateral tire forces estimated by the UTFE. The yaw moment controller combines the yaw rate and sideslip angle into a switching function used by a sliding mode controller (SMC) to compute the desired yaw moment required to meet the request of the supervisory controller. The desired yaw moment goes to the torque-vectoring controller, which allocates the torque to satisfy the desired yaw dynamics imposed by the yaw moment and the desired longitudinal dynamics imposed by the throttle while also attempting to minimize excessive longitudinal slip.

Each of the four following major sections summarizes the results of each simulated maneuver. These results are presented as plots. The first plots are related to the performance of the closed loop controller, include plots of the yaw rate response, and sideslip angle response in that order. Responses from DYC systems with CSMC, HSMC, and MSMC are shown on a single plot so that they can be compared. The next plot is the torque distribution computed by the TVC for the system with MSMC. The choice to present a torque plot for MSMC was made because chatter in the CSMC and HSMC systems make the torque distributions practically unintelligible, whereas distribution from the MSMC was smooth and easily interpreted. The last part of each section presents the results of the UTFE. Included in these results are plots of the longitudinal force, lateral force, and vertical force, with the results of the RT tire model overlaid for comparison. The tire force plots for each section number twelve in total. Unlike for the other three maneuvers, the results of the skid pad includes a plot of the USG following the sideslip angle response because this maneuver involves the vehicle traversing a constant radius circle so the ideal steering angle is constant and nonzero so it is obvious from a plot of the USG whether a vehicle demonstrates understeer, oversteer, or neutral steer.

7.3.1 J-TURN

This section presents the results of a J-turn simulated in CarMaker performed at the upper end of intermediate lateral acceleration (~ 0.6g). The maneuver is carried out at 45 km/h, an appropriate speed for urban driving and the steering profile is as shown in Figure 7.3. The speed and steering profile of this maneuver is very similar to what one might expect entering and negotiating a roundabout.

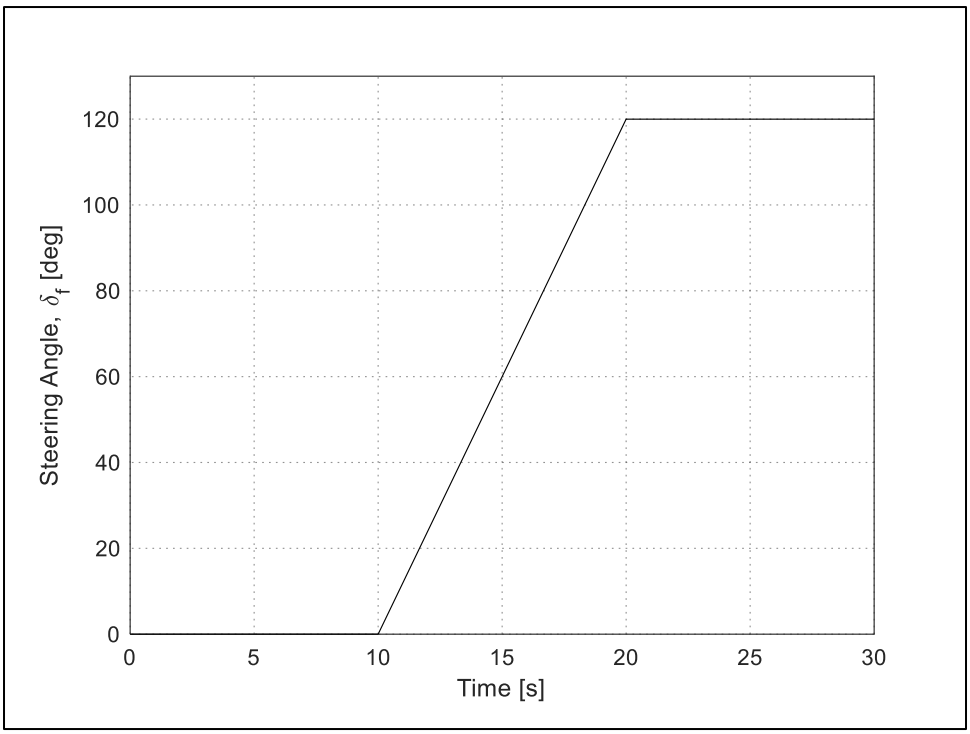

Figure 7.3 Front wheel steer angle for the ramp steer maneuver at u = 45 km/h.

Recall that the supervisory controller generates a yaw rate setpoint, which would drive the system towards neutral steer. This corresponds to the yaw rate setpoint shown in Figure 7.4 below plotted against the actual yaw rate achieved by each of the three controllers as well as the open loop system. As can be seen in Figure 7.5, the MSMC steady-state yaw rate error e_r = -0.14 deg/s, or -0.5%; the open loop error is -0.44 deg/s, or -1.6%; the CSMC average error is -1.30 deg/s, or -4.7% and the HSMC average error is -1.36 deg/s or -4.9%. The CSMC and HSMC yaw responses chatter with an amplitude of 0.12 deg/s and frequency of 11.5 Hz. One can also see that the HSMC lags the CSMC response by 180˚. The MSMC method clearly tracks the desired yaw rate very closely while the CSMC, HSMC and open loop systems lag at a lower yaw rate than the ideal, demonstrating understeering behavior. In fact, the CSMC and HSMC perform worse than the open loop system. This is because these methods produce intense chattering, which dilutes the desired yaw moment and torque allocation. It is also notable that the CSMC and HSMC produce similar yaw rates. This is because the switching gain term in the controller is the primary contributor to the desired yaw moment signal while the tire force terms tend to shape the transient response, so the HSMC would track similarly to the CSMC with a poorer transient response.

Figure 7.6 illustrates the sideslip angle response of the vehicle during the J-turn for the four systems. The sideslip angle setpoint is $\beta_d = 0^\circ$ so a lower sideslip angle is always good. No matter how good a controller is, sideslip is unavoidable so long as a vehicle is turning. The results demonstrate that the modified DYC outperforms all three of the other systems having the smallest sideslip angle throughout the entire maneuver and a 3.5% improvement relative to the open loop sideslip angle.

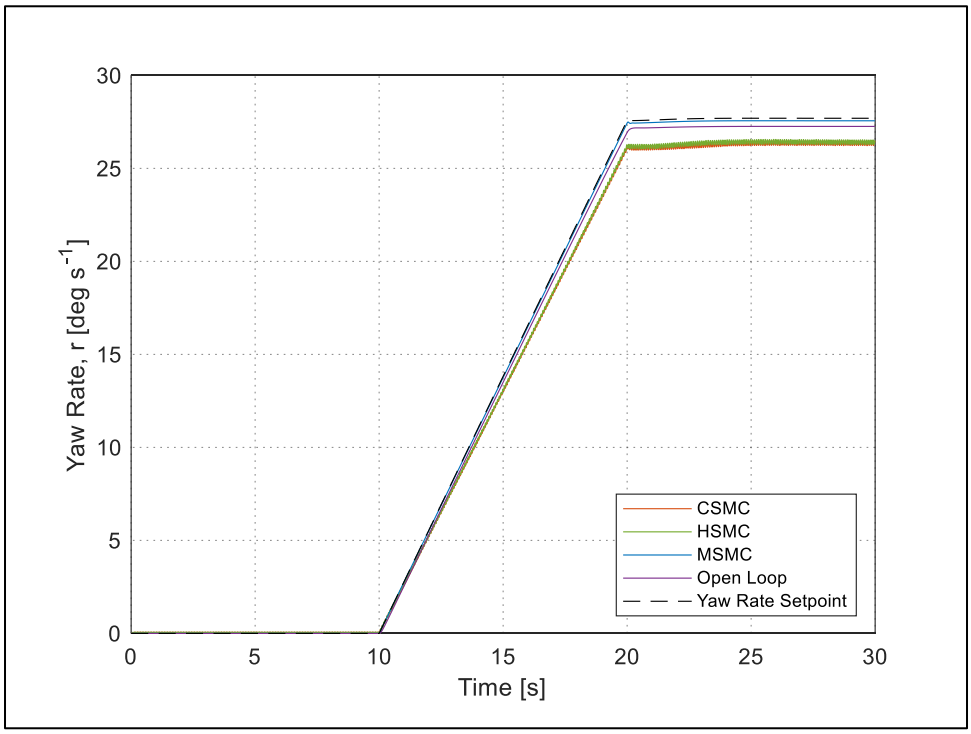

Figure 7.4 Yaw rate response during the ramp steer maneuver when u = 45 km/h and $\delta_{ss} = 120^\circ$.

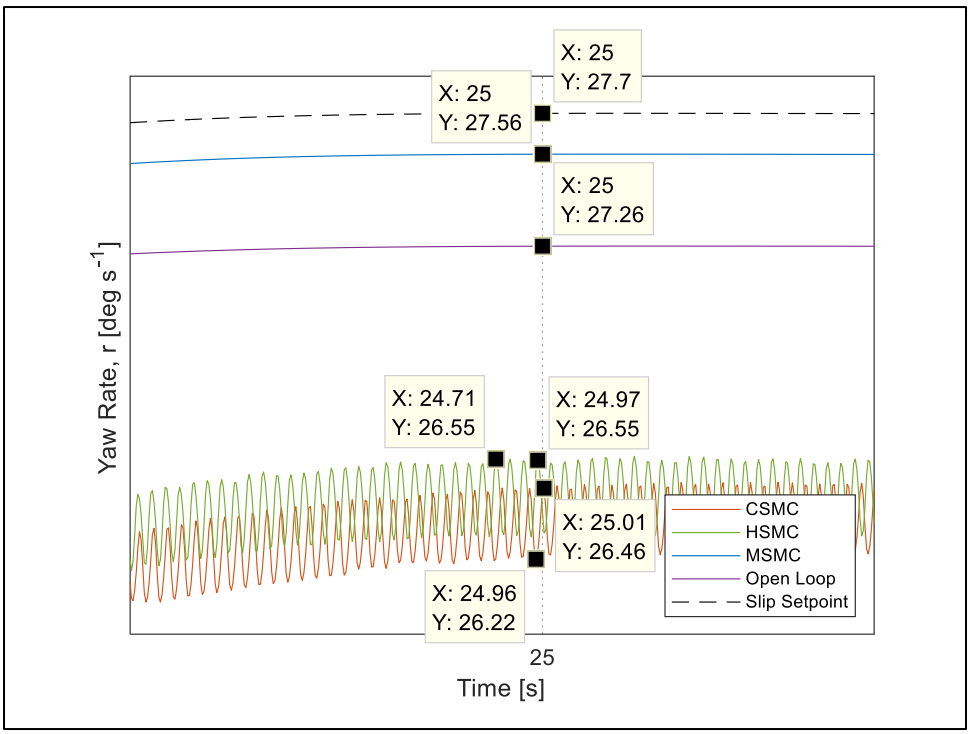

Figure 7.5 Controller steady-state error and CSMC/HSMC switching frequency.

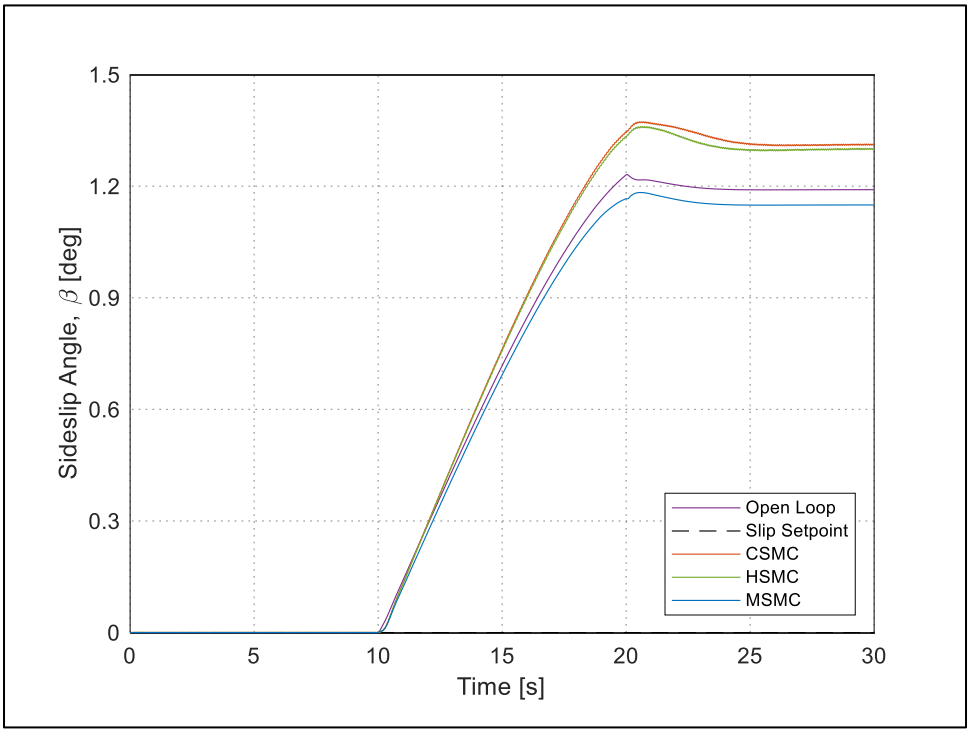

Figure 7.6 Sideslip angle response during the ramp steer maneuver when u = 45 km/h and δ_{ss} = 120˚.

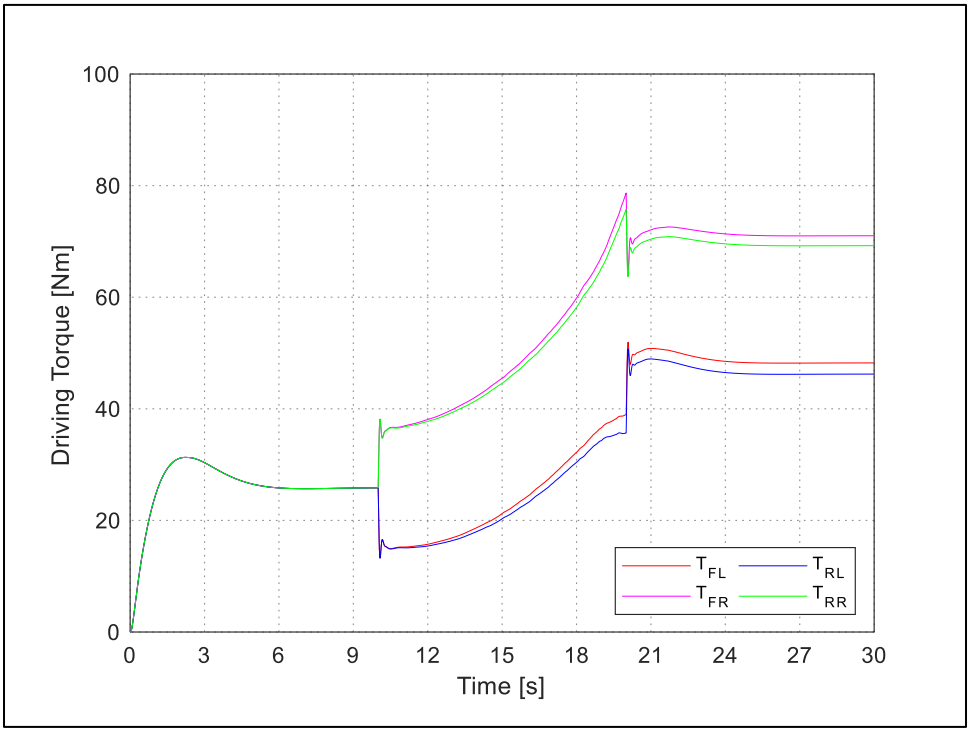

Figure 7.7 Torque response of the DYC system using the modified sliding mode controller during the ramp steer maneuver when u = 45 km/h and δ_{ss} = 120˚.

Figure 7.7 shows the torque allocation developed by the TVC over the course of the J-turn. The response shows three distinct phases of evolution in the torque allocation, which illustrates how the primal-dual gradient descent algorithm responds to different stimuli because of the tuning process. In the first phase there is no steering or other lateral disturbances so the TVC produces equal torque at all the wheels just to maintain the speed at 45 km/h; in the second phase, the steering angle begins turning at a rate of 12 deg/s and the TVC generates a second-order response at both the initiating and termination of the ramp; during the third phase, the steering angle is held steady at 120˚ and, following the settling of second-order response, the torque distribution remains constant. This elegant torque profile makes it trivial to characterize the second-order dynamic response of the TVC for the chosen set of tuning parameters using the known overshoot, approximate steady-state value, rise time and settling time. From the entry response of the right rear tire, it is obvious that the overshoot is 38.1 N while the steady-state value is approximately 36.5 N, or a 4.36% overshoot. The resulting damping ratio is ξ = 0.7. The peak time T_p = 0.08 s and the settling time T_s = 0.60 s. Using the peak time and

damping ratio, the computed natural frequency and damped natural frequency of the torque vectoring controller are f_n = 8.8 Hz and f_d = 6.3 Hz. The second order TVC system has two poles in the left-hand plane of the root locus at 38.5 ± 39.3j so the torque-vectoring controller is stable in closed loop.

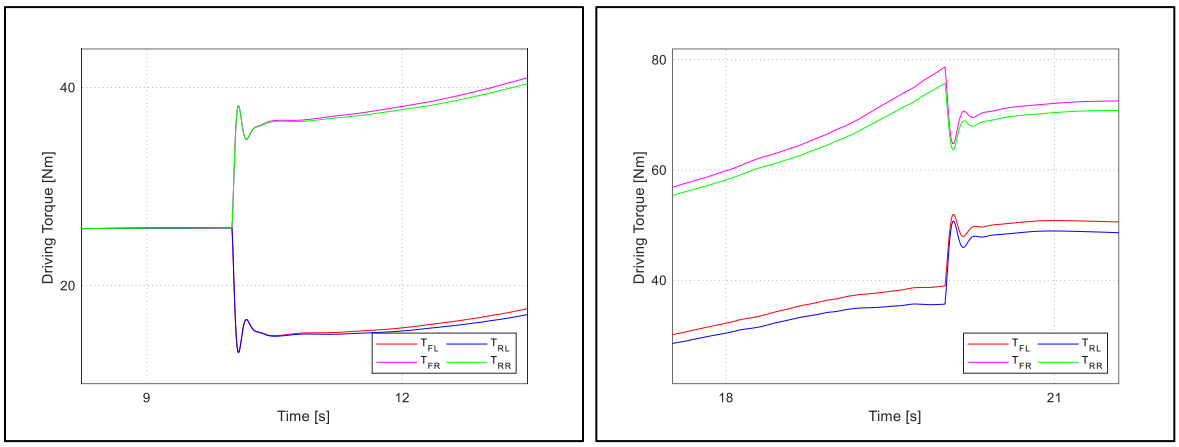

Figure 7.8 Second-order response at the entrance and termination of the second phase of the J-turn.

7.3.1.1 J-TURN TIRE FORCE ESTIMATION

This section presents results from the RT tire model and UTFE during the J-turn maneuver. The UTFE runs in open loop, meaning that it is runs without affecting the rest of the system, while the RT tire model forces feed back to the DYC. The purpose of this is to decouple the performance of the controller from the performance of the estimator.

7.3.1.1.1 LONGITUDINAL FORCE

The longitudinal tire force curves should look very similar to those of the driving torques shown in Figure 7.7 since torque directly generates the force. It is shown clearly in Figure 7.9-Figure 7.12 that the longitudinal force estimates are unable to track the actual force well. This is because the longitudinal force estimate is based on the wheel equation of motion in Equation (3.30), but does not account for dissipative rolling resistance term, variations in the vertical load on the tire, or braking force. As a result, the estimator over-predicts the force, especially during transient maneuvers where the suspension is highly active and the second phase of the J-turn is certainly transient. Moreover, the longitudinal tire force estimate assumes that the difference in the torque and angular acceleration terms always leads to a proportional rise in force. In other words, it assumes a linear relationship between torque and force. This holds true for operation within the linear region of the tire curves at

accelerations less than about 0.4 g, but the error increases the tire approaches its limits. Figure 7.13-Figure 7.16 and Figure 7.17-Figure 7.20 show the offset in force caused by the modeling error.

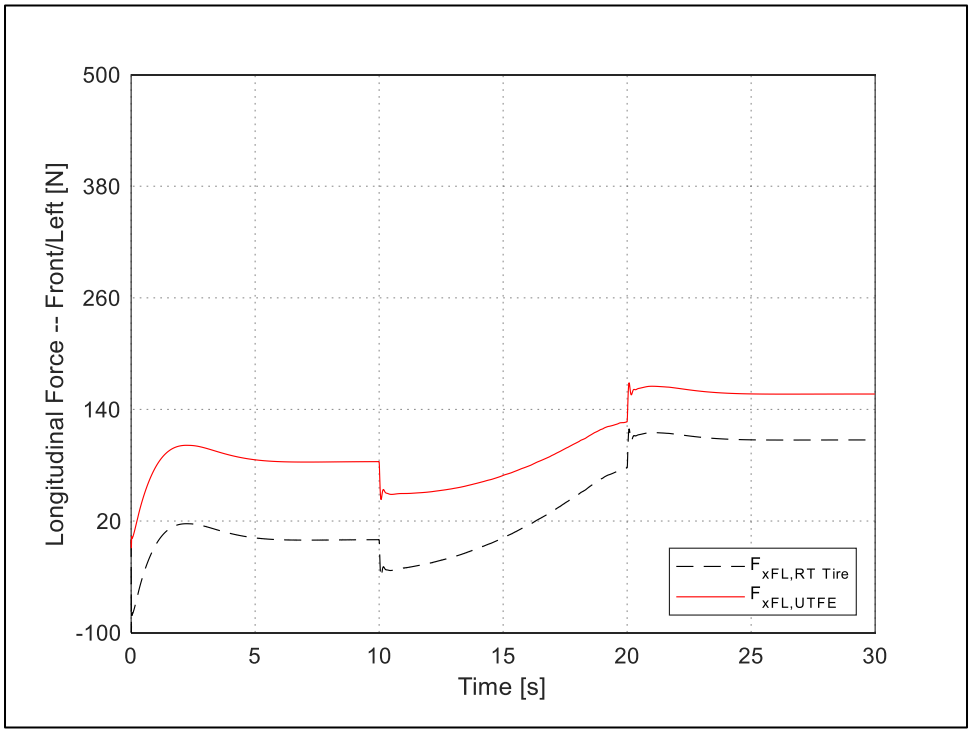

Figure 7.9 Comparison of the longitudinal force estimate and nonlinear model on the left front tire during a ramp steer maneuver when u = 45 km/h and δ_{ss} = 120˚.

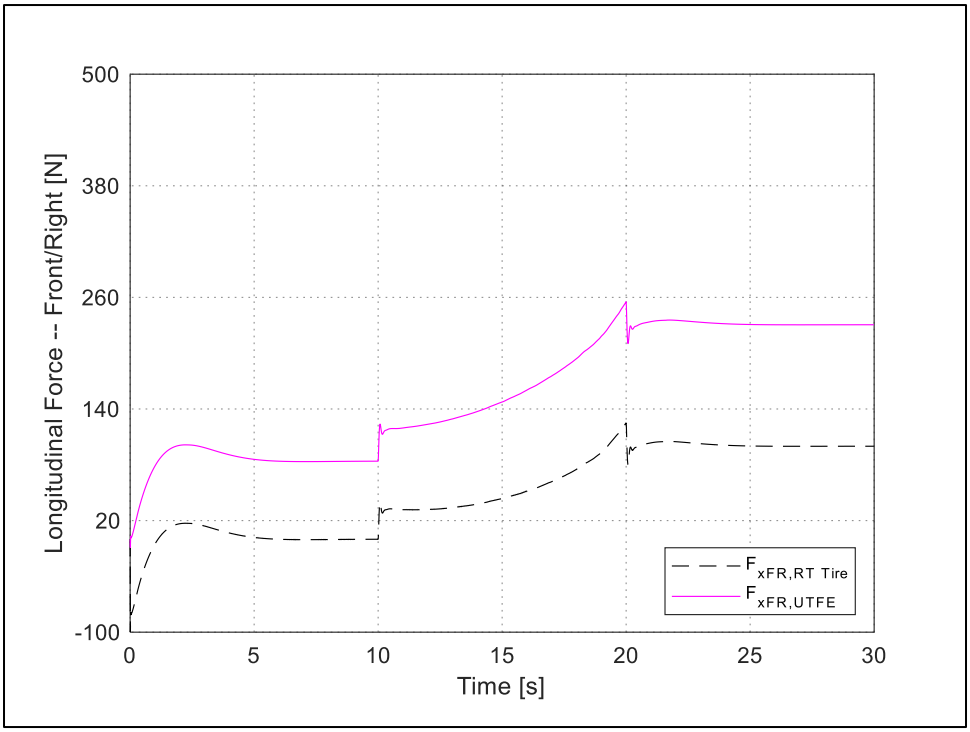

Figure 7.10 Comparison of the longitudinal force estimate and nonlinear model on the right front tire during a ramp steer maneuver when u = 45 km/h and δ_{ss} = 120˚.

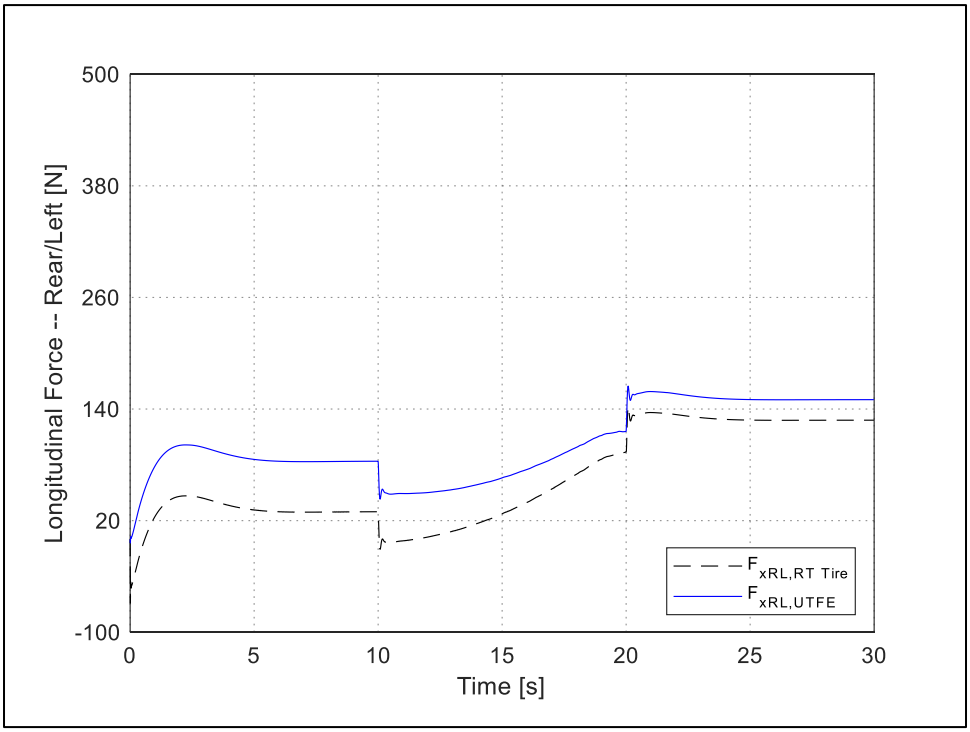

Figure 7.11 Comparison of the longitudinal force estimate and nonlinear model on the left rear tire during a ramp steer maneuver when u = 45 km/h and δ_{ss} = 120˚.

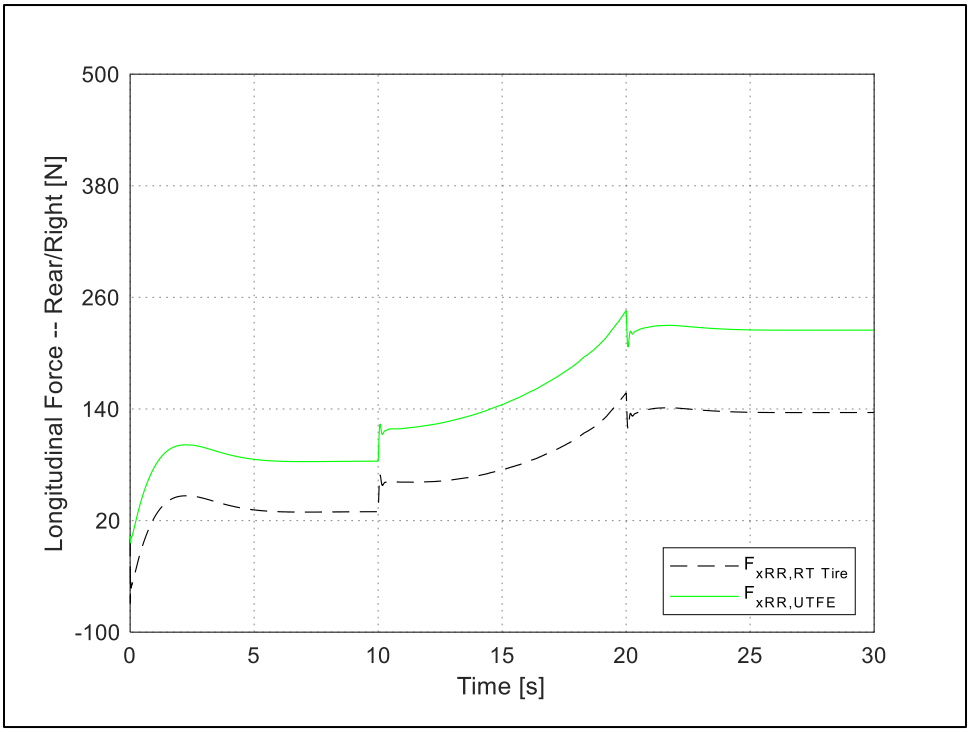

Figure 7.12 Comparison of the longitudinal force estimate and nonlinear model on the right rear tire during a ramp steer maneuver when u = 45 km/h and δ_{ss} = 120˚.

7.3.1.1.2 LATERAL FORCE

Despite being a more difficult quantity to observe than the longitudinal force and vertical force, the lateral force estimate for the front axle forces during the J-turn tracks quite well while the estimates for the rear axle are very poor. The likely cause of this is an inadequate choice of state and measurement covariance for the unscented Kalman filter (UKF), which constitutes the lateral estimation step. Tuning the covariance and parameters related to the Unscented Transformation has a great influence on how well the filter deals with modeling error and nonlinearities. One can expect that forcing the filter to track the lateral tire forces is an especially difficult task by virtue of low degree of observability, high degree of nonlinearity and modeling error introduced by the feedforward error in the longitudinal tire force estimation. The lateral force estimate during the transient response for the rear left tire is a good example of the filter struggling to overcome the function nonlinearity but being able to overcome the modeling error. The lateral force estimate for the rear right tire is an especially good example of the UKF being unable to overcome function nonlinearity during the transient response as well as the modeling error seeing as it fails to track the actual force even once the vehicle reaches steady-state in phase three of the J-turn.

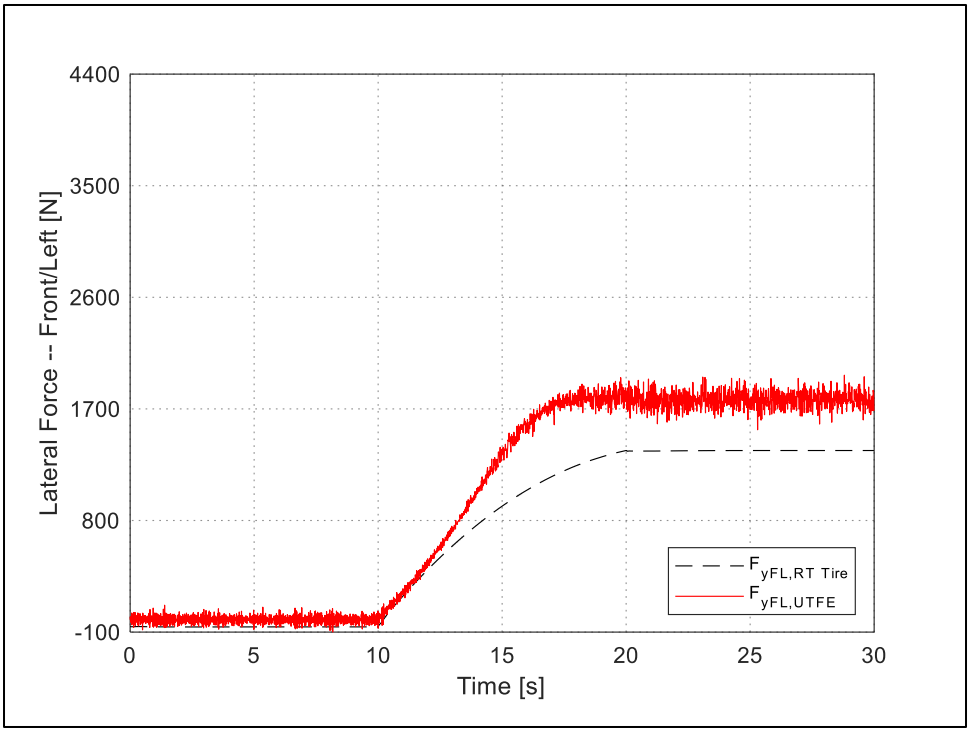

Figure 7.13 Comparison of the lateral force estimate and nonlinear model on the left front tire during a ramp steer maneuver when u = 45 km/h and δ_{ss} = 120˚.

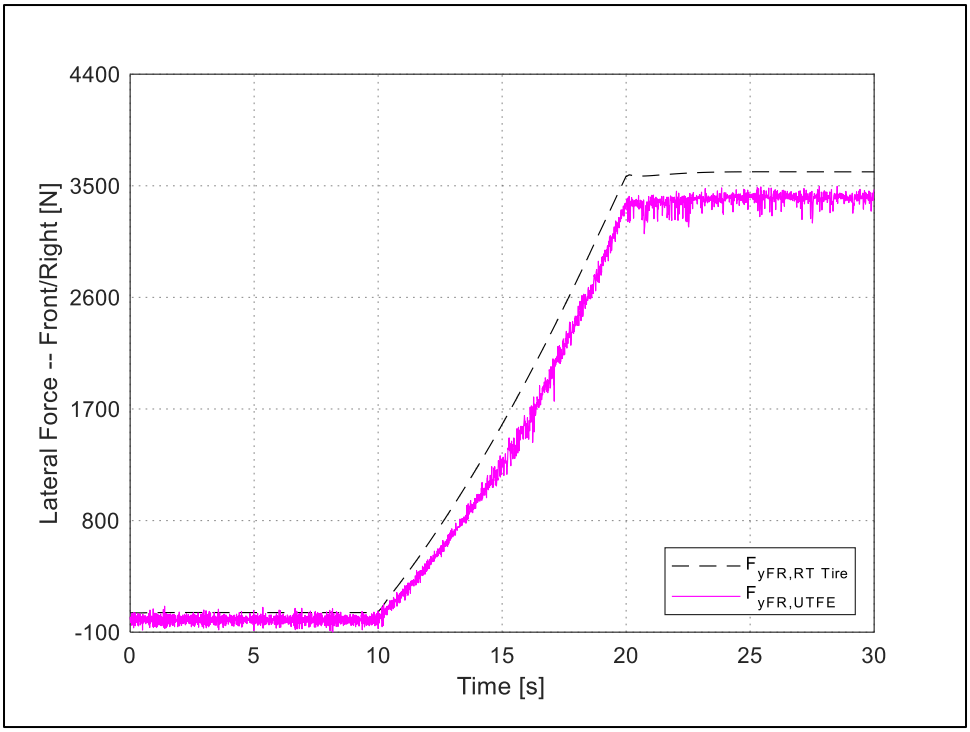

Figure 7.14 Comparison of the lateral force estimate and nonlinear model on the right front tire during a ramp steer maneuver when u = 45 km/h and δ_{ss} = 120˚.

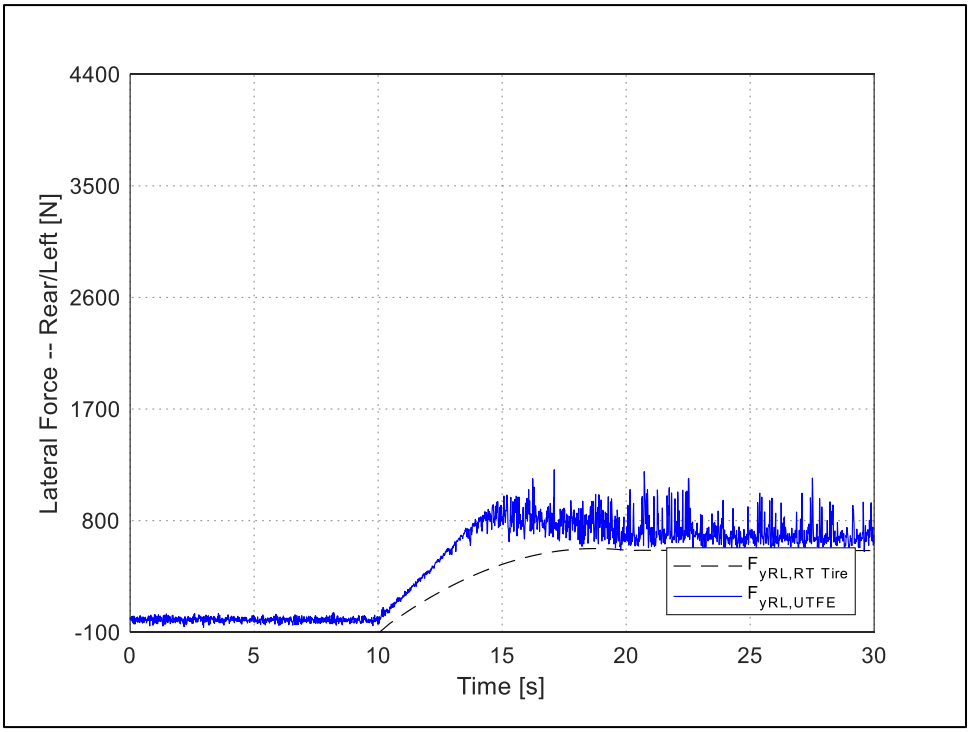

Figure 7.15 Comparison of the lateral force estimate and nonlinear model on the left rear tire during a ramp steer maneuver when u = 45 km/h and δ_{ss} = 120˚.

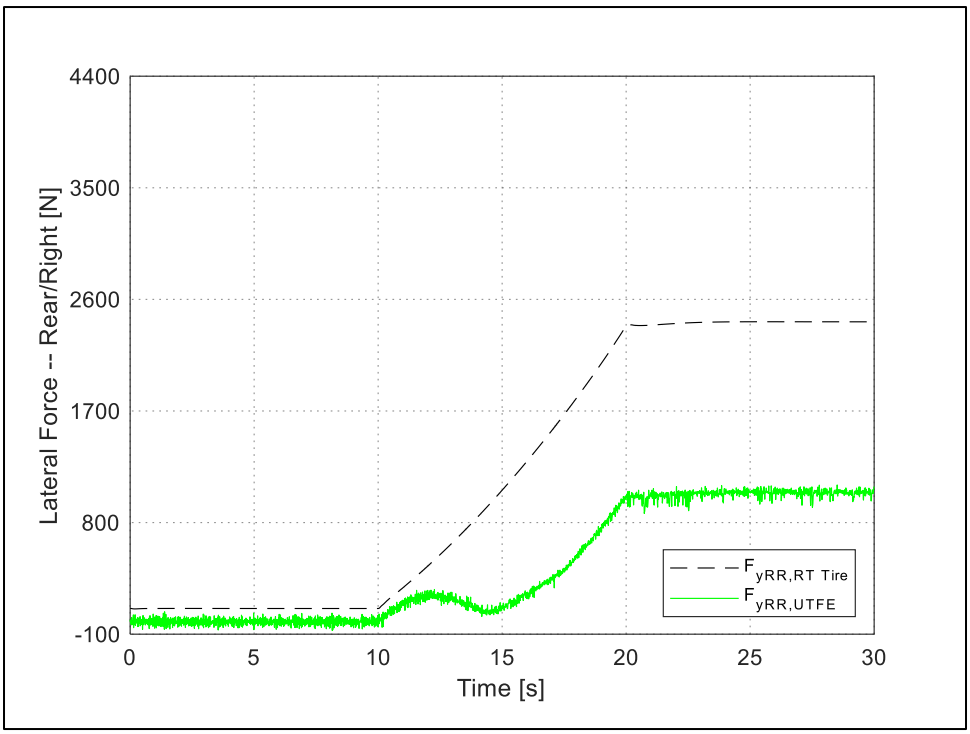

Figure 7.16 Comparison of the lateral force estimate and nonlinear model on the right rear tire during a ramp steer maneuver when u = 45 km/h and δ_{ss} = 120˚.

7.3.1.1.3 VERTICAL FORCE

Figure 7.17 through Figure 7.20 show that the vertical tire force estimator can track the actual force far better than either the longitudinal estimator or the lateral estimator. This is because the vertical force depends on the suspension and load transfer of the vehicle and avoids the modeling problems associated with slip and operation within the friction circle. The approximate average steady-state vertical force estimation error is as follows: e_{FL} = 147 N (6.7%), e_{FR} = -150 N (-2.6%), e_{RL} = -70.5 N (-7.1%), e_{RR} = 83 N (2.9%).

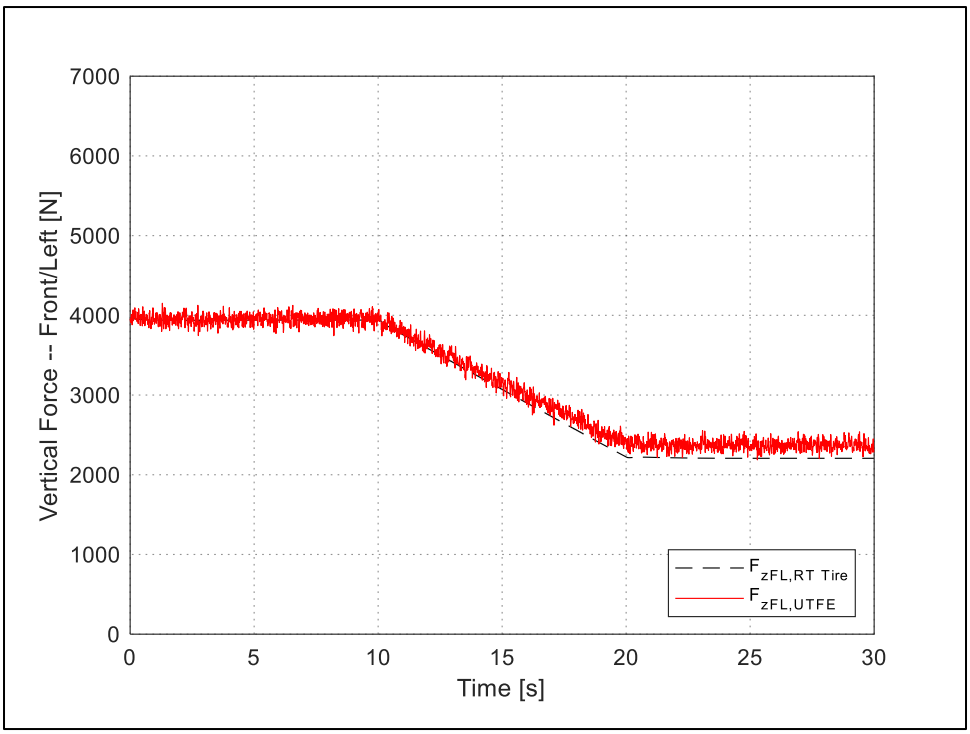

Figure 7.17 Comparison of the vertical force estimate and nonlinear model on the left front tire during a ramp steer maneuver when u = 45 km/h and δ_{ss} = 120˚.

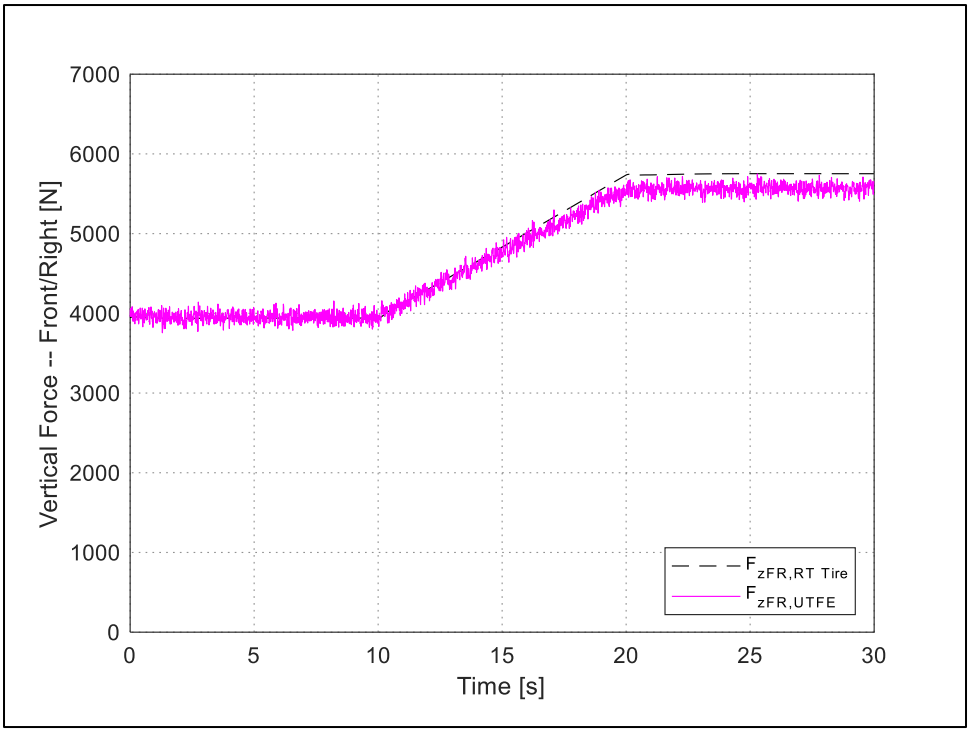

Figure 7.18 Comparison of the vertical force estimate and nonlinear model on the right front tire during a ramp steer maneuver when u = 45 km/h and δ_{ss} = 120˚.

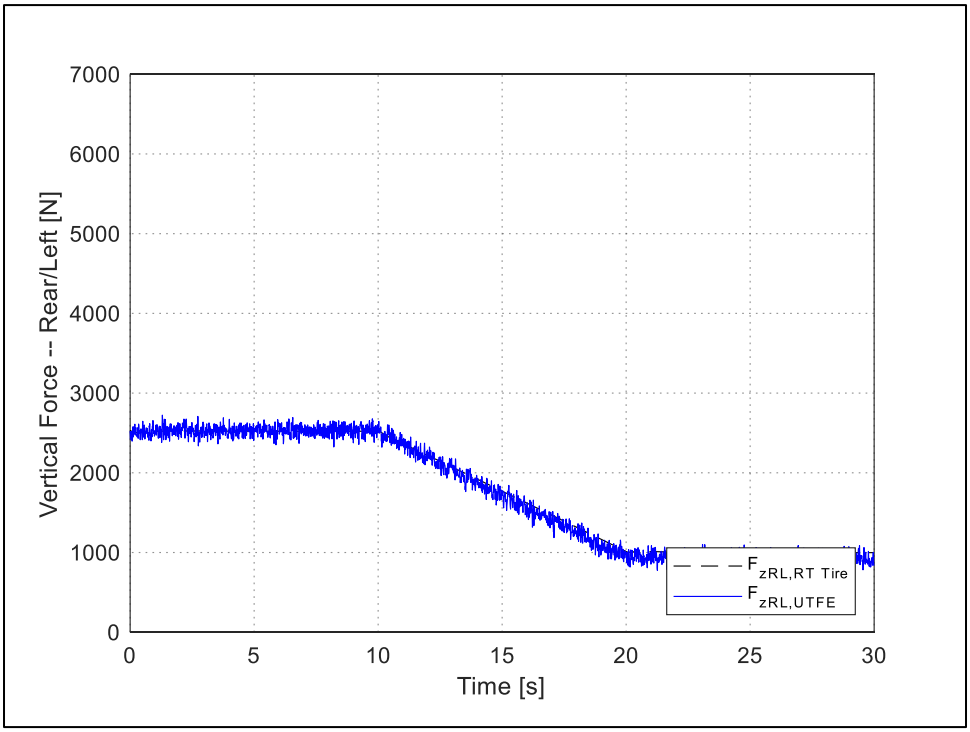

Figure 7.19 Comparison of the vertical force estimate and nonlinear model on the left rear tire during a ramp steer maneuver when u = 45 km/h and δ_{ss} = 120˚.

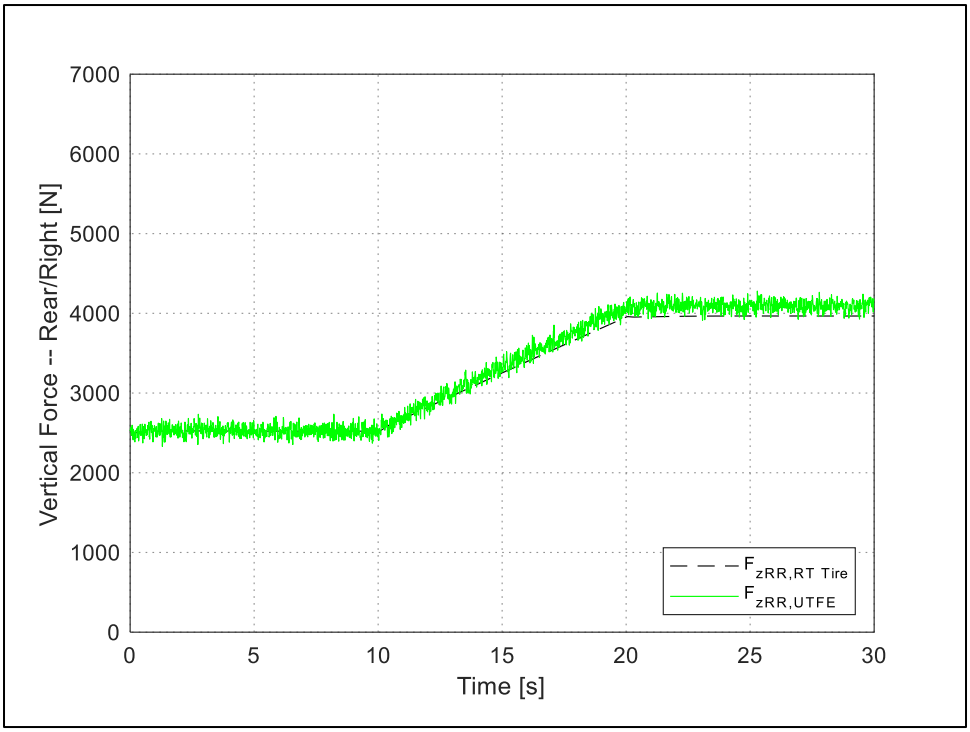

Figure 7.20 Comparison of the vertical force estimate and nonlinear model on the right rear tire during a ramp steer maneuver when u = 45 km/h and δ_{ss} = 120˚.

7.3.2 SINE STEER TEST

The next simulation is a sinusoidal steering, or “sine steer” maneuver. The sine steer maneuver aims at constantly exciting the yaw mode of the vehicle at an intermediate degree of lateral acceleration. Figure 7.21 shows the steering angle applied during the sine steer maneuver. At first, the vehicle travels straight at 60 km/h. After five seconds, the driver begins steering back and forth at constant velocity. This steering input has an amplitude of 60° and period of 2.5 seconds and lasts for one and a half cycles. This test induces a response resembling that of an aggressive lane-change and seeks to show good controller estimator tracking for a maneuver that is more complex and transient than a J-turn.

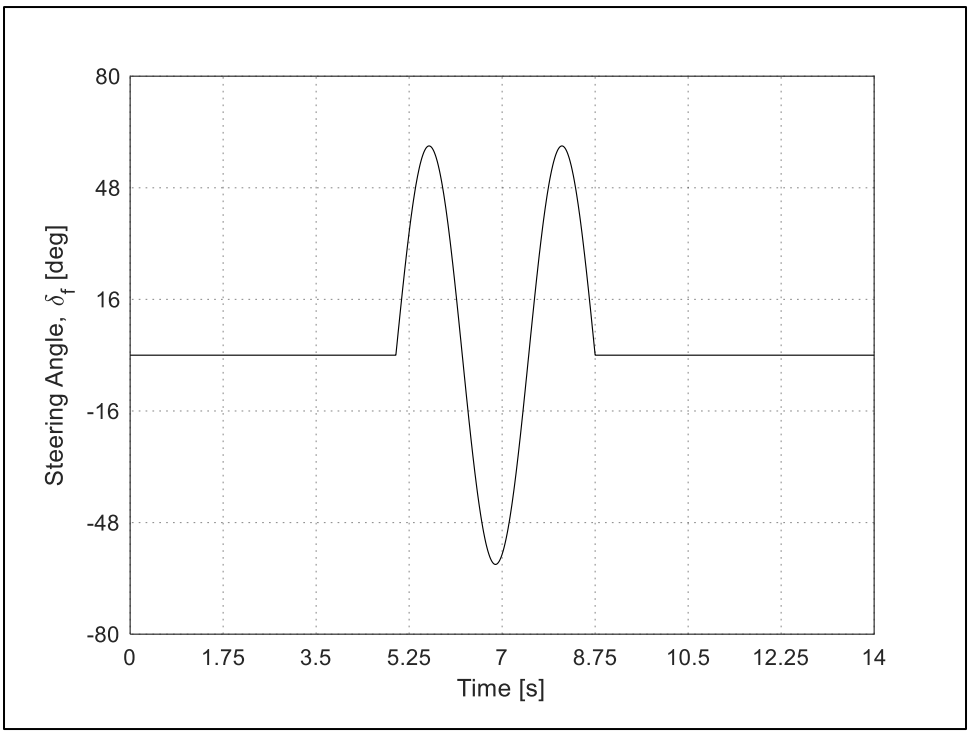

Figure 7.21 Front wheel steer angle for the sinusoidal steer maneuver at u = 60 km/h.

Figure 7.22 shows that all three controllers track the ideal yaw rate very closely while the open loop system perform worse. The modified sliding mode controller performs the best of the three controllers while the conventional and hybrid sliding mode controllers perform comparably. Although it is negligible, the MSMC demonstrates oversteer at the peak steer, overshooting the ideal by 0.01 deg/s, but settles in approximately 80 milliseconds with practically zero error during the rise and fall of the steering angle. On the other hand, the CSMC and HSMC both overshoot by about the same amount, 0.74 deg/s, and settle in approximately 830 milliseconds with very little error. Unlike the controlled systems, the open loop system demonstrates significant understeer and has a phase lag in its yaw rate response. The open loop system undershoots the ideal yaw rate by 1.82 deg/s and lags by 15.8°. Figure 7.23 shows how, once the vehicle straightens out, all three controllers' overshoot while the open loop vehicle approaches zero yaw rate asymptotically. It is evident from the controller response that they all have similar damping ratios, resembling what one might expect with a damping ratio around 0.5. Meanwhile, the open loop controller demonstrates an overdamped response with a response resembling what one might expect with a damping ratio of approximately 1.5. Although it appeared that the CSMC and HSMC performed the same during the sine steering, the response in Figure 7.23 seems to indicate that the HSMC outperforms the CSMC.

Figure 7.24 shows the sideslip angle response to the sine steer maneuver. It is immediately evident that the open loop vehicle has the smallest sideslip throughout the maneuver. This should not be construed as better performance because it is a consequence of the open loop vehicle understeering and not better control. The sliding mode controllers attempt to drive both the yaw rate and sideslip angle errors to zero, but in the case of an understeering baseline vehicle such as this, the controller must increase the yaw rate to achieve neutral steer. The consequence of increasing the yaw rate to satisfy the neutral steer condition is that it increases the sideslip angle. Hence, the sideslip angle response of the controllers can only be compared to each other, not to the open loop response. On that note, one can see that the modified sliding mode controller is more successful at decreasing the sideslip angle than the conventional sliding mode controller and the hybrid sliding mode controller. Part of this is explained by the reason the modified sliding mode controller was developed in the first place: to drive the absolute value of the yaw rate and sideslip angle to zero so that the switching function is driven to zero only when the yaw rate error and sideslip angle error both go to zero. In this scenario, the yaw rate and sideslip angle have opposite signs. Since the conventional and hybrid sliding mode controllers do not use the absolute value of the errors, the switching function may be driven to zero when there is finite error and the effect of this is to reduce the desired yaw moment fed to the TVC when the error is high. The MSMC avoids this problem, and so can outperform the CSMC and HSMC in its yaw rate response and its sideslip angle response. This is exactly what is observed in both this case and in the J-turn in the previous section.

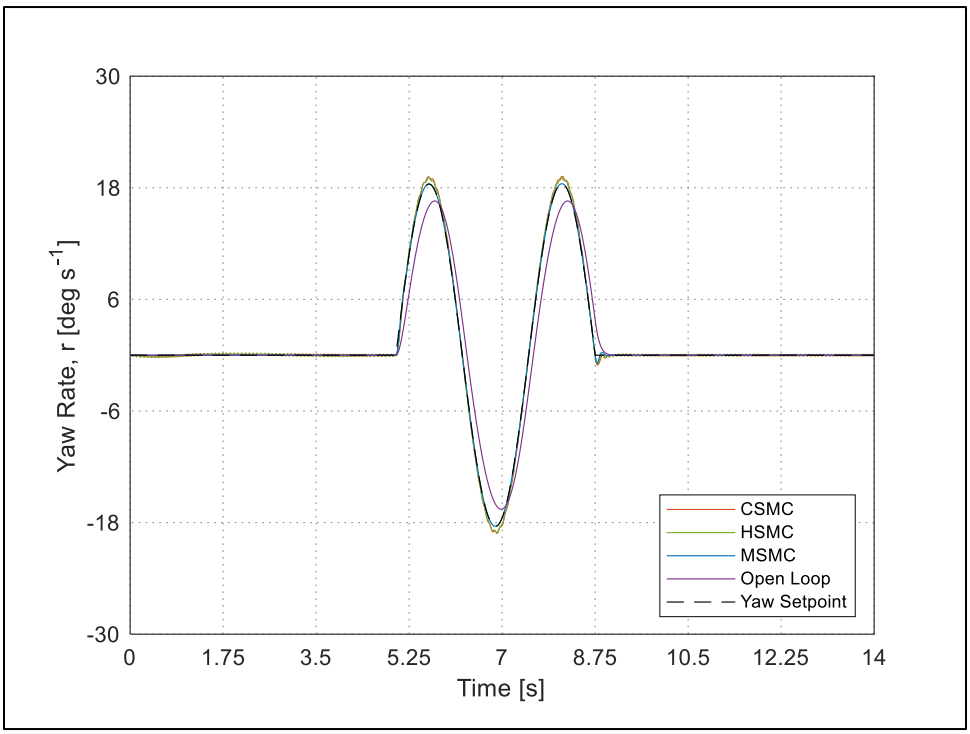

Figure 7.22 Yaw rate response during the sinusoidal steer maneuver when u = 60 km/h.

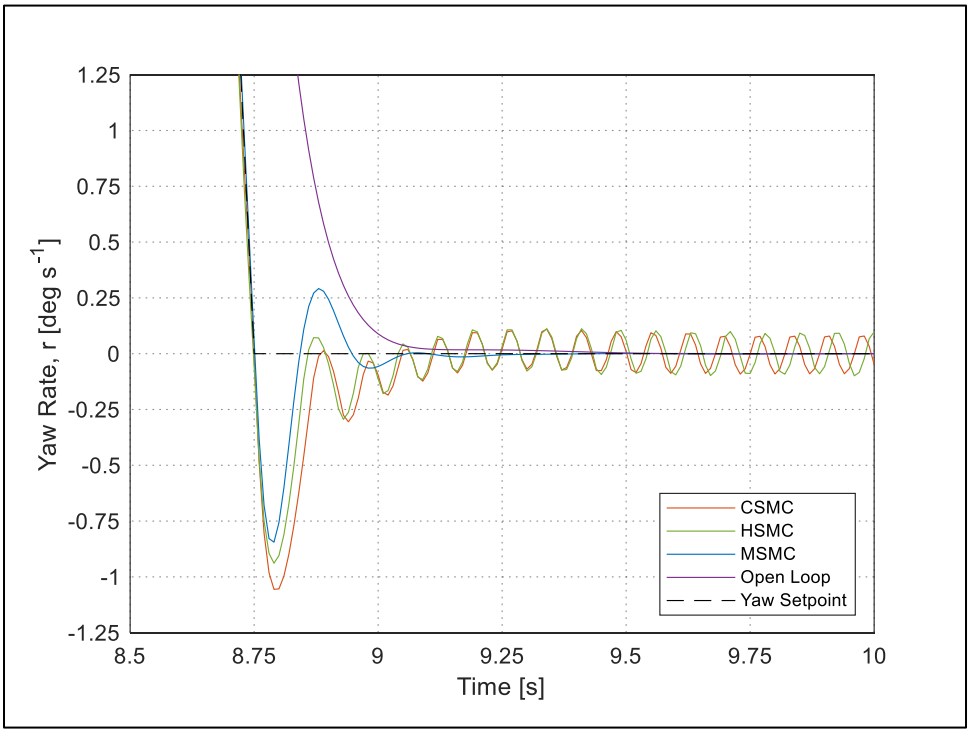

Figure 7.23 Dynamic response of the vehicle when r_d = 0 deg/s and u = 60 km/h. at the end of the sine steer maneuver.

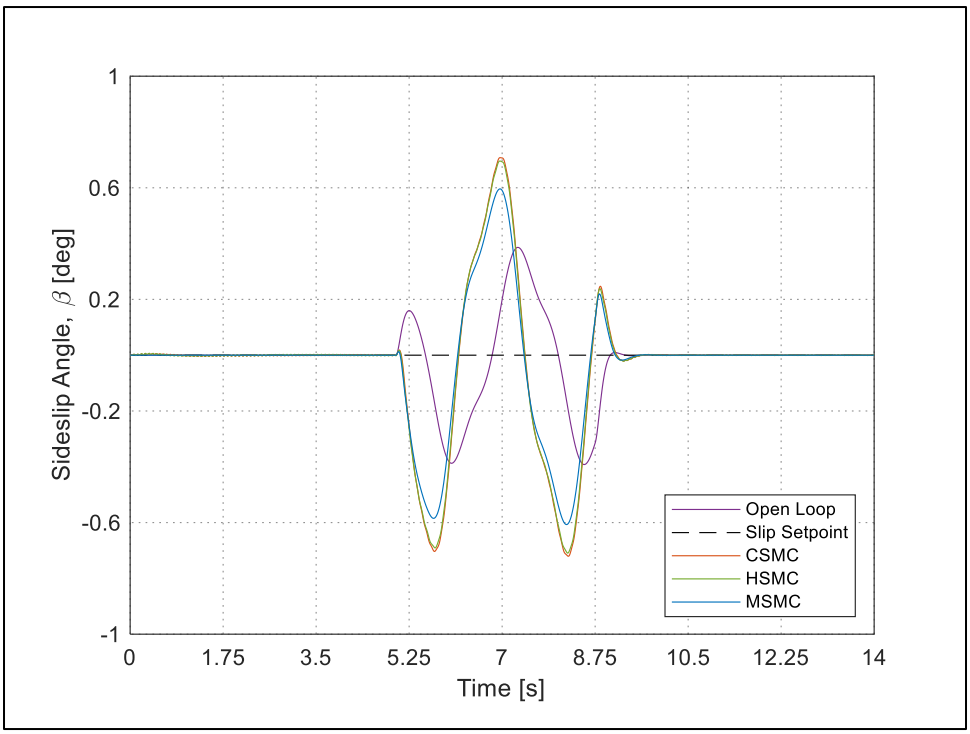

Figure 7.24 Sideslip angle response during the sinusoidal steer maneuver when u = 60 km/h.

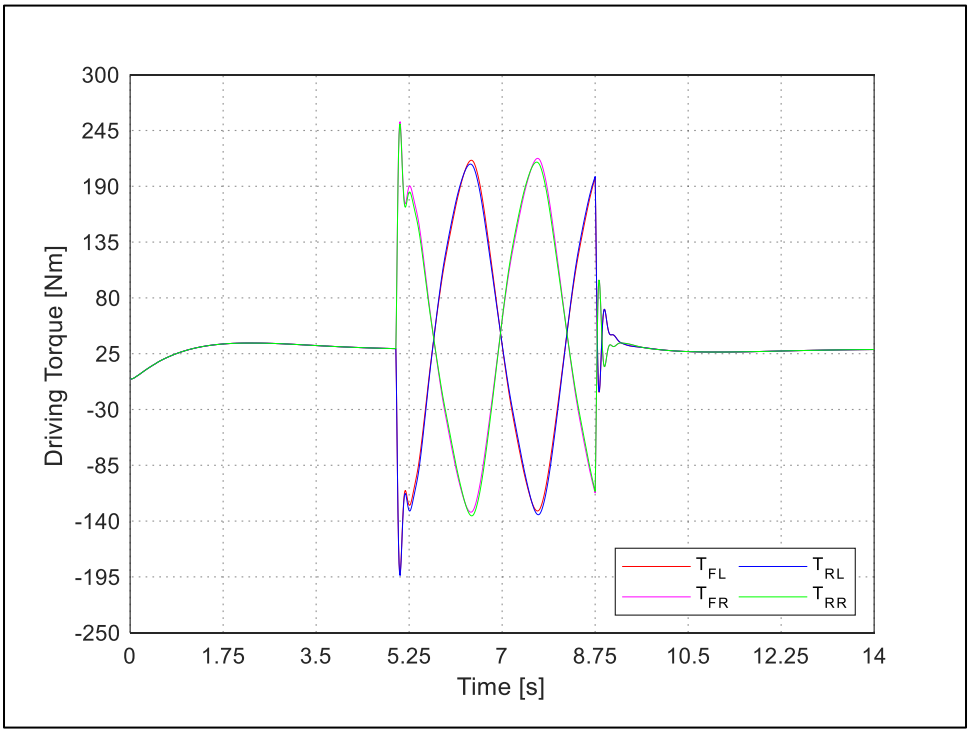

Figure 7.25 Torque response of the DYC system using the modified sliding mode controller during the sinusoidal steer maneuver when u = 60 km/h.

Figure 7.25 shows the torque allocation for the MSMC during the sine steer maneuver. During the maneuver, the TVC sends similar torques to the wheels on the left and to the right side of the powertrain. Except for the initiation and termination of the maneuver, the torque allocation varies smoothly in accordance with the intensity of the yaw behavior. The shape of the torque curve generated by the TVC is that of two sine waves of opposite sign that are in phase. During the maneuver, three cross-overs occur at t_1 = 5.72 s, t_2 = 6.97 s, 6.97 s and t_3 = 8.22 s and two maxima in the torque differential between left and right hand sides occur at t_1 = 6.42 s, t_2 =7.66 s. Cross-overs occur at the extremes of the steering profile and the torque differential maxima occur at the inflection points of the steering profile. This is driven by the $\dot{r}_d$ term in the corrective yaw moment command from the MSMC in Equation (4.49) because the yaw rate error is very small and $\dot{\beta}$ is an order of magnitude smaller than $\dot{r}_d$. At the extremes of the steering angle, $\dot{r}_d = 0$ so no moment is generated by the TVC at that moment. At the inflection points of the applied steering angle, $\dot{r}_d$ is at its highest, so the greatest moment is generated by the TVC at these points.

7.3.2.1 SINUSOIDAL STEERING SWEEP TEST TIRE FORCE ESTIMATION

This section presents results from the RT tire model and UTFE during the sine steer maneuver. The UTFE runs in open loop, meaning that it is runs without affecting the rest of the system, while the RT tire model forces feed back to the DYC. The purpose of this is to decouple the performance of the controller from the performance of the estimator.

7.3.2.1.1 LONGITUDINAL FORCE

The longitudinal force estimation performs very well in this maneuver. One can see that the shape of the two forces are the same and are in phase with each other, but there is an offset in the magnitude of the force at any given instant, with the UTFE overestimating the model force. This overestimation is due to the modeling error within the estimator from neglecting rolling resistance, drag, and suspension dynamics.

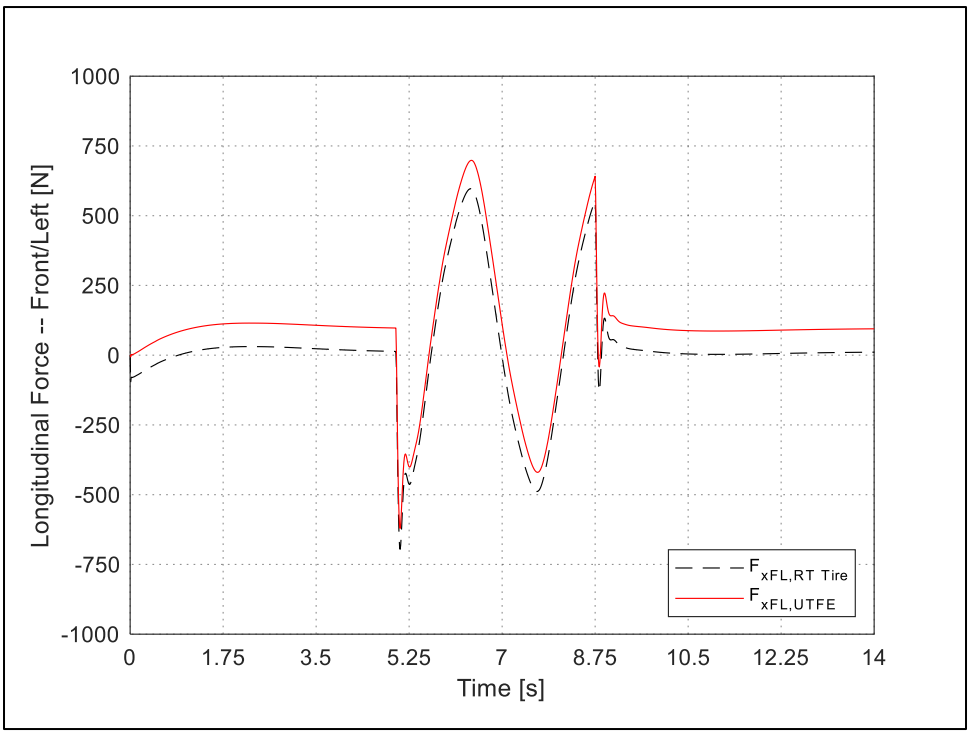

Figure 7.26 Comparison of the longitudinal force estimate and nonlinear model on the left front tire during a sinusoidal steer maneuver when u = 45 km/h and δ_{ss} = 120˚.

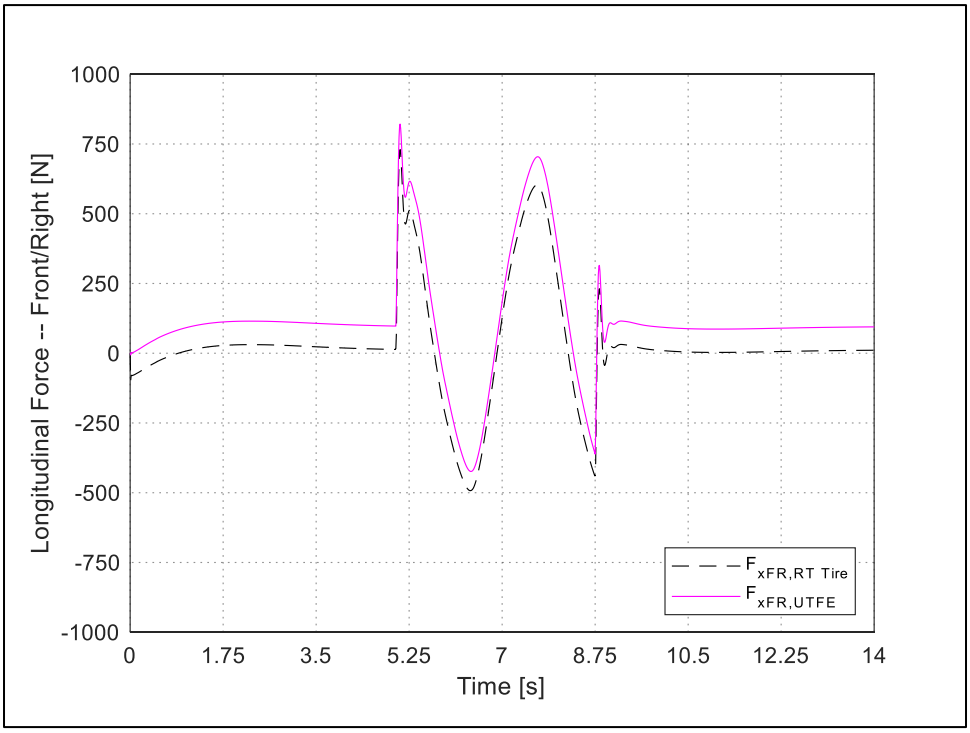

Figure 7.27 Comparison of the longitudinal force estimate and nonlinear model on the right front tire during a sinusoidal steer maneuver when u = 45 km/h and δ_{ss} = 120˚.

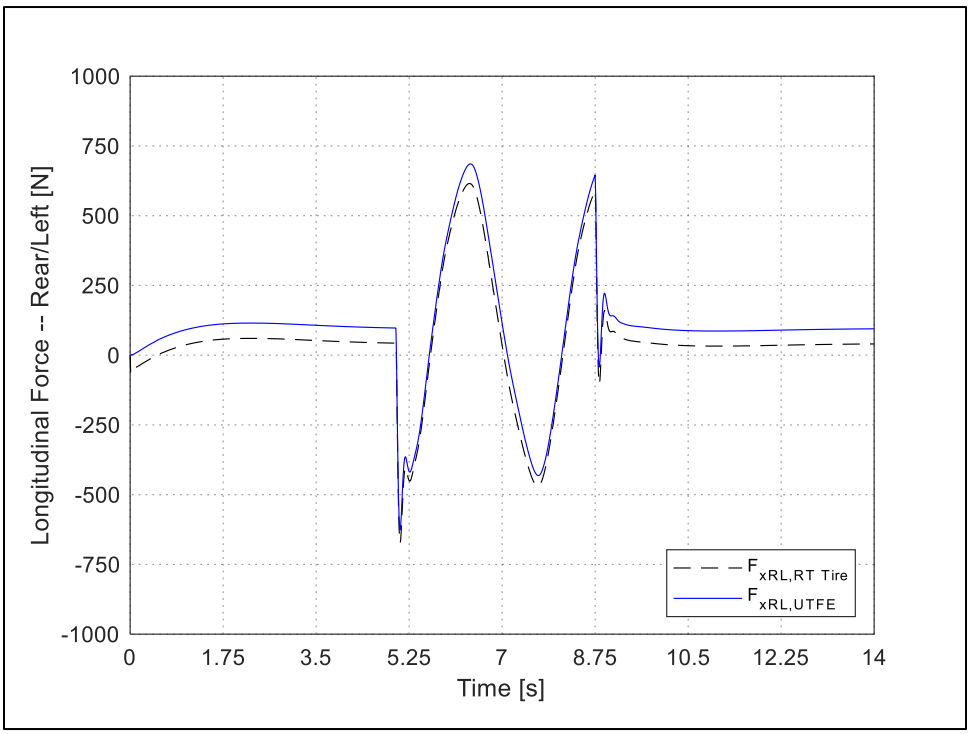

Figure 7.28 Comparison of the longitudinal force estimate and nonlinear model on the left rear tire during a sinusoidal steer maneuver when u = 45 km/h and δ_{ss} = 120˚.

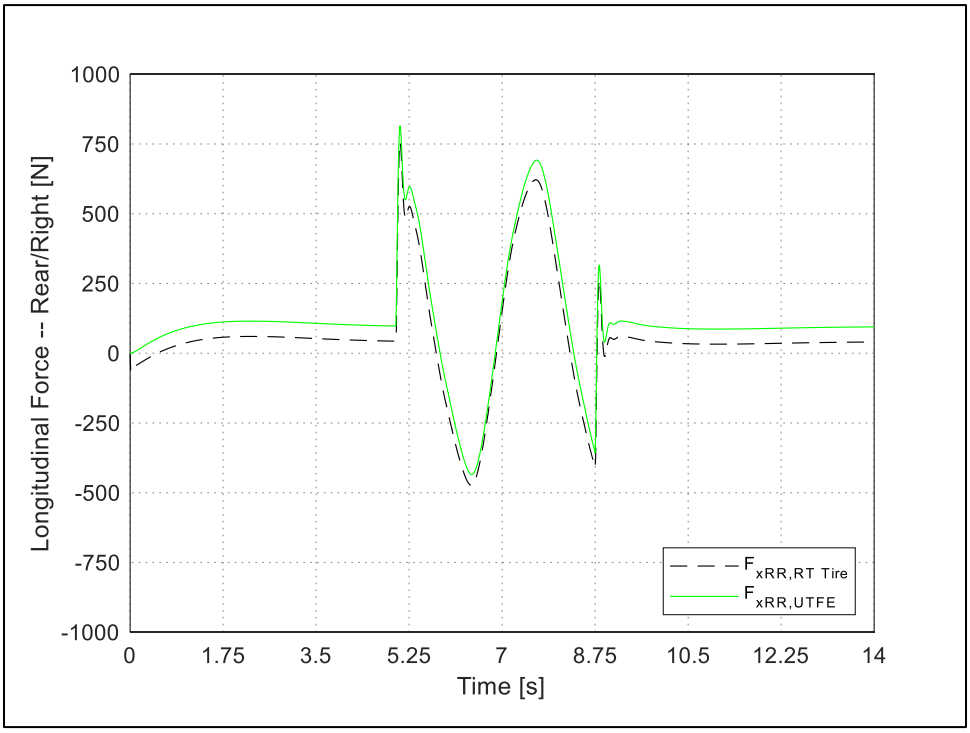

Figure 7.29 Comparison of the longitudinal force estimate and nonlinear model on the right rear tire during a sinusoidal steer maneuver when u = 45 km/h and δ_{ss} = 120˚.

7.3.2.1.2 LATERAL FORCE

The lateral force estimation of the UTFE tracks the model force very well for the most part considering the high degree of nonlinearity of the lateral force. Evolution of the lateral force experiences a greater degree of nonlinearity than the longitudinal or lateral forces because it exists closer to the nonlinear region of the tire force curve than the longitudinal force because of the magnitude of the force, while the vertical force does not depend on the tire force curve whatsoever. As opposed to the longitudinal force, the model is a good representation of the true force because it is zero when there is no steering input. The UKF, which constitutes the lateral tire force estimator, also predicts zero force when there is zero input. During the steering phase of the maneuver, the estimator tracks the true force closely during the rise and fall, but overshoots for positive steer and undershoots for negative steer for the tires on the inside of the turn. On the other hand, it undershoots for positive steer and overshoots for negative steer on the outside tires. This is because, for the inside tires, the positive longitudinal force and lateral force peaks coincide, leading the tires to be operating near the edge of the friction circle and nonlinear region of the tire curve for positive steer. For the outside tires, the negative longitudinal force and lateral force peaks coincide so the tires operate near the edge of the friction and nonlinear region of the tire curve for negative steer. Consequently, the lateral force tracking is worse for the inside wheels during positive steer and poor for the outside wheels during negative steer. An exception to this rule is the rear right lateral tire force estimation. For the tuning parameters used in this study, the unique dynamics of the rear right tire are poorly estimate. This tracking performance is a testament to how difficult it is to estimate the lateral force because the UKF is designed to track highly nonlinear functions.

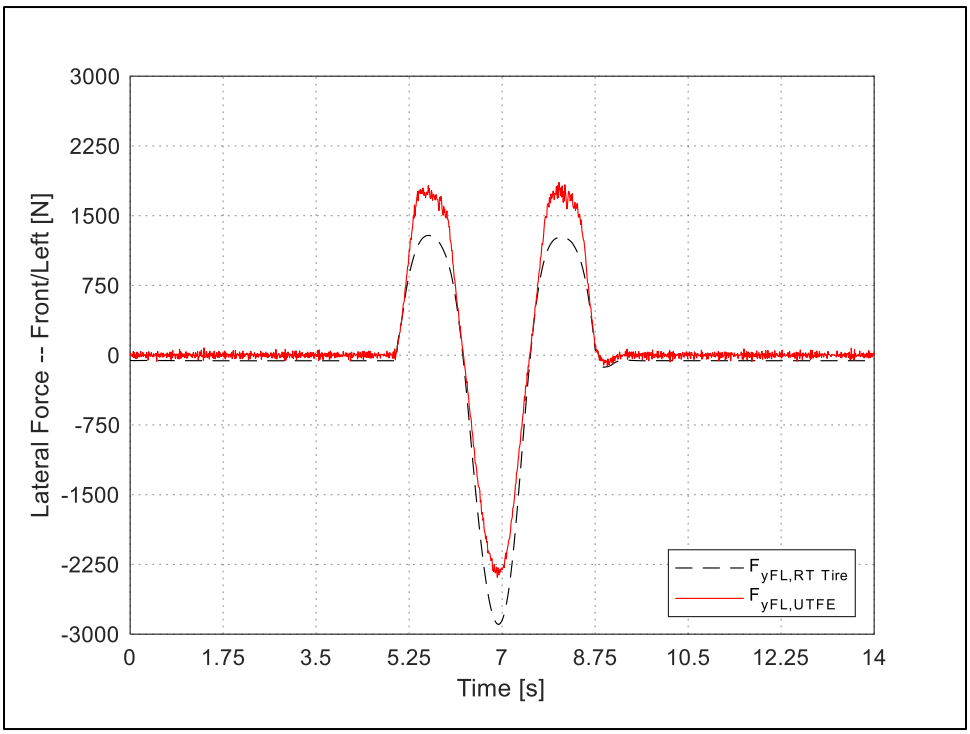

Figure 7.30 Comparison of the lateral force estimate and nonlinear model on the left front tire during a sinusoidal steer maneuver when u = 45 km/h and δ_{ss} = 120˚.

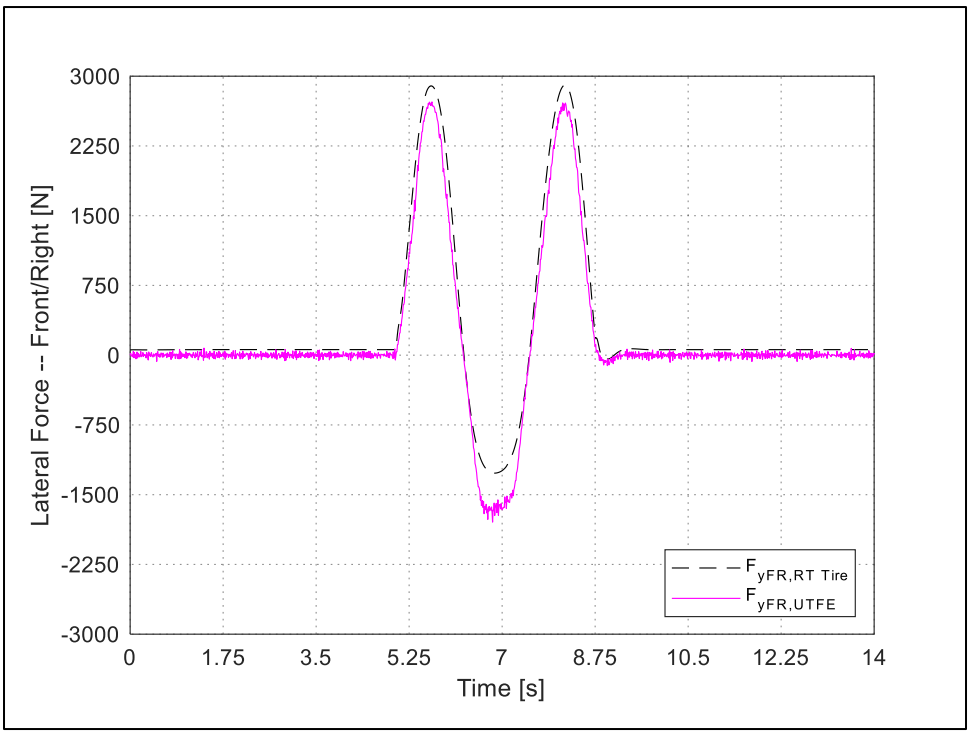

Figure 7.31 Comparison of the lateral force estimate and nonlinear model on the right front tire during a sinusoidal steer maneuver when u = 45 km/h and δ_{ss} = 120˚.

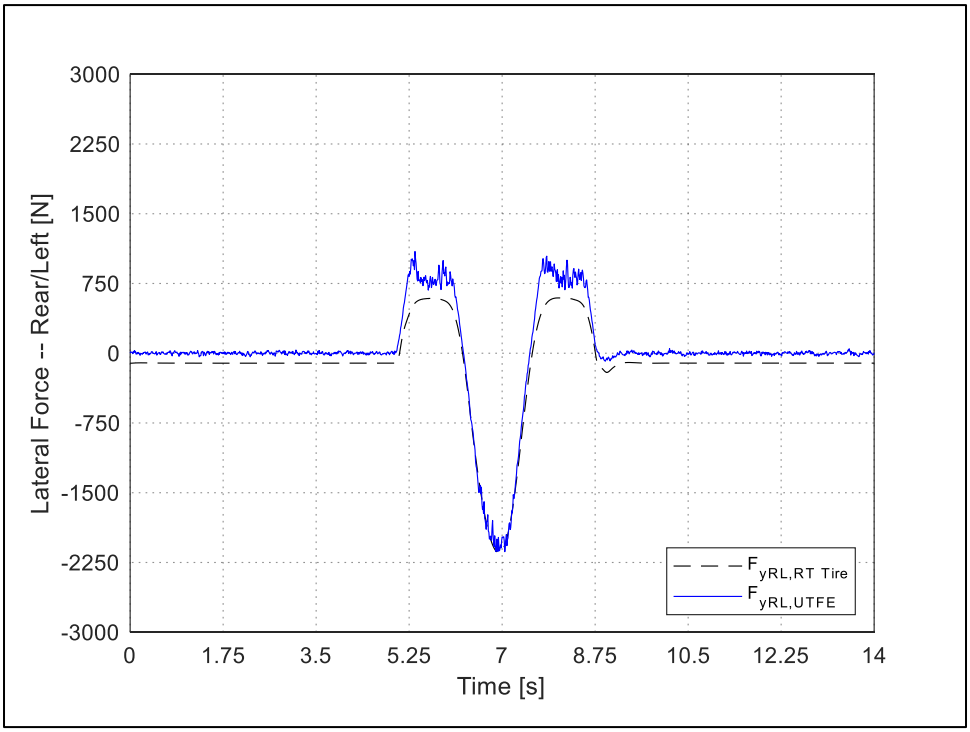

Figure 7.32 Comparison of the lateral force estimate and nonlinear model on the left rear tire during a sinusoidal steer maneuver when u = 45 km/h and δ_{ss} = 120˚.

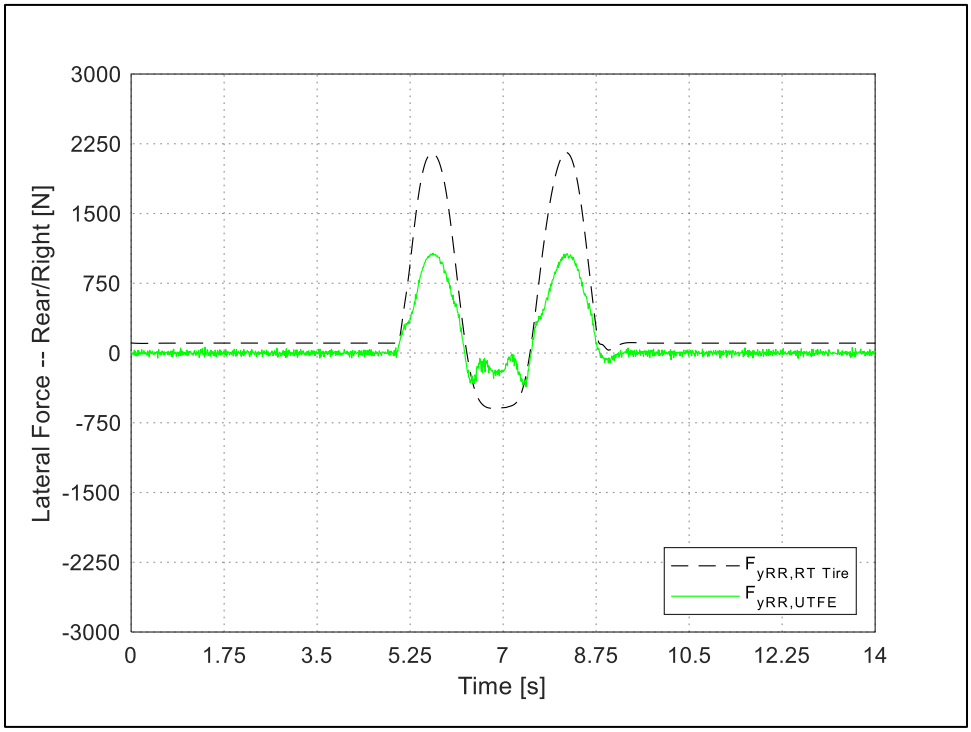

Figure 7.33 Comparison of the lateral force estimate and nonlinear model on the right rear tire during a sinusoidal steer maneuver when u = 45 km/h and δ_{ss} = 120˚.

7.3.2.1.3 VERTICAL FORCE

The cascaded linear and extended Kalman filters easily track the vertical forces during the sine steer maneuver because these forces do not develop according to a tire force curve or friction circle, but rather the vehicle suspension. The governing equation of the lateral load transfer has a far lower degree of nonlinearity than the planar tire forces. While the linear Kalman filter is unable to deal with a great deal of nonlinearity, the extended Kalman filter is quite good at it since it calculates the linearized lateral load transfer at each instant using the Jacobian of the system (6.14), (6.15), (6.16) and (6.17). One can see that the shape of the vertical tire forces follows the shape of the steering profile, but the inner tire forces are phase offset by 180˚ and the outer tire forces are in phase because of the load shifting from the inside wheels to the outside wheels.

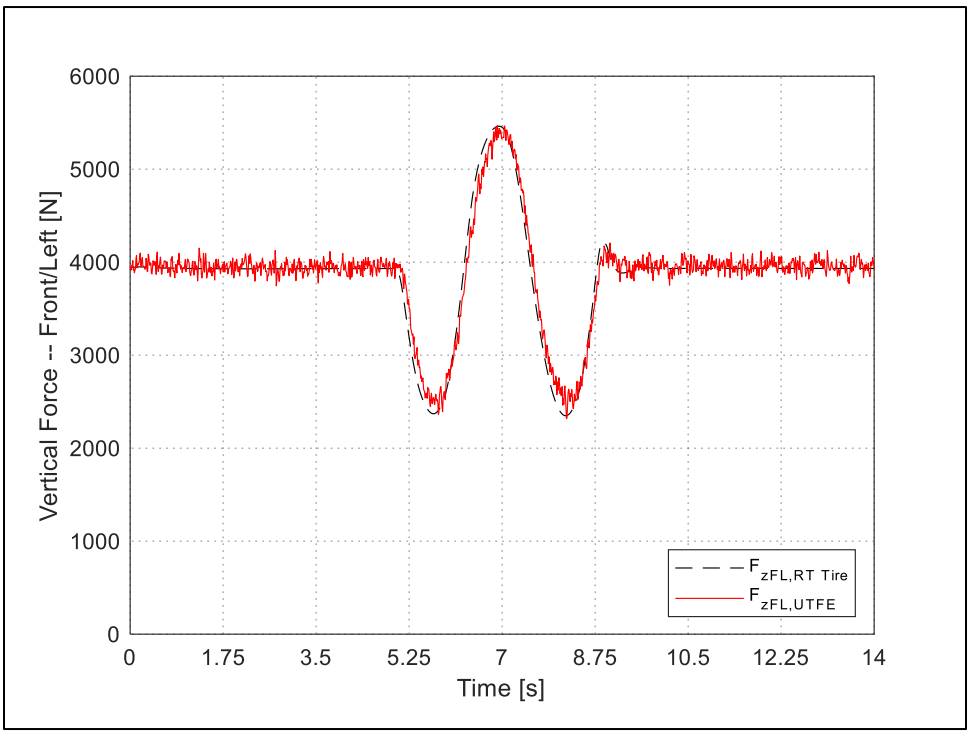

Figure 7.34 Comparison of the vertical force estimate and nonlinear model on the left front tire during a sinusoidal steer maneuver when u = 45 km/h and δ_{ss} = 120˚.

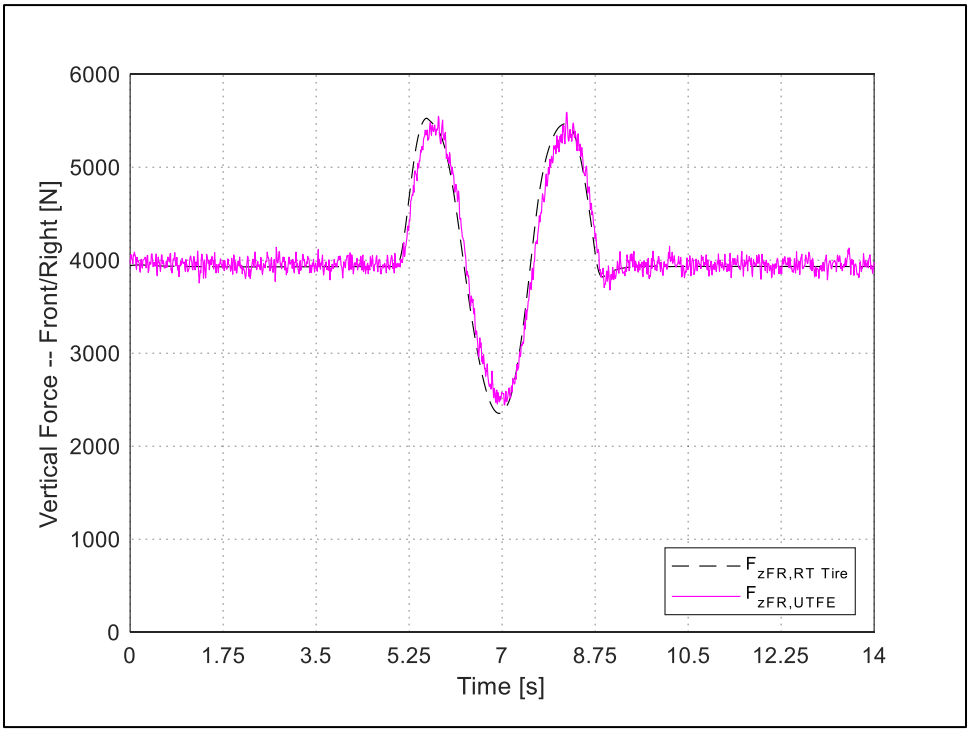

Figure 7.35 Comparison of the vertical force estimate and nonlinear model on the right front tire during a sinusoidal steer maneuver when u = 45 km/h and δ_{ss} = 120˚.

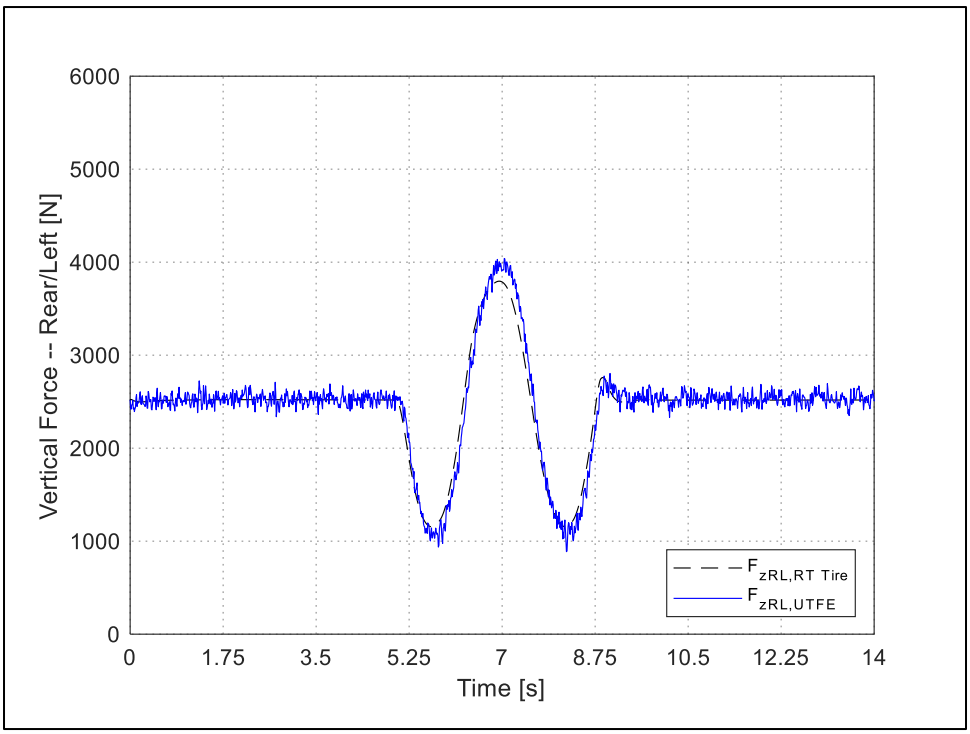

Figure 7.36 Comparison of the vertical force estimate and nonlinear model on the right front tire during a sinusoidal steer maneuver when u = 45 km/h and δ_{ss} = 120˚.

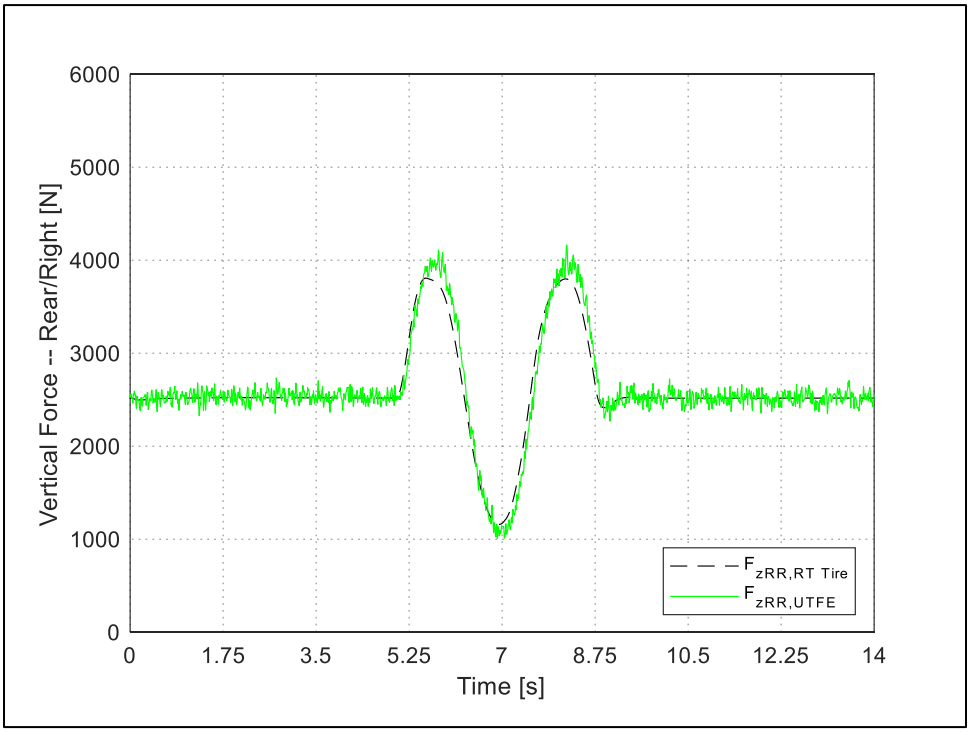

Figure 7.37 Comparison of the vertical force estimate and nonlinear model on the right rear tire during a sinusoidal steer maneuver when u = 45 km/h and δ_{ss} = 120˚.

7.3.3 SKID PAD TEST

The skid pad maneuver tests a vehicle's handling and identifies its understeer gradient over its entire operating range. For conventional vehicles, the powertrain can only send equal torque to the ends of each axle, so the steering angle must change during the skid pad maneuver. Since, for a torque-vectoring electric vehicle, the wheels can produce torque independently, the wheels take over some of the responsibility for steering the vehicle and the understeer gradient can be shaped, to a degree, depending on the torque allocation algorithm. In this case the controllers attempt to achieve a neutral understeer gradient which results in an acceleration versus steering angle curve with zero slope, or $\delta(a_y) = b$ where b is the neutral, or Ackermann steering angle from Equation (4.4). The resulting understeer gradient for each controller and the open loop system is shown in Figure 7.40. For this to be true, the yaw rate may only vary due to the change in longitudinal velocity, u. Since the ideal steering angle is constant and the velocity changes linearly due there being a constant longitudinal acceleration of 0.2 m/s^2, the ideal yaw rate changes linearly according to Equation (4.14) as shown in Figure 7.38.

This study was able to successfully produce neutral steer performance because of Direct Yaw Moment Control. In Figure 7.38, the yaw rate response from all three controller systems as well as the open loop system spike at t = 8 s because the driver model inputs a step steer at $t = 0$ s when the vehicle is at rest. Throughout the response, the CSMC and HSMC yaw rate responses experience several yaw rate spikes because of chattering from the controllers, which becomes more severe the closer the controller tracks the ideal response. This shows a cycle of the yaw rate of the two controllers settling towards neutral steer, chattering more severely, and then overshooting. The HSMC tracks the ideal yaw rate more closely than the CSMC response and chatters less severely but slips off course before the CSMC. The CSMC remains on course longer than the HSMC and open loop systems, but its limit behavior is terminal oversteer. In all these cases, the vehicle leaves the road as opposed to fishtailing since the yaw rates drops below the ideal yaw rate, indicating terminal understeer.

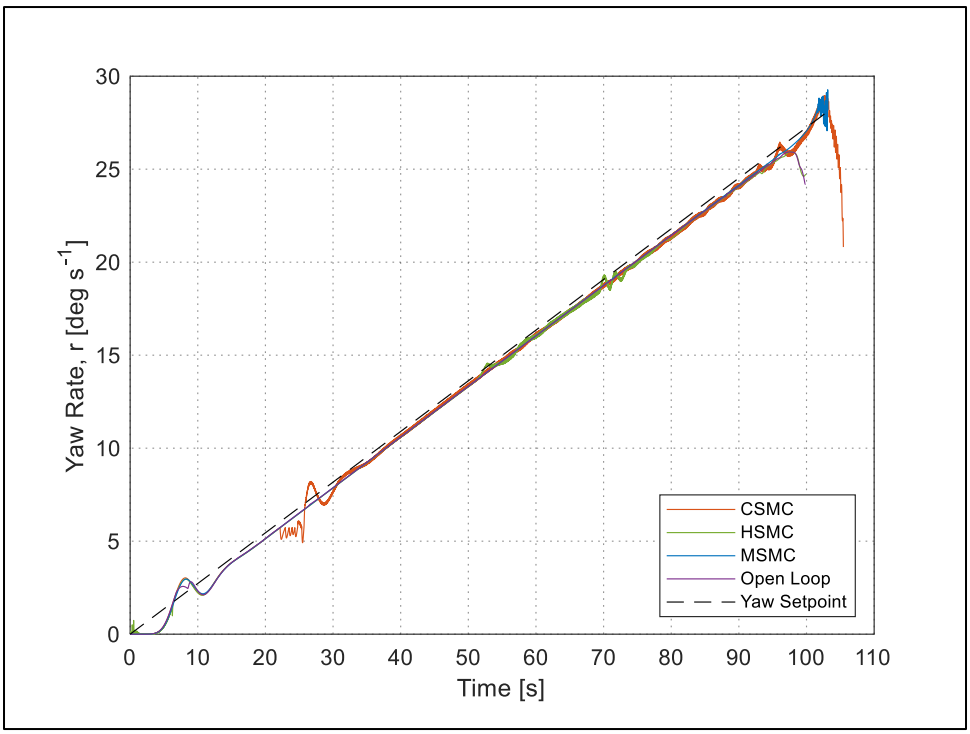

Figure 7.38 Yaw rate response during the skid pad maneuver when a_x = 0.2 m/s^2 and ρ = 0.0238 m^{-1}.

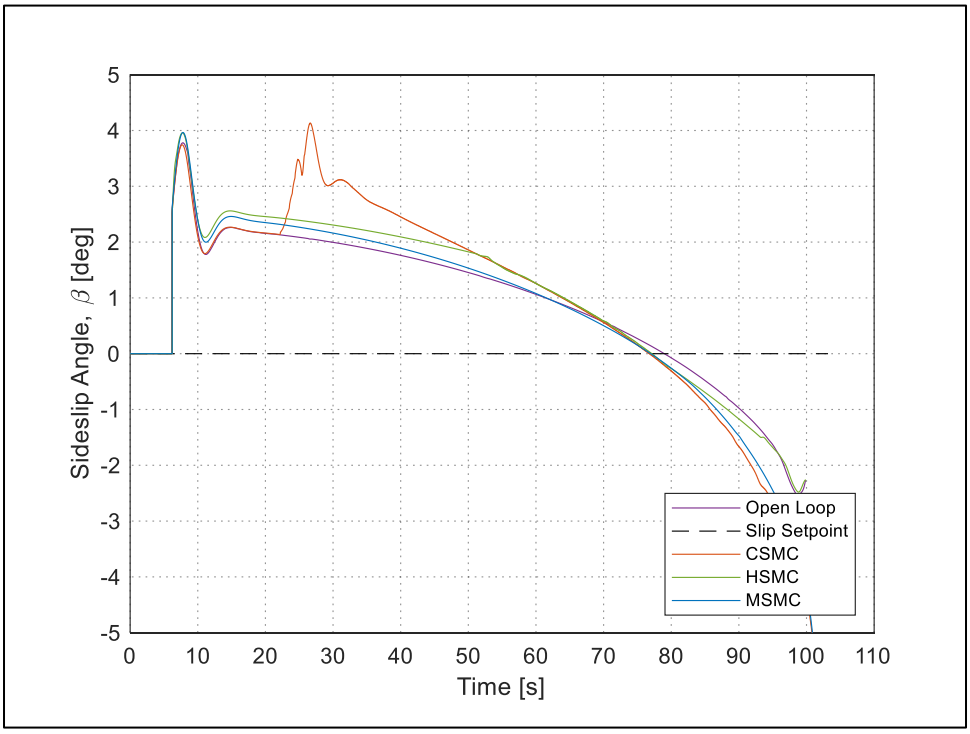

Figure 7.39 Sideslip angle response during the skid pad maneuver when a_x = 0.2 m/s^2 and ρ = 0.0238 m^{-1}.

As expected, the open loop yaw rate remains stable throughout its entire response but deviates from the ideal yaw rate at the same time as the HSMC and with a comparable peak lateral acceleration. On the other hand, the MSMC experiences no overshoot or chattering and deviates from the ideal yaw rate at the same time as the CSMC. In addition, the MSMC reaches a similar peak lateral acceleration as the CSMC. Additionally, the MSMC tracks the ideal yaw rate during its entire response. The MSMC deviates from the ideal yaw rate at t = 104 s in a much different manner than any of the other three systems: it begins fishtailing slightly, indicating limit oversteer, but remains stable. This limit behavior is neither terminal understeer nor terminal oversteer. The vehicle equipped with MSMC becomes marginally stable about the ideal yaw rate with a slight bias towards terminal oversteer. The vehicle begins fishtailing, but before it can go unstable the front tires slip and the vehicle enters a turn with a wider radius, which is concentric with the original turn radius and becomes stable again.

While the yaw rate response indicates the limit behavior of the vehicle and shows the tracking performance of the vehicle, it does not say anything qualitative about the handling performance of the vehicle. The understeering gradient plot in Figure 7.40 frames the vehicle performance in terms of lateral acceleration, which is determined by the speed of the vehicle and radius of the turn with the formula $a_y = u^2/R$. A higher maximum lateral acceleration means the vehicle can negotiate a turn faster without loss of control. The CSMC demonstrates a highly inconsistent understeer gradient and never achieves neutral steer. Although it does achieve a greater maximum lateral acceleration than the open loop and HSMC systems, it results in severe chattering and oversteer. The HSMC approaches neutral steer for a short period for intermediate lateral acceleration, but quickly deviates towards understeer. Both the open loop and HSMC systems terminate at approximately 8.4 m/s^2 (0.856 g), the CSMC terminates at approximately 8.95 m/s^2 (0.912 g) and the MSMC terminates at approximately 8.96 m/s^2 (0.913 g). Only the MSMC was able to achieve neutral steer with an Ackermann steering angle error of 1˚, or 1.4%.

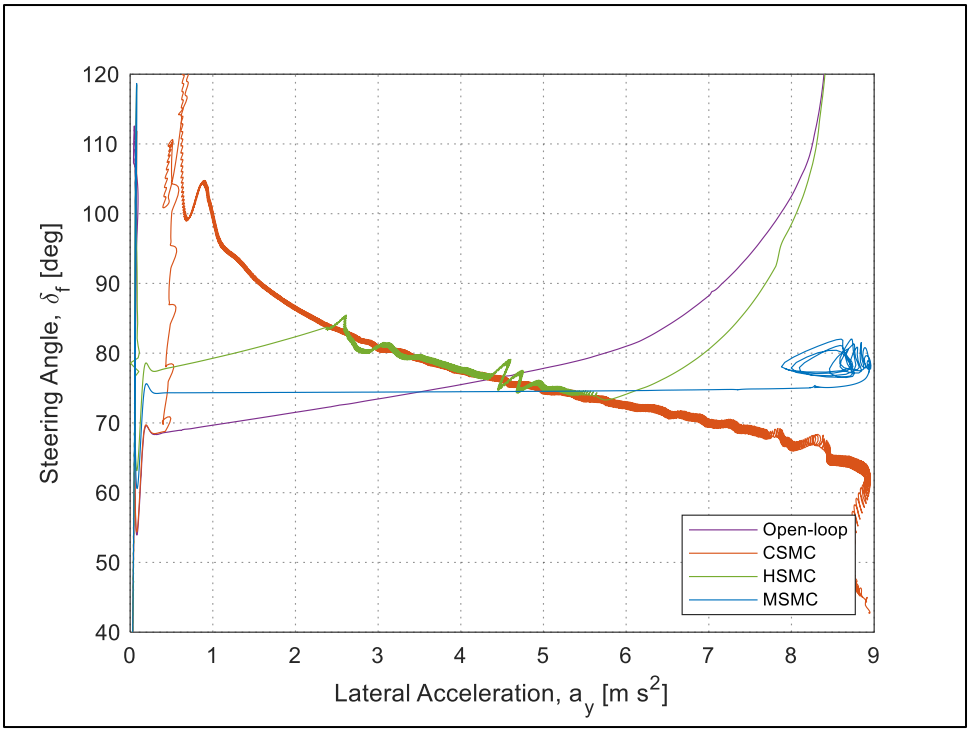

Figure 7.40 Understeer gradient during the skid pad maneuver when a_x = 0.2 m/s^2 and ρ = 0.0238 m^{-1}.

In the context of the performance that each system achieves, the MSMC is most successful in limiting the sideslip angle. Figure 7.39 shows the sideslip angle for each system over the duration of the skid pad test. The angle spikes toward the beginning of the maneuver because the driver model inputs a step steer at t = 0 s when the vehicle is at rest. Through the low and intermediate acceleration range, the sideslip angle of the MSMC tracks very closely to that of the open loop system, both of which remain lower than the CSMC and HSMC up until t = *80 s* and u = 58 km/h. After this point, the sideslip angle for all systems goes negative and each system settles into its characteristic understeer behavior. The sideslip angle of the open loop and HSMC systems track together, with the HSMC angle having a lower magnitude until right before they leave the track. On the other hand, the CSMC and MSMC systems track together, with the MSMC angle having a lower magnitude than that of the CSMC until right before they leave the track. These represent two pairs of understeering behavior, where the open loop and HSMC systems understeer, failing at a lower lateral acceleration, while the CSMC and MSMC systems oversteer and fail at a higher lateral acceleration. The sideslip angle of the different pairs cannot be compared because the lateral acceleration is directly related to the sideslip angle, so it would not make sense for the first pair to have a greater sideslip angle than the latter pair. However, the pair members can be compared to each other. This means the HSMC and MSMC outperform the other two.

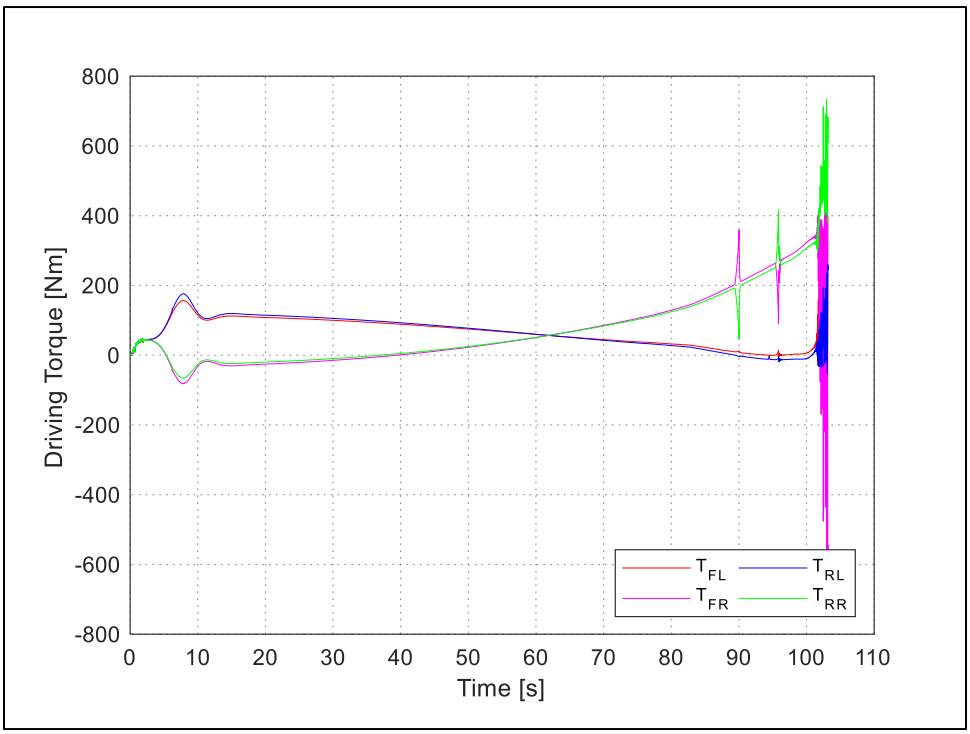

Figure 7.41 Torque response of the DYC system using the modified sliding mode controller during the skid pad maneuver when a_x = 0.2 m/s^2 and ρ = 0.0238 m^{-1}.

The controller does show some interesting behavior in terms of the torque allocation scheme. At low and intermediate lateral acceleration, the controller sends positive torque to the inside wheels and negative torque to the outside wheels which generates a clockwise moment about the vehicle, but the vehicle is turning to the left. This is because the initial steer step caused a large positive spike in yaw rate and sideslip angle, far above that which corresponds to neutral steer. A clockwise yawing moment was necessary to offset the counterclockwise yaw rate overshoot, which would have otherwise occurred. As the velocity increases, the sideslip angle decreases, and the ideal yaw rate increases until t = 62 s and u = 45 km/h at which point the yaw moment goes from opposing the steering moment to assisting it, requiring the torque to the outside wheels to exceed that of the inside wheels. The net torque shifts vertically to remain positive throughout the maneuver because it must meet the base torque required to accelerate the vehicle.

7.3.3.1 SKID PAD TEST TIRE FORCE ESTIMATION

7.3.3.1.1 LONGITUDINAL FORCE

The general trend of the longitudinal force closely matches the requested driving torque in terms of shape. The inner wheels initially generate a positive longitudinal force, which decreases over time while the outer wheels initially generate a negative, force, which increases over time until the yaw rate deviates. The inside wheels experience a small offset from the model force and the outside wheels track the model force very well. When the velocity is very small (< 1 m/s) there is a large spike in the estimate force due to the vehicle being at rest and lasts until t = 5 s. As the vehicle gains some speed, the spike subsides.

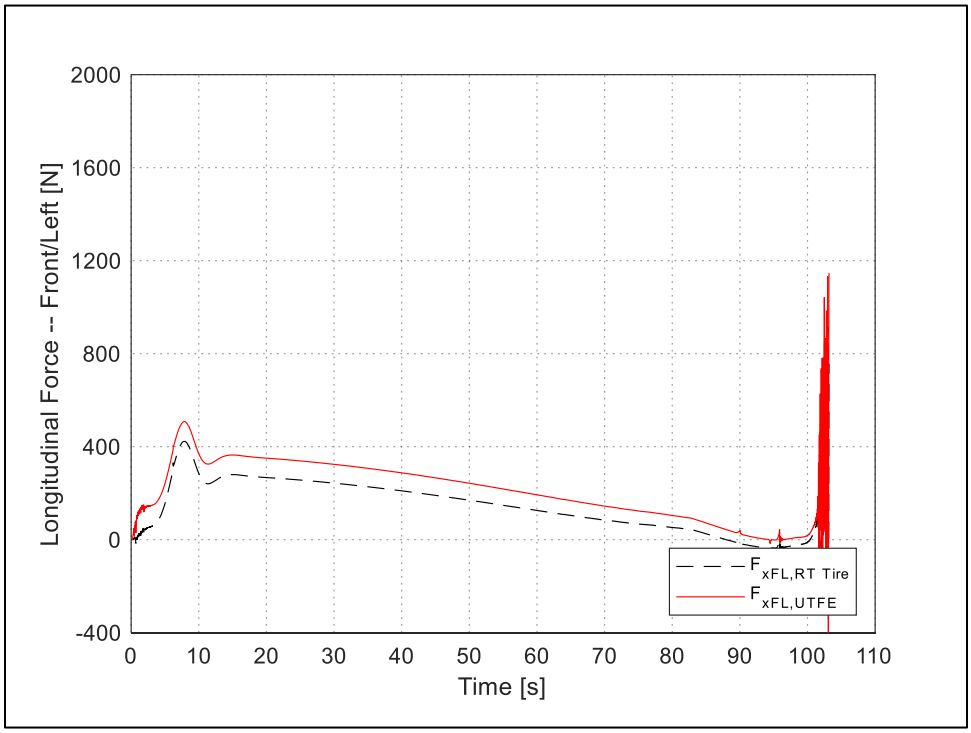

Figure 7.42 Comparison of the longitudinal force estimate and nonlinear model on the left front tire during a skid pad test where a_x = 0.2 m/s^2.

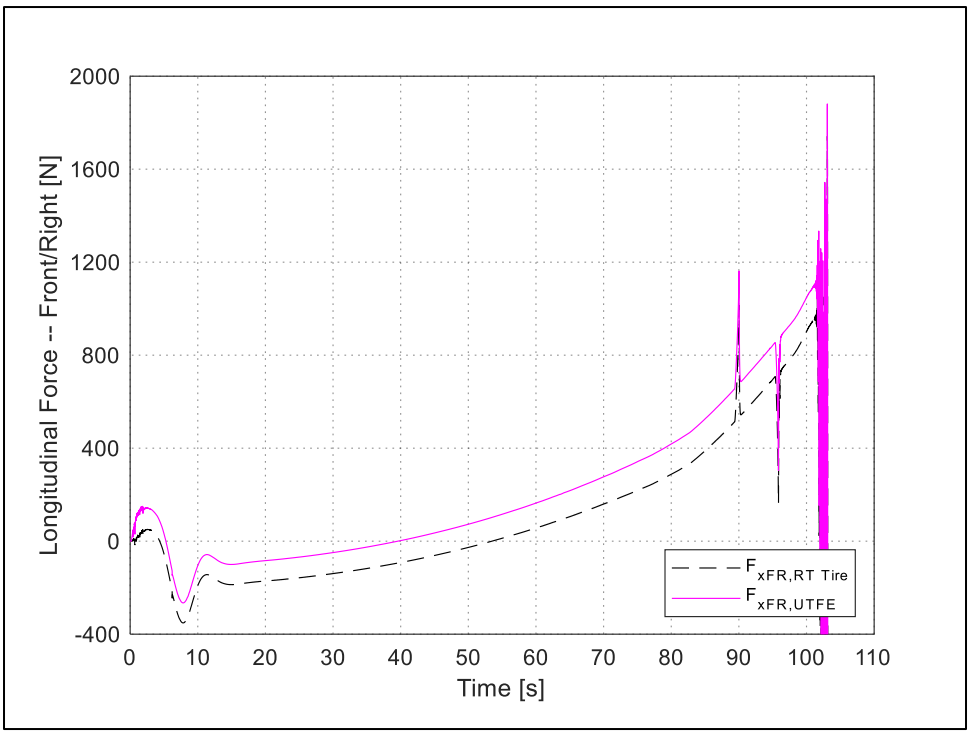

Figure 7.43 Comparison of the longitudinal force estimate and nonlinear model on the right front tire during a skid pad test where a_x = 0.2 m/s^2.

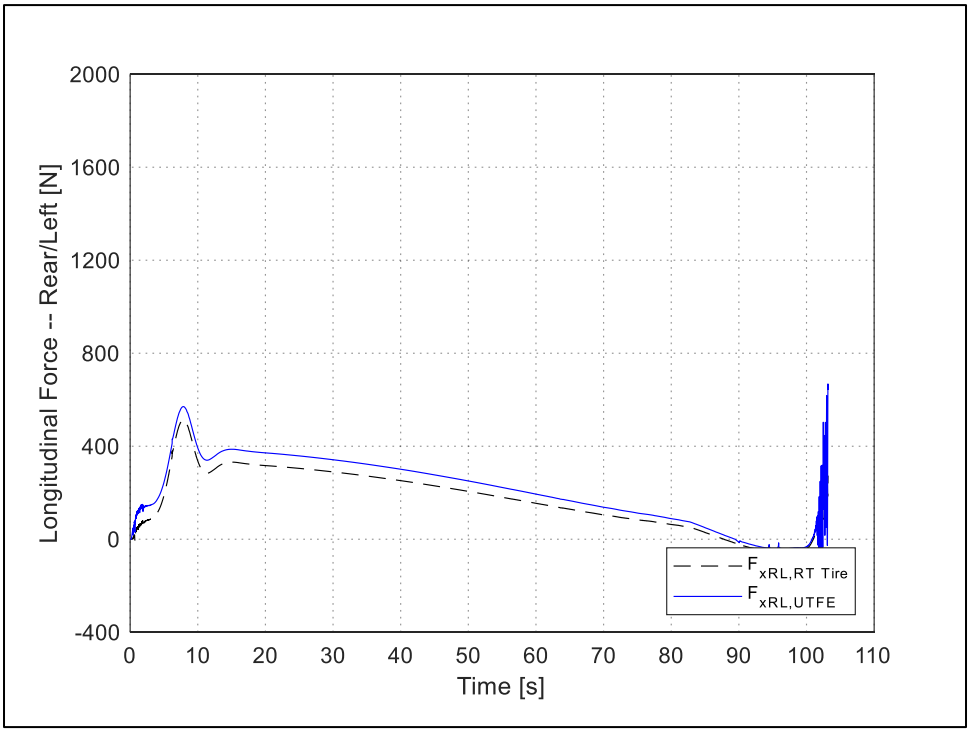

Figure 7.44 Comparison of the longitudinal force estimate and nonlinear model on the left rear tire during a skid pad test where a_x = 0.2 m/s^2.

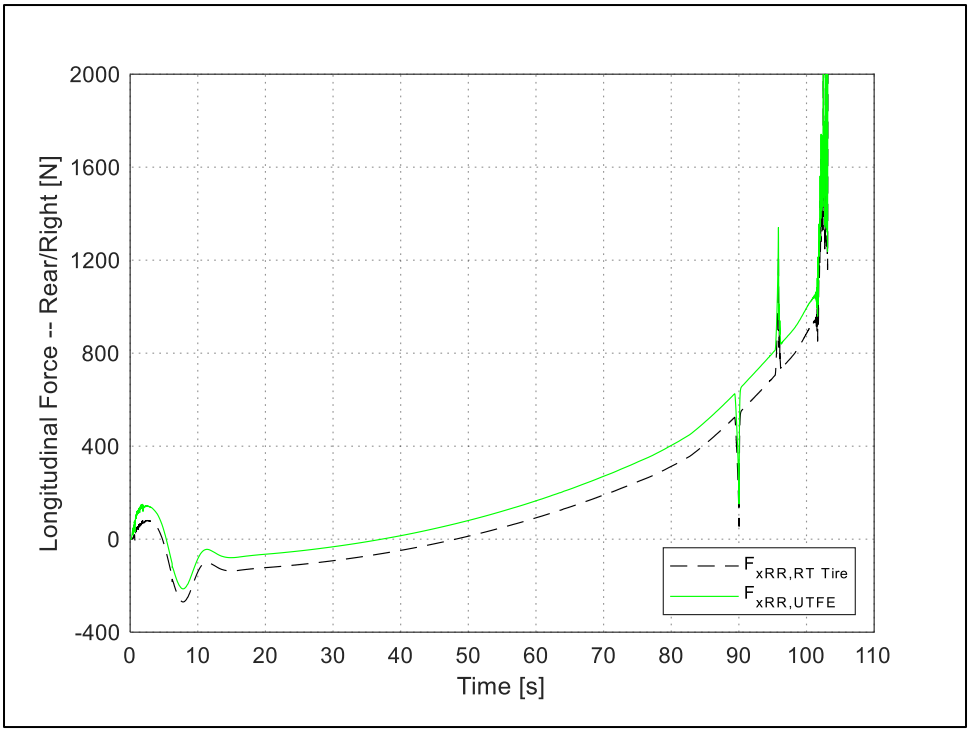

Figure 7.45 Comparison of the longitudinal force estimate and nonlinear model on the right rear tire during a skid pad test where a_x = 0.2 m/s^2.

7.3.3.1.2 LATERAL FORCE

In this case, the UTFE tracks the model lateral tire force better for the outside wheels than for the inside wheels. As with the longitudinal force estimation, the lateral force estimator predicts a spike at low speeds, which settles within the first five seconds of the maneuver. The UTFE does not track the model force precisely during the intermediate acceleration range of the maneuver (40 s < t < 80 s) for the outside wheels and tracks better at high acceleration (> 80 s). On the other hand, the UTFE does not track precisely at all beyond low acceleration (> 40 s). As with the J-turn and Sine steer maneuvers, the estimated right rear lateral tire force does not track the model force at all. However, it does follow the same general shape.

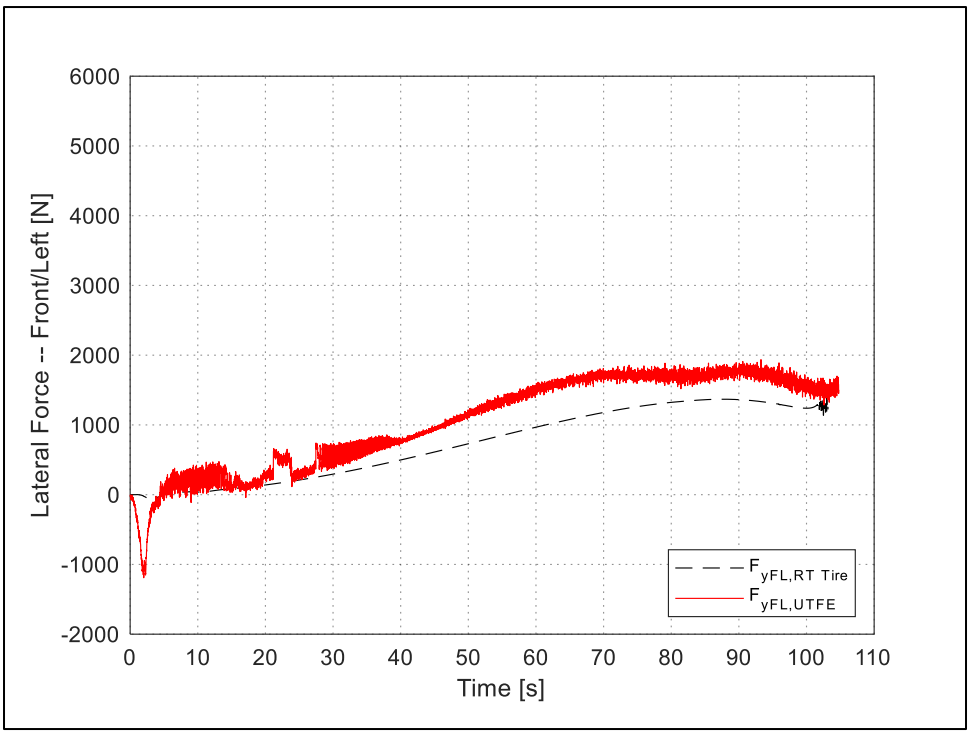

Figure 7.46 Comparison of the lateral force estimate and nonlinear model on the left front tire during a skid pad test where a_x = 0.2 m/s^2.

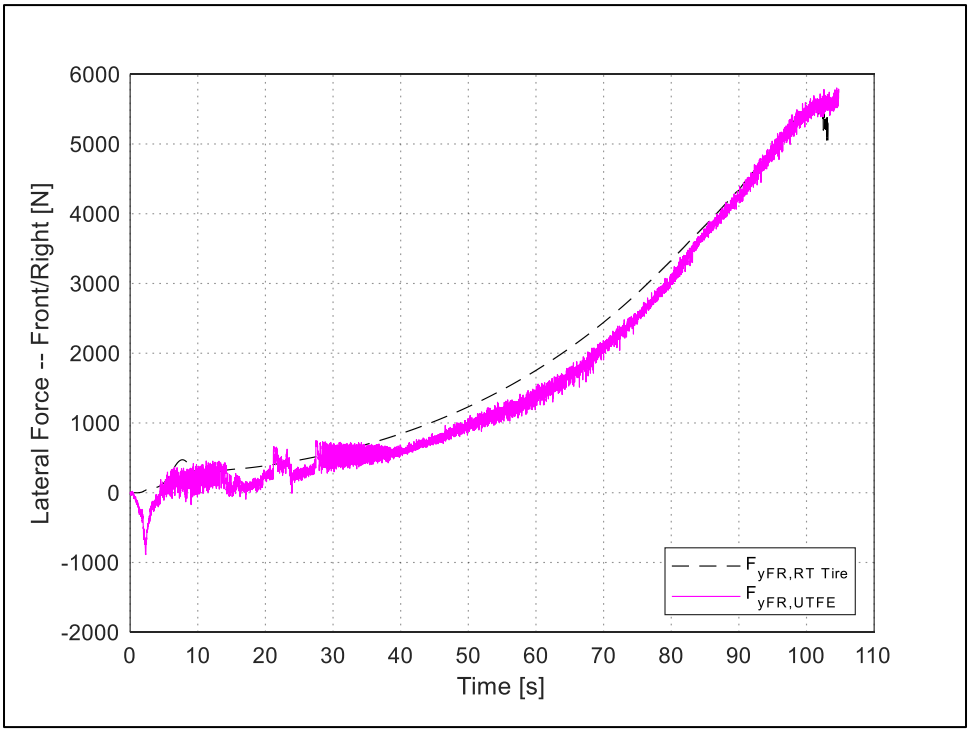

Figure 7.47 Comparison of the lateral force estimate and nonlinear model on the right front tire during a skid pad test where a_x = 0.2 m/s^2.

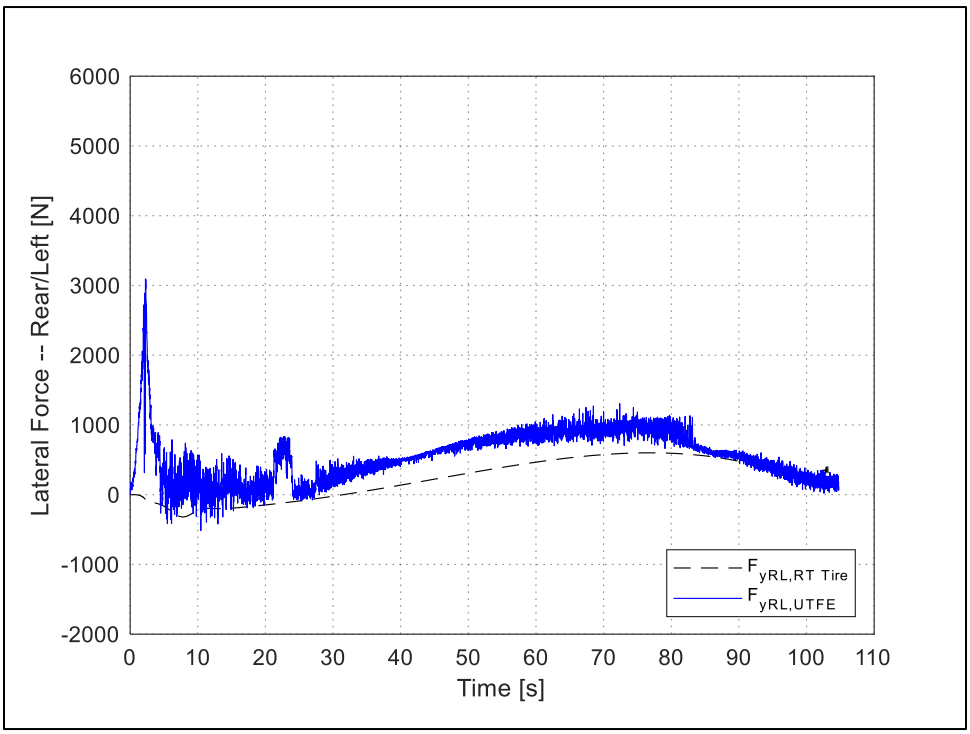

Figure 7.48 Comparison of the lateral force estimate and nonlinear model on the left rear tire during a skid pad test where a_x = 0.2 m/s^2.

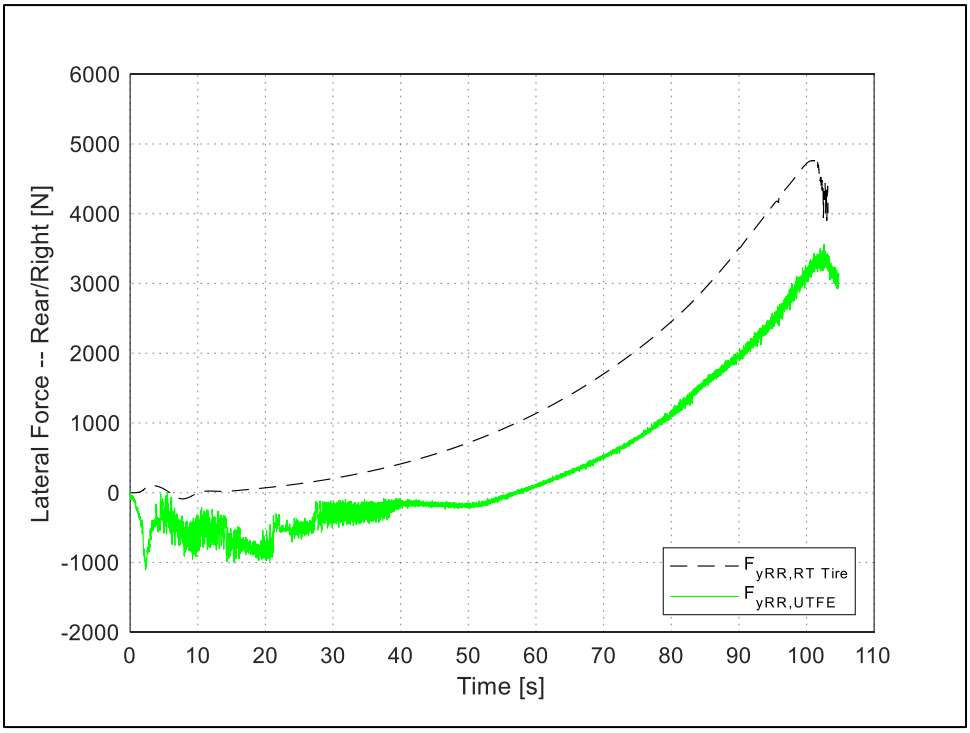

Figure 7.49 Comparison of the lateral force estimate and nonlinear model on the right rear tire during a skid pad test where a_x = 0.2 m/s^2.

7.3.3.1.3 VERTICAL FORCE

The vertical tire force estimation of the UTFE tracks the RT tire model very precisely. On the other hand, the front axle vertical force estimation begins deviating some beyond 80 seconds. This inconsistency arises because the roll dynamics become significant at high lateral accelerations and the UTFE assumes static roll parameters. Perhaps the most consequential of the modeling assumptions was that the roll center of the front axle is coincident with the ground to eliminate certain roll terms from the force computation.

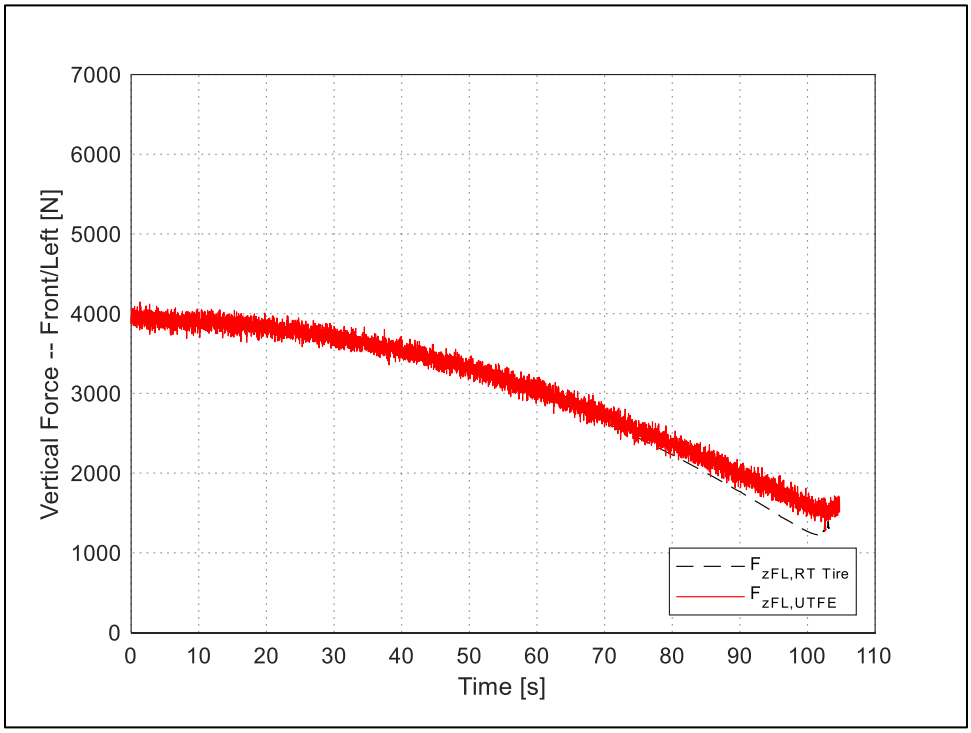

Figure 7.50 Comparison of the vertical force estimate and nonlinear model on the left front tire during a skid pad test where a_x = 0.2 m/s^2.

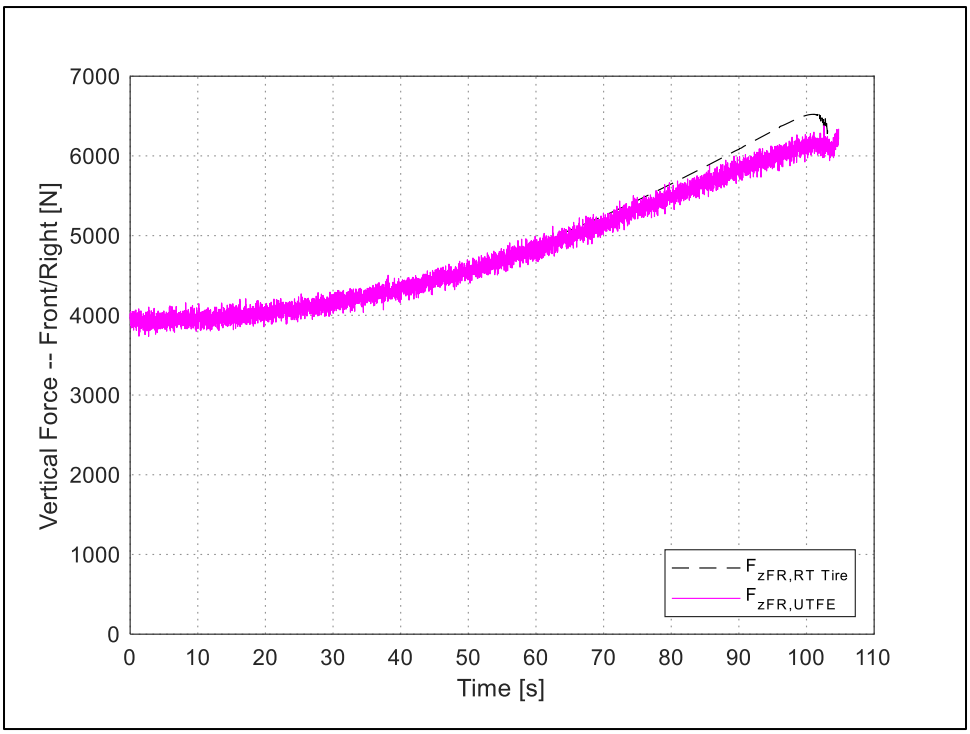

Figure 7.51 Comparison of the vertical force estimate and nonlinear model on the right front tire during a skid pad test where a_x = 0.2 m/s^2.

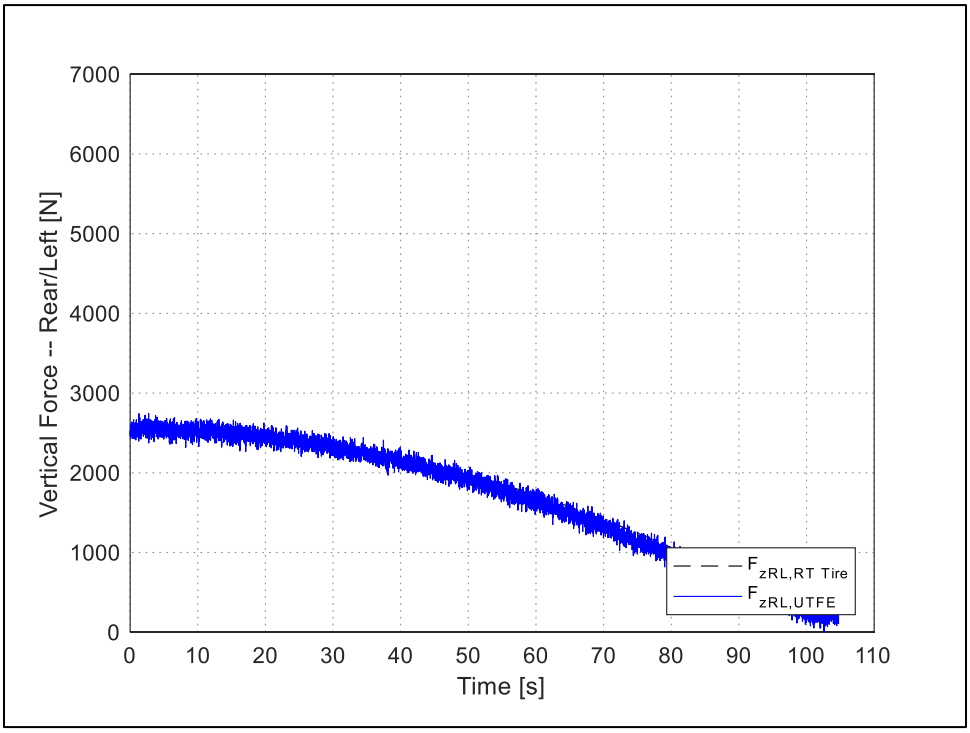

Figure 7.52 Comparison of the vertical force estimate and nonlinear model on the left rear tire during a skid pad test where a_x = 0.2 m/s^2.

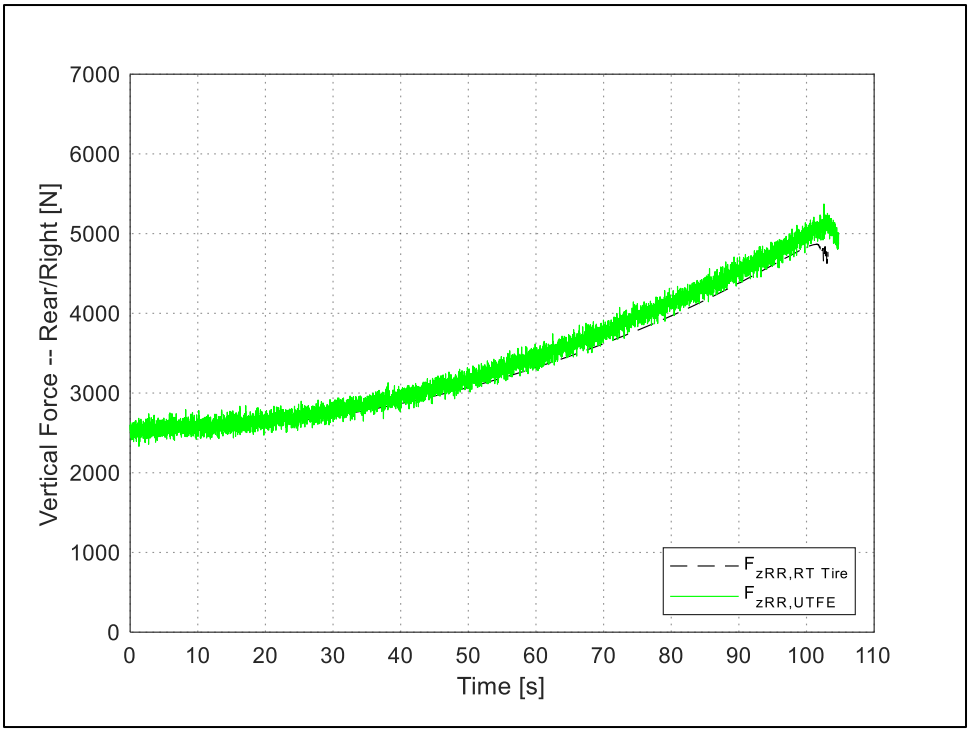

Figure 7.53 Comparison of the vertical force estimate and nonlinear model on the right rear tire during a skid pad test where $a_x = 0.2$ m/s^2.

7.3.4 BRAKING MU SPLIT TEST

This maneuver is intended to test the traction control capabilities of the control system. The vehicle drives ahead at a high speed until the left tires hit a low-friction strip on the road after 29 seconds simulating an ice slick. At this point, the driver slams on the brake pedal, applying 80% of the maximum pressure to the brake pads until the vehicle comes to rest. In this case, the driver does not input any steer, but the vehicle begins rotating because of the unequal braking force on the left and right-hand side. This would typically lead to the vehicle dangerously spinning out. However, the controller detects that the driver has not input a steering angle and attempt to straight the vehicle. The result of this test will show the relative performance of the controllers in preventing spinout and demonstrate the control system's robustness against uncertainty in the friction coefficient of the road.

Figure 7.54 and Figure 7.55 show the yaw rate and sideslip angle response of each system during the mu-split maneuver, respectively. Severe chattering in the CSMC because of the very small tracking error causes it to yaw at the beginning of the maneuver before straightening out again. When the vehicle begins braking on the slick, a large yaw moment occurs on the vehicle which the open loop system, CSMC system and HSMC system are unable to recover from, resulting in them spinning out

unstably as evident from the sudden deviation in the yaw rates and sideslip angles. On the other hand, the MSMC system experiences a relatively small deviation with peak yaw rate and sideslip magnitude 1.05 deg/s and 0.4˚, then begins slipping more severely with a peak yaw rate and sideslip magnitude of 1.35 deg/s and 1.8˚ respectively, then it fully corrects and comes to rest

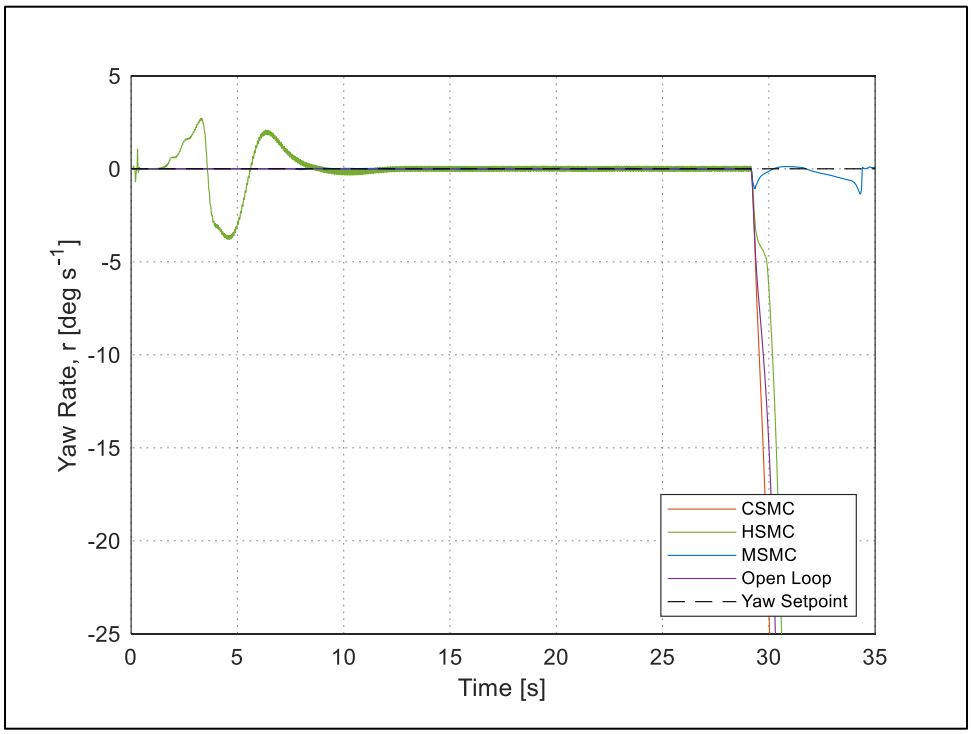

Figure 7.54 Yaw rate response during the skid pad maneuver where t = 29 s and u = 100 km/h when the friction patch is hit.

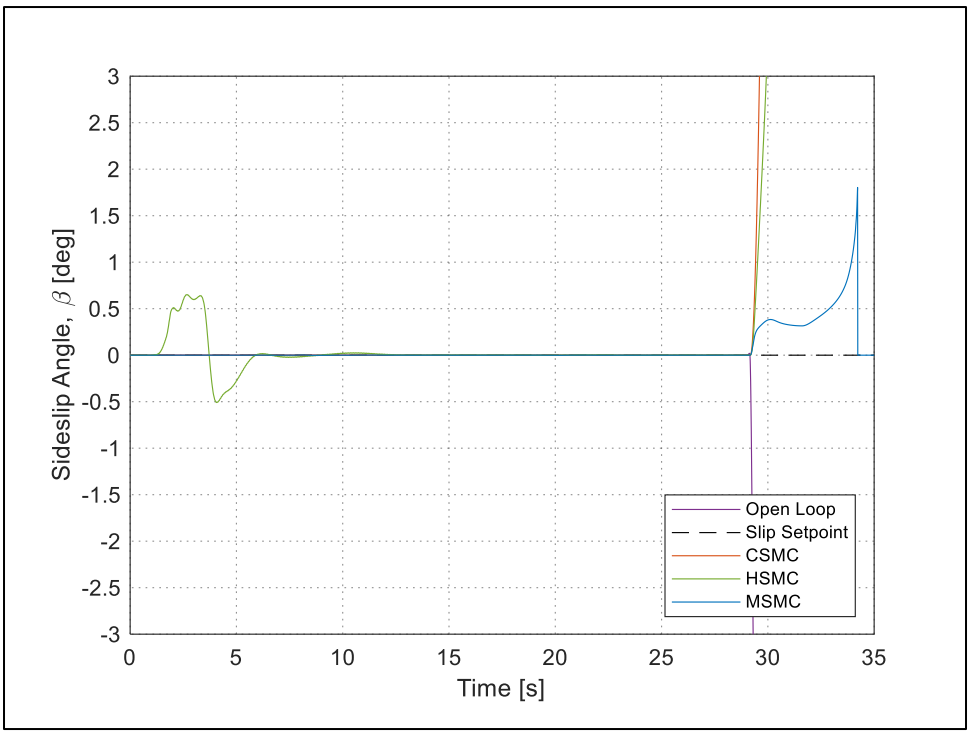

Figure 7.55 Sideslip angle response during the braking mu-split maneuver where t = 29 s and u = 100 km/h when the friction patch is hit.

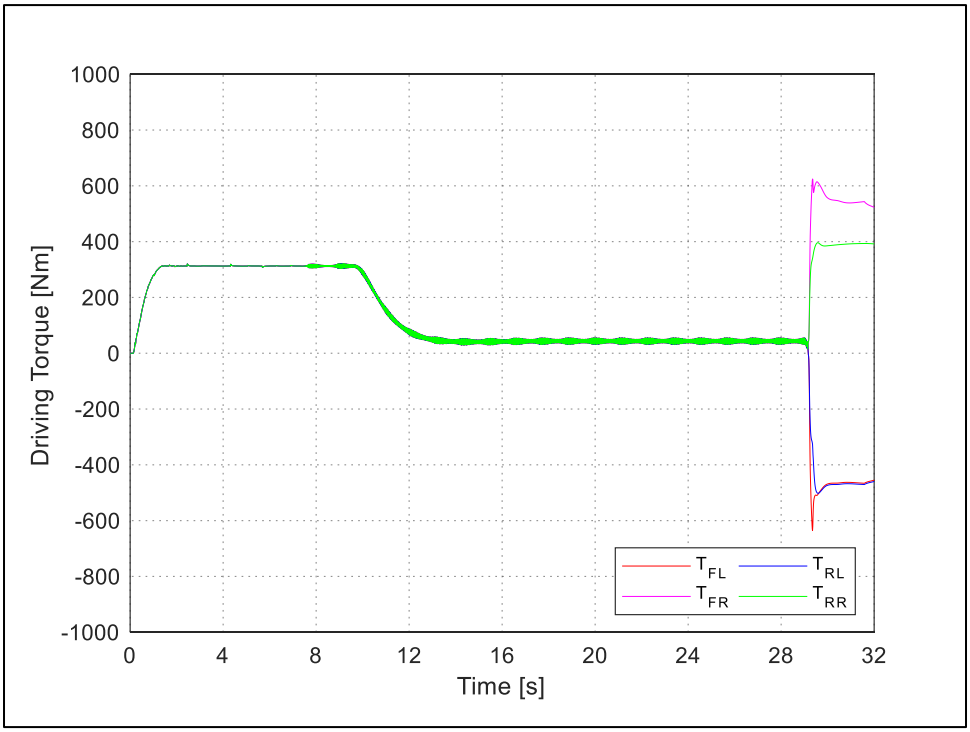

Figure 7.56 Torque response of the DYC system using the modified sliding mode controller during the braking mu-split maneuver where t = 29 s and u = 100 km/h when the friction patch is hit.

Since the yaw instability occurs due to a lesser braking force on the left-hand tires, the vehicle rotates clockwise. Figure 7.56 shows the torque allocation, which counters this rotation. The TVC allocates positive torque to the right-hand tires of the vehicle and negative torque to the left-hand tires. The TVC is unaware of the braking torque because it is not modeled in the longitudinal force estimator upon which the torque constraint module depends. Consequently, the torque-vectoring controller does not produce an optimal torque distribution during the braking mu-split scenario. This is evident by the fact that the controller tries to generate a large amount of negative torque on the left tires of the vehicle, which are skidding.

Figure 7.57 shows a simulation from CarMaker of the vehicle losing traction and spinning out during the mu-split maneuver after the driver begins braking after hitting a low mu strip. This figure demonstrates how the MSMC can keep the vehicle from spinning out while the CSMC and HSMC do not. The suboptimal solution results in the CSMC and HSMC systems spinning out clockwise even though they produce a counter moment. This scenario is exacerbated by chattering from these two controllers, which reduced the effectiveness of the torque allocation in the critical first moment of braking when spinning starts. On the other hand, the MSMC was able to stop the spinout. Since the left hand tires of the vehicle is already near the limit of the negative torque it can produce, the MSMC was able to steady the vehicle because it provided a sufficiently large driving torque on the right-hand tires to reduce the braking force such that severe spinning did not occur in the first moment of braking. Once the vehicle started slowing down, it became easier to control. Although the torque-vectoring controller did not have information from the braking system, the MSMC was able to prevent the vehicle from becoming unstable because it produced smooth, chatter-free counter moment compensated for uncertainty in the friction coefficient by tracking both the yaw rate and sideslip angle as well as their rates of change.

(a) (b) (c)

Figure 7.57 Demonstration of the yaw response of the three control methods in CarMaker during the braking mu-split test. The greyish-blue patch represents the low mu slick and the results, from left to right are with (a) conventional sliding mode, (b) hybrid sliding mode and (c) modified sliding mode.

7.3.4.1 BRAKING MU-SPLIT TEST TIRE FORCE ESTIMATION

7.3.4.1.1 LONGITUDINAL FORCE

Figure 7.58 to Figure 7.61 show a comparison of the longitudinal force estimated by the UTFE and the nonlinear RT tire model in CarMaker during the braking mu-split maneuver. In this case, the estimator performs extremely poorly because it assumes the only torque applied to the tires comes from the in-hub electric motors of the 4MIDEV vehicle and because the tires on the left side of the vehicle are slipping after 29 seconds into the simulation. As shown in Figure 7.56, the torque-vectoring controller sends a negative torque signal to the motors on the left side wheels and a positive torque signal to the motors on the right side wheels. The longitudinal force estimates in the following four figures comes purely from the applied motor torques, but the actual force comes from the sum of the braking force and force transmitted by the motors. As such, none of the forces track, and the estimated force on the right tires is the wrong sign.

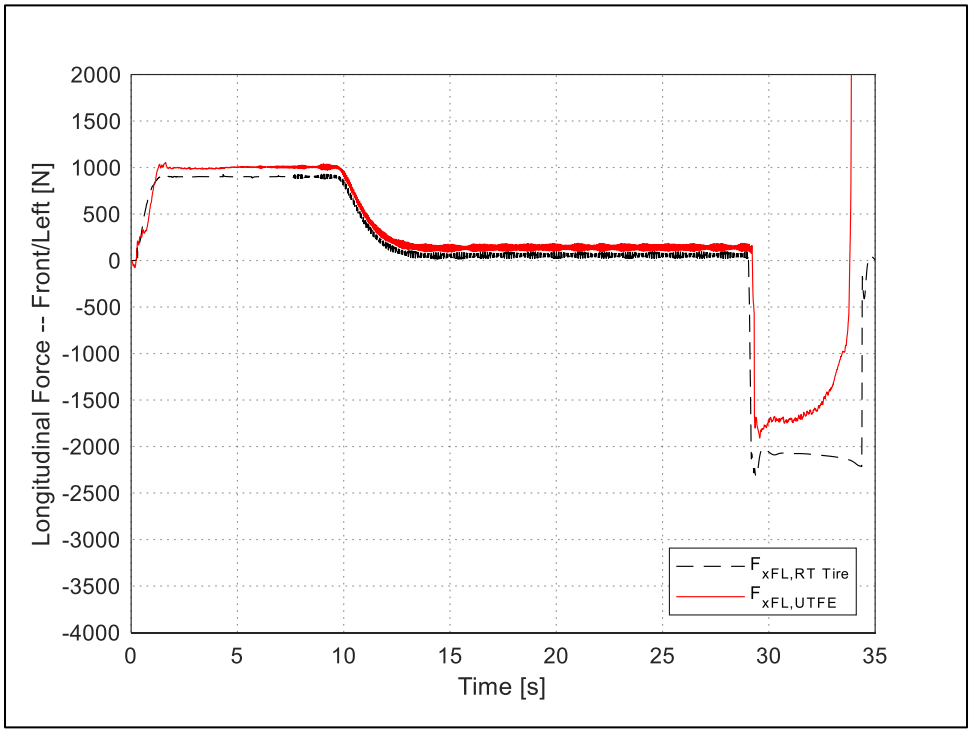

Figure 7.58 Comparison of the longitudinal force estimate and nonlinear model on the left front tire for a braking mu-split test where u = 100 km/h when the left tires hit a slick with μ = 0.5 at t = 29 s.

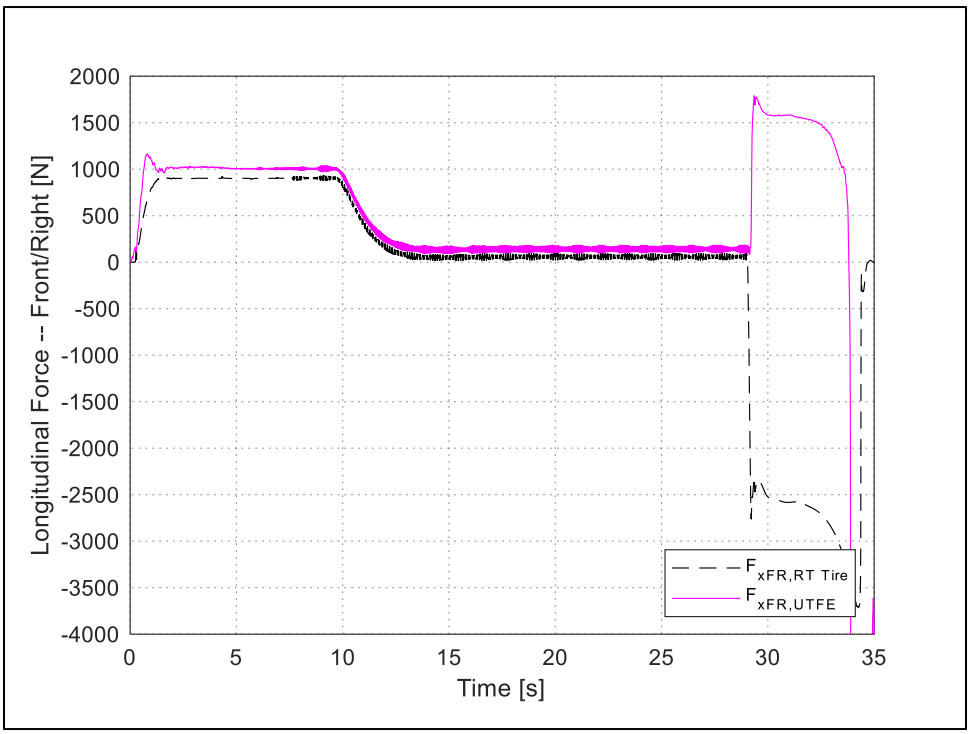

Figure 7.59 Comparison of the longitudinal force estimate and nonlinear model on the right front tire for a braking mu-split test where u = 100 km/h when the left tires hit a slick with μ = 0.5 at t = 29 s.

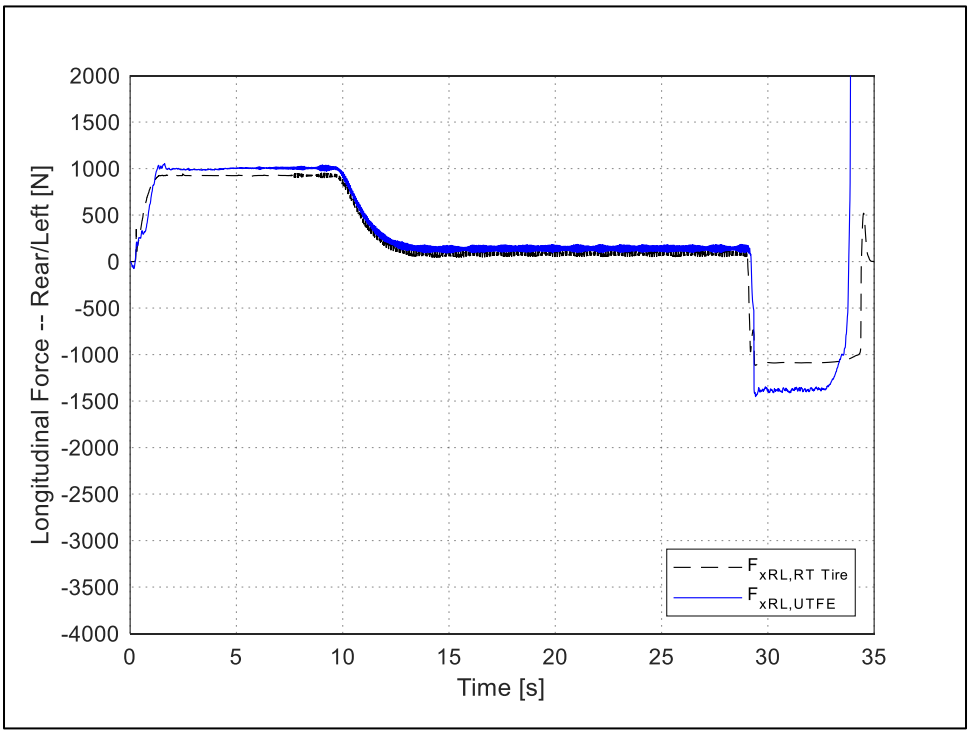

Figure 7.60 Comparison of the longitudinal force estimate and nonlinear model on the left rear tire for a braking mu-split test where u = 100 km/h when the left tires hit a slick with μ = 0.5 at t = 29 s.

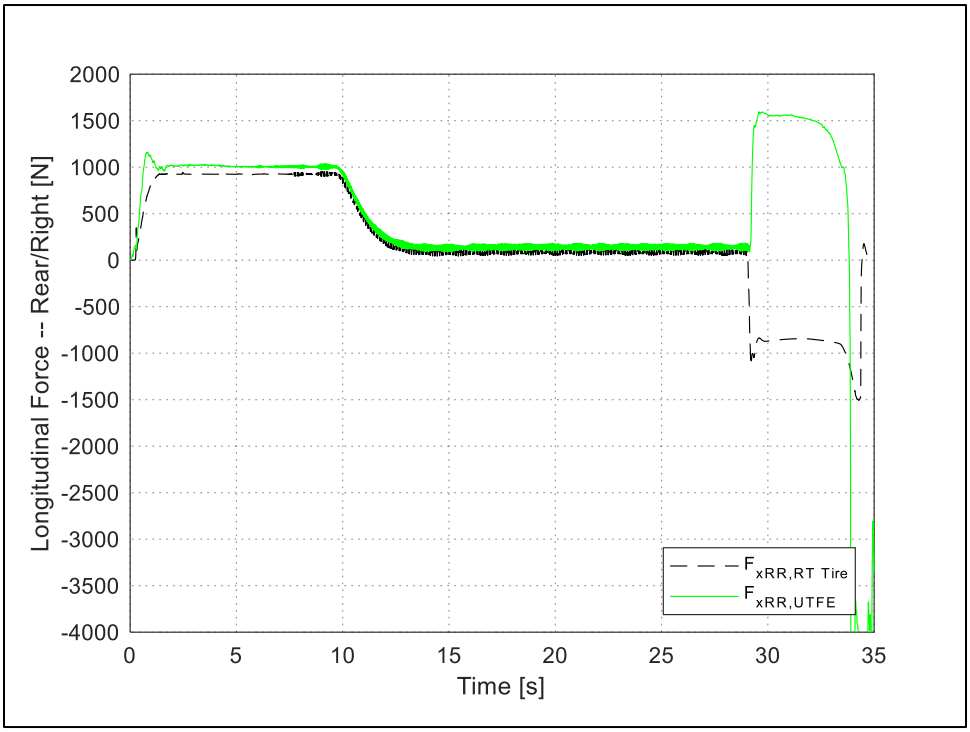

Figure 7.61 Comparison of the longitudinal force estimate and nonlinear model on the right rear tire for a braking mu-split test where u = 100 km/h when the left tires hit a slick with μ = 0.5 at t = 29 s.

7.3.4.1.2 LATERAL FORCE

Figure 7.62 to Figure 7.65 show a comparison of the lateral force estimated by the UTFE and the nonlinear RT tire model in CarMaker during the braking mu-split maneuver. Since the lateral force during this maneuver is small, the scale of these figures is much finer, so the nuances of the lateral force curves are observable. The estimated lateral force for all four wheels is centered on zero as one would expect, but the RT tire model predicts some fluctuation around 0 ± 300 N when the vehicle is just driving straight. This force arises because the closed loop DYC system is running all the time, so any small deviation whatsoever leads to a control action. Unless a switch triggers the controller only above a certain yaw rate, there will always be small fluctuations like this even when driving straight.

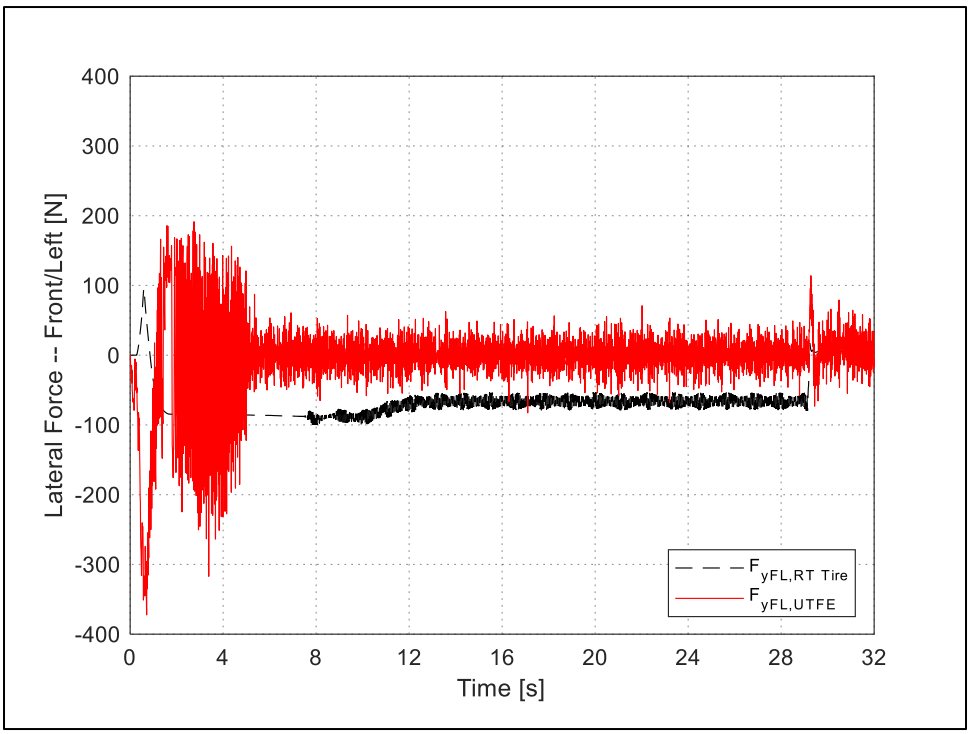

Figure 7.62 Comparison of the lateral force estimate and nonlinear model on the left front tire for a braking mu-split test where u = 100 km/h when the left tires hit a slick with μ = 0.5 at t = 29 s.

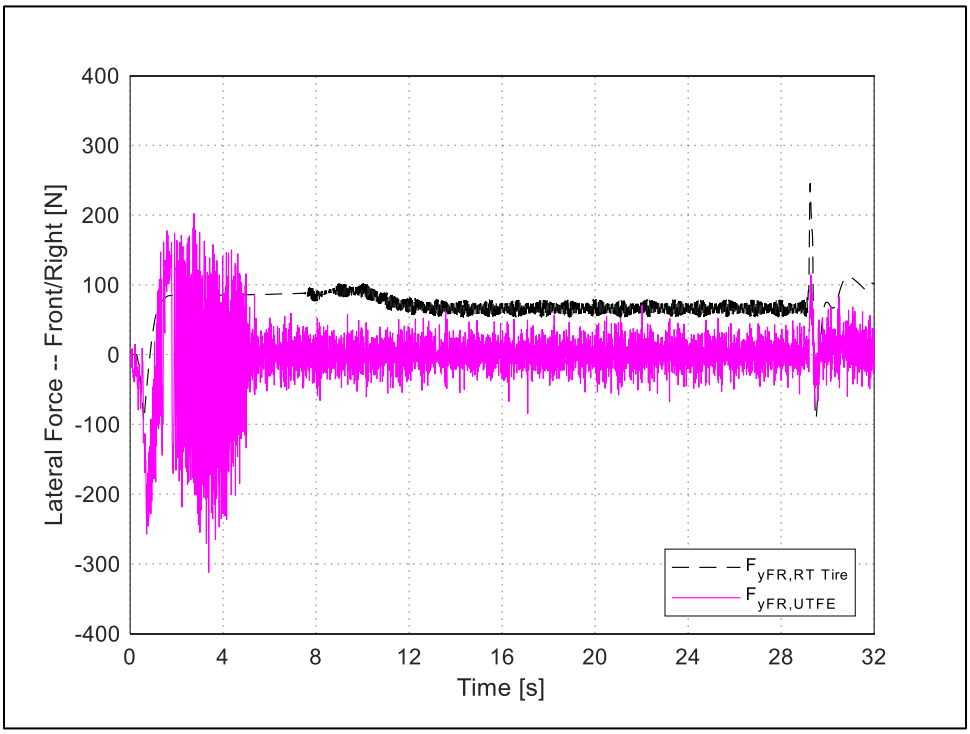

Figure 7.63 Comparison of the lateral force estimate and nonlinear model on the right front tire for a braking mu-split test where u = 100 km/h when the left tires hit a slick with μ = 0.5 at t = 29 s.

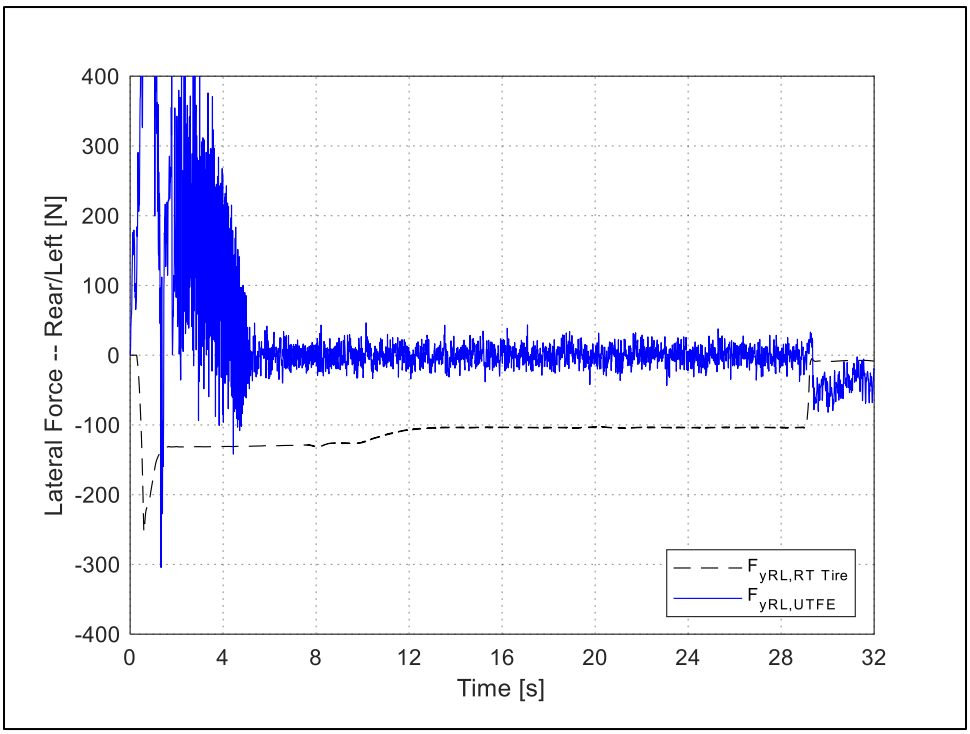

Figure 7.64 Comparison of the lateral force estimate and nonlinear model on the left rear tire for a braking mu-split test where u = 100 km/h when the left tires hit a slick with μ = 0.5 at t = 29 s.

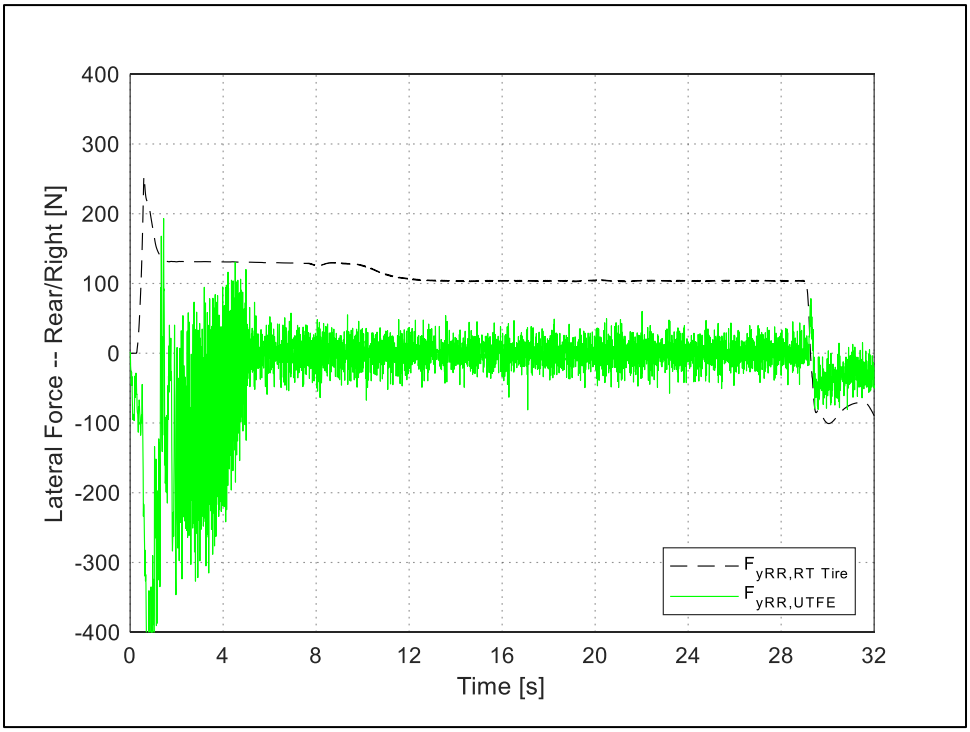

Figure 7.65 Comparison of the lateral force estimate and nonlinear model on the right rear tire for a braking mu-split test where u = 100 km/h when the left tires hit a slick with μ = 0.5 at t = 29 s.

7.3.4.1.3 VERTICAL FORCE

Figure 7.66 to Figure 7.69 show a comparison of the vertical forces estimated by the UTFE and the nonlinear RT tire model in CarMaker during the braking mu-split maneuver. As with the previous three cases, the vertical force estimation tracks the RT model the most precisely of the three modules of the UTFE. There is a small deviation between the two forces at the rear axle. Deviations like this are difficult to avoid at the handling limits because there is a marked difference in the dynamics of the vehicle when it is slipping. Accurate tracking of the forces at the limit requires a more sophisticated model in the Kalman filters. The filters still estimate the vertical forces very well for all four wheels despite this.

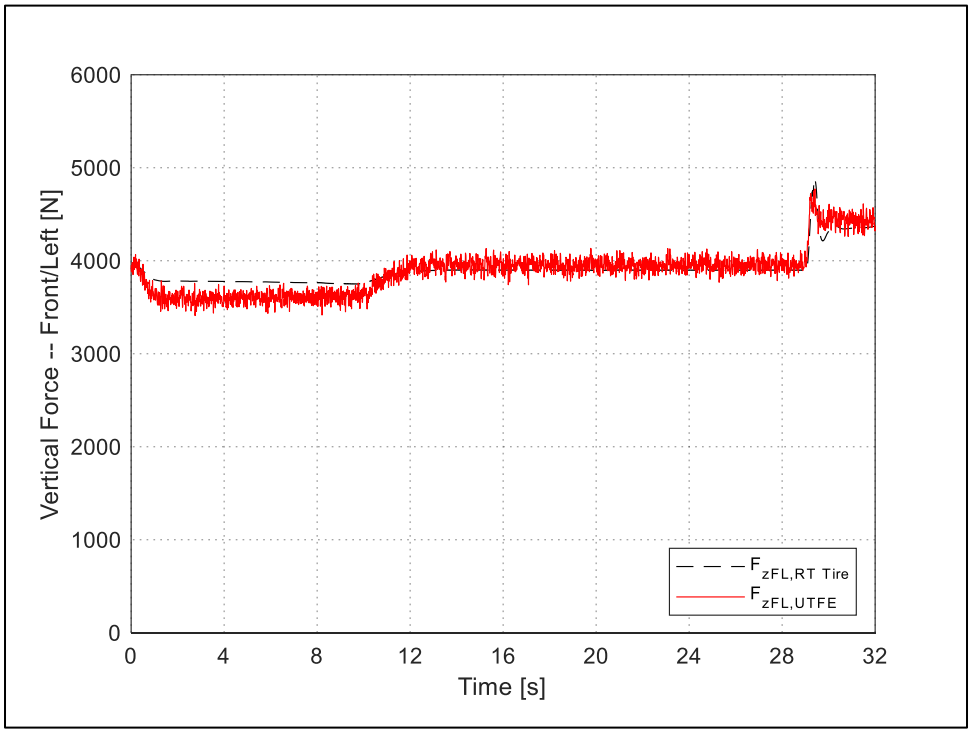

Figure 7.66 Comparison of the vertical force estimate and nonlinear model on the left front tire for a braking mu-split test where u = 100 km/h when the left tires hit a slick with μ = 0.5 at t = 29 s.

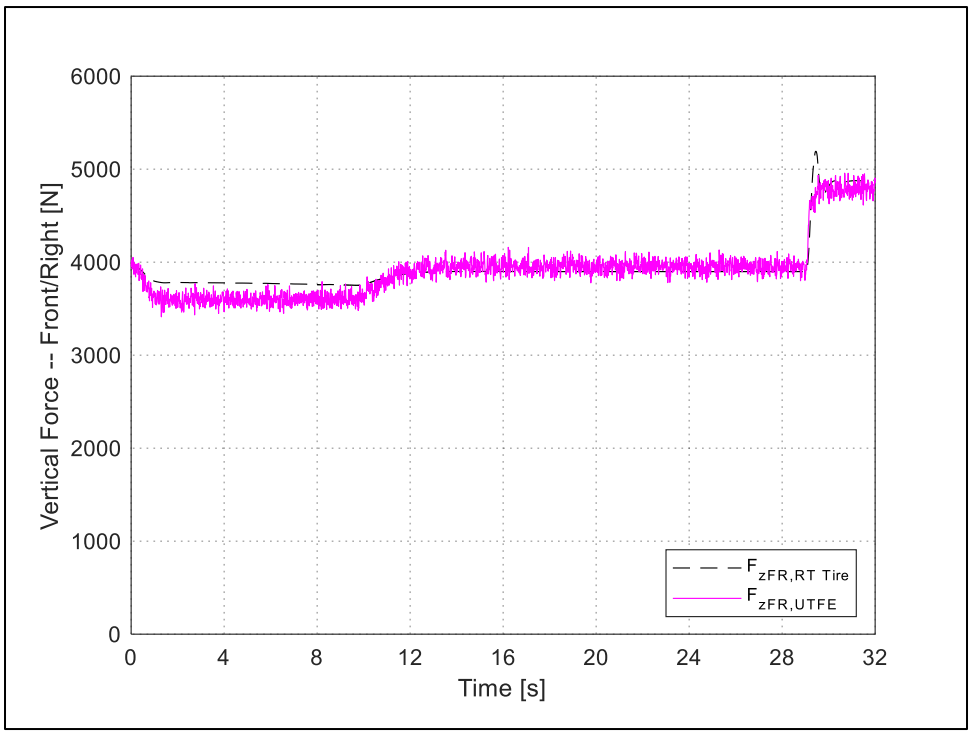

Figure 7.67 Comparison of the vertical force estimate and nonlinear model on the right front tire for a braking mu-split test where u = 100 km/h when the left tires hit a slick with μ = 0.5 at t = 29 s.

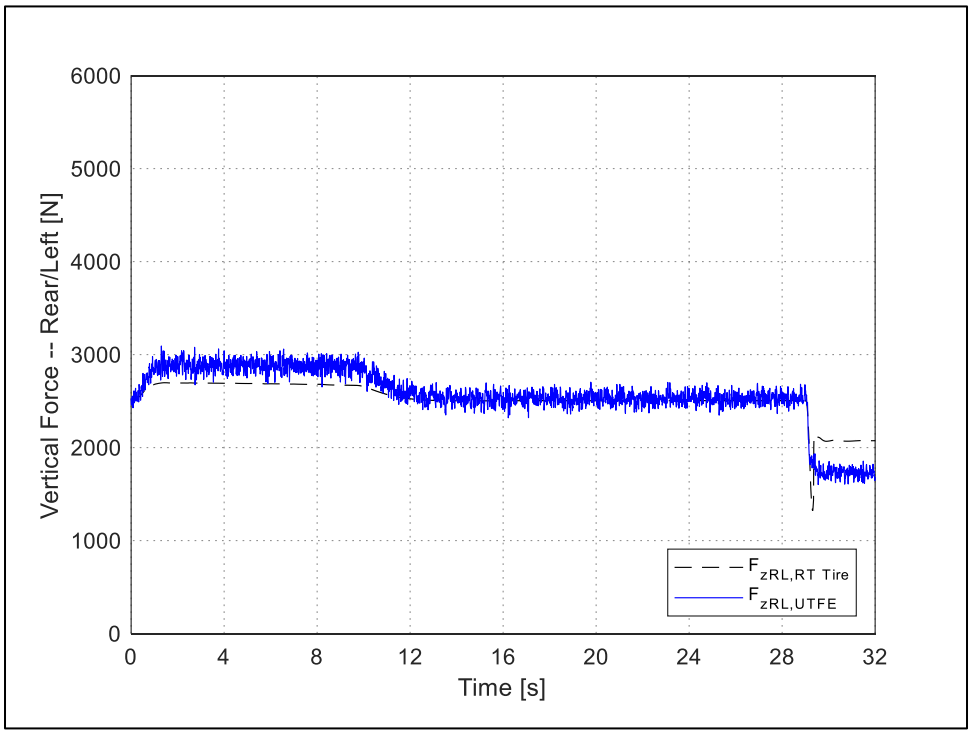

Figure 7.68 Comparison of the vertical force estimate and nonlinear model on the left rear tire for a braking mu-split test where u = 100 km/h when the left tires hit a slick with μ = 0.5 at t = 29 s.

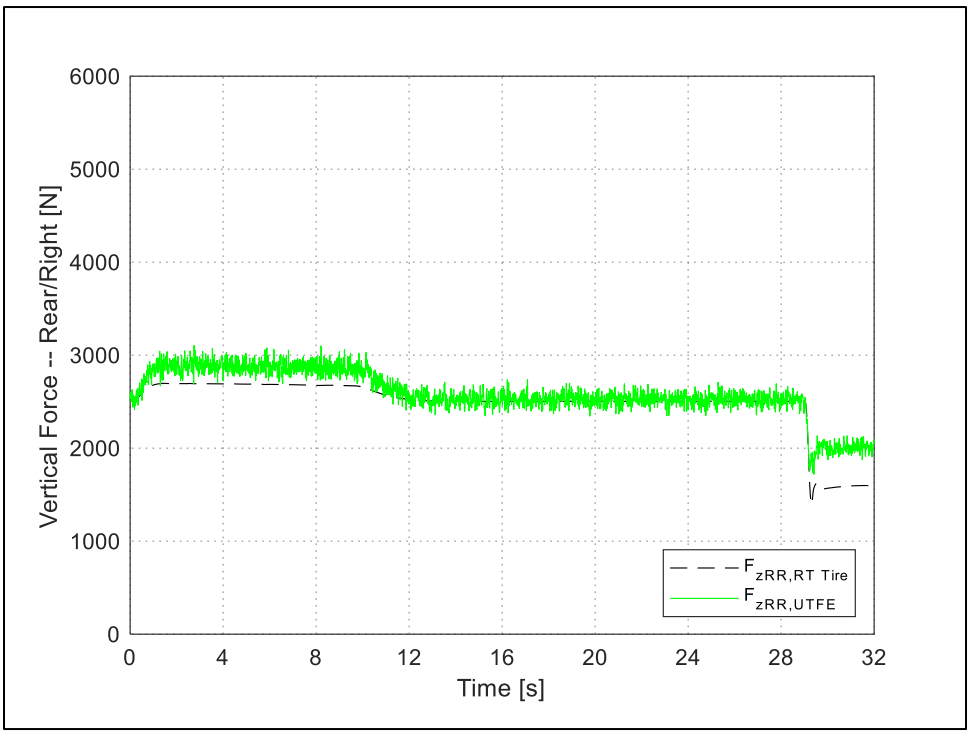

Figure 7.69 Comparison of the vertical force estimate and nonlinear model on the right rear tire for a braking mu-split test where u = 100 km/h when the left tires hit a slick with μ = 0.5 at t = 29 s.

8 CONCLUSION AND RECOMMENDATIONS

8.1 CONCLUSIONS

The initial motivation of this study was to show the usefulness and viability of all-wheel drive torque vectoring control (TVC) for powertrain control of an electric vehicle with four independent hub-motors. In the past, powertrain control has largely been limited by mechanical components such as the mechanical differential. Differentials allowed the wheels on a single axle to rotate at different speeds, but both wheels would receive the same torque. Sophisticated active differentials exist today, which allow torque splitting, such as the limited slip differential, but these are highly complex mechanical systems with many moving parts. Research on TVC goes back decades—it is nothing new. However, the focus of TVC implementation has remained primarily in the mechanical world. The viability of electric vehicles and availability of high quality, efficient motors have encouraged researchers to develop new algorithms specific to torque vectoring of electric vehicles. These algorithms leverage the fact that a vehicle with four independently controlled motors and front wheel steering can simultaneously achieve optimal longitudinal and lateral control tasks.

In the pursuit of a viable torque-vectoring control system, a comprehensive and modular framework for implementation of a direct yaw moment control (DYC) arose. DYC systems produce a corrective yaw moment in a high-level controller to enhance vehicle handling and safety by means of a torque allocation generated by the torque vectoring low-level controller, which individually varies the longitudinal tire forces, in either braking or traction. In accomplishing this task, three approaches to direct yaw moment control for the simultaneous control of vehicle yaw rate and sideslip angle. These approaches for the high-level control module include a conventional sliding mode controller employing a linear combination of the yaw rate and sideslip angle errors as the switching function; a hybrid sliding mode controller employing the same switching function as the conventional sliding mode controller and with integral control replacing force-feedback from a unified tire force estimator and; a modified sliding mode controller employing a linear combination of the normalized absolute values of the yaw rate and sideslip error as the switching function [11]. The dynamic terms of the sliding mode controller and the basis of the unscented Kalman filter constituting the lateral tire force estimator employ the nonlinear eight degree of freedom vehicle model developed in Chapter 3. The cost function and gradient descent algorithm derived in Chapter 5 constitute the low-level TVC takes the output of the sliding mode controller and computes an appropriate optimal torque distribution among the four electric motors on the vehicle using a cost function, which minimizes power loss due to tire slippage. Lastly, the tire force estimation framework laid out in Chapter 4 takes the states of the vehicle system and computes an estimate of twelve tire forces. This estimation framework includes

the wheel equation of motion derived in Chapter 3, one Kalman filter, one extended Kalman filter and one unscented Kalman filter.

The open loop simulation of the TVC demonstrated promising results using the longitudinal slip power loss cost function. For the set of parameters used in this study, the optimization quickly and reliably found an optimal solution and was stable for all simulated maneuvers.

Simulations of four driving maneuvers showed relative effectiveness of the three DYC systems. Simulated J-turn, sine steer, skid pad and braking mu-split maneuvers challenged the control systems in unique ways to draw out specific results. Each maneuver employed either controlled steering angle, velocity, acceleration, or some combination of the three. The simulations demonstrate that the DYC system with the modified switching function outperformed the other two systems in simultaneously achieving neutral steer and driving down the sideslip angle as well as having some traction control functionality.

The Unified Tire Force Estimator demonstrated mixed results. The vertical force estimator consistently tracked the RT model very well, even for intense maneuvers. The longitudinal force estimator performed well when the tires are not operating at their limits and the brakes are not applied. The lateral force estimator performed inconsistently at best, but this is due to the high degree of nonlinearity of the lateral tire force and the difficulty of tuning the unscented Kalman filter constituting this estimator. Although the Unified Tire Force Estimator did not perform as well as hoped in the scope of this study, there is no doubt it that could be improved with minor changes.

8.2 RECOMMENDATIONS

The direct yaw moment controller developed and successfully implemented in this thesis provide a good foundation for understanding control strategies that enhance a vehicle's handling and stability up to its operational limits while satisfying multiple control objectives. It also provides a solid framework for real-time estimation of tire forces. From this foundation, there are several directions for future projects.

8.2.1 IMPLEMENTATION ON THE CAL POLY SSIV

Although the simulator used to validate the direct yaw moment control system is a good representation of reality, it cannot account for all variables and challenges in operating such a system in the real world. Cal Poly's Small-Scale Intelligent Vehicle Platform (SSIV) is a $1/10^{th}$ scale car equipped with the microcontroller unit, sensors, and powertrain which would be necessary to port all components included in this thesis and run it in real-time. The system depends on a set of measured or

approximated physical for the control system to perform optimally. A follow up task to implementing the system in hardware could be to run experiments to determine these parameters.

8.2.2 REFINEMENT OF THE UNIFIED TIRE FORCE ESTIMATOR

This thesis derived the estimator with certain assumptions built in which limit its performance, which include but are not limited to neglecting the braking torque and rolling resistance in the longitudinal force estimator and making very rough estimates of the physical, vehicle-specific parameters related to the lateral and vertical estimation processes. Refinement in tuning the process and measurement covariance matrices of the UKF of the lateral force estimator and the EKF of the vertical force estimator would yield better force tracking. Tuning the parameters α, β and κ of the UT would improve the filter's ability to deal with function nonlinearity.

The UKF Filter in the Unified Tire Force Estimator has the capacity to estimate the vehicle sideslip angle. It is essential to estimate the sideslip angle to perform simultaneous control of the yaw rate error and sideslip angle error because it is very difficult to measure this quantity. It currently functions decently but would be improved by the tuning methods discussed above.

8.2.3 EXPERIMENT WITH NEW COST FUNCTIONS

The longitudinal slip power loss cost function is just one of many cost functions, which might work well for the purpose of optimal torque-vectoring control. It would be an interesting area of future research to find and run simulations or experiments on the control system with different cost functions or different optimization algorithms. A good starting place to research compatible cost functions would be in [17].

9 APPENDIX

9.1 DIRECT YAW MOMENT CONTROL

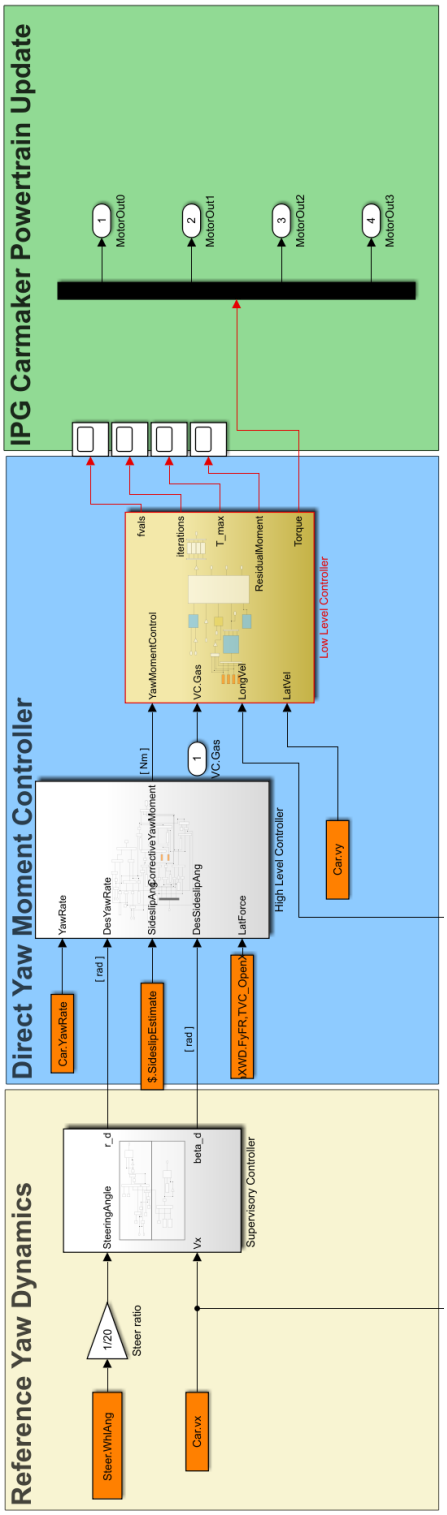

9.1.1 SUPERVISORY CONTROLLER (K=0)

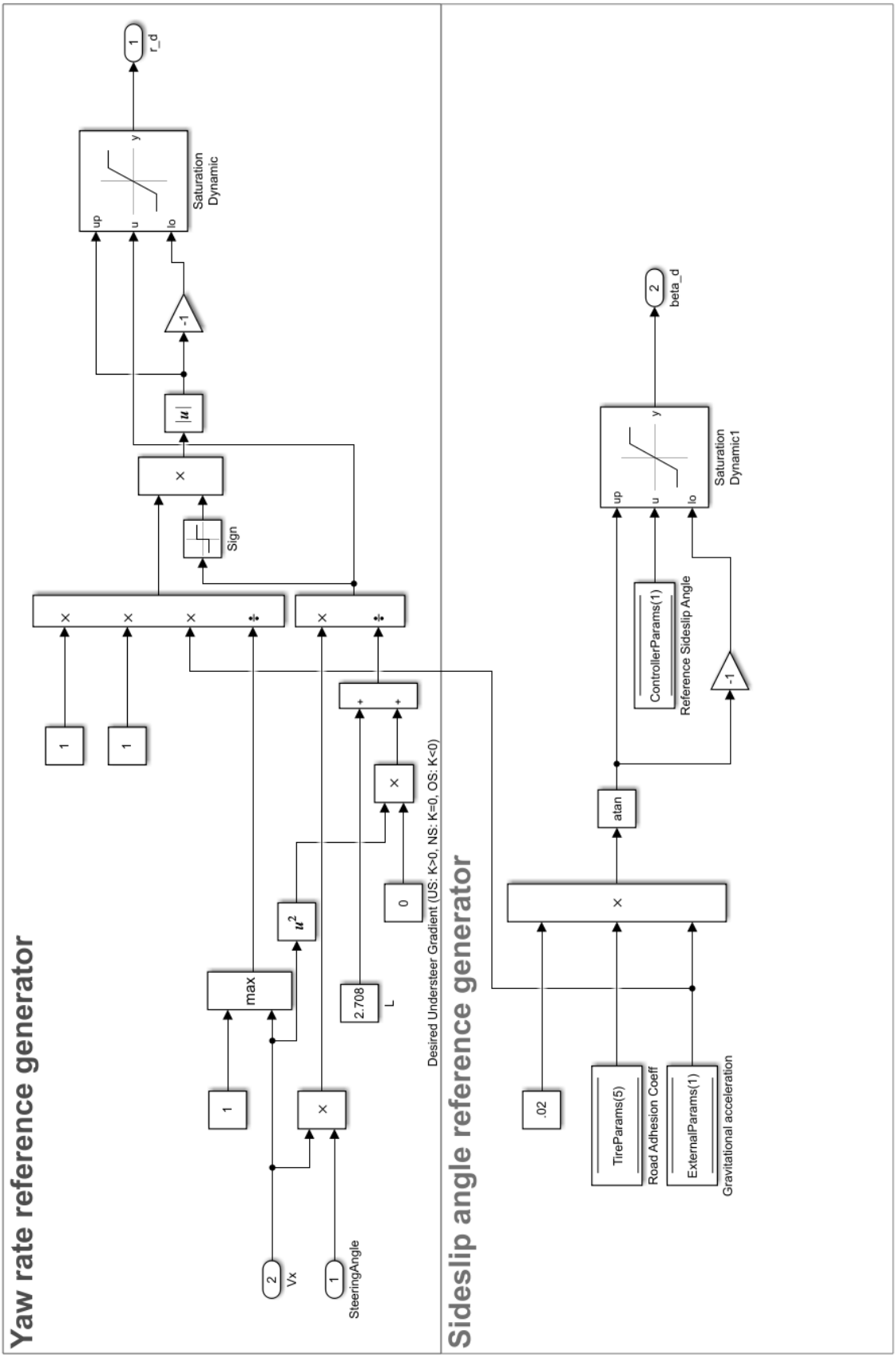

9.1.2 CONVENTIONAL SLIDING MODE CONTROLLER

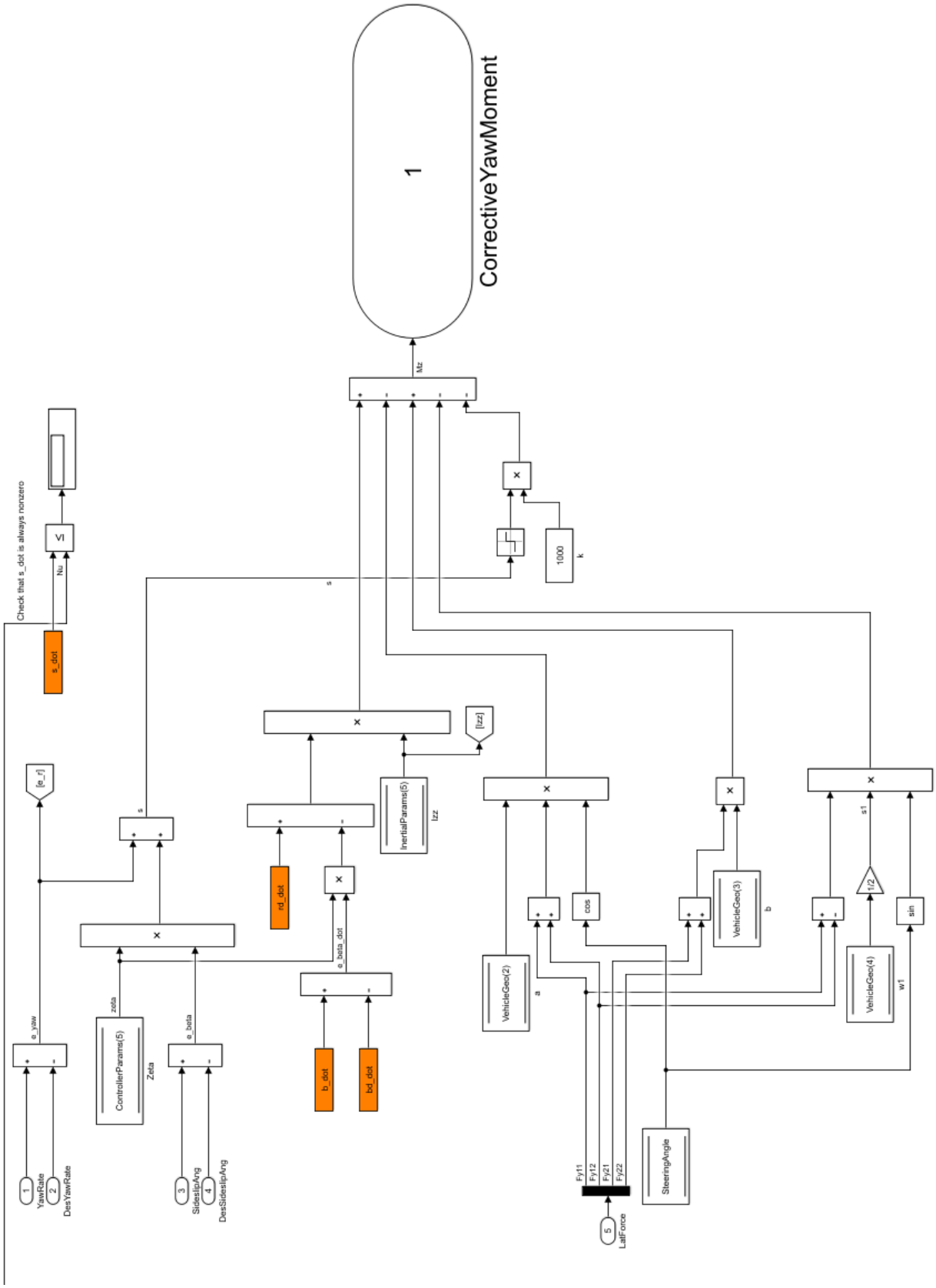

9.1.3 MODIFIED SLIDING MODE CONTROLLER

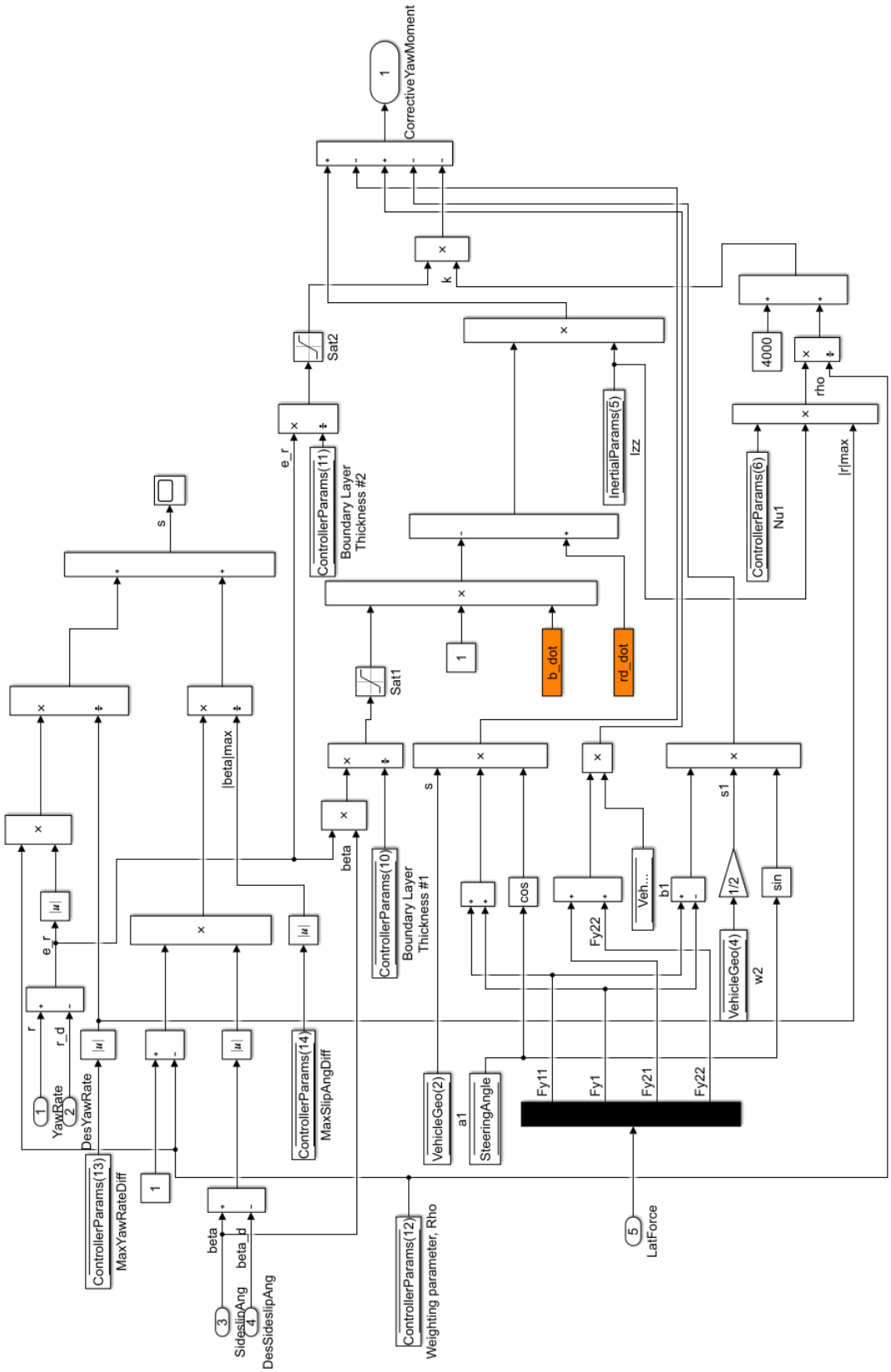

9.1.4 PRIMAL-DUAL GRADIENT DESCENT

```
function [moto_torque, fval, iter, ResidualMoment] =...
    DualPrimalGradientDescent(V_wx, M_des, T_base, T_max, B_TV)

% This function solves a constrained optimization problem for optimal
% torque allocation which satisfies the yaw moment control signal
% Cost function: longitudinal slip power loss
% Method: Lagrangian algorithm
% Reference: Wei-Ta Chu, "Algorithms for Constrained Optimization"

%% Call Global Variables

global TireParams VehicleGeo GDParams

% Axle cornering stiffness
C_lf = TireParams(3);
C_lr = TireParams(4);

R    = VehicleGeo(8);

% Primal-dual parameters
alpha = GDParams(1);
kappa = GDParams(2);
gamma = GDParams(3);

% Optimization parameters
max_iter = GDParams(4);
func_tol = GDParams(5);

% Wheel longitudinal velocity in heading direction
V_wx_1 = V_wx(1);
V_wx_2 = V_wx(2);
V_wx_3 = V_wx(3);
V_wx_4 = V_wx(4);

% Tire longitudinal stiffness
C_l1 = C_lf;
C_l2 = C_lf;
C_l3 = C_lr;
C_l4 = C_lr;

% Torque constraint
T_min = - T_max;

% Initialize A,c,x

x    = [ 0, 0, 0, 0 ]';              % Initial torque guess
A    = B_TV;                    % Dynamic constraint coefficient matrix
c    = [ M_des, T_base / R ]';  % Vector of dynamic constraints

%% Longitudinal Slip Power Loss Cost Function Derivation

D    = [ V_wx_1 / (R ^ 2 * C_l1), 0, 0, 0;
         0, V_wx_2 / (R ^ 2 * C_l2), 0, 0;
         0, 0, V_wx_3 / (R ^ 2 * C_l3), 0;
```

```
          0, 0, 0, V_wx_4 / (R ^ 2 * C_l4) ];

% Function F(x) to minimize for LSPL
F  = @(x) x' * D * x;  % Cost function
dF = @(x) 2 * D * x;   % Cost function gradient

% fvals       = zeros(max_iter, 1); % store F(x) values across iterations

% Iterate
lambda      = [ 0, 0 ]';            % Initial guess for equality...
                                    % ...Lagrange multipliers
mu_1        = [ 0, 0, 0, 0 ]';      % Initial guess for inequality...
                                    % ...Lagrange multiplier #1 update
mu_2        = [ 0, 0, 0, 0 ]';      % Initial guess for inequality...
                                    % ...Lagrange multiplier #2 update
iter        = 1;                    % Iterations counter
fval        = 1;                    % Function cost
step        = [ 10, 10, 10, 10 ]';  % Initialize step larger than func_tol
% fvals(iter) = F(x);
```

```
%% Run Primal-Dual Gradient Descent in Iterative Loop
```

```
while iter < max_iter && any(abs(step) > func_tol)
    iter        = iter + 1;
    current_x   = x;
    lambda      = lambda + kappa * (A * current_x - c);
    mu_1        = max(mu_1 + gamma * (T_min - current_x), [ 0, 0, 0, 0 ]');
    mu_2        = max(mu_2 + gamma * (current_x - T_max), [ 0, 0, 0, 0 ]');
%     fvals(iter) = F(current_x);
    x           = current_x + alpha * (-dF(current_x) - A' * lambda + ...
                  mu_1 - mu_2);
    step        = x - current_x;
end
```

```
% Output dynamic constraint error, torque allocation and cost
```

```
ResidualMoment = A * x - c;
moto_torque    = x;
% fval           = fvals(iter);
```

9.1.5 TORQUE-VECTORING CONTROLLER

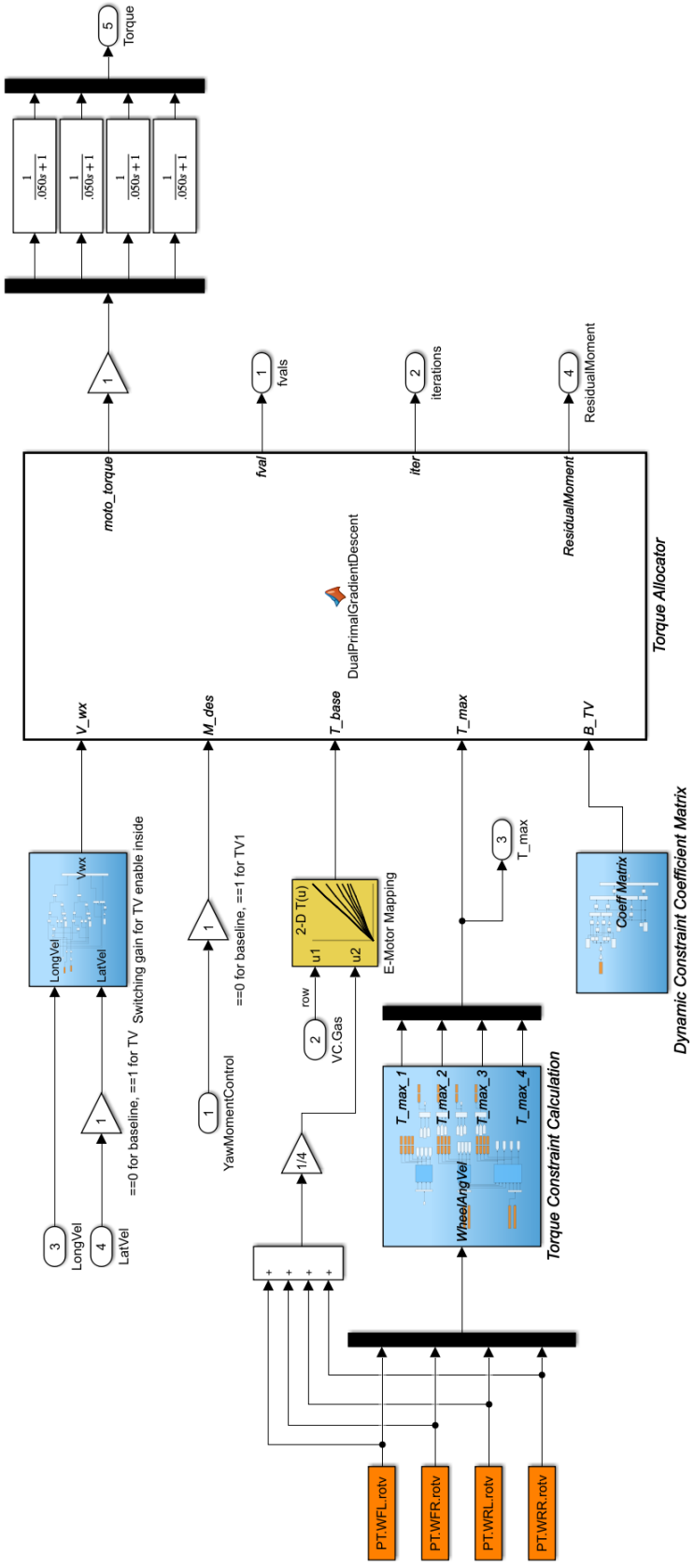

9.1.6 WHEEL SYSTEM LONGITUDINAL VELOCITY

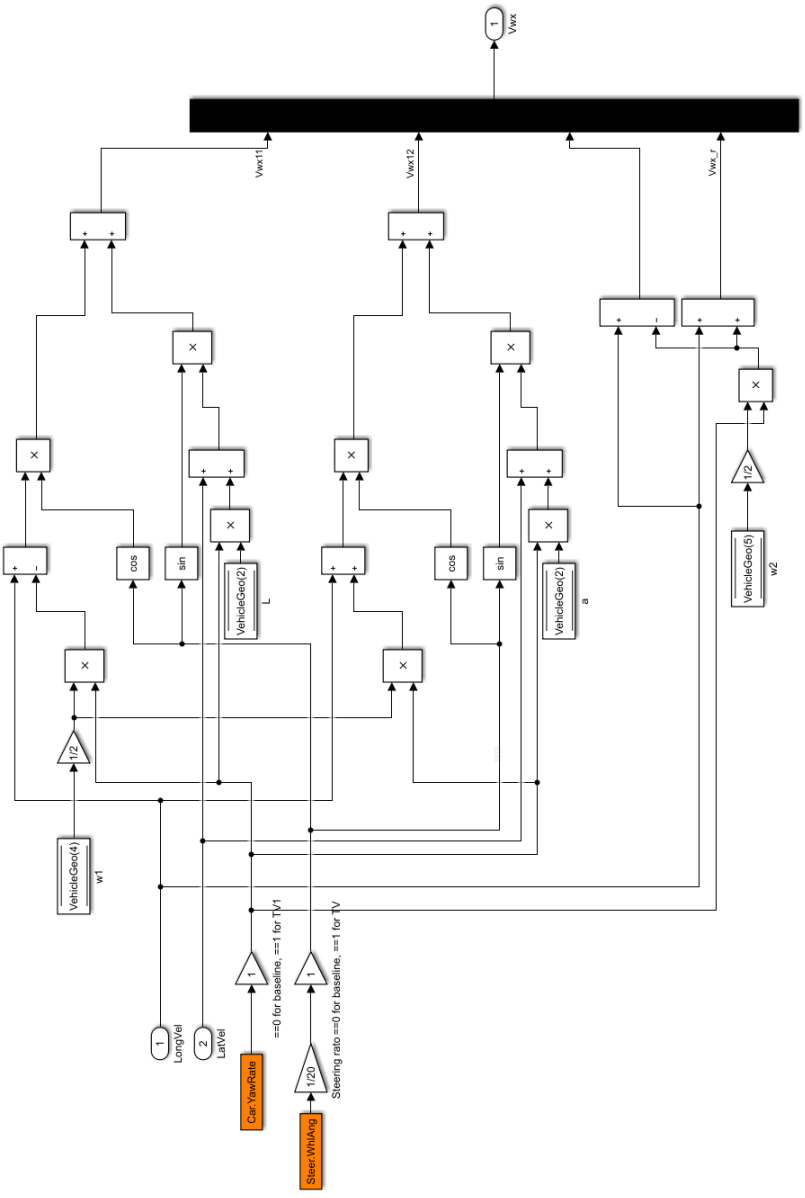

9.1.7 TORQUE CONSTRAINTS (LEVEL 1)

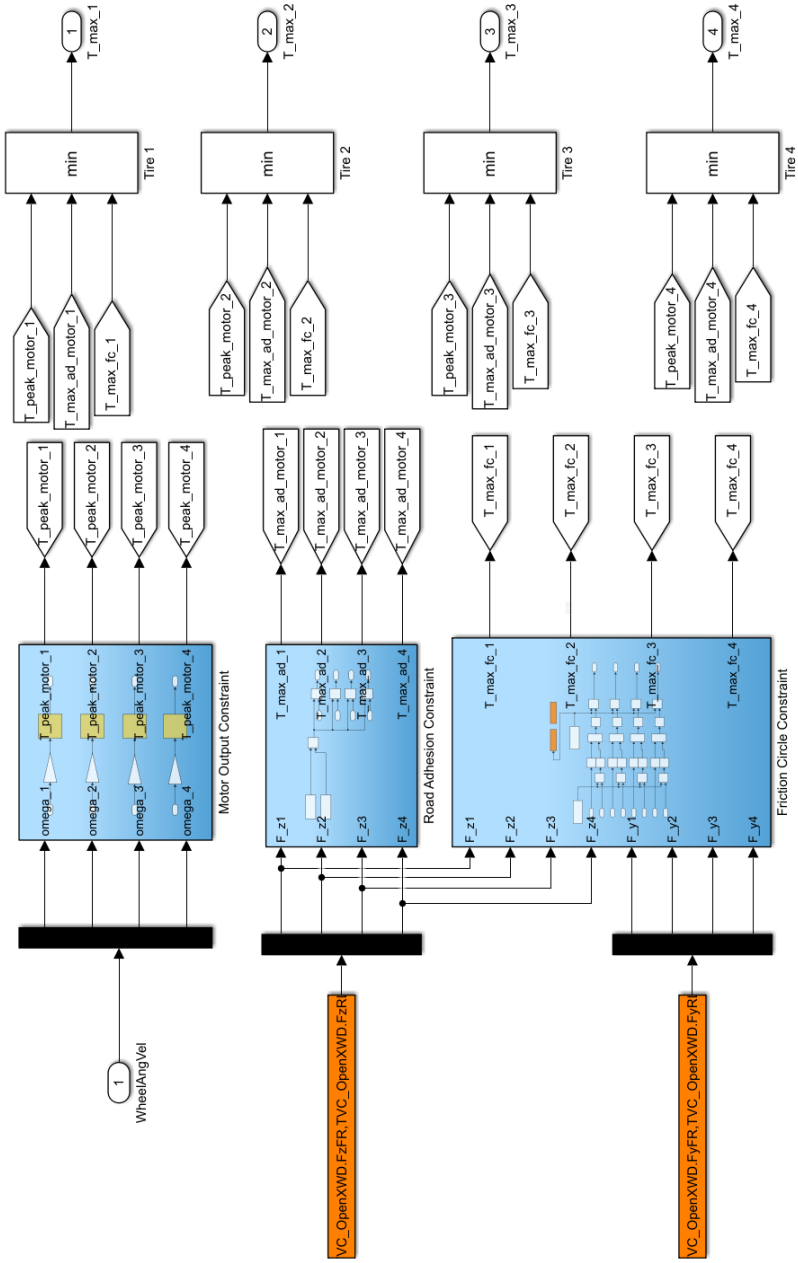

9.1.8 TORQUE CONSTRAINTS--MOTOR (LEVEL 2)

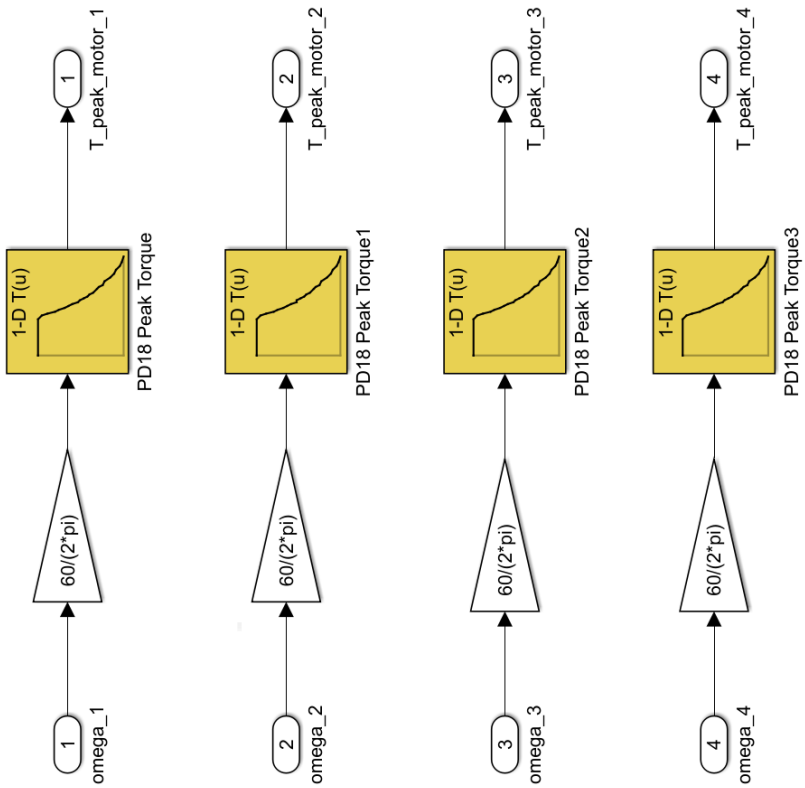

9.1.9 TORQUE CONSTRAINTS—ROAD ADHESION (LEVEL 2)

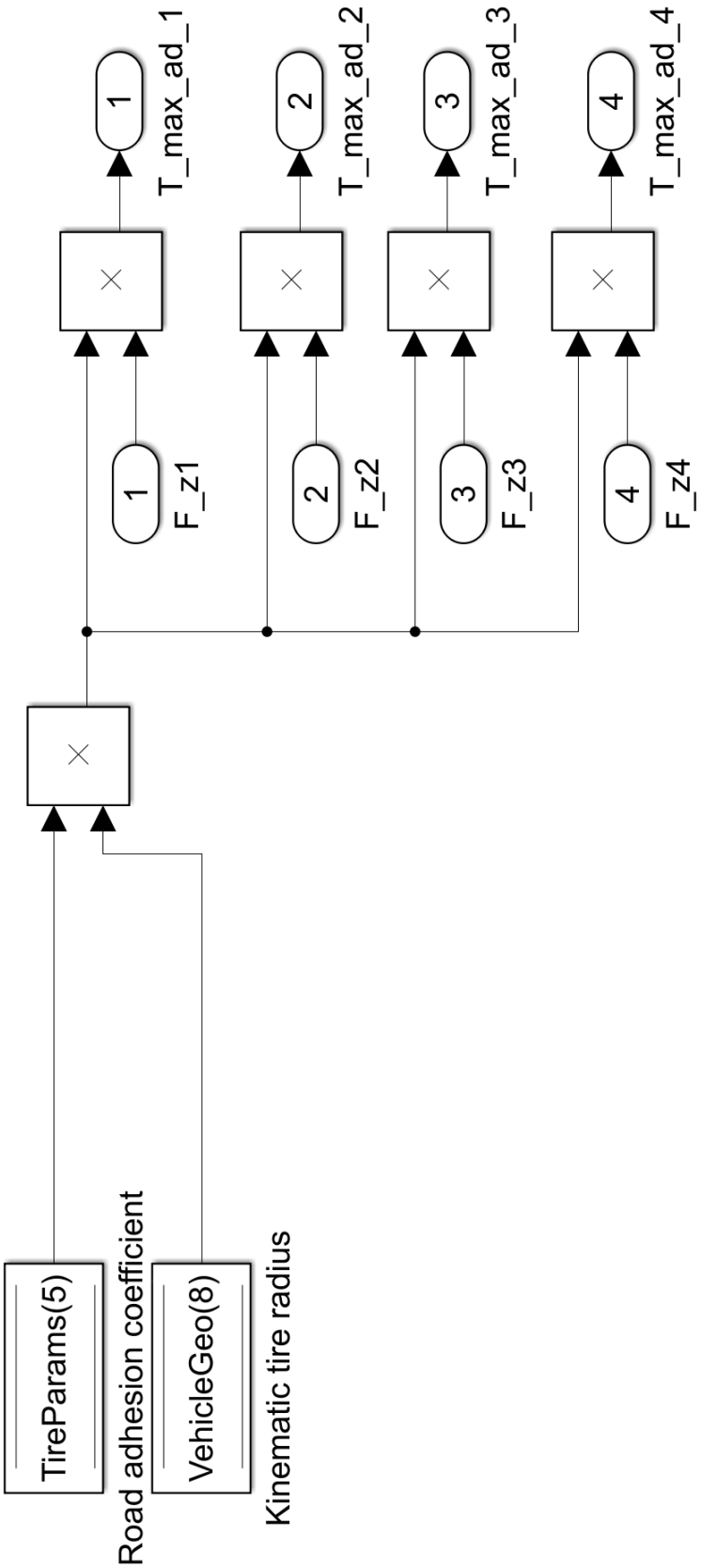

9.1.10 TORQUE CONSTRAINTS—FRICTION CIRCLE (LEVEL 2)

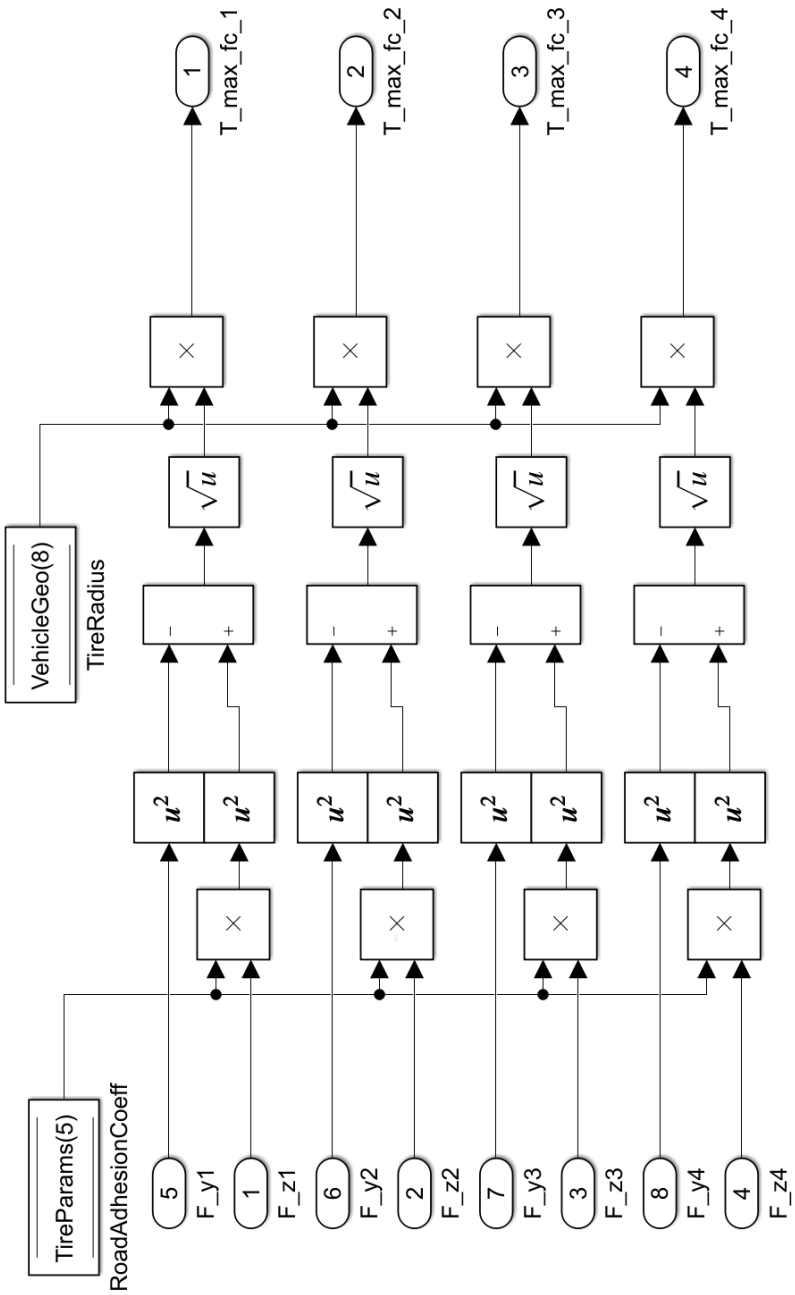

9.1.11 DYNAMIC CONSTRAINT MATRIX

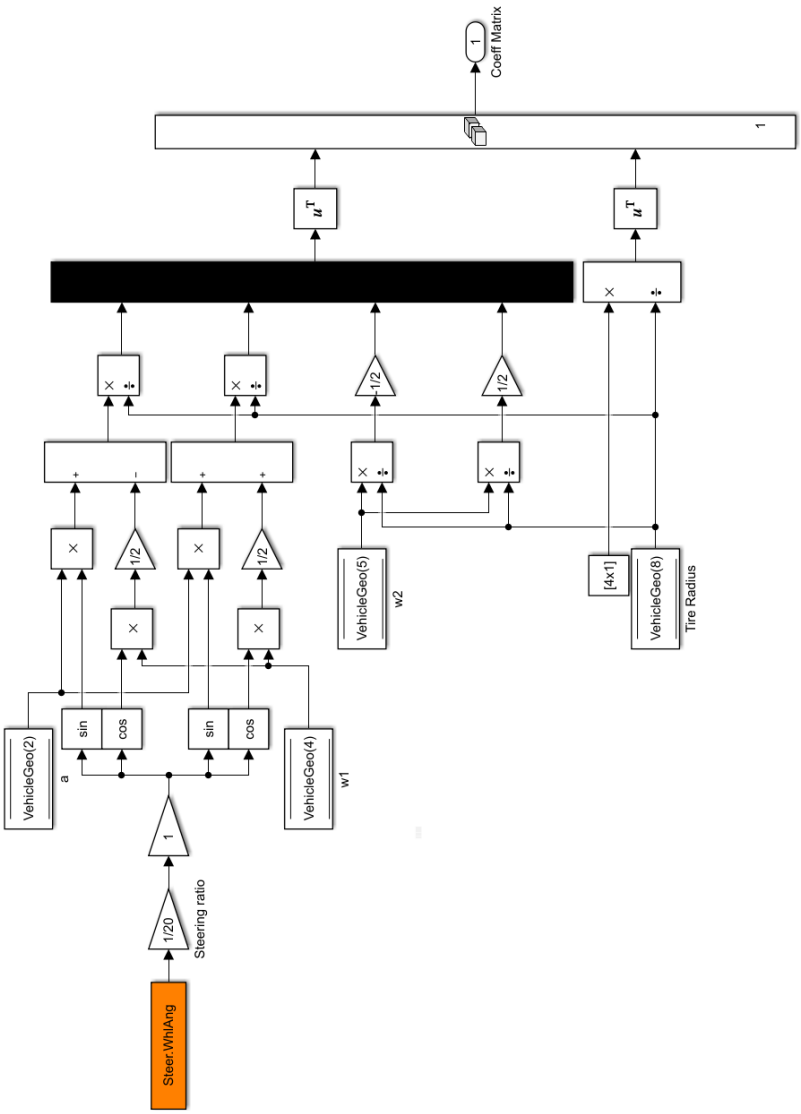

9.2 UNIFIED TIRE FORCE ESTIMATOR

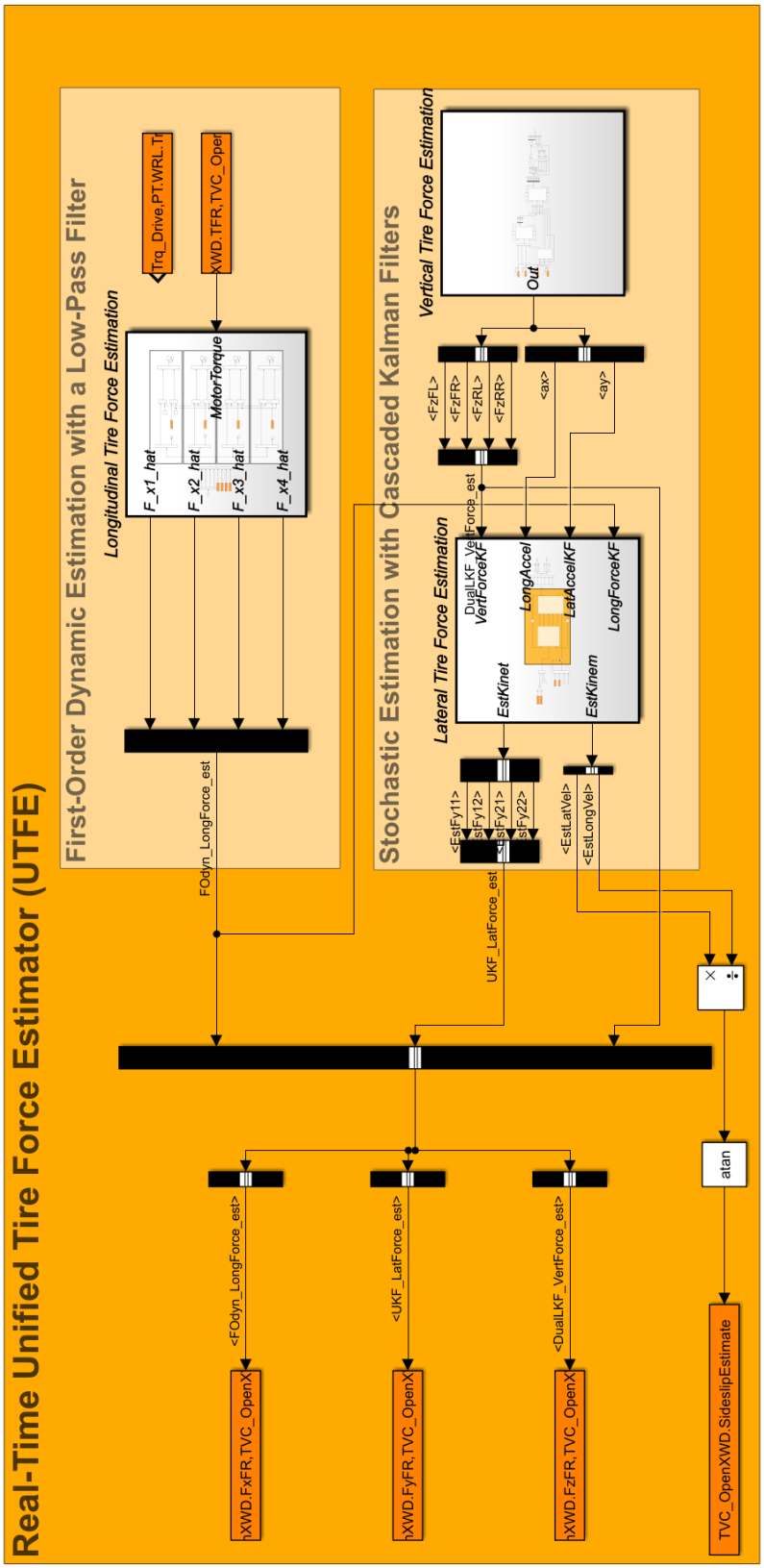

9.2.1 LONGITUDINAL TIRE FORCE ESTIMATOR BLOCK WITH I/O

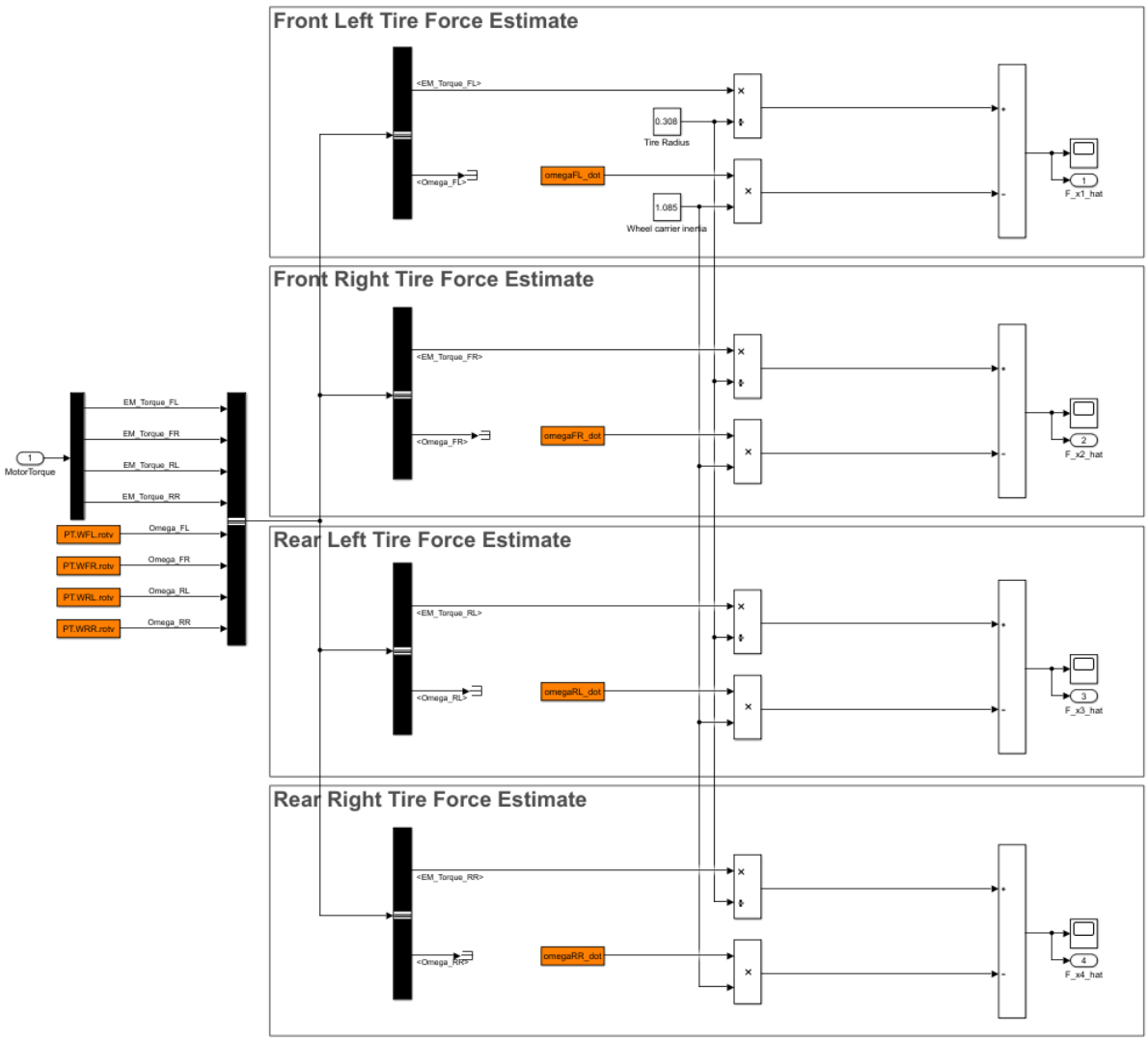

9.2.2 LATERAL TIRE FORCE ESTIMATION

9.2.2.1 UKF ESTIMATION STEP

```
function [EstState,EstCovar]=UKFEstLatForce(PredState,PredCovar,PredOut,...
    KalmanGain, Pz_P, Msrmnt)

% Compute Estimate
EstState=PredState+KalmanGain*(Msrmnt-PredOut);

% Compute error covariance
EstCovar=PredCovar-KalmanGain*Pz_P*KalmanGain';

end
```

9.2.2.2 UKF PREDICTION STEP

```
function [X_P, P_P, Z_P, Kk, Pz_P] = UKFPredictLatForce(EstState,Input,EstCovar)
```

```
% Unscented Kalman Filter to predict the lateral tire force of each tire on a vehicle as well
as the sideslip angle.
```

- States -- [r,u,v,FyFL,FyFR,FyRL,FyRR]'
- Inputs -- [steer,FzFL,FzFR,FzRL,FzRR,FxFL,FxFR,FxRL,FxRR]'

```
m  = 1321;      %Total mass of vehicle [kg]
Iz = 2083.5;    %Mass moment of inertia about vehicle z-axis [kg-m^2]
a  = 1.056;     %Distance from front axle to center of gravity [m]
b  = 1.652;     %Distance from rear axle to center of gravity [m]
w1 = 1.500;     %Front track width [m]
w2 = 1.498;     %Rear track width [m]

C_af = 80000;   %Tuned front tire cornering stiffness [N/rad]
C_ar = 80000;   %Tuned rear tire cornering stiffness [N/rad]
mu = 1.0;       %Assumed tire-road friction coefficient [-]
RlxLen1 = 0.05; %Relaxation length of front tires [m]
RlxLen2 = 0.05; %Relaxation length of rear tires [m]

T  = 0.001;     %Sample rate [s]
```

```
% Process Covariance
```

```
Q1 = 1e-3;      %Process yaw rate covar
Q2 = 1e-2;      %...   long. velocity covar
Q3 = 1e-1;      %...   lat. velocity covar
Q4 = 1e2;       %...   FyFL covar
Q5 = 1e2;       %...   FyFR covar
Q6 = 1e2;       %...   FyRL covar
Q7 = 1e2;       %...   FyRR covar
Q_v = [Q1 Q2 Q3 Q4 Q5 Q6 Q7];
Q = diag(Q_v,0);   % Make diagonal matrix
```

```
% Measurement Covariance
R1 = 5e-2;      %Measurement yaw rate covar
R2 = 1e-1;      %... long. velocity covar
R3 = 1e-2;      %... long. acceleration covar
R4 = 1e-2;      %... lat. acceleration covar
R_v = [R1 R2 R3 R4];
R = diag(R_v,0);   % Make diagonal matrix
```

```
alpha = .9;     % 1e-4 <= alpha <= 1
beta  = 2;      % 2 is optimal for Gaussian dist.
k     = 0;
```

```
%% Nonlinear Vehicle Model
```

```
% Tire slip angle
ALF = @(X, U) [U(1) - atan((X(3,:) + a * X(1,:)) ./ (X(2,:)-w1/2*X(1,:)));
               U(1) - atan((X(3,:) + a * X(1,:)) ./ (X(2,:)+w1/2*X(1,:)));
                    - atan((X(3,:) - b * X(1,:)) ./ (X(2,:)-w2/2*X(1,:)));
                      atan((X(3,:) + b * X(1,:)) ./ (X(2,:)+w2/2*X(1,:)))];


% Dynamic Dugoff, Tau --- see Chapter 3.3
TAU = @(ALF, U) [mu * U(2) / 2 / C_af ./ abs(tan(ALF(1,:)));
                 mu * U(3) / 2 / C_af ./ abs(tan(ALF(2,:)));
                 mu * U(4) / 2 / C_ar ./ abs(tan(ALF(3,:)));
                 mu * U(5) / 2 / C_ar ./ abs(tan(ALF(4,:)))];

% Simplified Dugoff Tire Force
F_y_bar = @(ALF, f_LAM) [-C_af * tan(ALF(1,:)) .* f_LAM(1,:);
                         -C_af * tan(ALF(2,:)) .* f_LAM(2,:);
                         -C_ar * tan(ALF(2,:)) .* f_LAM(3,:);
                         -C_ar * tan(ALF(2,:)) .* f_LAM(4,:)];

% Nonlinear State Evolution Function (Vehicle EOMs)
f = @(X, U, F_y_bar) [X(1,:) + T / Iz * (a * (X(4,:) + X(5,:)) * cos(U(1))...
     + (U(6)+U(7)) * sin(U(1)) - b * (X(6,:) + X(7,:)) + w1 / 2 *...
     ((X(4,:)- X(5,:)) * sin(U(1)) + (U(7)-U(6)) * cos(U(1))));
```

```
     X(2,:) + T / m * (-(U(6)+U(7)) * cos(U(1)) -...
     (X(4,:) + X(5,:)) * sin(U(1)))+ T * X(1,:) .* X(3,:);
```

```
     X(3,:) - T * X(1,:) .* X(2,:) + T / m * ((U(6)+U(7)) * sin(U(1)) +...
     (X(4,:) + X(5,:)) * cos(U(1)) + X(6,:) + X(7,:));
```

```
     X(4,:) + T * X(2,:) / RlxLen1 .* (-X(4,:) + F_y_bar(1,:));
```

```
     X(5,:) + T * X(2,:) / RlxLen1 .* (-X(5,:) + F_y_bar(2,:));
```

```
     X(6,:) + T * X(2,:) / RlxLen2 .* (-X(6,:) + F_y_bar(3,:));
```

```
     X(7,:) + T * X(2,:) / RlxLen2 .* (-X(7,:) + F_y_bar(4,:))];
```

```
h = @(X,U) [X(1,:);
            X(2,:);
            1 / m * (-(X(4,:) + X(5,:)) * sin(U(1)) + (U(6)+U(7)) * cos(U(1)));
            1 / m * ((X(4,:) + X(5,:)) * cos(U(1)) + X(6,:) + X(7,:) + ...
            (U(6)+U(7)) * sin(U(1)))];

% Init UKF Parameters
L=length(EstState);
chi_E = zeros(L,2*L+1);
W_m   = zeros(1,2*L+1);
W_c   = zeros(1,2*L+1);
lambda=alpha^2*(L+k)-L;

% Init Dugoff Matrix
f_lt = zeros(4,2*L+1);
```

```
% Computation of Sigma Points and Corresponding Mean and Covariance Weights
```

```
chi_E(:,1)=EstState;                          % Sigma point
W_m(1)=lambda/(L+lambda);                     % Mean weight
W_c(1)=lambda/(L+lambda)+(1-alpha^2+beta);    % Covar weight
A = chol(EstCovar);                           % Cholesky Inverse of Pxx

% Sigma points 1-->L
for ii=1:L
    temp=((L+lambda))^0.5*A;
    chi_E(:,ii+1)=EstState+temp(ii,:)';
    W_m(ii+1)=1/(2*(L+lambda));
    W_c(ii+1)=1/(2*(L+lambda));
end

% Sigma points (L-1)-->(2L)
for ii=L+1:2*L
    temp=((L+lambda))^0.5*A;
    chi_E(:,ii+1)=EstState-temp(ii-L,:)';
    W_m(ii+1)=1/(2*(L+lambda));
    W_c(ii+1)=1/(2*(L+lambda));
end
```

```
%% Propagate 2n+1 [nx1] Sigma Points (chi) through nonlinear model
```

```
slip = ALF(chi_E, Input);
tau_tire = TAU(slip, Input);
for i = 1:4
    for j = 1:(2*L+1)
        if tau_tire(i,j) < 1
            f_lt(i,j) = (2-tau_tire(i,j))*tau_tire(i,j);
        else
            f_lt(i,j) = 1;
        end
    end
end

% Compute Dugoff Model lateral force
F_y_qs = F_y_bar(slip, f_lt);
```

```
% Compute transformed process/measurement sigma points
chi_P=f(chi_E, Input, F_y_qs);
zed_P = h(chi_E, Input);
```

```
%% Compute mean and Covariance for Sigma Points
```

```
P_P=Q;
X_P=chi_P*W_m';
for ii=1:2*L+1
    P_P=P_P+W_c(ii)*(chi_P(:,ii)-X_P)*(chi_P(:,ii)-X_P)';
end

Pz_P=R;
Z_P=zed_P*W_m';
for ii=1:2*L+1
    Pz_P=Pz_P+W_c(ii)*(zed_P(:,ii)-Z_P)*(zed_P(:,ii)-Z_P)';
end

Pxz_P=zeros(7,4);
for ii=1:2*L+1
    Pxz_P=Pxz_P+W_c(ii)*(chi_P(:,ii)-X_P)*(zed_P(:,ii)-Z_P)';
end
```

```
%% Compute Kalman Gain
```

```
Kk=Pxz_P/Pz_P;
```

9.2.2.3 LATERAL FORCE ESTIMATION BLOCK IN SIMULINK WITH I/O

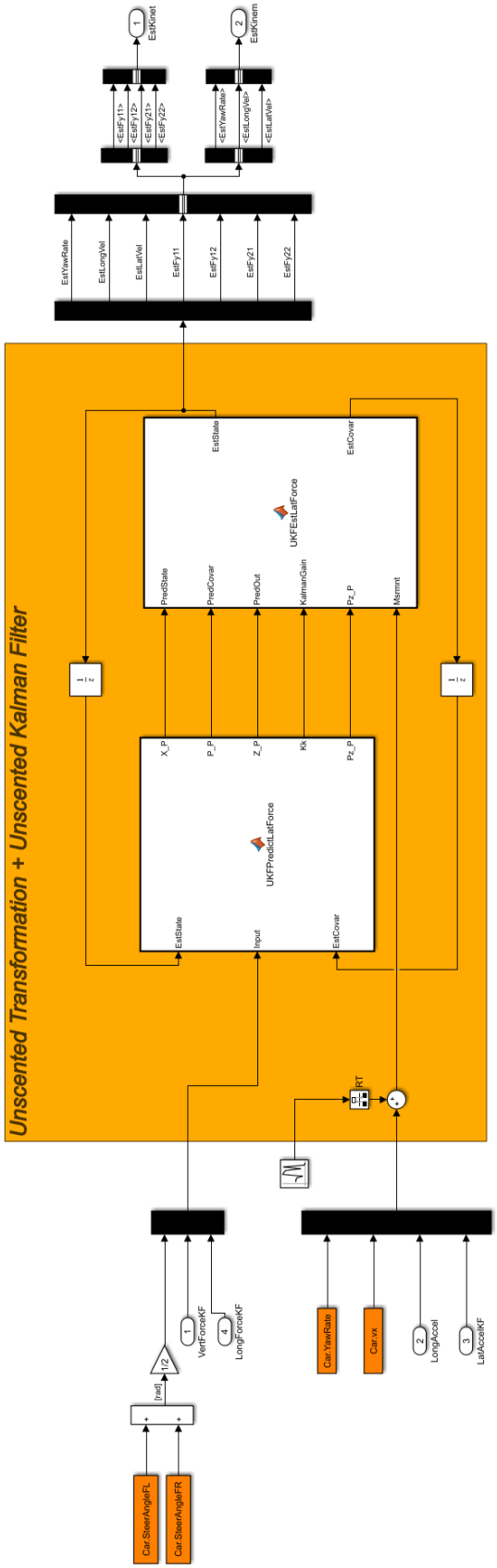

9.2.3 VERTICAL TIRE FORCE ESTIMATION

9.2.3.1 ROLL PLANE AND GEOMETRIC LOAD TRANSFER MODELS

```
function [LLT,sum_Fz11Fz12,Fz_tot]= Sum_Fzf(ax,ay,phi)
%Computation of feedforward, "measurement" quantities for
% Suspension Model Observer and Pitch & Roll Dynamics Observer

m  = 1321;   %Total vehicle mass [kg]
ms = 55*m;   %Sprung mass of vehicle [kg]
L = 2.708;   %Wheelbase [m]
a = 1.056;   %Distance from front axle to center of gravity [m]
b  = 1.652;  %Distance from rear axle to center of gravity [m]
w1 = 1.500;  %Front track width 2*s1 [m]
w2 = 1.498;  %Rear track width 2*s2 [m]
g = 9.81;    %Gravitational acceleration [m/s^2]
hcg = 0.536; %Height of center of gravity [m]
hf = 0.0;    %Front roll center height [m]
hr = 0.05;   %Rear roll center height [m]


kf = 45000;  %Front axle suspension stiffness
kr = .82*kf; %Rear axle suspension stiffness

% Left/right front tire vertical load -- geometric transfer
Fz11 = m/2*(b*g/L-hcg*ax/L)-m*(b*g/L-hcg*ax/L)*hcg*ay/w1/g;
Fz12 = m/2*(b*g/L-hcg*ax/L)+m*(b*g/L-hcg*ax/L)*hcg*ay/w1/g;

% Roll plane model -- elastic transfer
LLT = -2*(kf/w1+kr/w2)*phi-2*ms*ay/L*(b*hf/w1+a*hr/w2);

% Front axle vertical load
sum_Fz11Fz12 = Fz11+Fz12;

% Total vehicle weight
Fz_tot = m*g;
```

9.2.3.2 SUSPENSION MODEL OBSERVER

```
function [x,P] = VertForce_LKF(x,y,P)

% Estimates the lateral load transfer associated with suspension
% dynamics of a vehicle. Random-walk model.

m  = 1321;    %Total vehicle mass [kg]
ms = 0.55*m;  %Sprung mass of vehicle [kg]
hcg = 0.536;  %Height of center of gravity (COG) from the ground [m]
L = 2.708;    %Wheelbase [m]
a = 1.056;    %Distance from front axle to COG [m]
b  = 1.652;   %Distance from rear axle to COG [m]
w1 = 1.500;   %Front track width 2*s1 [m]
w2 = 1.498;   %Rear track width 2*s2 [m]
h1 = 0;       %Front roll center height [m]
```

```
h2 = 0.05;    %Rear roll center height [m]
hs = hcg-(h1+h2)/2;   %Vertical distance from roll axis to COG [m]
kphi1 = 45000;        %Front axle suspension stiffness [N/rad]
kphi2 = .82*kphi1;    %Rear axle suspension stiffness [N/rad]
kphi = kphi1+kphi2;   %Total suspension stiffness [N/rad]
bphi1 = 0;            %Front axle shock damping rate
bphi2 = 0;            %Rear axle shock damping rate
bphi = bphi1+bphi2;   %Total shock damping rate
Ix = 508.7;           %Mass moment of inertia about vehicle x-axis [kg-m^2]
g = 9.81;             %Gravitational acceleration [m/s^2]

T  = 0.001;

% Process Covariance
Q1 = 10^3;     %Process left lateral load transfer Eq. (6.6) covar
Q2 = 0.1;      %... lat. acceleration covar
Q3 = 0.1;      %... lat. d(lat. acceleration)/dt covar
Q4 = 0.1;      %... roll angle covar
Q5 = 0.1;      %... roll rate covar
Q_v = [Q1 Q2 Q3 Q4 Q5];
Q = diag(Q_v,0);   %Make diagonal matrix

% Measurement Covariance
R1 = 0.01;     %Measurement lat. acceleration covar
R2 = 0.01;     %... roll angle covar
R3 = 0.01;     %... roll rate covar
R4 = 10^3;     %... left lateral load transfer covar
R_v = [R1 R2 R3 R4];
R = diag(R_v,0);   %Make diagonal matrix

% State Evolution Matrix
A = [1 0 -2*T*ms/L*(b*h1/w1+a*h2/w2) 0 -2*T*(kphi1/w1+kphi2/w2);
     0 1  T                          0  0;
     0 0  1                          0  0;
     0 0  0                          1  T;
     0 T*ms*hs/Ix 0 T*(ms*g*hs-kphi)/Ix 1-T*bphi/Ix];

% Measurement Matrix
H = [0 1 0 g 0;
     0 0 0 1 0;
     0 0 0 0 1;
     1 0 0 0 0];

% Time update
x = A*x;
P = A*P*A'+Q;

% Measurement update
K = P*H'/(H*P*H'+R);
x = x+K*(y-H*x);
P = (eye(5)-K*H)*P;
```

9.2.3.3 PITCH AND ROLL DYNAMICS OBSERVER

```
function [x,P] = LLT_EKF_p2(x,y,P)

%Extended Kalman Filter for estimating the nonlinear lateral load
% transfer arising from coupled pitch/roll acceleration effects

m  = 1321;   %Total vehicle mass [kg]
hcg = .536;  %Height of the center of gravity (COG) above ground [m]
L = 2.708;   %Wheelbase [m]
b  = 1.652;  %Distance from front axle to COG [m]
w1 = 1.500;  %Distance from rear axle to COG [m]
g = 9.81;    %Gravitational acceleration [m/s^2]

T  = 0.001;  %Sampling rate

% Process Covariance
Q1 = 1e2;    %Process FzFL covar
Q2 = 1e2;    %... FzFR covar
Q3 = 1e2;    %... FzRL covar
Q4 = 1e2;    %... FzRR covar
Q5 = 1e-1;   %... long. acceleration covar
Q6 = 1e-3;   %... d(long. acceleration)/dt covar
Q7 = 1e-1;   %... lat. acceleration covar
Q8 = 1e-3;   %... d(lat. acceleration)/dt covar
Q_v = [Q1 Q2 Q3 Q4 Q5 Q6 Q7 Q8];
Q = diag(Q_v,0);   %Make diagonal matrix

R1 = 1e-1;   %Measurement Fz,l covar
R2 = 1e2;    %... sum Fzf covar
R3 = 1e-2;   %... long. acceleration covar
R4 = 1e-2;   %... lat. acceleration covar
R5 = 1e2;    %... total vehicle weight covar
R_v = [R1 R2 R3 R4 R5];
R = diag(R_v,0);   %Make diagonal matrix

% Nonlinear State Evolution Function
f = @(X) [X(1)+T*(-m*hcg/2/L*X(6)-
m*b*hcg/L/w1*X(8)+m*hcg^2/L/w1/g*X(5)*X(8)+m*hcg^2/L/w1/g*X(6)*X(7));

          X(2)+T*(-m*hcg/2/L*X(6)+m*b*hcg/L/w1*X(8)-m*hcg^2/L/w1/g*X(5)*X(8)-
m*hcg^2/L/w1/g*X(6)*X(7));

          X(3)+T*(m*hcg/2/L*X(6)-m*b*hcg/L/w1*X(8)-m*hcg^2/L/w1/g*X(5)*X(8)-
m*hcg^2/L/w1/g*X(6)*X(7));

X(4)+T*(m*hcg/2/L*X(6)+m*b*hcg/L/w1*X(8)+m*hcg^2/L/w1/g*X(5)*X(8)+m*hcg^2/L/w1/g*X(6)*X(7));
          X(5)+T*X(6);

          X(6);
```

```
          X(7)+T*X(8);
```

```
          X(8)];

% Measurement Function
h = @(X) [X(1)-X(2)+X(3)-X(4);
          X(1)+X(2);
          X(5);
          X(7);
          X(1)+X(2)+X(3)+X(4)];

% Jacobian, State Evolution Function
A = [ 1, 0, 0, 0,  (T*x(8)*hcg^2*m)/(L*g*w1), -T*((hcg*m)/(2*L) - (x(7)*hcg^2*m)/(L*g*w1)),
(T*x(6)*hcg^2*m)/(L*g*w1), -T*((b*hcg*m)/(L*w1) - (x(5)*hcg^2*m)/(L*g*w1));
```

```
      0, 1, 0, 0, -(T*x(8)*hcg^2*m)/(L*g*w1), -T*((x(7)*m*hcg^2)/(L*g*w1) + (m*hcg)/(2*L)), -
(T*x(6)*hcg^2*m)/(L*g*w1),  T*((b*hcg*m)/(L*w1) - (x(5)*hcg^2*m)/(L*g*w1));
```

```
      0, 0, 1, 0, -(T*x(8)*hcg^2*m)/(L*g*w1),  T*((hcg*m)/(2*L) - (x(7)*hcg^2*m)/(L*g*w1)), -
(T*x(6)*hcg^2*m)/(L*g*w1), -T*((x(5)*m*hcg^2)/(L*g*w1) + (b*m*hcg)/(L*w1));
```

```
      0, 0, 0, 1,  (T*x(8)*hcg^2*m)/(L*g*w1),  T*((x(7)*m*hcg^2)/(L*g*w1) + (m*hcg)/(2*L)),
(T*x(6)*hcg^2*m)/(L*g*w1),  T*((x(5)*m*hcg^2)/(L*g*w1) + (b*m*hcg)/(L*w1));
```

```
      0, 0, 0, 0, 1, T, 0, 0;
```

```
      0, 0, 0, 0, 0, 1, 0, 0;
      0, 0, 0, 0, 0, 0, 1, T;
      0, 0, 0, 0, 0, 0, 0, 1];

% Jacobian, Measurement Function
H = [ 1, -1, 1, -1, 0, 0, 0, 0;
      1,  1, 0,  0, 0, 0, 0, 0;
      0,  0, 0,  0, 1, 0, 0, 0;
      0,  0, 0,  0, 0, 0, 1, 0;
      1,  1, 1,  1, 0, 0, 0, 0];

% Time update
x = f(x);
P = A*P*A'+Q;

% Measurement update
K = P*H'/(H*P*H'+R);
x = x+K*(y-h(x));
P = (eye(8)-K*H)*P;
```

9.2.3.4 VERTICAL FORCE ESTIMATION BLOCK WITH I/O

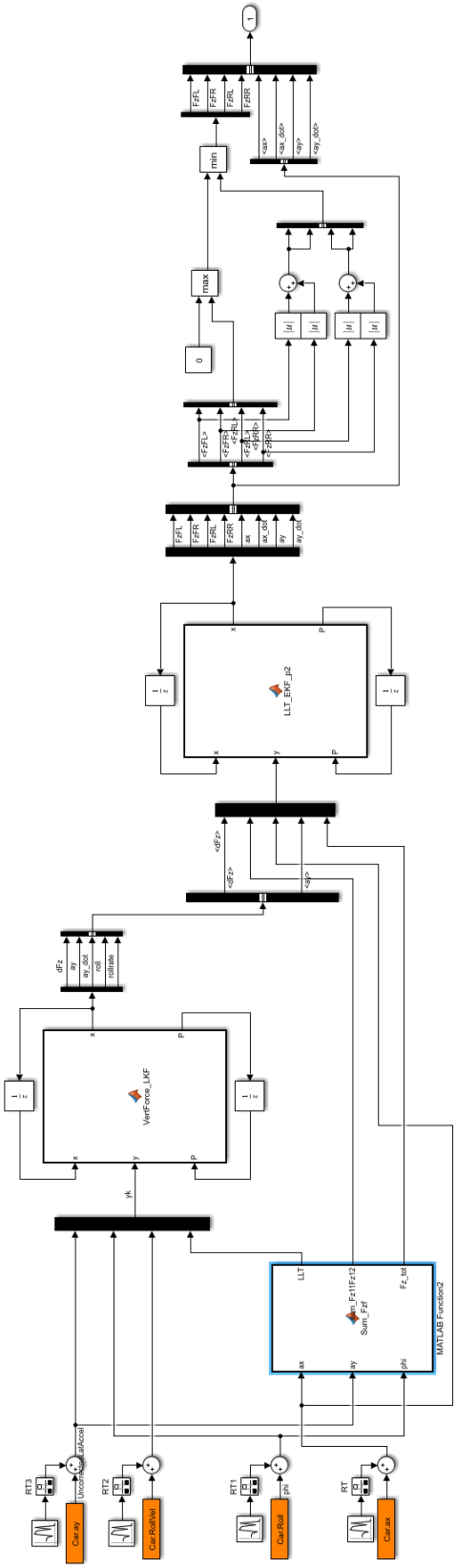

10 BIBLIOGRAPHY

[1] A. Sorniotti, L. De Novellis and P. Gruber, "Torque Vectoring for Electric Vehicles with Individually Controlled Motors: State-of-the-Art and Future Developments," in *International Battery, Hybrid and Fuel Cell Electric Vehicle Symposium*, Los Angeles, 2012.

[2] H. Fujimoto, K. Fujii and N. Takahashi, "Vehicle stability control of electric vehicle with slip-ratio and cornering stiffness estimation," in *IEEE/ASME International Conference on Advanced Intelligent Mechatronics*, 2007.

[3] "Traffic Safety Facts Annual Report Tables," 11 January 2019. [Online]. Available: https://cdan.nhtsa.gov/tsftables/tsfar.htm.

[4] R. Rajamani, Vehicle Dynamics and Control, Springer, 2012.

[5] R. Ghandour and A. Victorino, "Tire/Road Friction Coefficient Estimation Applied to Road Safety," in *18th Mediterranean Conference on Control and Automation (MED)*, 2010.

[6] J. Dixon, Tires, Suspension, and Handling, London: Society of Automotive Engineers, 1996.

[7] U. Kiencke and L. Nielsen, Automotive Control Systems: For Engine, Driveline, and Vehicle, Berlin: Springer, 2005.

[8] J. Park, H. Jeong, I. Gyu Jang and S.-H. Hwang, "Torque Distribution Algorithm for an Independently Driven Electric Vehicle Using a Fuzzy Control Method," *Energies*, pp. 8537-8561, 2015.

[9] W. Sun, J. Wang, Q. Wang, F. Assadian and B. Fu, "Simulation investigation of tractive energy conservation for a cornering rear-wheel-independent-drive electric vehicle through torque vectoring," *Science China Technological Science*, pp. 257-272, 2018.

[10] M. Dendaluce, I. Iglesias, A. Marin, P. Prieto and A. Pena, "Race-Track Testing of a Torque Vectoring Algorithm on a Motor-in-wheel Car Using a Model-Based Methodology with a HiL and Multibody Simulator Setup," in *IEEE 19th International Conference on Intelligent Transportation Systems*, 2016.

[11] F. Chunyun, "Direct Yaw Moment Control for Electric Vehicles with Independent Motors," RMIT University, 2014.

[12] K. H, P. Luque Rodriguez, D. Alvarez Mantaras, J. Wideberg and S. Bendre, "Obtaining Desired Vehicle Dynamics Characteristics with Independently Controlled In-Wheel Motors: State of Art Review," *Society of Automotive Engineers International Journal of Passenger Cars*, pp. 413-425, 2017.

[13] L. De Novellis, A. Sorniotti, P. Gruber and A. Pennycott, "Comparison of feedback control techniques for torque-vectoring control of fully electric vehicles," *IEEE Transactions on Vehicular Technology*, pp. 3612-3623, 2014.

[14] S. Ding, L. Liu and W. Zheng, "Sliding Mode Direct Yaw-Moment Control for In-Wheel Electric Vehicles," *IEEE Transactions on Industrial Electronics*, pp. 6752-6762, 2017.

[15] L. Yue-Lin, H. Ping-Wen and X. Tao, "A Research on Adaptive Neural Network Control Strategy of Vehicle Yaw Stability," in *Fourth International Conference on Intelligent Systems Design and Engineering Application*, 2013.

[16] M. Ghezzi, A. Doria-Cerezo and J. Olm, "Yaw moment MRAC with optimal torque vectoring for a four in-wheel motor EV," in *IEEE International Conference on Industrial Technology (ICIT)*, 2018.

[17] L. De Novellis, A. Sorniotti and P. Gruber, "Wheel Torque Distribution Criteria for Electric Vehicles with Torque-Vectoring Differentials," *IEEE Transactions on Vehicular Technology*, pp. 1593-1602, 2014.

[18] E. Sabbioni, "Comparison of Torque Vectoring Control Strategies for a IWM Vehicle," *SAE International Journal of Passenger Cars*, pp. 565-572, 2014.

[19] V. &. L. Siampis, "Model Predictive torque vectoring control for electric vehicles near the limits of handling," in *European Control Conference (ECC)*, 2015.

[20] J. Gosh, A. Tonoli, N. Amati and W. Chen, "Sideslip Angle Estimation of a Formula SAE Racing Vehicle," *SAE International Journal of Passenger Cars*, pp. 944-951, 2016.

[21] C. Chatzikomis, A. Sorniotti, P. Gruber, M. Zanchetta, D. Willians and B. Balcombe, "Comparison of Path Tracking and Torque-Vectoring Controllers for Autonomous Electric Vehicles," *IEEE Transactions on Intelligent Vehicles*, p. 1, 2018.

[22] A. Parra, A. Zubizarreta, J. Perez and M. Dendaluce, "Intelligent Torque Vectoring Approach for Electric Vehicles with Per-Wheel Motors," *Complexity*, p. 14, 2018.

[23] T. Goggia, A. Sorniotti, L. De Novellis, A. Ferrara, P. Gruber, J. Theunissen and e. al., "Integral Sliding Mode for the Torque-Vectoring Control of Fully Electric Vehicles: Theoretical Design and Experimental Assessment," *IEEE Transactions on Vehicular Technology*, pp. 1701-1715, 2015.

[24] K. Jalali, T. Uchida, S. Lambert and K. Mcphee, "Development of an Advanced Torque Vectoring Control System for an Electric Vehicle with In-Wheel Motors using Soft Computing Techniques," *SAE International Journal of Alternative Powertrains*, pp. 261-278, 2013.

[25] G. Kaiser, M. Korte, Q. Liu, C. Hoffmann and H. Werner, "LPV Torque Vectoring for an Electric Vehicle with Experimental Validation," in *The International Federation of Automatic Control (IFAC)*, Cape Town, 2014.

[26] J. Ahmadi, A. Sedigh and M. Kabganian, "Adaptive Vehicle Lateral-Plane Motion Control Using Optimal Tire Friction Forces with Saturation Limits Considerations," *IEEE Transactions on Vehicular Technology*, pp. 4098-4107, 2009.

[27] C. Fu, R. Hoseinnezhad, K. Li and M. Hu, "A novel adaptive sliding mode control approach for electric vehicle direct yaw-moment control," *Advances in Mechanical Engineering*, vol. 10, no. 10, pp. 1-12, 2018.

[28] R. Yusef Hindiyeh, "Dynamics and Control of Drifting in Automobiles," Stanford University, 2013.

[29] M. Doumiati, Vehicle Dynamics Estimation using Kalman Filtering: Experimental Validation, 2012.

[30] M. Acosta and S. Kanarachos, "Tire lateral force estimation and grip potential identification using Neural Networks, Extended Kalman filter, and Recursive Least Squares," *Neural Computing & Applications*, pp. 1-21, 2017.

[31] M. Acosta, S. Kanarachos and M. Fitzpatrick, "A Virtual Sensor for Integral Tire Force Estimation using Tire Model-less Approaches and Adaptive Unscented Kalman Filter," in *ICINCO*, 2017.

[32] E. Bakker, L. Nyborg and H. Pacejka, "Tyre Modelling for Use in Vehicle Dynamics Studies," SAE Technical Paper Series, 1987.

[33] H. Dugoff, P. Fancher and L. Segel, "Tire Performance Characteristics Affecting Vehicle Response to Steering and Braking Control Inputs," Highway Safety Research Institute, Ann Arbor, 1969.

[34] H. Dugoff, P. S. Fancher and L. Segel, "Tire Performance Characteristics Affecting Vehicle Response to Steering and Braking Control Inputs," Highway Safety Research Institute, Ann Arbor, 1969.

[35] H. Pacejka, Tire and Vehicle Dynamics, Elsevier Science, 2012.

[36] S. o. A. Engineers, "SAE J1733: Sign Convention for Vehicle Crash Testing," 1994. [Online]. Available: https://archive.org/details/gov.law.sae.j1733.1994. [Accessed 25 May 2019].

[37] J. Fabijanic, "Ground Vehicle Dynamics: Tires, Rolling Resistance, and More," San Luis Obispo, 2018.

[38] C. Chatzikomis, A. Sorniotti and P. Gruber, "Torque-Vectoring Control for an Autonomous and Driverless Electric Racing Vehicle with Multiple Motors," *SAE International Journal of Vehicle Dynamics, Stability, and NVH*, pp. 338-351, 2017.

[39] A. Bhoraskar and P. Sakthivel, "A Review and a Comparison of Dugoff and Modified Dugoff Formula with Magic Formula," in *International Conference on Nascent Technologies in the Engineering Field*, 2017.

[40] "FSE_Define_MotorCharacteristics," IPG Automotive, Karlsruhe, 2011.

[41] J. Gonzales, "Planning and Control of Drift Maneuvers with the Berkeley Autonomous Race Car," University of California, Berkeley, Berkeley, 2018.

[42] S. Ding, L. Liu and W. X. Zheng, "Sliding Mode Direct Yaw-Moment Control Design for In-Wheel Electric Vehicles," *IEEE Transactions on Industrial Electronics,* vol. 64, no. 8, pp. 6752-6763, 2017.

[43] M. Wielitzka, M. Dagen and T. Ortmaier, "Joint Unscented Kalman Filter for State and Parameter Estimation in Vehicle Dynamics," in *IEEE Conference on Control Applications*, Sydney, 2016.

[44] A. Rezaeian and e. al., "Novel Tire Force Estimation Strategy for Real-Time Implementation on Vehicle Applications," *IEEE Transactions on Vehicular Technology,* vol. 64, no. 6, pp. 2231-2241, 2015.

[45] "Pd18 Datasheet," Protean Electric, May 2018. [Online]. Available: https://www.proteanelectric.com/f/2018/05/Pd18-Datasheet-Master.pdf. [Accessed 28 May 2019].

[46] "Product Navigator," Maxon Motor, 2019. [Online]. Available: https://www.maxonmotor.com/maxon/view/product/motor/ecmotor/ecflat/ecflat45/411812. [Accessed 28 May 2019].

[47] A. Cherukuri, E. Mallada and J. Cortes, "Asymptotic convergence of constrained primal-dual dynamics," *Systems & Control Letters,* vol. 87, pp. 10-15, 2016.

[48] D. Feijer and F. Paganini, "Stability of primal-dual gradient dynamics and applications to network optimization," *Automatica,* vol. 46, pp. 1974-1981, 2010.

[49] W.-T. Chu, "Algorithms for Constrained Optimization," 2015. [Online]. Available: https://www.cs.ccu.edu.tw/~wtchu/courses/2015s_OPT/Lectures/Chapter%2023%20Algorithms%20for%20Constrained%20Optimization.pdf. [Accessed 4 June 2019].

[50] W. Cho, J. Yoon, S. Yim, B. Koo and K. Yi, "Estimation of Tire Forces for Application to Vehicle Stability Control," *IEEE Transactions on Vehicular Technology,* vol. 59, no. 2, pp. 638-649, 2010.

[51] D. Gingras, "Lectures on Autonomous Vehicles and Driving Automation," San Luis Obispo, 2019.